Relating Mechanical and Genetic Data at Single Cell Level across the Genome to Investigate Metastasis

A Dissertation Presented to
The Academic Faculty

By

Katherine Monnet Young

In Partial Fulfillment of the Requirements
for the Degree Doctor of Philosophy in the
Wallace H. Coulter Department of Biomedical Engineering

Georgia Institute of Technology
Emory University

December 2021

Copyright © 2021 by Katherine M. Young

Relating Mechanical and Genetic Data at Single Cell Level across the Genome to Investigate Metastasis

Approved by:

Dr. Todd Sulchek
George W. Woodruff School of Mechanical Engineering
Georgia Institute of Technology

Dr. James Dahlman
Wallace H. Coulter Department of Engineering
Georgia Institute of Technology and Emory University

Dr. John McDonald
School of Biology
Georgia Institute of Technology

Dr. Peng Qiu
Wallace H. Coulter Department of Engineering
Georgia Institute of Technology and Emory University

Dr. Wilbur Lam
Wallace H. Coulter Department of Engineering
Georgia Institute of Technology and Emory University

Date Approved: November 17, 2021

To all those who came before me:
You have shaped this work because you have shaped me.

Grandpa Bill, metastasis prevented us from meeting, but your life and death inspired me to make a career out of making cancer less sad.

I dedicate this thesis to my family and friends who are a constant source of encouragement, joy, and love – I would not be who or where I am today without all of you.

ACKNOWLEDGMENTS

I would like to sincerely thank and acknowledge the many people who made this work possible, who helped me grow as a scientist and researcher, and who supported me through the entire graduate education process.

Thank you to my advisor, Todd Sulchek, who created a supportive environment for me to thrive as an independent thinker. Your enthusiasm and curiosity about the world first drew me to your lab and your mentorship has pushed me to think deeply about problems in our field as well as encouraged me to pursue my own career as an academic. I know my future lab will be shaped greatly by the wonderful five years I have spent as a “Toddler”.

Thank you to my thesis committee members, John McDonald, James Dahlman, Peng Qiu, and Wilbur Lam. You have all supported me and helped expand my work by your expertise in other fields. Thank you for always being so willing to offer help in areas where I needed expert biologists, physicians, and engineers.

Thank you to the BME faculty and staff who have supported me both as a graduate student and as a whole person and for creating a department that truly cares about inclusion and building community. To Shannon Sullivan for being a listening ear, to Kyla Ross who encouraged me to be a bridge between students and faculty and always caring about the student experience, to Susan Margulies for being an excellent chair and role model, and to Joe LeDoux for being an excellent educator and meeting with me regularly to help me grow as an educator.

I would also like to thank a number of Georgia Tech faculty and administrators, including Kate Williams for inspiring so many students to learn how to teach in a way that helps students learn, as well as Steve McLaughlin, Raheem Beyah, and Larry Jacobs for organizing the College of Engineering Advisory Board and truly caring about improving the graduate student experience at our institute.

Thank you to the Petit Institute staff and core facilities who have made the IBB building feel like a second home. Thank you to Michelle Wong for your support and friendship, to Colly Mitchell for being a truly great communicator, and to Laura Paige for accepting me as an honorary BioE student. Thanks as well to Sommer Durham, Dalia Arafat, Andrew Shaw, Naima Djeddar, Shweta Bilya, and Anton Bryskin for your support with running experiments, teaching me to use equipment, and general support in experimental planning and execution.

Many, many thanks to my wonderful lab mates. I have been shaped so much by our friendships and have grown as a scientist because of our (extended) time together in lab. Thank you to Tom Bongiorno for setting me up so well as a first year student and teaching me so much about atomic force microscopy and single cell technologies. I have really enjoyed being the “new Tom”! Thank you to Anna Liu for being such a great example of a strong woman in science, for choosing me as your close friend, and continuing to love and support me though our many adventures, from watching Chef at CMBE to bioluminescent algae excursions to your beautiful wedding festivities. Thank you to Nick Stone for always making me feel like an important part of the group, giving me a desk in the Kat Kave on my

first day in the lab, for being a great sounding board for scientific ideas, for supplying much of the custom code for the lab, and for being a great lifelong friend. Thank you to the other Kat Kave members, Kathryn Murray and Katily Ramirez – I am so grateful for each of your friendships. Thank you to Aaron Enten for always making us laugh (and sometimes groan) at your jokes and for being a wonderful host of many get-togethers. Thank you to Alan Liu for being my AFM buddy, for imparting so much of your wisdom to me and our many undergrads, and for inviting us all to your wedding in Taiwan, a trip I will never forget. Thank you to Tong Yu for being an excellent biologist and for bringing your whole self to lab, you are a great friend, researcher, and mom. Thank you to Mike Bellavia and Shawn Newlan for the great memories in lab and out. Thank you to Peter Shankles, not only for your tremendous help in generating, iterating, and fabricating the designs for the multiplex device and for your help with microfluidic operation and cell tracking, but also for being my bike buddy. Thank you to Dan Potter, Betsy Campbell, Bushra Tasadduq, Muhymin Islam, Srinivas Hanasoge, and Abhishek Raj for being wonderful coworkers and friends. Thank you as well to Avi Gupta, Adi Pall, and Steven Swingle – I am excited to see the rise of the next generation of Toddlers and I know you all will continue the great research happening in our lab.

Thank you to the many undergraduate students I had the pleasure of working with and mentoring over the years. I learned so much from getting to know each of you and grew as a mentor and teacher because of our time together, including many hours in the AFM room. Thank you to Jill Ortner, Maureen McGough,

Nathan Palmer, Vaish Andra, Eric Biederman, Kyle Turbyfield, Alex Chapman, Lilly King, and Varun Rajagopal for your hard work and friendship. Thank you to Sydney Bules, Jimmy Hankish, Mariana Holguin-Lopez, and Kelly Ahkee for your specific help on much of the work on the temporal dynamics of cell death mechanics as well as single cell genomechanics PCR primer validation. Thank you to Saif Kabariti for your work on the linear elastography work and to Nicole Latka for your bioinformatics and PCR help on the viscosity regulators project.

Thank you to my many collaborators for inviting me into your projects and helping me on my own work. Thank you to Congmin Xu in Peng Qiu's lab for your valuable help on the principal component analysis in the single cell genomechanics project, to Dahlman lab members Curtis Dobrowolski for your help processing and interpreting my sequencing data and to Kalina Paunovska for your tremendous help in making the GeCKO mechanics project happen as well as for your sweet friendship. Thank you to the many Forest lab members who helped me with micropipette aspiration of single cells, including Corey Landry, Mighten Yip, and Colby Lewellen. Thank you to the McDonald lab for accepting me and Nick as honorary lab members and teaching us so much about cancer biology – thank you DeEtte Walker, Lilya Matyunina, Minati Satapathy, Evan Clayton, and Mengnan Zhang. Thank you to the Ethier lab for being excellent lab wing neighbors, for lending us materials, and teaching me a number of molecular biology techniques – thank you specifically to Eric Snider, Lisa Schildemeyer, Tom Read, and Ke Wang. Thank you to Roman Mezencev for your help with the network analysis project.

Thank you as well to the collaborators who reached out to include our lab in your work – Fatima Chrit, Fang Ni, Meredith Fay, Olga Chernaya, Primal de Lanerolle, and Aaron Simmons.

I will be forever grateful to the many friends I made here in Atlanta who made my time in grad school some of the most joyous years of my life. Thank you so much to my random roommate turned best friend, Katie Birmingham – I couldn't have imagined a better friend and adventure buddy to do life with for four years. From puzzling and watching Grace & Frankie, to beach trips and New York excursions, and to many great conversations, I will always remember grad school fondly because of the memories I made with you! Thank you to my loving Ponce Presbyterian Church community who made me feel welcomed from day one and always points me back to the love of Christ – many special thanks to the Pickren family for loving me like a third daughter, to Tolivar Wills for pastoring well, and to my community group and bible study family for the many sweet memories of doing life together (too many kind friends to even name all here!). Thank you to my Young Life team and partners in ministry, I have loved getting to love on middle school and high school students with y'all – special thanks to G and Neosha Lawhorn for inviting me into your family and helping me live out my dream of spending time at Young Life camp, to Kristin Grimaud for your steadfast commitment to Midtown Atlanta students, and to Stacy Mosby for your invaluable friendship and leadership. Thank you to my many grad school friends who have made this experience so enjoyable – to Abby Paulson for being my best friend

from the moment we went to the Buzz Card office together during orientation, to Veronica Montgomery, Alyssa Pybus, Kristie Garza, and Sitara Sankar for helping me appreciate literature and fancy things, and to Seleipiri Charles and Lauren Sestito for both being great friends. Thank you to my lifelong friends who are always willing to talk with me on the phone and stay connected when we live far away – Catherine Pierce, Alyssa Russell, and Laura Strong. Thank you to my Atlanta friends who made life here feel so full – Maddie Collmus, Rachel Furnish, Crystal Gillett, Miriam Gutman, Krithika Shanmugashandaram, and Becca Kiriazes. Life is so much better because all of you are in it.

Finally, thank you so much to my wonderful family who has fostered in me a love of learning, a love of others, and a love of Jesus. Thank you to my grandparents who are no longer with us, Terry Young and Jean and Bill Cunningham, I hope to carry on your legacies of love. Thank you to June Young, my Grammie, for loving and leading our family well as the beautiful and adventurous matriarch. Thank you to my many aunts, uncles, and cousins for making my childhood so much fun and continuing to support me as we all grow up together. And the biggest of thanks to my fellow Seasons of Young bandmates, Mitch, Jeannette, and Caroline Young. Thank you for your constant encouragement and support to follow my passions, even to the other side of the country. I know I can always count on you all to make me feel loved and cared for.

Many, many thanks to all listed here and the many others who also supported me along the way. I am the person and scientist I am today because of each of you.

TABLE OF CONTENTS

ACKNOWLEDGMENTS iv

LIST OF TABLES xiv

LIST OF FIGURES xv

LIST OF ABBREVIATIONS xx

SUMMARY xxiv

CHAPTER 1 – INTRODUCTION 1

1.1 – Understanding Cancer Metastasis at the Intersection of Mechanotype, Phenotype, and Genotype 1

1.2 – Research Motivation and Significance 2

1.3 – Dissertation Overview 6

CHAPTER 2 – BACKGROUND 11

2.1 – The Metastatic Spread of Cancer 11

2.2 – Cell Mechanics 14

2.3 – Single Cell Techniques 16

2.4 – Genome-Scale CRISPR Knockout (GeCKO) Screening 19

2.5 – Previous Supporting Studies 19

CHAPTER 3 – SINGLE CELL GENOMECHANICS: METHOD DEVELOPED TO GENERATE HYPOTHESES RELATING CANCER CELL MECHANOTYPE, GENOTYPE, AND PHENOTYPE 30

3.1 – Abstract 30

3.2 – Introduction 31

3.3 – Materials and Methods 33

3.4 – Results 41

3.5 – Discussion 71

CHAPTER 4 – SCALING COMPLEX MICROFLUIDICS BY MULTIPLEXING WITH PASSIVE FLOW CONTROL FOR IMPROVED THROUGHPUT 75
4.1 – Abstract 75
4.2 – Introduction 76
4.3 – Materials and Methods 80
4.4 – Results 90
4.5 – Discussion 102

CHAPTER 5 – GECKO MECHANICS: GENOME-SCALE CRISPR KNOCKOUT SYSTEM TO EXPLORE GENOMECHANICAL RELATIONSHIPS 106
5.1 – Abstract 106
5.2 – Introduction 107
5.3 – Materials and Methods 110
5.4 – Results 120
5.5 – Discussion 127

CHAPTER 6 – HYPOTHESIS TESTING TO EXPLORE PHENOTYPIC AND MECHANOTYPIC IMPORTANCE OF GENES OF INTEREST 131
6.1 – Abstract 131
6.2 – Introduction 132
6.3 – Materials and Methods 133
6.4 – Results 141
6.5 – Discussion 169

CHAPTER 7 – EXPLORING THE RELATIONSHIP BETWEEN CELL PHENOTYPE AND MECHANOTYPE BEYOND THE METASTATIC CONTEXT 174
7.1 – Introduction 174
7.2 – Mechanical Properties of Healthy Cells 174
7.3 – Mechanical Properties of Diseased Cells 189
7.4 – Mechanical Properties of Dying Cells 210
7.5 – Conclusions 223

CHAPTER 8 – CONCLUSIONS 225
8.1 – Summary 225
8.2 – Next Steps, Future Work, and Further Applications 226

REFERENCES..... 232

LIST OF TABLES

Table 1 – Curated list of genes of interest.....44

Table 2 – PCR primers for list of genes of interest 56

Table 3 – Network analysis reveals master regulators that could control cell stiffness..... 142

Table 4 – miR183 expression levels after transfection 147

Table 5 – Network analysis reveals master regulators that could control cell fast viscous time constant (tau1) 156

Table 6 – Network analysis reveals master regulators that could control cell slow viscous time (tau2) 157

LIST OF FIGURES

Figure 1 – Thesis overview in three aims.....8

Figure 2 – Ovarian cell stiffness correlates with potential for migration and invasion.....21

Figure 3 – Microfluidic device for sorting cells based off of biophysical properties 24

Figure 4 – Genomechanics raft manufacturing.....25

Figure 5 – Cell localization optimization 27

Figure 6 – Development of new method to combine single cell morphological, mechanical, and gene expression data 43

Figure 7 – Example video of cell isolation using micropipette aspiration 44

Figure 8 – Comparison of mechanical properties of ovarian cancer cell lines.....48

Figure 9 – No change in mechanics over time of experiment.....48

Figure 10 – Epithelial and mesenchymal morphology for populations.....50

Figure 11 – Violin plots of the distribution of normalized single cell gene expression data for each cell type and each gene of interest 52

Figure 12 – Population vs. single cell gene expression.....53

Figure 13 – Comparing gene expression of cells isolated by FACS sorting and micropipette aspiration.....55

Figure 14 – FACS vs. micropipette cell isolation 56

Figure 15 – Comparison of population behavior of HEY A8, HEY, and OVCAR3 cell lines 60

Figure 16 – Single cell gene expression profiles for each cell type and each gene of interest.....61

Figure 17 – Single cell correlations between genetic, morphological and mechanical parameters 63

Figure 18 – Single cell correlations between genetic, morphological and mechanical parameters for each cell type 65

Figure 19 – Single data type measurements insufficient but combining data types improves cell type clustering 70

Figure 20 – Device parallelization allows for linear improvement of processing throughput 78

Figure 21 – Design process for linearizing and parallelizing microfluidic stiffness-based sorting device for increased throughput. 79

Figure 22 – Modeling microfluidic device enables balancing of volumetric output to each outlet 93

Figure 23 – Top manifold layer evenly splits fluid flow to bottom multiplex device layer 96

Figure 24 – Heat treatment of cells used as model system for separating soft and stiff cells 98

Figure 25 – Flow rate optimization using cell trajectory analysis for single device 99

Figure 26 – Sorting enrichment maintained when multiplexing 100

Figure 27 – Sorting purity and cell yield maintained when multiplexing 101

Figure 28 – Throughput and processing time are greatly improved with multiplexing 101

Figure 29 – Schematic overview of GeCKO mechanical screen 110

Figure 30 – Cas9-expressing cells capable of gene editing 121

Figure 31 – Cell mechanical changes due to single gene knockouts could be sorted by microfluidic device 123

Figure 32 – Cell distribution to each outlet for GeCKO mechanical sort bio-replicates 124

Figure 33 – DESeq2 analysis reveals hundreds of genes enriched in mechanically sorted subpopulations 126

Figure 34 – Network of genes predicted to be under the control of stiffness master regulators 143

Figure 35 – Changes in *MIR183* expression result in cell stiffness changes in cell type specific manner 148

Figure 36 – Gene expression did not change as expected with *MIR183* overexpression and inhibition 150

Figure 37 – Cell stiffening 17-ODYA treatment results in gene expression changes that are slight, but consistent with predictions and reduces cell migration 152

Figure 38 – *MIR520c* acts as a cell softener contrary to prediction, but the gene expression changes are consistent with predicted changes 154

Figure 39 – Network of genes predicted to be under the control of tau1 master regulators 158

Figure 40 – Network of genes predicted to be under the control of tau2 master regulators 159

Figure 41 – *AKT2* inhibition results in increase of tau1 as predicted..... 162

Figure 42 – Lacidipine does not increase tau1 as predicted 164

Figure 43 – *ITGB6* knockdown leads to slight, but not significant, decrease in tau2 as predicted 166

Figure 44 – AG879 decreases tau2 as predicted for the HEY A8 cell line..... 168

Figure 45 – Schematic of cell permeabilization and volume loss, subsequent recovery, and repeated volume exchange with compressions 175

Figure 46 – AFM measurement of leukocyte and epithelial cell mechanical properties 176

Figure 47 – Relationship between cell viscoelastic properties and volume loss178

Figure 48 – Biophysical properties of PBMCs characterized using AFM..... 180

Figure 49 – Embryonic stem cells become stiffer during differentiation..... 181

Figure 50 – Cytoskeleton remodeling during differentiation 183

Figure 51 – Good CPC differentiators are less adhesive..... 188

Figure 52 – As differentiation potential decreases, stiffness of soft subpopulation of cells decreases..... 188

Figure 53 – Loss of Ptpn21 Decreases Cell Stiffness and Increases Mobility in HSCs..... 191

Figure 54 – Changes in actomyosin cytoskeleton associated with loss of CCM protein expression result in increased stiffness of cells with knockdown of *KRIT1* and *CCM2* but not *PDCD10* 193

Figure 55 – Netarsudil (NT) reduced steroid-induced trabecular meshwork (TM) stiffening measured directly by atomic force microscopy (AFM)..... 195

Figure 56 – Images and linear elastographies of ovarian cancer cell lines (HEY A8, HEY), and breast cancer cell lines (MCF10-A, MCF10-CA) 198

Figure 57 – Modulus values of the perinuclear region and lamellipodia region for three MCF10-A cells (non-malignant) and three MCF10-CA cells (metastatic) 199

Figure 58 – Sorting of primary ascites samples 203

Figure 59 – Breast cancer cell stiffness negatively correlated with *MYLK* expression and cell aggressiveness 205

Figure 60 – Nuclear actin filament formation possibly associated with cell softening 208

Figure 61 – Force mapping reveals negative correlation between stiffness measurements and fluorescent intensity of labelled actin 209

Figure 62 – Large stiffness changes observed in necrotic cells after 5 minutes of 65°C heat treatment 212

Figure 63 – Fast stiffness change response also observed in apoptotic cells heated to 42°C on AFM stage 214

Figure 64 – Temporal dynamics of mechanical changes observed in chemotherapeutic-treated cells..... 215

Figure 65 – Pyroptosis induced cells show significant increase in cell stiffness218

Figure 66 – Mechanical properties of viable and nonviable Jurkat cells after heat treatment from AFM measurement 221

Figure 67 – PCA analysis of nonviable and viable cells based on cell trajectory features in microfluidic device 223

LIST OF ABBREVIATIONS

17-ODYA – 17-octadecynoic acid

AFM – atomic force microscopy

ANOVA – analysis of variance

BLAST – Basic Local Alignment Search Tool

BSA – bovine serum albumin

$CaCl_2$ – calcium chloride

CAD – computer aided design

CCM – cerebral cavernous malformation

cm - centimeter

CO_2 – carbon dioxide

CRISPR – clustered regularly interspaced short palindromic repeats

C_t – cycle threshold

CTC – circulating tumor cell

CSC – cancer stem cell

cDNA – complementary DNA

DAVID – Database for Annotation, Visualization, and Integrated Discovery

DB index – Davies-Bouldin index

DMSO – dimethyl sulfoxide

DNA – deoxyribonucleic acid

EASE – Expression Analysis Systematic Explorer

ECM – extracellular matrix

EDTA – Ethylenediaminetetraacetic acid

EMT – epithelial-to-mesenchymal transition

Er – Ericksen number

ESC – embryonic stem cell

FACS – fluorescent activated cell sorting

FBS – fetal bovine serum

FEA – finite element analysis

GeCKO – genome-scale CRISPR knockout

GFP – green fluorescent protein

hiPSCs – human induced pluripotent stem cells

HKG – housekeeping gene

HSC – hematopoietic stem cell

ID – inner diameter

in – inch

KD – knockdown

KEGG – Kyoto Encyclopedia of Genes and Genomes

mbar – millibar

MET – mesenchymal-to-epithelial transition

MFI – mean fluorescence intensity

mg – milligram

$MgCl_2$ – magnesium chloride

min – minute

mL – milliliter

mm – millimeter

mM – millimolar

MMP – matrix metalloproteinase

MOI – multiplicity of infection

ms – millisecond

MYLK – myosin light chain kinase

µg – microgram

µL – microliter

µm – micrometer

µM – micromolar

µs – microsecond

NGS – next generation sequencing

nm – nanometer

nM – nanomolar

nN – nanonewton

NT – netarsudil

OD – outer diameter

Pa – Pascal

PBS – phosphate buffered saline

PCA – principal components analysis

PDMS – polydimethylsiloxane

PL – placebo

PLS – partial least squares

pN – piconewton

RIE – reactive ion etching

RIGER – RNA Interference Gene Enrichment Ranking

RNA – ribonucleic acid

ROCK – rho-associated protein kinase

rpm – rotations per minutes

RT-qPCR – reverse transcriptase quantitative polymerase chain reaction

s – second

scRNA-Seq – single cell RNA sequencing

sgRNA – single guide RNA

shRNA – short hairpin RNA

tau1 – fast viscous time constant

tau2 – slow viscous time constant

TIDE – Tracking of Indels by Decomposition

TM – trabecular meshwork

TSG – tumor suppressor gene

VECT – volume exchange for convective transfer

v/v – volume per volume

WT – wild type

SUMMARY

Nine out of every ten cancer-related deaths is caused by metastasis, but the molecular mechanisms driving this process are still not fully understood. Several studies have implicated that as a cell's metastatic potential increases, cell stiffness decreases. Yet while certain genes that affect cell mechanics have been studied, a genome-wide study of networks that modulate cell biophysical properties has not been attempted. The long-term goal of this research is to understand the molecular and mechanical mechanisms driving metastasis. To reach this goal, a new methodology was developed to combine mechanical and gene expression data for the same single cells. Additionally, a novel microfluidics approach for cell sorting based upon biophysical properties was leveraged for the high-throughput discovery of genes linked to cell mechanics and metastasis. These approaches led to deeper understanding of how cellular mechanics are regulated within the context of networks of genes associated with increased metastatic potential. I investigated this intersection through the following aims: 1) Create and validate a combined single cell mechanics and gene expression methodology, 2) Identify genes related to mechanical changes in cancer cells through GeCKO high-throughput mechanical screen, and 3) Validate phenotypic and mechanotypic importance of genes of interest.

CHAPTER 1 – INTRODUCTION

1.1 – Understanding Cancer Metastasis at the Intersection of Mechanotype, Phenotype, and Genotype

Cancer cell softening has been demonstrated in many different cell types and it has been shown that as metastatic potential increases, cell stiffness will decrease[1,2]. Because of the relation between disease state and cell mechanics, cell stiffness has been suggested as an important biomarker that could be used in detection and treatment of disease. There is currently a gap in our understanding of the molecular and genetic mechanisms driving this phenomenon, which will be necessary to understand if we wish to utilize cell mechanics, which integrate the signals of many molecular pathways, as a better biomarker for diagnostics and possible therapeutics. The advent of single cell and genome-wide analyses have been important in gaining a better understanding of cellular mechanisms and diseases. Being able to combine the power of single cell reverse transcriptase quantitative polymerase chain reaction (RT-qPCR) data, genome-wide gene editing technologies, and single cell stiffness measurements from atomic force microscopy (AFM) will allow for great advancement of our understanding of cell mechanics. From the perspective of metastasis and cell mechanics alone, looking at the single cell level allows us to distinguish the correlation between expression levels and stiffnesses in the highly heterogeneous environment of tumors while

investigation at the genome-wide level allows for the discovery of correlations between genes with mechanics that have not previously been considered. Additionally, these studies can lead to a more precise understanding of what is happening intracellularly during both the epithelial-to-mesenchymal and mesenchymal-to-epithelial transitions (EMT/MET) and cell migration on the molecular level. Not only does this work play a significant role in the understanding metastasis, which leads to approximately 8 million deaths annually worldwide, but the development of these new methods and uncovering the molecular mechanisms of cell migratory potential could also lead to improved biomechanical understanding of several other biophysical processes, including stem cell differentiation, immune cell development and activation, mechanotransduction, and wound healing.

1.2 – Research Motivation and Significance

The objective of this research is to understand the coordination of molecular and mechanical mechanisms driving metastasis on the cellular level. Prior work in the field has focused on studying cell mechanics alone or following mechanical measurements with bulk population gene expression analysis. Previously, because AFM measurements must be performed on a large flat surface and single cell lysates for gene expression analysis are typically taken from small, multidimensional containers (like 96-well plates), it was impossible to collect both AFM and single cell lysate for RT-qPCR from the same cell, thus motivating the

development of the novel single cell genomechanics methodology. This method allows for the combination of two unique technologies, atomic force microscopy and single cell molecular analysis techniques, to gain a fuller understanding on the molecular mechanisms driving biophysical processes like metastasis. This method is contributing to a mechanistic understanding of the metastatic process within the context of tumor heterogeneity, determining the genes that are differentially expressed between cell types (e.g. invasive and non-invasive cancer cells). Understanding this problem on a single cell level reveals new mechanisms that can then be exploited to develop cutting-edge diagnostics and therapeutics that focus on the integration of several cell processes into a quantifiable, mechanical measurement. By allowing novel investigation of both the mechanical properties and genetic expression of single cells, the single cell genomechanics method can also be applied to other novel mechanistic questions surrounding biomechanical processes. Here I describe a new method, the first of its kind, to combine mechanical, morphological, and gene expression data for the same single cells to investigate the metastatic process. I demonstrate the necessity of single cell study and the use of multiple data types to fully characterize three ovarian cancer cell lines of varying metastatic potential. I hypothesize that there are correlations between particular genes and cell mechanics that will help predict the metastatic potential of a particular cell, leading to a mechanistic understanding of mechanical regulation of metastasis.

Complex cellular processes cannot be fully explained with a single data type and therefore linked cell data is highly important and valuable for understanding cell phenotypes such as metastatic potential. Beyond the single cell genomechanics method, I also wanted to expand my linked genomechanical data set further, sacrificing the level of single cell precision in order to gain the ability to rapidly explore the relationships of cell mechanics with all protein-coding genes across the genome. Genome-scale CRISPR Knock Out (GeCKO) screens have typically been used to investigate binary states of cells, such as cell viability or chemoresistance, but by using a mechanical sort with a multiple outlet device, I have the unique opportunity to explore how genes and mechanics work together across a spectrum of phenotypes. It has been seen both on the population level and on the single cell level that there are important relationships linking cell genotype, phenotype, and mechanotype. By delivering a pooled lentiviral library of single guide RNAs (sgRNAs) optimized to target over 19,000 genes (most protein-coding genes in the human genome) to a Cas9-expressing ovarian cancer cell line, I produced a library of cells with single gene knockouts with representation across the entire genome. By using a high-throughput microfluidic device to mechanically screen cells by their stiffness into 5 biomechanical subpopulations and analyzing the sgRNA distribution of each subpopulation, I was able to see which gene knockouts are associated with each mechanical phenotype. This will provide a list of genes of interest to investigate and will allow us to identify genes responsible for the changing mechanical properties of cells and

potentially those that confer metastatic advantage to cells. This thesis represents the first attempt to evaluate the entire genome for its role in directing cell mechanics to understand the connection between cancer cell genotype, phenotype, and mechanotype both across the whole genome and on the single cell level. Being able to collect the combination of gene expression data and cell stiffness measurements in a high throughput fashion with an in-depth exploration of genes related to mechanics and metastatic potential will lead to tremendous advancement of our understanding of the metastatic cascade with potential application to many other fields in which cell mechanics play a role in disease. I hypothesize that we will be able to identify particular gene knockouts that are significantly enriched in each bin of stiffness-sorted cells, allowing us to draw convincing conclusions about the gene's roles in both cell softening and cell stiffening. Through this work, we demonstrate a twenty-fold improvement in throughput of our stiffness-based cell sorting microfluidic device design while maintaining the ability to successfully sort cells into biologically important stiffness-based subsets. Additionally, this work for the first time uses the novel GeCKO technique combined with a mechanical screen to efficiently increase both the width and depth of our knowledge of the relationship between cell mechanics and cell gene expression.

Beyond a mechanistic understanding of cell mechanics and its relation to the metastatic process, my ultimate goal is to work toward a basic understanding that would result in revealing new biomarkers for earlier diagnosis of disease,

predictors for patient prognosis, or treatable therapeutic targets. By testing the hypotheses derived from the earlier aims of this thesis, we are able to work toward this goal with appropriate tools. If we can start to understand the underlying mechanisms driving metastatic spread of cancer to the point of having potential therapeutic targets, this knowledge could one day lead to a great reduction of cancer fatalities. A list of genes of interest generated by earlier aims was used to investigate the metastatic process by connecting the phenotype and genotype of cancer cells of varying metastatic ability. We used bioinformatics and network analyses to investigate the pathways of importance related to genes highly correlated genes in our single cell genomechanics aim. Although many groups have identified the cell softening phenotype associated with cancer and metastatic cells, there have not been many attempts at using this information to help patient outcome. Through my study, I hope to explore novel gene pathways or mechanical programs at a much wider scale, which can be validated and exploited to help prevent the spread of cancer. I hypothesize that there is a link between cell softening and mesenchymal, migratory phenotypes that is controlled by the expression of a network of genes of interest that could be potentially leveraged to help patient outcome.

1.3 – Dissertation Overview

Metastasis is the cause of 90% of cancer-related deaths, a statistic that has changed little over the past 50 years. During that time, cancer researchers

have recognized that changes in cells' mechanical phenotypes dictate their ability to generate force, invade through tissues, and migrate throughout the body. Several studies have implicated that as a cell's metastatic potential increases, cell stiffness decreases. While certain genes that affect cell mechanics have been studied, a genome-wide study of genes and gene networks that modulate cell biophysical properties has not been attempted. To understand gene networks that control cell mechanics and their role in metastatic potential, we will need to uncover the genetic molecular mechanisms that allow cells from an inherently heterogeneous tumor population to change their mechanical properties to successfully form a metastatic tumor. We must determine the single cell correlation of mechanical properties and gene expression that governs the subset of metastatic cells in a tumor. Chapter 2 describes the current understanding of the metastatic spread of cancer, the field of cell mechanics, single-cell and genome-scale technologies, as well as an overview of previous studies that led to the genesis of this work.

The long-term goal of this research is to understand the molecular and mechanical mechanisms driving metastasis. To reach this goal, I developed a novel methodology to combine atomic force microscopy (AFM) measurements of particular cells with the genetic expression of the same single cells. Secondly, I developed a novel microfluidics approach for cell sorting based upon biophysical properties for the high-throughput discovery of genes linked to cell mechanics and metastasis. I used this approach to determine how cellular mechanics are

regulated within the context of networks of cytoskeletal and structural proteins, transcription factors, and signaling proteins associated with increased metastatic potential. I will investigate the intersection of cell genotype, mechanotype, and phenotype with the following aims represented in Figure 1.

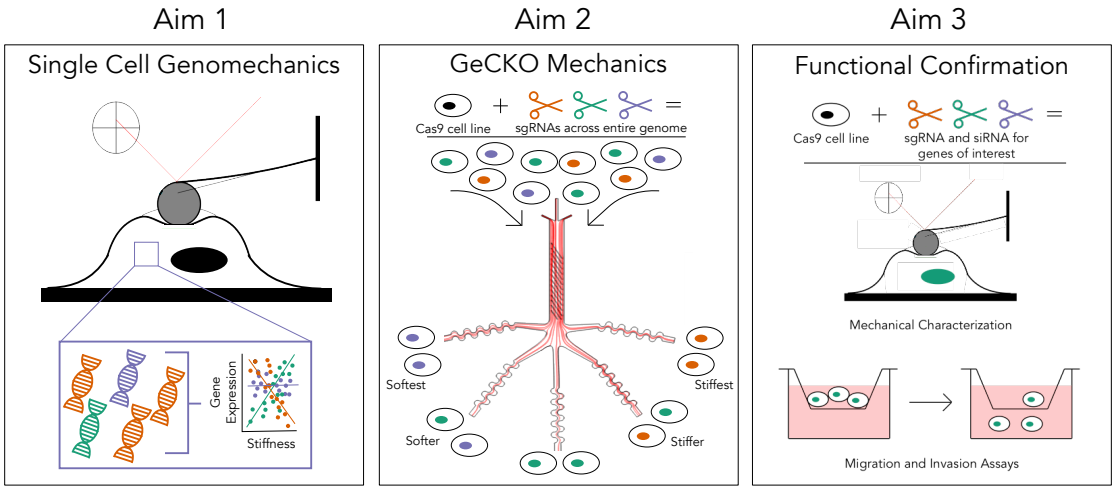

Figure 1 – Thesis overview in three aims – Aim 1: Create and validate a combined single cell mechanics and gene expression methodology. Aim 2: Identify genes related to mechanical changes in cancer cells through GeCKO high-throughput mechanical screen. Aim 3: Validate phenotypic and mechanotypic importance of genes of interest

Aim 1: Create and validate a combined single cell mechanics and gene expression methodology. Individual cells from three ovarian cancer cell lines were plated onto gridded coverslips allowing cell mechanical measurements to be conducted with an AFM, immediately followed by micropipette aspiration of the same individual cells. After isolation, each cell was lysed individually to extract and amplify mRNA for examination by high-throughput targeted PCR. I identified 96

genes through literature review including genes differentially expressed in metastatic cancer cells as well as genes related to cell mechanics and migration. I then used biostatistical and systems biology approaches to compare the expression of these genes of interest with stiffness measurements on the single cell level. **Chapter 3** describes the process of developing and validating the single cell genomechanics method.

Aim 2: Identify genes related to mechanical changes in cancer cells through GeCKO high-throughput mechanical screen. By delivering a pooled lentiviral library of single guide RNAs (sgRNAs) optimized to target over 19,000 genes to a Cas9-expressing ovarian cancer cell line, I produced a library of cells with single gene knockouts with representation across the entire genome. Using a microfluidic mechanical screen, of which we greatly improved the throughput as described in **Chapter 4**, to sort 150 million cells by their stiffness into 5 subpopulations to analyze a statistically significant set of genetic knockouts in each subpopulation, I was able to start to identify which gene knockouts are associated with the mechanical phenotypes to understand the molecular mechanisms of cellular mechanics and their relation to metastasis more fully. **Chapter 5** describes the GeCKO mechanical screen process and results.

Aim 3: Validate phenotypic and mechanotypic importance of genes of interest. A list of genes of interest determined from the aims above was used to investigate the metastatic process by connecting the phenotype and genotype of cancer cells of varying metastatic ability. The relationships identified between

gene expression and cell mechanical properties will be further explored by using small molecule inhibitors, siRNA, and miRNA technologies to affect the expression of particular genes of interest. Cell migration assays were used to confirm our generated hypotheses of the role of some genes in the metastatic process as well as further mechanical characterization through AFM analysis to confirm the effect of gene expression on cell mechanics. **Chapter 6** describes this hypothesis testing process and exploration of genes of interest. We hypothesize that there is a link between cell softening and mesenchymal, migratory phenotypes that is controlled by the expression of a network of genes of interest.

Beyond the specific investigation of the role of genotype and mechanotype in the metastatic phenotype, I also explore the role of cell mechanics in the behavior of healthy cells, diseased cells, and dying cells in **Chapter 7.** Finally, **Chapter 8** summarizes the findings of this work, the major conclusions, limitations of each methodology, and potential future directions and applications.

CHAPTER 2 – BACKGROUND

2.1 – The Metastatic Spread of Cancer

Metastasis is the cause of 90% of cancer-related deaths, a statistic that has changed little over the past 50 years[3]. The process of metastasis is highly complicated and involves the collection of mutations that allow primary tumor cells to modify their mechanics, undergo epithelial-to-mesenchymal transition (EMT), break away from their tumor, degrade the extracellular matrix (ECM), migrate to neighboring tissues and undergo mesenchymal-to-epithelial transition (MET) to form a new metastatic tumor. There are several routes for tumor metastasis, including hematogenous spread (through the circulatory system), lymphatic spread (through the lymphatic vessel system), and trans-coelomic (through invasion of body cavities, such as the peritoneal cavity)[4]. Metastasis is a multistep process where only 0.01% cancer cells that enter circulation develop into metastatic tumors; the process involves many barriers to cell survival, but the cells that persist and proliferate to form a secondary tumor are incredibly dangerous[5]. There are several theories to explain metastatic cell behavior and their interactions with their environment that allow for the formation of macrometastases; as the field of research progresses, we are continuing to converge on a common understanding of this complicated process[6].

In a sequential understanding of hematogenous spread of cancer cells, for example, there first must be local invasion of cells where they break away from

their primary tumor and degrade surrounding ECM with proteases such as matrix metalloproteinases (MMPs). Cells are then able to move or migrate toward vascularized tissue. Next, cells go through a process of intravasation where cancer cells enter the blood vessel lumen, helped by the increased permeability of vasculature associated with the tumor due to pro-angiogenic factors in the tumor microenvironment[7]. This process is facilitated through cancer cell interaction with endothelial cell barriers through specific molecular changes, such as breaking down connections between cells, going through EMT (see 2.1.1), or changing cytoskeleton structure so the cancer cell can invade through endothelial cell lining of vessels. Once inside the circulatory system, a metastatic cell must survive in transport, resisting anoikis, a form of apoptosis when cells lose contact with ECM or neighboring cells[8]. Next in transit, cells must slow down and stop in regions of micro vessels near distant organs. This occurs through the physical trapping of circulating tumor cells (CTCs) in capillary beds due to size restriction of the vessels' diameters[9]. Additionally, CTCs may be attracted to specific metastatic sites because of ligand-receptor interactions where cancer cell receptor expression is attracted to particular cell surface proteins on organs and secondary site microenvironment. Once cells have arrested near their future metastatic site, they go through the process of extravasation, where cells leave the vessel lumen and move into the tissue by penetrating through endothelial and pericyte layers. This process is more difficult than intravasation because there are no tumor-associated macrophages at this new metastatic site and the vessels there are less

permeable than the vessels at the primary tumor site. For this reason, primary tumors will often secrete soluble MMPs to remodel the secondary site, preparing the microenvironment to support the arrival of metastatic cells so that they can begin to colonize and to form micrometastases[10]. Finally, cells that arrive at the secondary site need the ability to self-renew, reactivate growth machinery, and start up angiogenesis to spawn large malignant growth, forming macrometastases.

This dissertation is focused on investigating the intersection of cell mechanics and gene expression for many of the processes in the invasion-metastasis cascade described above. Of particular interest to our group is the epithelial-to-mesenchymal transition.

2.1.1 Epithelial-to-mesenchymal transition

EMT causes cells to change from being polarized and epithelial-like to being spindly, solitary, motile, and mesenchymal-like[11]. This transition occurs with the loss of cell-cell interactions, the activation of certain transcription factors, changes in surface protein expression, a reordering of the internal cytoskeleton, and the production of enzymes to degrade the extracellular matrix[12–15]. While this process is important for normal biological processes such as embryonic development and wound healing, cancer cells have co-opted this process in order to induce many of the attributes of migratory cells necessary for metastasis. The activation of several transcription factors, such as Snail, Slug, Twist and Zeb1/2,

first identified by developmental biologists, have been associated with important EMT pathways which lead to loss of adhesion molecules and epithelial markers, expression of ECM degrading proteins and some that directly repress E-cadherin, an adhesion molecule that serves as an important marker of epithelial cells[15,16]. EMT and the reverse process, MET, have been associated with stem-cell like qualities of cancer, with many overlapping genetic pathways that allow cells to plastically change between identities to move and survive in different parts of the body. Some of these overlapping pathways include activation of Wnt signaling through the accumulation of beta-catenin in colon cancer, as well as elevated *CD44/CD24* ratios and PI3K/AKT pathway activation in samples of metastatic breast cancer[17,18]. In addition to increasing migration and cell stemness, EMT also helps promote cell survival during detachment from their primary tumor by resisting anoikis through increase of N-cadherin expression and loss of E-cadherin expression[19]. Interestingly, although we sometimes tend to think of the EMT as a switch between two states (a cell either existing as an epithelial-like cell or a mesenchymal-like cell), recent studies, *in vitro* and *in vivo*, point to a spectrum of cell phenotypes with differing metastatic and differentiation potential[20].

2.2 – Cell Mechanics

Most of the dynamic transitions described above, including the invasion and migration of metastatic cells, are affected by the mechanical properties of a cell. The processes of EMT and MET rely heavily on the reorganization of a cell's

cytoskeleton, the proteins within a cell which provide structural support and allow for cell motility[1,12]. Beyond the mechanical processes of EMT/MET, cancer cells undergo other mechanical processes that influence their extracellular microenvironment in addition to affect the mechanics of the cell itself. Cancer cell softening has been demonstrated in many different cell types and it has been shown that for many cancer types, as metastatic potential increases, cell stiffness will decrease[1,2,21,22]. Because of the relation between disease state and cell mechanics, cell stiffness has been suggested as an important biomarker for disease detection and treatment.

One of the most sensitive methods to measure cell stiffness is atomic force microscopy (AFM). AFM works by using a small cantilever to apply nanonewton magnitude forces to a material at a localized spot. By using a laser and a photodiode detector, the AFM is able to measure the amount of deflection of laser light off of the cantilever to calculate both the applied force and the amount of deformation the cell undergoes when probed[23]. A spherical tip can be added to the end of the cantilever to increase the surface area between the tip and cell, preventing cellular damage and increasing the accuracy of the global measurement of the cell[24]. We can then use the Hertzian contact mechanics mathematical model, with the inputs of the tip geometry, amount of applied force, and amount of cell indentation, to calculate a specific Young's modulus or stiffness for each cell[25]. Additionally, by holding the cantilever in contact with a cell during the force displacement curve, we can measure the cell displacement during viscoelastic

relaxation. By fitting this portion of the force curve to a biexponential fit, we can apply the Maxwell model to obtain fast and slow viscous time constants, which represent how a cell responds to deformation at different time scales[26].

2.2.1 Cell mechanics as a biomarker for disease

In addition to the importance of mechanics in cancer cell behavior, our group has also studied the role of mechanics in cell viability[27], chemoresistance[28], sickle cell transport[29], leukocyte demargination[30], endothelial tube formation[31], stem cell differentiation[32–34], liver fibrosis[35] and fibrogenesis[36]. Because of the relationship between disease state and cell mechanics, cell stiffness has been suggested as an important biomarker that could be used in detection and treatment of disease. There is currently a gap in our understanding of the molecular mechanisms driving this phenomenon, which will be necessary to understand if we wish to utilize cell mechanics, which integrate the signals of many molecular pathways, as a better biomarker for diagnostics and therapeutic targets. To dive deeper into the role cellular mechanics plays in both healthy and diseased cell states, see chapter 7.

2.3 – Single Cell Techniques

The advent of single cell analysis has led to a better understanding of cellular mechanisms and diseases. Looking at the genetic expression taken from a population of cells often means that small up- and down-regulations of particular

genes from subpopulations of cells are lost due to the averaging out of genetic expression. Single cell RT-qPCR allows for the targeted observation of gene expression in single cells and thus within these distinct subpopulations[37]. Fluidigm has several platforms for studying single cell mRNA expression, such as the integrated fluidic circuit 96.96 Dynamic Array, which allows for multiplexed RT-qPCR of 9,216 total PCR reactions of 96 different assays for 96 different samples. Another way to study single cell gene expression is single cell RNA sequencing (scRNA-Seq). Several methods have been developed for scRNA-Seq, such as CEL-seq2, Drop-seq, MARS-seq, SCRB-seq, Smart-seq, and Smart-seq2 that utilize different methods of single cell isolation, such as fluidic chip loading, drop encapsulation, and FACS, as well as different cDNA amplification and library construction schemes, with some incorporating unique molecular identifiers and some utilizing full length coverage[38]. There are several single cell technologies available for separation and isolation of single cells. These include limiting dilution, fluorescence activated cell sorting (FACS), laser capture microdissection, microfluidic cell traps, microfluidic pneumatic membrane valving, microfluidic droplet encapsulation, and micromanipulator control of micropipette aspiration[39]. These methods differ in efficiency, time, cost, cell viability, and control over cell selection.

2.3.1 Linking single cell genotype and phenotype

Although there is opportunity to gather large data sets from single cell transcriptomes, gene expression measurements alone are likely not sufficient to fully describe and understand complex cellular processes, including the various processes described above[40–42]. For this reason, there are several groups attempting to study single cells using multiple modalities and connecting gene expression with function. For example, methods have been developed to link transcriptome level data with epigenomic regulation and proteomic expression on the single cell level[43,44]. Additionally, pooled genetic screens involving CRISPR editing across the entire genome have been used in conjunction with RNA sequencing to investigate how transcriptional profiles are controlled by various gene functions[45,46]. Various studies have also demonstrated the ability to study the spatial localization of single cells and their transcriptional profiles within 2D and 3D tissues[47,48]. Moreover, methods have been developed to specifically link single cell transcriptional profiles with specific biophysical and functional measurements, such as cell size, morphology, and electrophysiology[49–51]. These studies help demonstrate the importance of the ability to link cell transcriptomics with cell function and phenotype. However, there has not previously been a study linking single cell mechanics and gene expression, making my study the first of its kind.

2.4 – Genome-Scale CRISPR Knockout (GeCKO) Screening

The use of genome-scale CRISPR knockout (GeCKO) pooled screens has allowed researchers to start exploring the connection between a cell's genotype and various phenotypes, including chemoresistance, gene essentiality, *in vivo* metastasis and immune activation[45,52–55]. The GeCKO process involves delivering a pooled lentiviral library of single guide RNAs targeted to over 19,000 genes (approximately every protein-coding gene in the human genome) to a Cas9-expressing cell line at a low multiplicity of infection so that statistically each cell will only carry one CRISPR knockout[52]. Cells with the single gene knockouts are screened for the phenotype of interest and sequencing is used to determine the sgRNA distribution to compare to the distribution before the screen to identify which genes are related to the applied screening pressure.

2.5 – Previous Supporting Studies

2.5.1 Ovarian cancer cells soften with increasing metastatic potential

Using force spectroscopy techniques with an AFM, our lab measured various mechanical properties including the Young's Modulus of multiple single cells of non-malignant and malignant ovarian cell lines. We calculated the Young's modulus by analyzing the force-displacement curves from measurements of 50-100 cells per cell type using Hertzian contact mechanics (see representative curves in Figure 2a, inset). IOSE cells are immortalized but used in various studies to represent normal ovarian epithelia. HEY A8 cells are a derivative cell line isolated

from the HEY ovarian carcinoma model cell line with substantially different mechanical and invasive properties as well as higher tumorgenicity[56]. The AFM measurements of five ovarian cell lines revealed that the nominally more invasive cancer cell type (HEY A8) was significantly softer than the less invasive cancer cell types (OVCAR-3, HEY, and OVCAR-4), which were also significantly softer than the non-malignant IOSE cells (see the distribution of individual cell stiffnesses in Figure 2a). To further confirm the inverse relationship between cell invasiveness and cell stiffness, our group tested the ability of the IOSE, HEY, and HEY A8 cells to migrate and invade through a substrate and confirmed that the HEY A8 cells display the greatest migratory and invasive ability followed by HEY cells and the IOSE control (see Figure 2b and Figure 2c).

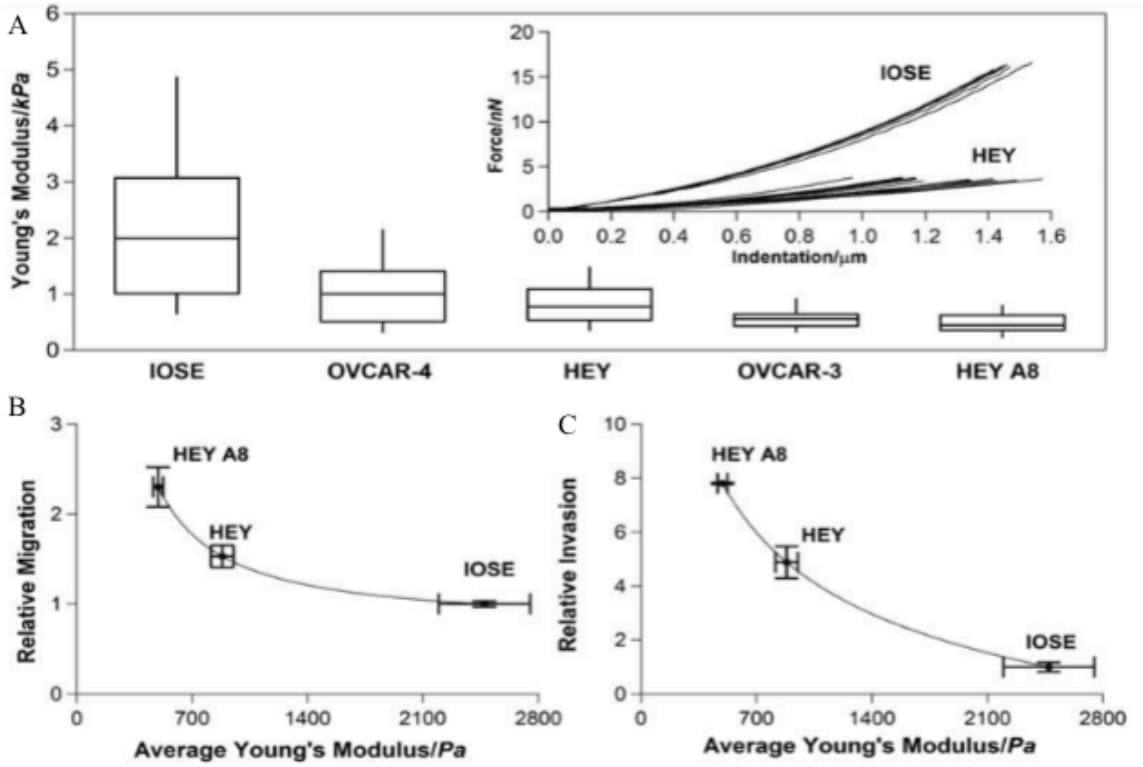

Figure 2 – Ovarian cell stiffness correlates with potential for migration and invasion – a) Single cell stiffnesses of 5 different ovarian cell lines, including non-malignant phenotype (IOSE) and cancer cell lines of increasing metastatic potential. The inset shows example force-displacement curves for healthy ovarian cells (IOSE) and ovarian cancer cells (HEY), with a steeper slope corresponding to lower deformability. b) *In vitro* migration vs. cell stiffness. c) *In vitro* invasion vs. cell stiffness.[21]

2.5.2 Population gene expression profiling links increased deformability and actin-mediated cytoskeletal remodeling pathways

After establishing the relationship between cell stiffness and metastatic potential for the HEY and HEY A8 cell types, our lab performed population based comparative gene expression analysis with mRNA microarrays. Although these two cell types were originally derived from the same tumor sample, there were 1,258 upregulated genes and 1,272 downregulated genes when comparing the HEY A8

and HEY cell samples. Looking at the genes with the most significant differential expression, the softer HEY A8 cells had upregulated genes that control the remodeling of the cytoskeleton and the reduction of cytoskeletal tension. Additionally, there were important changes in genes related to the cell cycle, the process of EMT, and TGF and Wnt signaling. Specifically and interestingly, we saw overexpression of cofilin-2 (*CFL2*) and twinfilin (*TWF1*) and downregulation of myosin light chain kinase (*MYLK*) in HEY A8 cells, genes that enhance the depolymerization of actin filaments, sequester actin monomers, and promote cytoskeleton tension generation, respectively[57–59]. While this population level data reveals interesting information about the metastatic process, the inability to explore which genes are necessary for cell mechanical regulation and variation on the single cell level further necessitates this study. This result represents a direction to begin investigation that will be further enhanced by a single cell understanding of how gene expression is directly correlated with changes in cell stiffness and other mechanical properties.

2.5.3 Microfluidic biomechanical sorting to isolate and sort functional subsets of cells

The Sulchek lab has developed and demonstrated a microfluidic platform that can be used to isolate biophysical phenotypes of cells across four dimensions: stiffness, viscoelasticity, size, and adhesion[60–64]. The technology consists of a microchannel with multiple diagonal ridges that compress cells as they flow

through the channel. Highly deformable cells are able to squeeze under the ridges and follow the hydrodynamic forces of the flowing buffer around the cells. Alternatively, stiffer cells resist compression and are moved by the diagonal ridges perpendicular to the fluid flow. As a proof of concept that this platform can be used to isolate functional phenotypes, we have shown that we can isolate subpopulations of viable cells and chemo-resistive cells, due to the three-fold increase in cell stiffness that occurs at early stages of apoptosis[27,28]. The schematic of this sorting process is shown in Figure 3a and a micrograph of the device is shown in Figure 3b. Drug-sensitive cells translate along the ridge due to increased cell stiffness while softer resistant cells flow slightly perpendicular following the fluid streamlines (see Figure 3c). The advantage of using biophysical properties of the cell as a surrogate of function is that they can be now quickly assessed in a single measurement to isolate cells akin to flow cytometry while representing the integration of many gene networks.

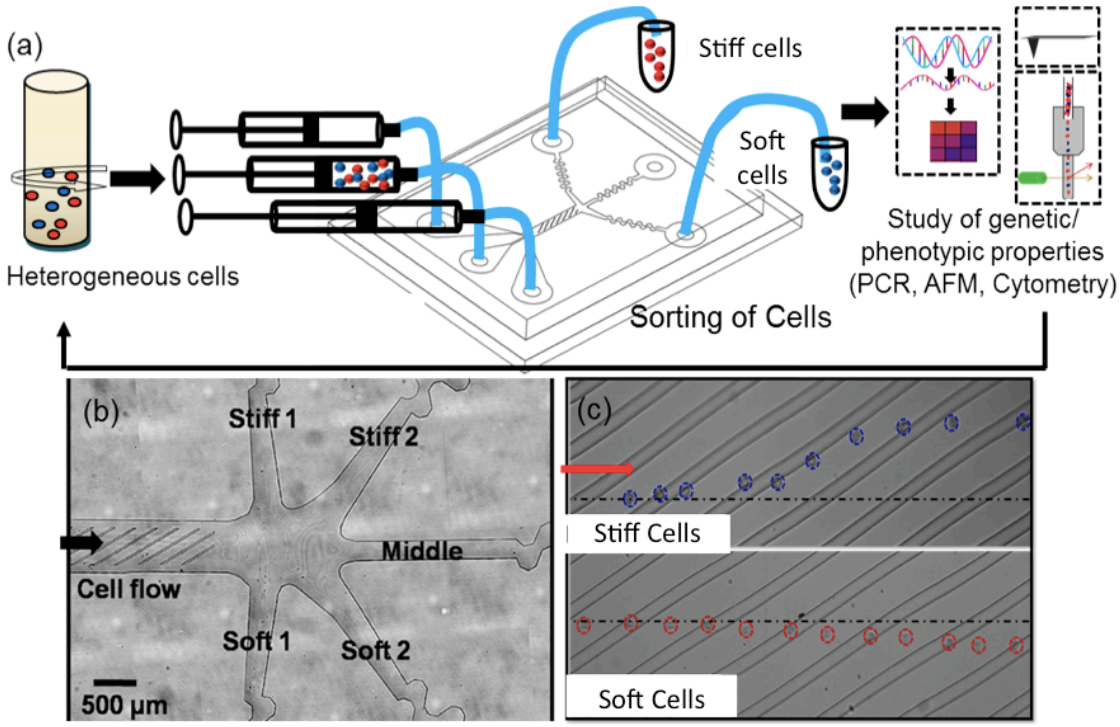

Figure 3 – Microfluidic device for sorting cells based off of biophysical properties – a) Schematic showing the biomechanical sorting of a heterogeneous cell population using microfluidics and subsequent characterization of gene expression and phenotype. b) Optical micrograph of a five-outlet device. c) Representative trajectories of stiff and soft cells inside the device.

2.5.4 Previous method for correlating single cell mechanics and gene expression

Prior to using the single cell genomechanics method I developed that is detailed in chapter 3, I helped a previous graduate student, Tom Bongiorno, on developing another methodology to collect both mechanical and genetic information from the same single cells. In our first method iteration, we created a custom sample holder compatible with both AFM measurements and isolation of single cells for preparation of individual cell lysate. First, we manufactured the

custom sample holder, which we refer to as rafts, by layering polydimethylsiloxane (PDMS) and green fluorescent beads that serve as positional markers on top of a stainless-steel washer. Using a polypropylene mask, we selectively plasma treated the center of each raft to create a hydrophilic region surrounded by the hydrophobic PDMS. These hydrophilic islands allow for the collection of individual cell lysates by manual pipetting of a lysis buffer (Figure 4). Lastly, we coated these hydrophilic regions with cell-adhesive ligands (Cell-Tak) to allow for immobilization of single cells on each raft.

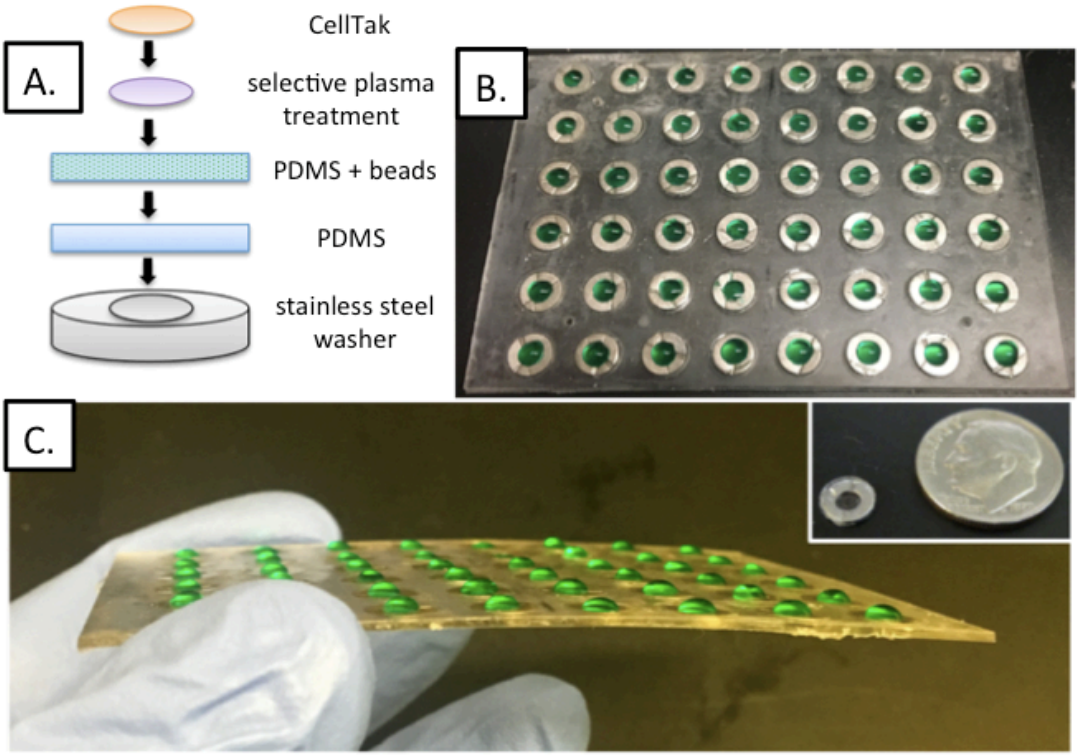

Figure 4 – Genomechanics raft manufacturing – a) Layers that make up the single cell genomechanics rafts. b) Array of manufactured rafts. c) Demonstration of hydrophilic islands that allow for single 5 μL drops of liquid on each raft. The inset in this figure shows the approximate size of each raft as compared to a dime.

After manufacturing the rafts, the next step was to deposit and immobilize single cells on each raft. In order to isolate and visualize single cells, we stained cells with 25 μM Cell Tracker Red CMPTX dye. The dyed cells were trypsinized and resuspended for single cell dispensation using fluorescence activated cell sorting or FACS. A FACS Aria Fusion cell sorter was used to gate for red fluorescent single cells and deposit a single cell onto each raft, which were arranged in a six-by-eight array matching the set-up of a 96-well plate. The cells were allowed to adhere to the Cell-Tak coated rafts for 1-2 hours before all cells that were not firmly adhered to their raft were washed away.

Next, we used a Cytation 3 imaging plate reader to identify whether each raft had an adhered cell as well as identify that cell's location in respect to the green fluorescent position markers in the top layer of the raft (Figure 5). First, the plate reader, using the GFP channel, focused on the focal plane of the fluorescent beads and then it used the Cy5 channel to determine the presence or absence of a cell on each raft. Once each cell was identified and located, we transferred the raft with that single cell to a glass bottom dish containing phosphate-buffered saline (PBS) for probing with the AFM. The focal plane with the cell was again identified using the GFP channel to find the green fluorescent beads, which were also used as positional markers to locate the identified cell. Cell stiffness measurements were taken using a probe velocity of 2 μm/s and a force trigger of 5 nN. We use the Hertzian contact model to fit the compression segment of each force-indentation curve and a cellular Poisson's ratio of 0.5 to

calculate the Young's Modulus of each cell as an average of 3 independent measurements.

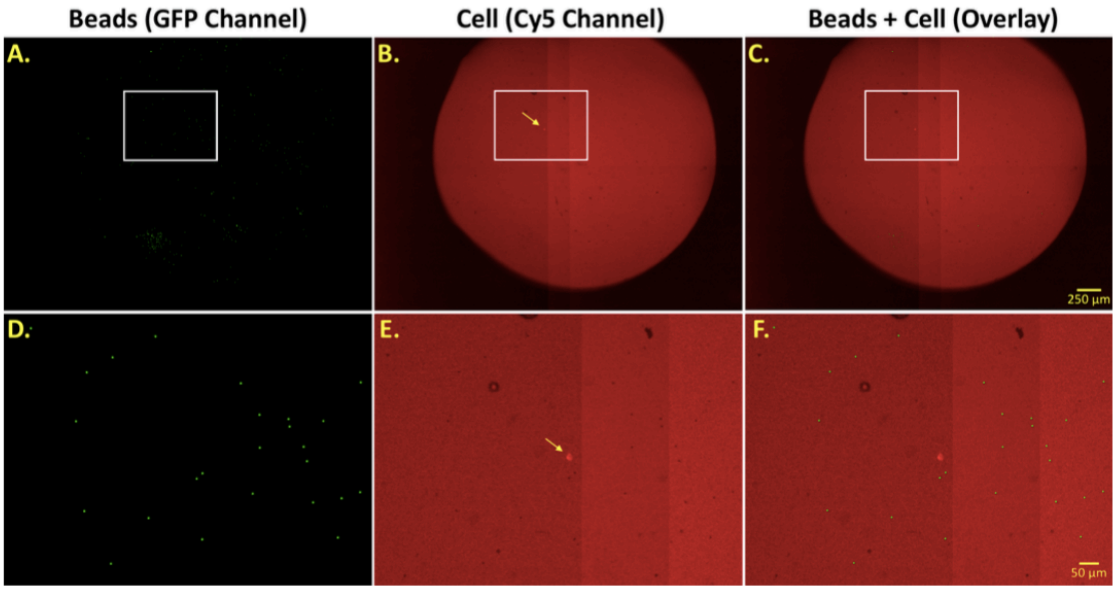

Figure 5 – Cell localization optimization – a) Image of green positional beads in GFP channel. b) Montage of 2x2 images of red fluorescent cell in Cy5 channel. c) Overlay of the GFP and Cy5 channels. d-f) Magnified images of the beads, cell, and overlay images from the panels a-c.

After taking each cell measurement, the raft was transferred from the dish and all residual liquid was removed. We used 5 µL of lysis buffer (CellsDirect 2x reaction mix with an RNAse inhibitor) manually pipetted onto the hydrophilic region of the raft to lyse the cell before transferring the lysate to PCR tubes for storage at -80°C. These cell lysates were mixed with a pooled set of primers of interest along with a SuperScript III RT Platinum Taq mix and nuclease-free water. RNA transcripts were converted to cDNA with reverse transcription in a

thermocycler and amplified before being added to a Fluidigm FLEX six IFC chip. This chip, when used with the Fluidigm BioMark imaging thermocycler system, is able to perform multiplexed quantitative PCR to compare the expression of at least 12 genes with at least 12 different samples. The ΔCt method, implemented with LinRegPCR software, was used to determine the threshold fluorescence signal for each target, the threshold cycle number for each sample, and the reaction efficiency compared against the expression levels of the housekeeping gene.

After completing these experiments and analysis, we recognized that the method was inefficient. From 96 manufactured rafts each with a deposited single cell, we were only able to get 2-6 actual cell measurements, an efficiency of approximately 2-6%. Because it takes 15-18 hours per experiment plus several days of preparation prior to the day of data collection, this poor efficiency greatly limited our sample size. Being limited by a small sample size and the desire for statistically significant results, the method needs to be statistically powerful to detect small effect sizes. In an effort to decrease the required power of the method, we decided to increase the method's efficiency so that we can increase our sample size.

Optimizing the method required resolving several issues. One of the greatest issues was in localizing where the cell landed and adhered to the raft. The area of the raft was 5 orders of magnitude larger than the area of the cell so there was a need for a strong fluorescent signal to make the cell more easily identifiable. I attempted to increase the visibility of the cell in the Cytation imaging

plate reader by switching from Cell Tracker Red dye to Cell Tracker Blue dye which had better spectral overlap with our instrument's excitation and emission filters. Because it was difficult to identify each cell on the raft, it was unclear whether our poor efficiency was due to 1) cells adhering to the raft but remaining invisible to our detection, 2) cells not properly adhering to each raft, or 3) low viability of cells after FACS leading to dead cells being deposited on each raft. The low efficiency of this previous method directly contributed to the development of the new single cell genomechanics method described in chapter 3.

CHAPTER 3 – SINGLE CELL GENOMECHANICS: METHOD DEVELOPED TO GENERATE HYPOTHESES RELATING CANCER CELL MECHANOTYPE, GENOTYPE, AND PHENOTYPE

3.1 – Abstract

Cancer cell stiffness has been observed to decrease for many cancer cell types as metastatic potential increases. While cell mechanics and metastatic potential are related, the underlying molecular factors associated with these behaviors remain unknown. Developing hypotheses to understand how molecular signaling networks are related to cellular phenotype and mechanotype is needed to help elucidate how metastasis and mechanics are coupled. Therefore, we have developed a workflow to measure the mechanical properties and gene expression of single cells that can be used to generate large linked-datasets and develop new hypotheses concerning molecular networks and their relationship with cell mechanics. The process combines atomic force microscopy and optical microscopy to measure the mechanics and morphology of individual cells, followed by multiplexed RT-qPCR gene expression analysis on the same single cells. We demonstrated the workflow using ovarian cancer cells along with 96 genes of interest to cancer metastasis and mechanics. Surprisingly, the genes that most strongly correlated with mechanical properties were not cytoskeletal, but rather were markers of extracellular matrix remodeling, epithelial-to-mesenchymal transition, cell adhesion, and cancer stemness. Additionally, dimensionality

reduction analysis showed that the clustering of cells by differential metastatic potential could be improved by combining mechanical and gene expression data types. The single cell genomechanics method demonstrates how single cells can be studied to identify molecular drivers that disable the biophysical processes underpinning metastasis.

3.2 – Introduction

Metastasis is the cause of 90% of cancer-related deaths[3]. The metastatic cascade is a multi-step process that allow tumor cells to undergo epithelial-to-mesenchymal transition (EMT), dissociate from the tumor, degrade the extracellular matrix (ECM), migrate to neighboring tissues and undergo mesenchymal-to-epithelial transition (MET) to form a new metastatic tumor. Mechanical property changes to cancer cells can facilitate invasion and migration. The processes of EMT and MET reorganize the cytoskeleton to allow cell motility[1,12]. Cancer cell softening has been observed in many cancer types[1,22]; more specifically, as metastatic potential increases, cell stiffness decreases[21,22,65,66]. However, we lack a full understanding of how molecular pathways are related to these mechanical phenotypes. Such knowledge may unlock potential control points in these pathways to determine how cells respond to therapeutic agents and to understand how mechanics can be used as diagnostic biomarkers.

The advent of single cell analysis has been critical to understand the heterogeneity of cellular mechanisms of disease. When studying whole populations of cells, responses from subsets of cells are lost due to the averaging of genetic expression[67]. In contrast, single cell methods can discern gene expression in single cells within a heterogeneous population[37]. However, gene expression measurements alone do not fully describe complex cellular processes, including the various processes in metastasis. In fact, a poor correlation between mRNA measurements and protein content in cells is often observed [40,41]. For this reason, the study of single cells using multiple modalities can better connect cell properties with function. To this end, methods have been developed to link transcriptome level data with epigenomic regulation and proteomic expression on the single cell level[43,44]. Moreover, new methods can specifically link single cell transcriptional profiles with cell size, morphology and electrophysiology[49,51]. However, there has not been a study linking single cell mechanics and gene expression, as needed to understand the biomechanical aspects of metastasis.

Here we describe the first method of its kind to combine mechanical, morphological, and gene expression data from individual cells to link molecular and biophysical processes in metastasis. Single cell RT-qPCR data, single cell mechanical measurements from atomic force microscopy (AFM), and morphological measurements obtained by optical microscopy were used to study three ovarian cancer cell lines of varying metastatic potential. We identified several genes related to the metastatic process that are significantly correlated

with cell mechanics. We find the migratory and invasive ability of cells are linked to mechanical and morphological markers as strongly as sets of molecular readouts, resulting in more effective clustering by the metastatic potential of cells. This finding substantiates the close coupling between mechanics and metastasis. Furthermore, the understanding of mechanical properties and metastatic pathways can lead to the discovery of new diagnostic biomarkers and therapeutic targets that may benefit the identification and treatment of invasive cancers.

3.3 – Materials and Methods

3.3.1 Ovarian cell culture and sample preparation

The mesenchymal ovarian cancer cell line HEY and its derivative cell line HEY A8 were cultured in RPMI-1640 media (Sigma-Aldrich) supplemented with 10% fetal bovine serum (Atlanta Biologicals) and 1% penicillin-streptomycin (Sigma-Aldrich). The epithelial ovarian cancer cell line OVCAR3 was cultured in RPMI-1640 media supplemented with 20% fetal bovine serum and 1% penicillin-streptomycin. Cells were cultured at 37°C at 5% CO_2. All three cell lines were provided by Dr. John McDonald. The day before AFM experiments, 10,000 cells were seeded on a gelatin-coated (Fisher Scientific) gridded coverslip (Electron Microscopy Sciences) in 24-well plates.

3.3.2 AFM and force curve analysis

For better global stiffness measurements of the cell, 5.46 µm spherical polystyrene particles were attached to tipless silica nitride cantilevers (Bruker Probes) using a two-part epoxy. To characterize the mechanical properties of each cell, we used force spectroscopy to obtain force-indentation curves with an atomic force microscope (Asylum Research) with an integrated optical microscope (Nikon) on a vibration isolation table. Before each day of measurements, each cantilever was calibrated to determine the deflection inverse optical lever sensitivity and spring constant (k is approximately 10 – 25 pN/nm). For measurements, the cantilever probe was visually aligned with the cell center and moved with a velocity of 2 µm/s to indent the cell with increasing compressive force until a force trigger of 10 nN was reached. The cantilever was held in position for 5 seconds, dwelling towards the surface, allowing for viscous relaxation of the cell before reversing the direction of its velocity.

We used custom code written in R (https://github.com/nstone8/Rasylum) relying on the Hertzian contact model, which describes non-adhesive elastic contact between two bodies, to calculate the cellular Young's modulus[25]. The contact point was estimated by the intersection of the flat, undeformed region of the force curve with a line fit to the force curve region where the cantilever was in contact with the cell. Next, we identified the true contact point by iteratively testing the points around the estimated contact point with the minimal residual difference between the measured force curve and a nonlinear fit described by the

governing equation Hertz used to describe the contact between an elastic sphere and an elastic half space. We additionally used the Rasylum custom R package to fit the dwell region of the force curve to a biexponential decay curve to identify the fast and slow viscous time constants[26].

3.3.3 Image analysis

For every cell mechanically probed, we additionally captured an optical microscopy image to be analyzed for size and various shape descriptors using ImageJ software. Each cell was outlined, and its area was measured. This outline was then fit with an ellipse to determine the major and minor axis of each cell. We defined four shape descriptors to describe each cell: the aspect ratio (the ratio of the major axis to the minor axis), circularity (4π*area/perimeter^2), roundness (4*area/(π*major axis^2)) and solidity (area/convex area).

3.3.4 Micropipette isolation

To collect the cells after AFM, the coverslip with the cells attached was moved to a micropipette rig for aspiration. Micropipettes were pulled from borosilicate standard wall glass capillaries (1.5 mm OD, 0.86 mm ID, Warner Instruments) using a PC-10 vertical puller (Narishige) producing pipettes with an opening diameter of approximately 6.5 µm. Due to the sensitivity of single cell gene expression techniques, caution was exercised in the decontamination of the system along with the removal of all RNAse and DNAse enzymes. Using

micromanipulators (Scientifica) to control the x-y-z position of the micropipette, the micropipette tip was located with a 40x objective light microscope and lowered to each cell of interest. Once together, 345 to 500 mbar of negative pressure was applied for 0.2 to 2 seconds to aspirate the cell of interest into the micropipette. The micropipette was then removed from the bath and 1000 mbar of positive pressure was applied for 3 seconds to displace the aspirated cell into an individual PCR tube containing 5 µL of CellsDirect One-Step qRT-PCR 2x reaction mix (Invitrogen) with 1 U/ µL of SUPERase-In, a RNAse inhibitor (Ambion). These individual cells were stored at -80°C.

3.3.5 Fluorescent activated cell sorting (FACS)

To compare micropipette isolation with FACS single cell isolation, HEY A8 cells were resuspended to $1x10^6$ cells/mL in a sorting buffer (PBS + 1% FBS + 1 mM EDTA + 25 mM HEPES) and sorted using a FACS Aria Illu Cell Sorter (Becton Dickinson) into a PCR plate containing 5 µL of CellsDirect One-Step qRT-PCR 2x reaction mix (Invitrogen) with 1 U/ µL of SUPERase-In, a RNAse inhibitor (Ambion) in each well. Cells were gated based on forward and side scatter to select living, single cells.

3.3.6 Primer design and validation

A list of genes of interest was curated from various published sources and experimental comparisons of gene expression between cell lines of varying

metastatic potential[15,68–74]. Designs for these 96 genes of interest were collected from previously published studies, choosing primer sets predicted by the Basic Local Alignment Search Tool (BLAST). We validated each primer set (ThermoFisher) using qPCR with SsoAdvanced Universal SYBR Green Supermix (BioRad) and cDNA reverse transcribed from mRNA extracted and purified from HEY, HEY A8, and OVCAR3 cells. We then analyzed each PCR product with gel electrophoresis to confirm the expected product size. There were 90 primer sets that produced the correct single PCR product.

3.3.7 Fluidigm targeted qPCR

We followed the advanced development protocol from Fluidigm to investigate single cell gene expression using SsoFast EvaGreen with Low ROX on the BioMark system (Fluidigm, ADP 41). SuperScript III RT Platinum Taq Mix (Invitrogen) and a mix of 500 nM of all forward and reverse primers was added to the single cells stored in the reaction mix for reverse transcription and specific target amplification. To clean up unincorporated primers, we included an Exonuclease I (New England BioLabs) digestion. Amplified single cell samples were combined with SsoFast EvaGreen Supermix with Low ROX (BioRad) and DNA Binding Dye (Fluidigm) and each primer pair was diluted and combined with an assay-loading reagent (Fluidigm). The 96.96 Dynamic Array integrated fluidic chip (Fluidigm) was loaded with 96 samples (including a positive and negative control)

and 96 assays with the IFC Controller HX (Fluidigm). Using a BioMark machine (Fluidigm), we performed 40 cycles of PCR and a melt curve analysis.

Raw data was exported from the Fluidigm Real-Time PCR Analysis Software. R code (https://github.com/kyoung74/ThesisCode) was used to calculate R_n values at each cycle number for each sample and assay combination by taking the ratio of the difference between the raw and background EvaGreen fluorescence readings and the difference between the raw and background ROX fluorescence readings. These R_n values were then analyzed using LinRegPCR (https://www.medischebiologie.nl/files/) to determine a cycle threshold (C_t) value for each sample-assay pair. We transformed the C_t value by subtracting it from 45. Additionally, we identified *GAPDH* and *RPL32* as stable housekeeping genes in our 3 cell types and removed single cell samples where either of these housekeeping genes did not amplify. The transformed C_t values were normalized to the geometric mean of the *GAPDH* and *RPL32* expression and cells where the normalized *GAPDH* expression was lower than 0.8 were also removed.

3.3.8 Population gene expression qPCR

To compare the gene expression of each cell line population, we used qPCR with SsoAdvanced Universal SYBR Green Supermix (BioRad) and cDNA reverse transcribed from mRNA extracted and purified from T-25 flasks of HEY, HEY A8, and OVCAR3 cells (approximately 2 million cells each). Amplification curves from the ABI StepOne Plus qPCR machine were analyzed using LinRegPCR

(https://www.medischebiologie.nl/files/) to determine a C_t for each sample-assay pair. We transformed this C_t value by subtracting it from 45. The transformed C_t values were normalized to the geometric mean of the *GAPDH* and *RPL32* expression. The micropipette-isolated single cell values of normalized expression of each gene for each cell type was averaged and plotted against the population gene expression. A Pearson's correlation test was used to compare the population and average single cell gene expression.

3.3.9 Migration assay

To test the migratory properties of each cell type, we used the CytoSelect 96-well transwell migration assay (Cell BioLabs), where 50,000 cells of each cell population were seeded in serum free media (DMEM media supplemented with 0.5% BSA, 2 mM $CaCl_2$, 2 mM $MgCl_2$, and 1% penicillin-streptomycin) in an 8-micron pore well insert, leading to a well filled with complete media (RPM1-1640 media supplemented with 10% FBS and 1% penicillin-streptomycin). After 8 hours of incubation, cells that migrated through the pores and were detached, lysed and fluorometrically dyed with CyQuant GR fluorescent dye. The amount of fluorescence per well was read with a plate reader at 480 nm/520 nm (BioTek).

All assays were carried out in biological triplicate with an initial time course study conducted to ascertain at which time there was significant transmigration of cells.

3.3.10 PCA and PLS cell clustering analysis

First, we separately transformed the normalized gene expression data, the morphological measurements, and the mechanical data of all single cells using principal component analysis (PCA). Then we applied partial least squares (PLS) analysis to combine gene expression data with morphological and mechanical measurements followed by PCA to cluster cells based on the combination of two or three data types. We quantified the clustering results using the Davies-Bouldin index (DB index)[75], which characterizes the ratio of variance of data points in the same cluster and the variance of data points between clusters. After using PLS to combine the different data types, we selected the number of PLS components for each combination that minimized the DB index which indicates the most optimal clustering algorithm (4 PLS components for mechanical and morphological data, 3 PLS components for gene expression and morphological data, 7 PLS components for gene expression and mechanical data, and 8 PLS components for gene expression, morphological and mechanical data).

3.3.11 Correlation analysis

With the normalized gene expression of the 85 validated, non-housekeeping genes, 3 mechanical parameters, and 7 morphological parameters from the single cells from all three cell lines, we used Spearman's correlation analysis to investigate the pairwise correlation between all combinations of the 95 parameters and the significance of each correlation ($p < 0.05$ considered

significant). This analysis was repeated using the single cell data from each cell line separately. Literature review was used to identify the function of each gene of interest as well as its expected effect on cancer metastasis.

3.4 – Results

3.4.1 Single cell genomechanics method combines AFM and targeted RT-qPCR

The single cell genomechanics method was developed to collect mechanical, morphological, and gene expression data for individual cells. Cells were cultured on a gridded coverslip that was used to track the location of each cell throughout AFM measurements, optical imaging, and subsequent micropipette isolation for gene expression analysis (Figure 6a). Optical images of each cell were analyzed using ImageJ software to determine morphological properties, including cell size, aspect ratio, circularity, roundness, and solidity (Figure 6b). AFM cell indentation force curves were conducted to measure the Young's modulus and viscous relaxation time constants for each cell using a Hertzian contact mechanics model (Figure 6c) and Zener's model of cell viscoelasticity (Figure 6d), respectively. After mechanical probing, each cell was located using the gridded substrate as registry and isolated with a micropipette, using negative pressure aspiration (Figure 7 – multimedia file) and positive pressure to deposit the cell into a tube for immediate lysis and preparation for gene expression analysis. This analysis was conducted with the Fluidigm BioMark 96.96 Dynamic Array integrated

fluidic chip to perform RT-qPCR of 96 genes in 96 cells per chip. The genes tested include those associated with EMT, metastatic enhancers and suppressors, cancer stemness, extracellular matrix remodeling, cytoskeletal remodeling, cancer malignancy, and multiple growth signaling pathways as classified by the PANTHER Classification System (http://www.pantherdb.org) (Figure 6e and Table 1). For our investigation, we used three model ovarian cancer cell lines of varying metastatic potential. OVCAR3 is an epithelial cell line that represents serous adenocarcinoma, HEY is a mesenchymal cell line that represents serous carcinoma, and HEY A8 is a derivative cell line of HEY that is more metastatic and mesenchymal[56].

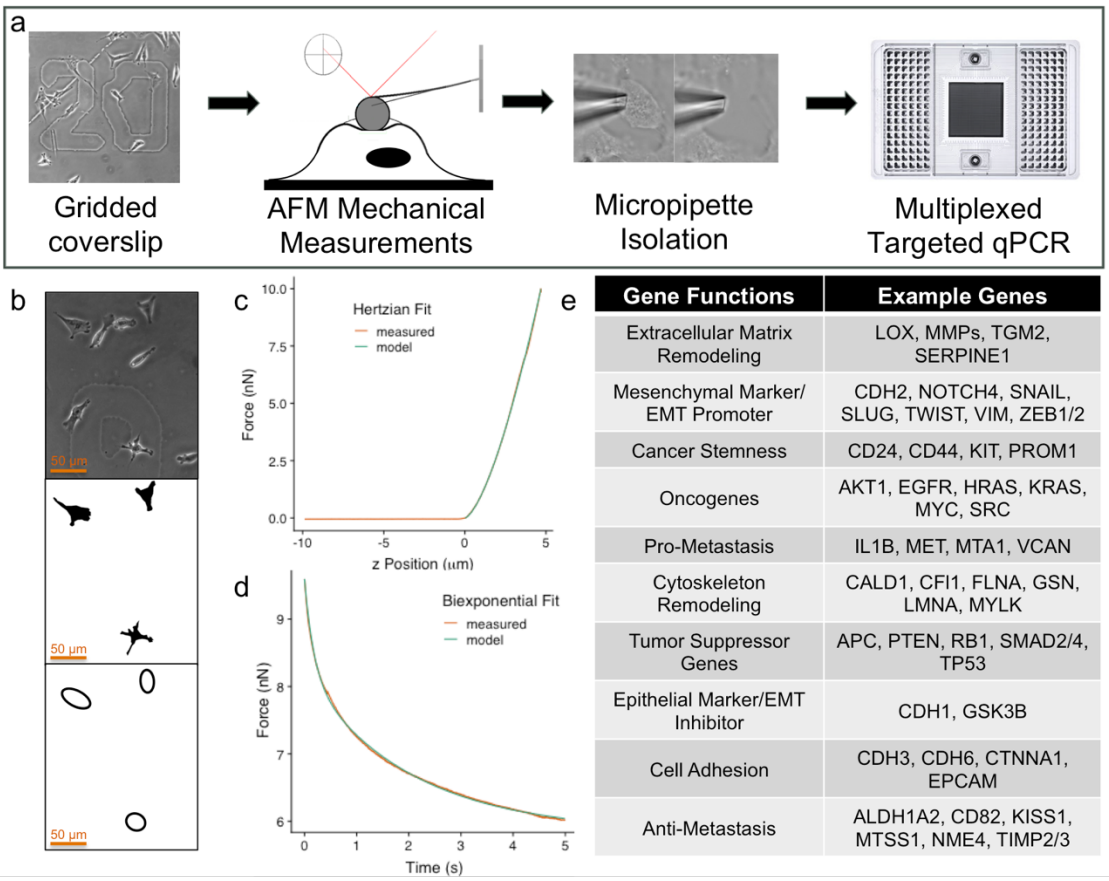

Gene Functions	Example Genes
Extracellular Matrix Remodeling	LOX, MMPs, TGM2, SERPINE1
Mesenchymal Marker/ EMT Promoter	CDH2, NOTCH4, SNAIL, SLUG, TWIST, VIM, ZEB1/2
Cancer Stemness	CD24, CD44, KIT, PROM1
Oncogenes	AKT1, EGFR, HRAS, KRAS, MYC, SRC
Pro-Metastasis	IL1B, MET, MTA1, VCAN
Cytoskeleton Remodeling	CALD1, CFI1, FLNA, GSN, LMNA, MYLK
Tumor Suppressor Genes	APC, PTEN, RB1, SMAD2/4, TP53
Epithelial Marker/EMT Inhibitor	CDH1, GSK3B
Cell Adhesion	CDH3, CDH6, CTNNA1, EPCAM
Anti-Metastasis	ALDH1A2, CD82, KISS1, MTSS1, NME4, TIMP2/3

Figure 6 – Development of new method to combine single cell morphological, mechanical, and gene expression data – a) Schematic describing the process to collect three types of data for each single cell in which cells are grown on a gridded coverslip, atomic force microscopy is used to measure cell's Young's modulus and viscous properties, a micropipette is used to aspirate and isolate each probed cell, and a Fluidigm integrated fluidic chip is used for multiplexed targeted qPCR to measure the gene expression of 96 genes. b) Cell morphological parameters are extracted from images of cells on the gridded coverslip, including cell size, aspect ratio, circularity, roundness and solidity. c) Each AFM force curve was fit using an equation defined by Hertzian contact mechanics to identify each cell's Young's modulus. d) Each dwell portion of the AFM force curve was fit using a biexponential equation to identify each cell's fast and slow time viscous time constants. e) A partial list of genes of interest to investigate the relationship between cell mechanics, gene expression, and metastatic potential.

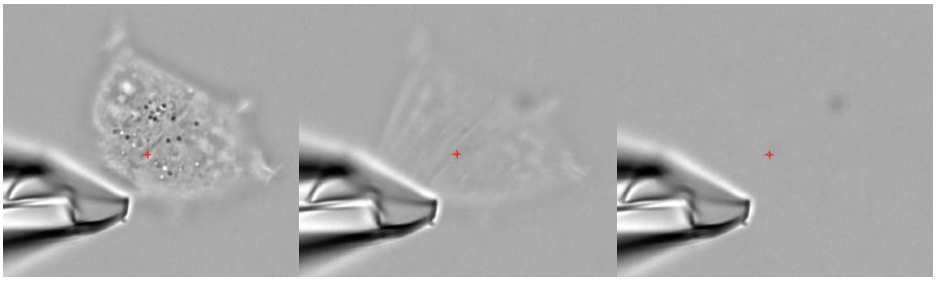

Figure 7 – Example video of cell isolation using micropipette aspiration – (Supplemental_Video1.mov, 3.9 MB) The x-y-z position of a micropipette with an opening diameter of approximately 6.5 µm is controlled using micromanipulators to lower the pipette close to a cell of interest. Once the micropipette and cell are brought in proximity, 345 to 500 mbar of negative pressure is applied for 0.2 to 2 seconds to aspirate the cell of interest.

Table 1 – Curated list of genes of interest – There are several genes of interest that are driven or are affected by the many processes described in the text that facilitate the metastatic spread of cancer. They are summarized below in the following table including the gene's symbol, general function as classified by the PANTHER Classification System (http://www.pantherdb.org), and any particular notes about its reported effect on metastasis. Some abbreviations included in the table include CSC (cancer stem cell marker), TSG (tumor suppressor gene), HKG (housekeeping gene), EMT (epithelial-to-mesenchymal transition), Met. Sup (metastasis suppressor), ECM (extracellular matrix), Wnt (Wnt signaling pathway), ECM remodel (ECM remodeling protein), Cell Diff. (cell differentiation), Met. Pro. (metastasis promoter), and Mechano. (mechanotransduction).

Symbol	Function	Notes
ACTA2	Cytoskeleton	Required for metastasis[76]
ACTB	Cytoskeleton	Associated with invasion[77]
AKT1	Kinase	Pro and Anti Metastatic Effect[78]
ALDH1A2	Dehydrogenase	CSC Marker, Migration suppressor[79]
APC	Cell Signaling	TSG
B2M	HKG	
CALD1	Cytoskeleton	Increased motility[80]
CAV1	Cytoskeleton	Tumor suppression and promotion[81]
CD24	Cell Signaling	CSC, Low expression → mets.[82]
CD44	Cell Signaling	CSC, High expression → mets.[82]
CD82	Cell Signaling	Metastasis suppressor[83]
CDH1	Cell Adhesion	Epithelial, Deletion → metastasis[84]
CDH2	Cell Adhesion	Mesenchymal, Enhance migration[84]

Table 1 (continued)

CDH3	Cell Adhesion	Enhance invasion[84]
CDH6	Cell Adhesion	Promote EMT and mets[85]
CFL1	Cytoskeleton	Metastasis biomarker[86]
COL11A1	ECM	Poor prognosis and mets[68]
COL1A2	ECM	
COL5A1	ECM	Poor prognosis and mets[68]
COL6A2	ECM	Poor prognosis and mets[68]
CTNNA1	Cytoskeleton	Catenin loss → mets[87]
CTNNB1	Cell Adhesion	Wnt, Induce migration/invasion[88]
CTSL	ECM remodel	Invasion and met marker[89]
CXCR4	Cell Signaling	Chemotaxis, Overexpression → mets[90]
EGFR	Cell Signaling	Microenvironment → mets[91]
EPCAM	Cell Adhesion	Invasion inhibition and tumor formation[92]
FLNA	Cytoskeleton	Tumor promotion and metastasis inhibition[93]
FN1	ECM	Intercellular signaling
GAPDH	HKG	
GPNMB	HKG	
GSK3B	Kinase	Wnt, Inhibit met through SNAI2[88]
GSN	Cytoskeleton	Metastasis suppressor[94]
HPRT1	HKG	
HRAS	GTPase	Oncogene
IL18	Interleukin	Inflammation
IL1B	Interleukin	Inflammation, Induce pro-metastatic gene expression[95]
ITGA6	Cell Adhesion	
ITGA7	Cell Adhesion	
ITGB1	Cell Adhesion	
KISS1	Cell Signaling	Anti-metastatic role[96]
KISS1R	Cell Signaling	Promotes tumor invasion[96]
KIT	Cell Signaling	Cell Diff., Deletion → metastasis [97]
KRAS	GTPase	Oncogene
LAMC2	ECM	
LMNA	Cytoskeleton	Inhibits metastasis[98]
LOX	ECM remodel	Increased metastasis[99]
MAPT	Cytoskeleton	
MET	Cell Signaling	
MMP11	ECM remodel	
MMP13	ECM remodel	
MMP2	ECM remodel	Increased metastasis[99]
MMP3	ECM remodel	

Table 1 (continued)

MMP7	ECM remodel	
MMP9	ECM remodel	Increased metastasis[99]
MTA1	Transcription Factor	Enable mets through AKT[100]
MTOR	Kinase	PIK3CA/AKT pathway important for metastasis[101]
MTSS1	Cytoskeleton	Inhibits motility[102]
MYC	Transcription Factor	Oncogene
MYLK	Cytoskeleton	
NME4	Kinase	Met. Sup.
NOTCH4	Cell Signaling	EMT
PIK3CA	Kinase	PIK3CA/AKT pathway important for metastasis[101]
POSTN	Cell Adhesion	Poor prognosis and mets[68]
PROM1	Cell Signaling	CSC Marker
PTEN	Phosphatase	TSG
RB1	Chromatin Binding	TSG, Loss increases invasion[103]
ROCK1	Cytoskeleton	Downregulation → invasion suppression[104]
RPL32	HKG	
SERPINE1	Protease Inhibitor	Downregulated → met sup[105]
SMAD2	Transcription Factor	Cell Cycle
SMAD4	Transcription Factor	Cell Cycle, Upregulate CDH2 and invasion[106]
SNAI1	Transcription Factor	EMT, Induce migration/invasion[88]
SNAI2	Transcription Factor	EMT, Induce migration/invasion[88]
SRC	Kinase	Oncogene
TGFB1	Cell Signaling	EMT, Promote metastasis[107]
TGM2	ECM remodel	EMT and metastasis in ovarian cancer[13]
THBS2	Cell Adhesion	Poor prognosis and mets[68]
TIMP2	Protease Inhibitor	
TIMP3	Protease Inhibitor	Decrease → Malignancy[108]
TP53	Transcription Factor	TSG
TPM1	Cytoskeleton	
TUBB3	Cytoskeleton	
TWIST1	Transcription Factor	EMT
VCAN	ECM	Poor prognosis and mets[68]
VEGFA	Cell Signaling	
VIM	Cytoskeleton	Mesenchymal, Overexpression → mets[109]
WNT5A	Cell Signaling	Wnt, Tumor suppression and promotion[110]
YAP1	Transcription Factor	Mechanotransduction
ZEB1	Transcription Factor	EMT, Induce migration/invasion[88]
ZEB2	Transcription Factor	EMT, High expression in mets[111]

We used custom R code (see 3.3.2) to automate the process of extracting the cell's Young's modulus and viscous time constants from many AFM force curves. The validation of this code is provided in Figure 8 comparing the analysis of cell stiffness measurements extracted automatically to those extracted manually using commercial software at low (10-50%) indentation. We found that the epithelial OVCAR3 cells are statistically stiffer than the mesenchymal HEY and HEY A8 cell types ($p < 0.05$, Tukey HSD post-hoc test). To confirm that the cell mechanical measurements were not biased by the amount of time the cells were out of the incubator, we compared the cell measurement number (a proxy for time of the experiment), to the cell stiffness (Figure 9). We found there was no significant correlation between cell measurement number and cell stiffness for any of the cell types ($p > 0.1$, t-test for significance of Pearson's correlation test).

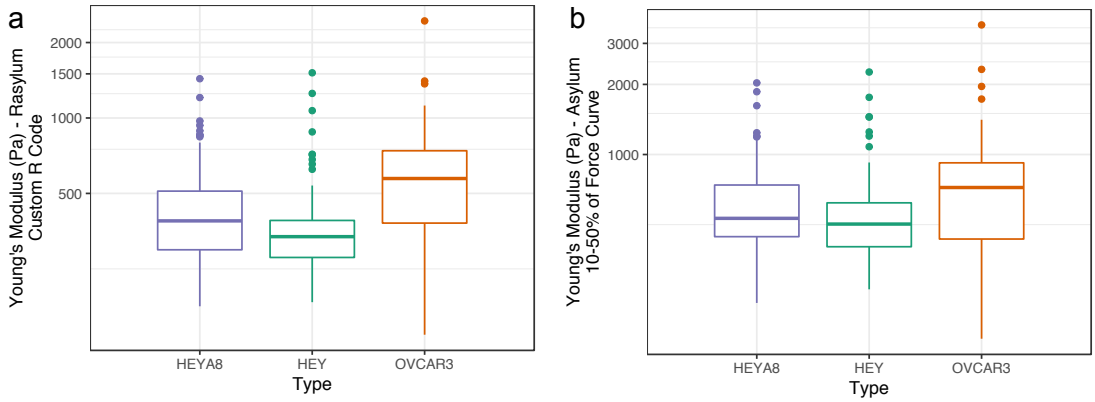

Figure 8 – Comparison of mechanical properties of ovarian cancer cell lines – The Young's modulus of cells of three ovarian cancer cell lines, HEY A8 (n=91), HEY (n=95) and OVCAR3 (n=87) were computed using custom R code (a), as well as commercially available Asylum software using 10-50% of the force curve (b). The epithelial OVCAR3 cells are statistically stiffer than the mesenchymal HEY and HEY A8 cell types ($p < 0.05$, Tukey HSD post-hoc test).

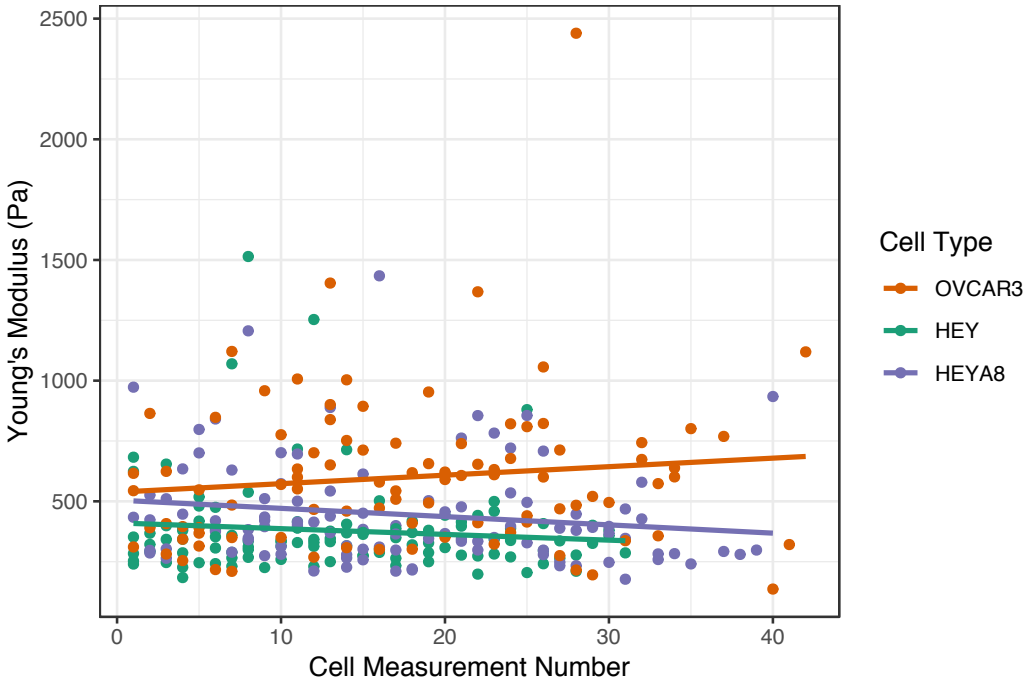

Figure 9 – No change in mechanics over time of experiment – Cell measurement number refers to the order in which cells' mechanical properties were measured over the course of a two-hour AFM session. There is no significant correlation between the cell's Young's modulus and the moment in time the cell's properties were measured during an experiment. ($p > 0.1$, t-test for significance of Pearson's correlation test)

The morphology analysis confirms the epithelial and mesenchymal status for each cell type. The epithelial cell line, OVCAR3, had shorter major axes with aspect ratios close to 1 while the mesenchymal cells HEY and HEY A8 were more elongated with elevated aspect ratios (Figure 10b and Figure 10c). Additionally, OVCAR3 cells were more circular than HEY cells which were more circular than HEY A8 cells (Figure 10d). Finally, the measure of solidity was used to compare the number of protrusions from each cell, with HEY A8 cells being the least solid and with the most protrusions, while OVCAR3 cells were the most solid (Figure 10e). Representative images of each cell type are included for comparison (Figure 10a).

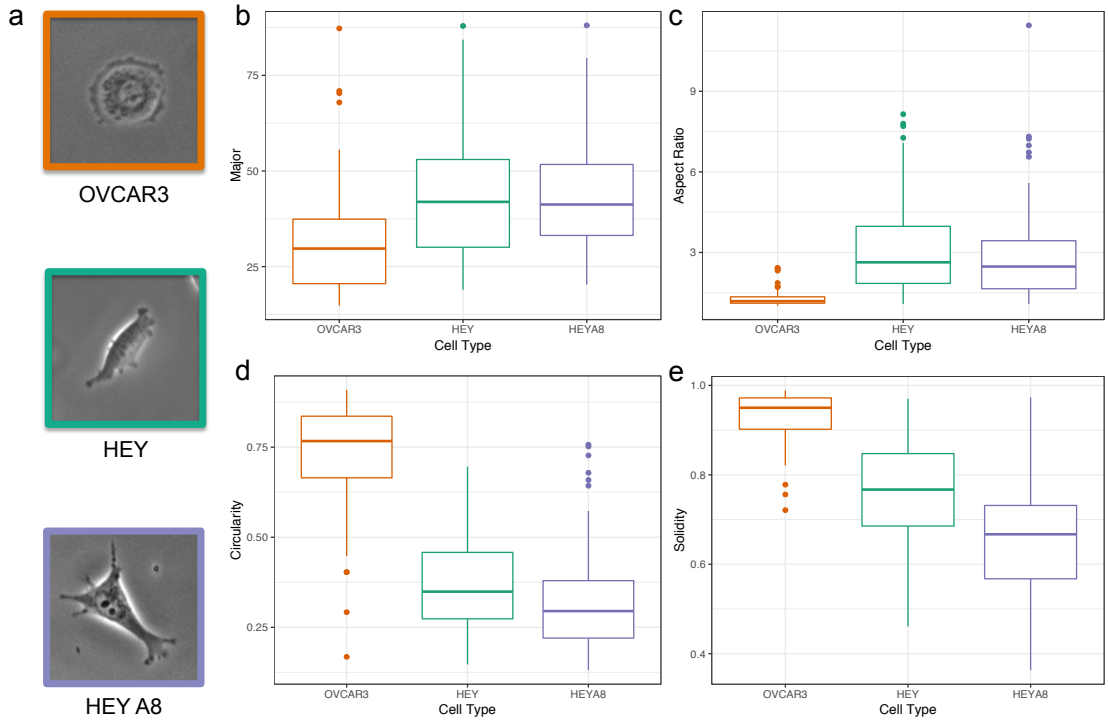

Figure 10 – Epithelial and mesenchymal morphology for populations – a) Representative bright field images of each ovarian cancer cell type. b) Comparison of the major axis of an ellipse fit to each cell across cell types. c) Comparison of the axis ratio of the major axis to minor axis of an ellipse fit to each cell across cell types. d) Comparison of the circularity of each cell across cell types (see 3.3.3 for calculation of circularity). e) Comparison of the solidity of each cell across cell types (see 3.3.3 for calculation of solidity).

To confirm the isolation of single cells without affecting gene expression, we plotted the normalized expression of each cell isolated through micropipette aspiration and compared the expression distribution to the normalized bulk expression of each gene for each cell type (Figure 11). We found that for all cell types the normalized gene expression was significantly correlated between the average single cell expression and the population measurement ($p < 1E-5$, HEY A8 cor = 0.557, HEY cor = 0.445, OVCAR3 cor = 0.627), supporting our hypothesis

that the isolation method had little effect on gene expression (Figure 12a). Importantly, we observed the population measurement of the average expression of the cells (represented as a point in the violin plot) does not represent the true expression of many actual single cells (Figure 12b, Figure 12c, Figure 12e, and Figure 12f). Additionally, the population measurement does not accurately capture the heterogeneity and sometimes bimodal distribution of single cell gene expression, sometimes representing the expression of the subset of cells with high expression, without accurately describing a large portion of low expressing cells (Figure 12d).

Figure 11 – Violin plots of the distribution of normalized single cell gene expression data for each cell type and each gene of interest – The datum point in the middle of each violin plot represents the population level expression level collected using RT-qPCR with bulk RNA.

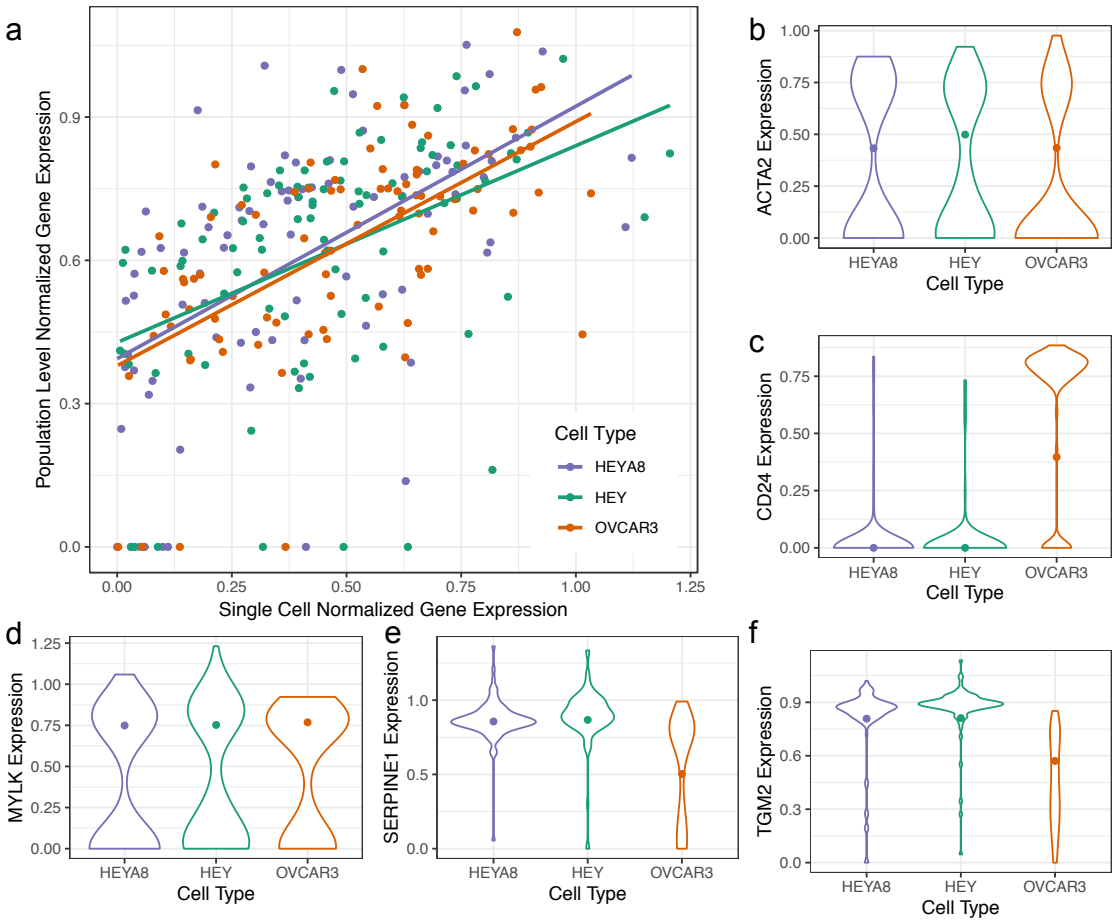

Figure 12 – Population vs. single cell gene expression – a) Comparison of population level normalized gene expression and average single cell normalized gene expression. Each point represents the expression of a particular gene in a cell type. Population level data was gathered using RT-qPCR of purified RNA from a flask of each cell type while single cell data is the mean expression of a gene across all single cells from each cell type. For all cell types the normalized gene expression was significantly correlated between the average single cell expression and the population measurement ($p < 1E-5$, HEY A8 cor = 0.557, HEY cor = 0.445, OVCAR3 cor = 0.627) b-f) Violin plots of the distribution of single cell data for each cell type. The datum point in the middle of each violin plot represents the population level expression level collected using RT-qPCR with bulk RNA for *ACTA2* (b), *CD24* (c), *MYLK* (d), *SERPINE1* (e), and *TGM2* (f).

To further confirm the lack of change in single cell gene expression due to micropipette aspiration, we compared the gene expression of cells collected by aspiration to those of cells isolated using fluorescence activated cell sorting

(FACS) (Figure 13). The average expression between the two groups of cells was significantly correlated (cor = 0.887, $p < 1E-15$), implying little effect of collection method on gene expression (Figure 14a). Micropipette aspiration, however, resulted in a higher efficiency of gene expression data collected, with 277 of 282 (98.227%) micropipette-isolated cells having measurable gene expression data while only 40 of 94 (42.553%) FACS isolated cells produced measurable data (Figure 14b). Finally, primer designs were collected from literature and validated to amplify the expected product (Table 2). With this validation, the genomechanical method represents the first process for linking mechanical and imaging data with gene expression data on the single cell level.

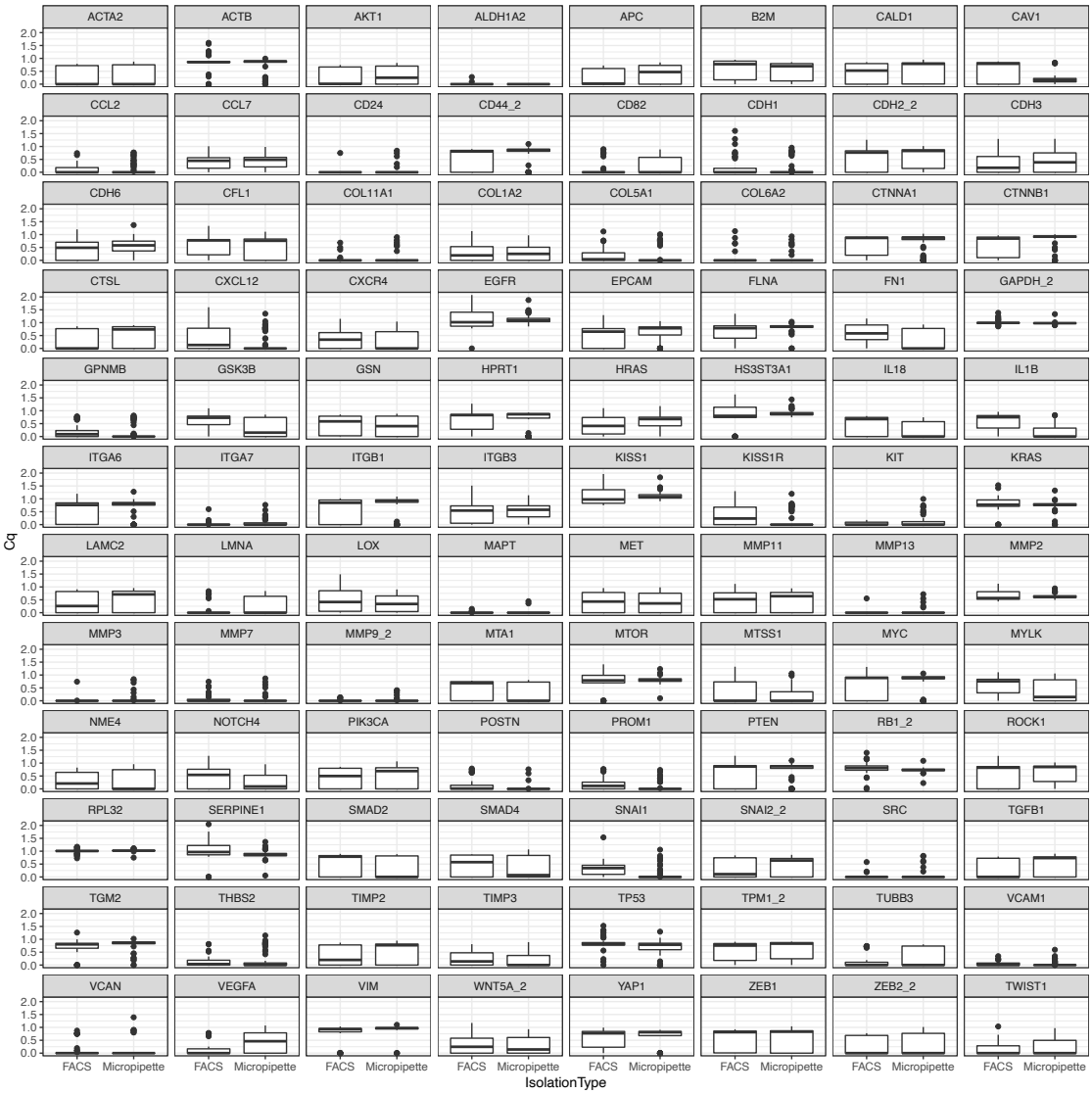

Figure 13 – Comparing gene expression of cells isolated by FACS sorting and micropipette aspiration – Box plots comparing gene expression transformed and normalized to the housekeeping genes *GAPDH* and *RPL32*.

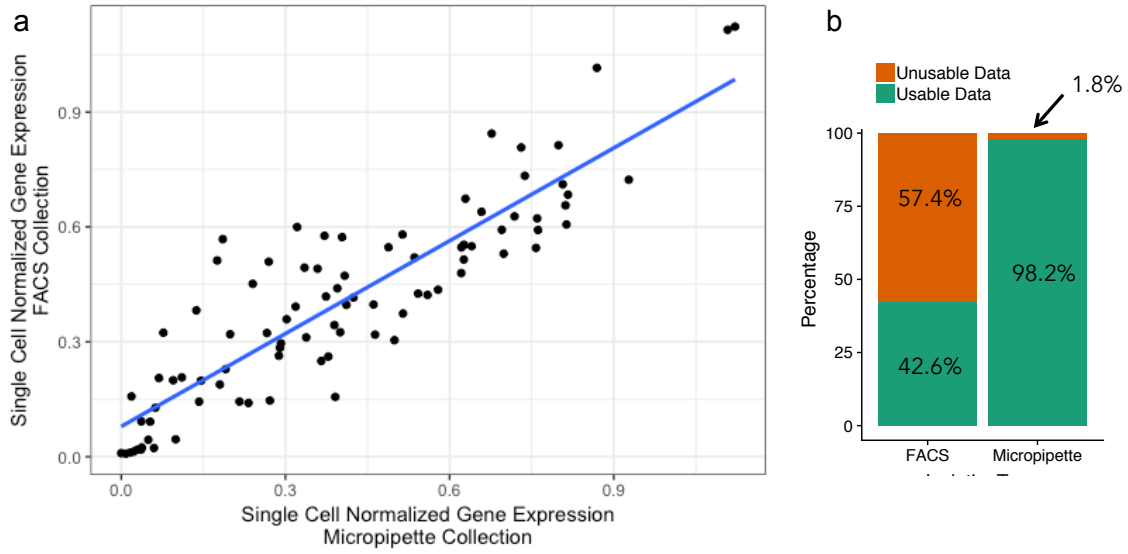

Figure 14 – FACS vs. micropipette cell isolation – a) Single cell normalized gene expression is well correlated for HEY A8 cells collected with either micropipette or FACS isolation. Each point represents a particular gene. The average expression between the two groups of cells was significantly correlated (cor = 0.887, $p < 1E-15$) b) Fewer FACS-isolated single cells pass the quality control pipeline (see 3.3.7 for further explanation) than the micropipette-isolated cells.

Table 2 – PCR primers for list of genes of interest – All primers were validated to produce a PCR product the correct size using gel electrophoresis.

Gene Symbol	Forward Primer	Reverse Primer
ACTA2	GTGTTGCCCCTGAAGAGCAT	GCTGGGACATTGAAAGTCTCA
ACTB	CATCGAGCACGGCATCGTCA	TAGCACAGCCTGGATAGCAAC
AKT1	TCCCGAGGCCAAGTCCTT	CCGCCAAGCCTCTGCTT
ALDH1A2	TGCATTCACAGGGTCTACTGA	TGCCTCCAAGTTCCAGAGTT
APC	GAGACAGAATGGAGGTGCTGC	GTAAGATGATTGGAATTATCTTCT
B2M	ACTGAATTCACCCCCACTGA	CCTCCATGATGCTGCTTACA
CALD1	CTGGCTTGAAGGTAGGGGTTT	TTGGGAGCAGGTGACTTGTTT
CAV1	CATCCCGATGGCACTCATCTG	TGCACTGAATCTCAATCAGGAAG
CD24	CCCACGCAGATTTATTCCAG	GACTTCCAGACGCCATTTG
CD44	TTTGCATTGCAGTCAACAGTC	GTTACACCCCAATCTTCATGTCCAC
CD82	GCCGACAAGAGCAGTTTCAT	GGAAGCCCATGAGCATAGTG
CDH1	ATTTTTCCCTCGACACCCGAT	TCCCAGGCGTAGACCAAGA
CDH2	GTCAGCAGAAGTTGAAGAAATAGTG	GCAAGTTGATTGGAGGGATG
CDH3	ATCATCGTGACCGACCAGAAT	GACTCCCTCTAAGACACTCCC
CDH6	ACAGTGACTGTCCGGGTCTGTGC	CAGTCCCGTGGGGTGGATGA

Table 2 (continued)

CFL1	GCCAACTTCTAACCGCAATAG	CCTTACTGGTCCTGCTTCC
COL11A1	GACTATCCCCTCTTCAGAACTGTTAAC	CTTCTATCAAGTGGTTTCGTGGTTT
COL1A2	GAGCGGTAACAAGGGTGAGC	CTTCCCCATTAGGGCCTCTC
COL5A1	CACAACTTGCCTGATGGAATAACA	GCAGGGTACAGCTGCTTGGT
COL6A2	AAAGGAGAGCCTGCGGATCC	TGTTGACCACGTTGATGACG
CTNNA1	GAGCTGTCTACGCAAGTCCC	TTTCGGAGTACATGGGCAAT
CTNNB1	GGGTCCTCTGTGAACTTGCTC	TTCTTGTAATCTTGTGGCTTGTCC
CTSL	CGGCATGAATGAAGAAGGAT	TGGGCTTACGGTTTTGAAAG
CXCR4	GGGCAATGGATTGGTCATCCT	TGCAGCCTGTACTTGTCCG
EGFR	TTGCCGCAAAGTGTGTAACG	GTCACCCCTAAATGCCACCG
EPCAM	CTTGTCTGTTCTTCTGACCCC	TGATCCTGACTGCGATGAGAG
FLNA	CATCAAGTACGGTGGTGACG	ACATCCACCTCTGAGCCATC
FN1	AGCAGACCCAGCTTAGAGTT	GCAGAAGTGTTTGGGTGACT
GAPDH	CTTTTGCGTCGCCAG	TTGATGGCAACAATATCCAC
GPNMB	TGCGTCCGTGAGAATTCA	TGTGCTCCCTCATGTAAGCA
GSK3B	GGAACTCCAACAAGGGAGCA	TTCGGGGTCGGAAGACCTTA
GSN	TGTCCTACCTTTCCAGCCATATCG	TGTCGCCTCCATAGAACTGTCC
HPRT1	CTCATGGACTAATTATGGACAGGAC	GCAGGTCAGCAAAGAATTTATAGCC
HRAS	AGCAGATCAAACGGGTGAAGGACT	GATCTCACGCACCAACGTGTAGAA
IL18	TGAATCCTCCTGATAACATC	TAGTCTTCGTTTTGAACAGT
IL1B	CGAATCTCCGACCACCACTAC	GCACATAAGCCTCGTTATCCC
ITGA6	GGCGGTGTTATGTCCTGAGTC	AATCGCCCATCACAAAAGCTC
ITGA7	GGATGGTGGGGAATGGAAGT	GGTCAGCAGGGTCCAAAGTT
ITGB1	GTAACCAACCGTAGCAAAGGA	TCCCCTGATCTTAATCGCAAAAC
KISS1	GGACCTGCCTCTTCTCACCA	ATTCTAGCTGCTGGCCTGTG
KISS1R	AACTTCTACATCGCCAACCTG	CACCGAGACCTGCTGGATGTA
KIT	GTTCTGCTCCTACTGCTTCG	ATAACAGCCTAATCTCGTCGC
KRAS	GACTGAATATAAACTTGTGGTAGTTGGA	CATATTCGTCCACAAAATGATTCTG
LAMC2	GATGGCATTCACTGCGAGAAG	TCGAGCACTAAGAGAACCTTTGG
LMNA	CGGTTCCCACCAAAGTTCA	CTCATCCTCGTCGTCCTCAA
LOX	CCTGGTTCCTGAATCTGACT	CTTCAGAACACCAGGCACTG
MAPT	TAGGCAACATCCATCATAAACCA	TCGACTGGACTCTGTCCTTGAA
MET	TGCAGCGCGTTGACTTATTCATGG	GAAACCACAACCTGCATGAAGCGA
MMP11	GGGGATGTCCACTTCGACTA	CAGTGGGTAGCGAAAGGTGT
MMP13	AACATCCAAAAACGCCAGAC	GGAAGTTCTGGCCAAAATGA
MMP2	TTTCCATTCCGCTTCCAGGGCAC	TCGCACACCACATCTTTCCGTCACT
MMP3	GGCTTTCCCAAGCAAATAGC	GTGCCCATATTGTGCCTTCT
MMP7	TCCAACCTATGGAAATGGAGA	GGAGTGGAGGAACAGTGCTT
MMP9	GGCCCTTCTACGGCCACT	CAGAGAATCGCCAGTACTT
MTA1	CTCTGCGCATCTTGTTGGACATA	TCAGCTTCGTCGTGTGCAGATAG
MTOR	GCAGATTTGCCAACTATCTTCGG	CAGCGGTAAAAGTGTCCCCTG
MTSS1	GGAGGCTGTGATTGAGAAGG	AGCTGGGACTGCAGCTTTCC

Table 2 (continued)

MYC	AAAGGCCCCCAAGGTAGTTA	GCACAAGAGTTCCGTAGCTG
MYLK	CCCGAGGTTGTCTGGTTCAAA	GCAGGTGTACTTGGCATCGT
NME4	GCGGAGGAAGCCCTTCTA	GCGTGGATGACATTCCTGCT
NOTCH4	CCTGGCTCCTTCAACTGCC	GCAAGTAGGTCCAGACAGGT
PIK3CA	CGACAGCATGCCAATCTCTTC	CTAAGGCTAGGGTCTTTCG
POSTN	TTGAGACGCTGGAAGGAAAT	AGATCCGTGAAGGTGGTTTG
PROM1	AGTCGGAAACTGGCAGATAGC	GGTAGTGTTGTACTGGGCCAAT
PTEN	AGGGACGAACTGGTGTAATGA	CTGGTCCTTACTTCCCCATAGAA
RB1	GGAAGCAACCCTCCTAAACC	TTTCTGCTTTTGCATTCGTG
ROCK1	GATCACACTGTTAGTCGGCTTG	ATCTCCTCCTCCTTCTCCAGTT
RPL32	ACAAAGCACATGCTGCCCAGTG	TTCCACGATGGCTTTGCGGTTC
SERPINE1	CAACTTGCTTGGGAAAGGAG	GGGCGTGGTGAACTCAGTAT
SMAD2	ACCGAAATGCCACGGTAGAA	TGGGGCTCTGCACAAAGAT
SMAD4	CATCCTGCTCCTGAGTATTGG	GGGTCCACGTATCCATCAAC
SNAI1	CCCCAATCGGAAGCCTAA	CCTTTCCCACTGTCCTCAT
SNAI2	TGATGAAGAGGAAAGACTACAG	GCTCACATATTCCTTGTCACAG
SRC	CGTCCAAGCCGCAGACTCA	TGAAACCACAGCATACAAC
TGFB1	CAATTCCTGGCGATACCTCAG	GCACAACTCCGGTGACATCAA
TGM2	CCAACTACAACTCGGCCCAT	CTGGTCATCCACGACTCCAC
THBS2	CCCAAGTGCCTTCAGAGGATAA	TGCCCAATTTTCACTCCACAT
TIMP2	GAGCCTGAACCACAGGTACCA	TCTGTGACCCAGTCCATCCA
TIMP3	CCAGGACGCCTTCTGCAA	CCCCTCCTTTACCAGCTTCTTC
TP53	TAACAGTTCCTGCATGGGCGGC	AGGACAGGCACAAACACGCACC
TPM1	TCATCATTGAGAGCGACCTG	CTTGTCGGAAAGGACCTTGA
TUBB3	GCAACTACGTGGGCGACT	CGAGGCACGTACTTGTGAGA
TWIST1	GTCCGCAGTCTTACGAGGAG	GCTTGAGGGTCTGAATCTTGCT
VCAN	CAAGCATCCTGTCTCACGAA	CAACGGAAGTCATGCTCAAA
VEGFA	AGGCCAGCACATAGGAGAGA	TTTCTTGCGCTTTCGTTTTT
VIM	AGTCCACTGAGTACCGGAGAC	CATTTCACGCATCTGGCGTTC
WNT5A	AGGGCTCCTACGAGAGTGCT	GACACCCCATGGCACTTG
YAP1	TAGCCCTGCGTAGCCAGTTA	TCATGCTTAGTCCACTGTCTGT
ZEB1	TTACACCTTTGCATACAGAACCC	TTTACGATTACACCCAGACTGC
ZEB2	AAGCCAGGGACAGATCAGC	GCCACACTCTGTGCATTTGA

3.4.2 Population level measurements insufficient to distinguish between cell types

At the population level, we observe several mechanotypic, genotypic, and phenotypic trends between the three ovarian cancer cell types. HEY A8 cells are

the most migratory, while the OVCAR3 cells are least migratory (Figure 15a). Both the mesenchymal HEY and HEY A8 cells are significantly softer than the epithelial OVCAR3 cells. Additionally, we observed OVCAR3 cells are the least viscous (Figure 15b). Comparing the morphological measurements of each cell type, increased migration correlated with increased cell elongation and cell protrusions (Figure 15c). From an analysis of all genes of interest (Figure 16), increasing migration correlated with increased gene expression associated with pro-metastatic processes, including EMT-driving transcription factors, ECM remodeling proteins, cancer stemness, and mesenchymal markers (Figure 15d), such as *SNAI2*, *TGM2,* and *VIM*. Also, increasing migratory ability correlates with decreased gene expression associated with anti-metastatic processes, including epithelial markers, metastasis suppressors, cell differentiation markers, and ECM remodeling inhibitors (Figure 15e), such as *CDH1*, *GSN,* and *KIT*. These population level trends support the existence of correlation between cancer cell mechanotype, genotype, and phenotype. However, we note there is substantial overlap between these parameters for the different cell types that preclude drawing accurate connections between cell morphology, mechanics, and genetic expression. Thus, single cell measurements are needed, even within these nominally uniform cell lines, due to the heterogeneity of expression profiles, to better determine how cell mechanics and gene expression work together during metastatic processes.

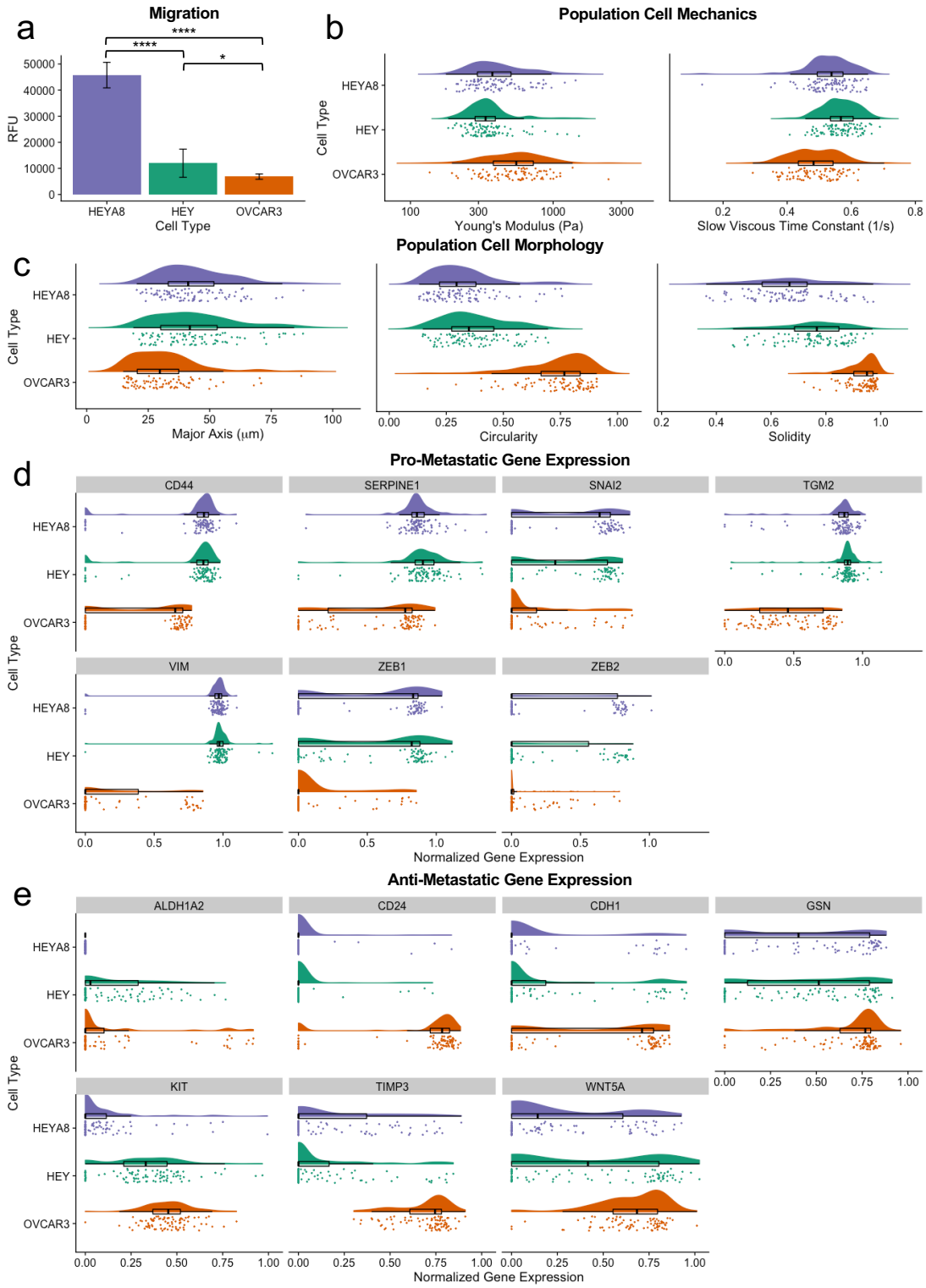

Figure 15 – Comparison of population behavior of HEY A8, HEY, and OVCAR3 cell lines – a) Transwell migration assay data demonstrate the increased migratory ability of the HEY A8 cells compared to the HEY cells (Tukey HSD, ****, $p < 0.0001$). The epithelial OVCAR3 cells are the least migratory (HEYA8 vs OVCAR3,

Tukey HSD, ****, p < 0.0001, HEY vs. OVCAR3, Tukey HSD, *, p < 0.05). Cells that migrated through the transwell were fluorescently quantified; RFU is relative fluorescent units. b) With increasing migratory ability, we see cell softening and changing viscous properties. c) With increasing migratory ability, we see increasing cell elongation and cell protrusions. d) With increasing migratory ability, we see increasing expression of EMT-driving transcription factors, ECM remodeling proteins, cancer stemness, and mesenchymal markers. e) With increasing migratory ability, we see decreasing expression of epithelial markers, metastasis suppressors, cell differentiation markers, and ECM remodeling inhibitors. Raincloud plots consist of an overlay of a half violin plot, a boxplot depicting summary statistics for each population as well as a jitter plot displaying single cell values.

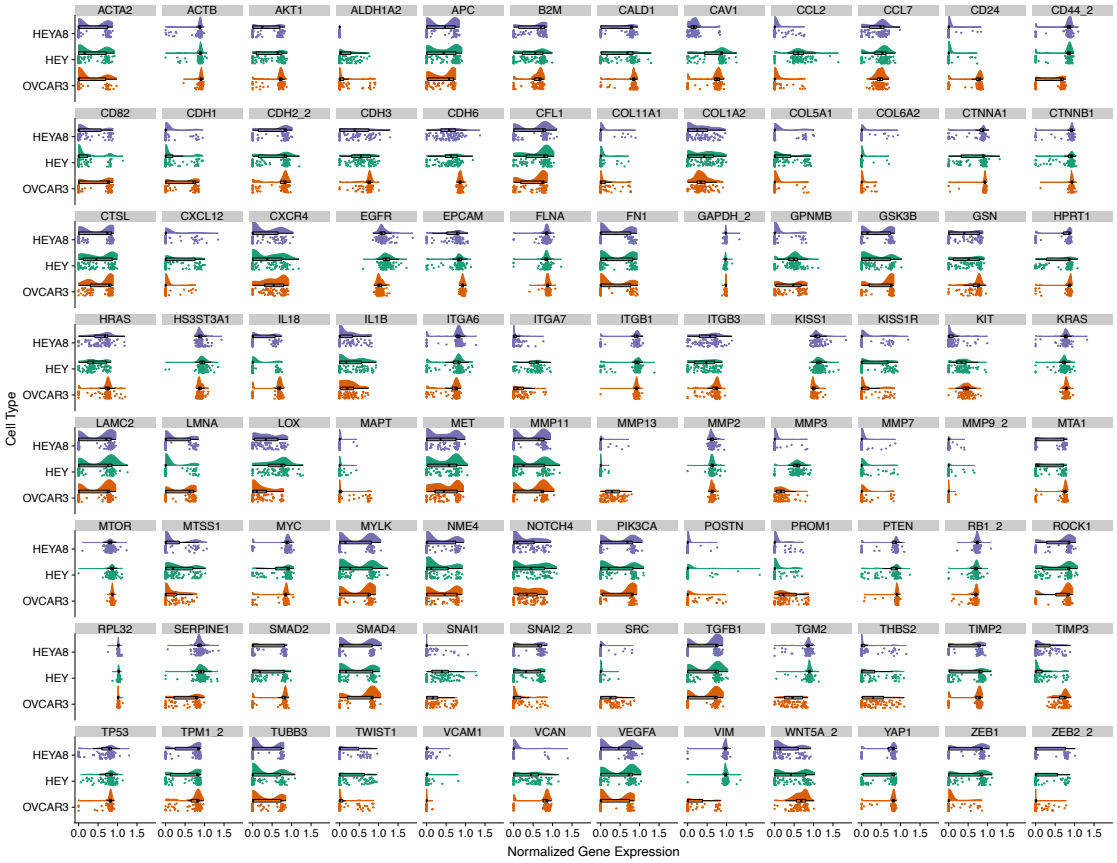

Figure 16 – Single cell gene expression profiles for each cell type and each gene of interest – Raincloud plots consist of an overlay of a half violin plot, a boxplot depicting summary statistics for each population as well as a jitter plot of each single cell datum.

3.4.3 Pro-metastatic gene expression pattern associated with soft single cells

We examined the single cell correlations between gene expression and cell mechanical properties of 282 ovarian cancer cells (92 HEY A8 cells, 100 HEY cells, and 90 OVCAR3 cells). After an initial quality control check for stable expression of housekeeping genes, we removed 9 cells, resulting in 273 cells for analysis (91 HEY A8 cells, 95 HEY cells, 87 OVCAR3 cells). A Spearman's rank correlations analysis found 39 genes that were significantly correlated with cell stiffness ($p < 0.05$) (Figure 17a). Of the 14 genes negatively correlated with stiffness, 10 genes were associated with pro-metastatic functions, such as extracellular remodeling, mesenchymal markers, cancer stemness, and oncogenic behavior (Figure 17b). Meanwhile, 16 of the 25 positively correlated genes are related to anti-metastatic functions, such as cell adhesion, epithelial markers, tumor and metastasis suppression, and cytoskeletal proteins.

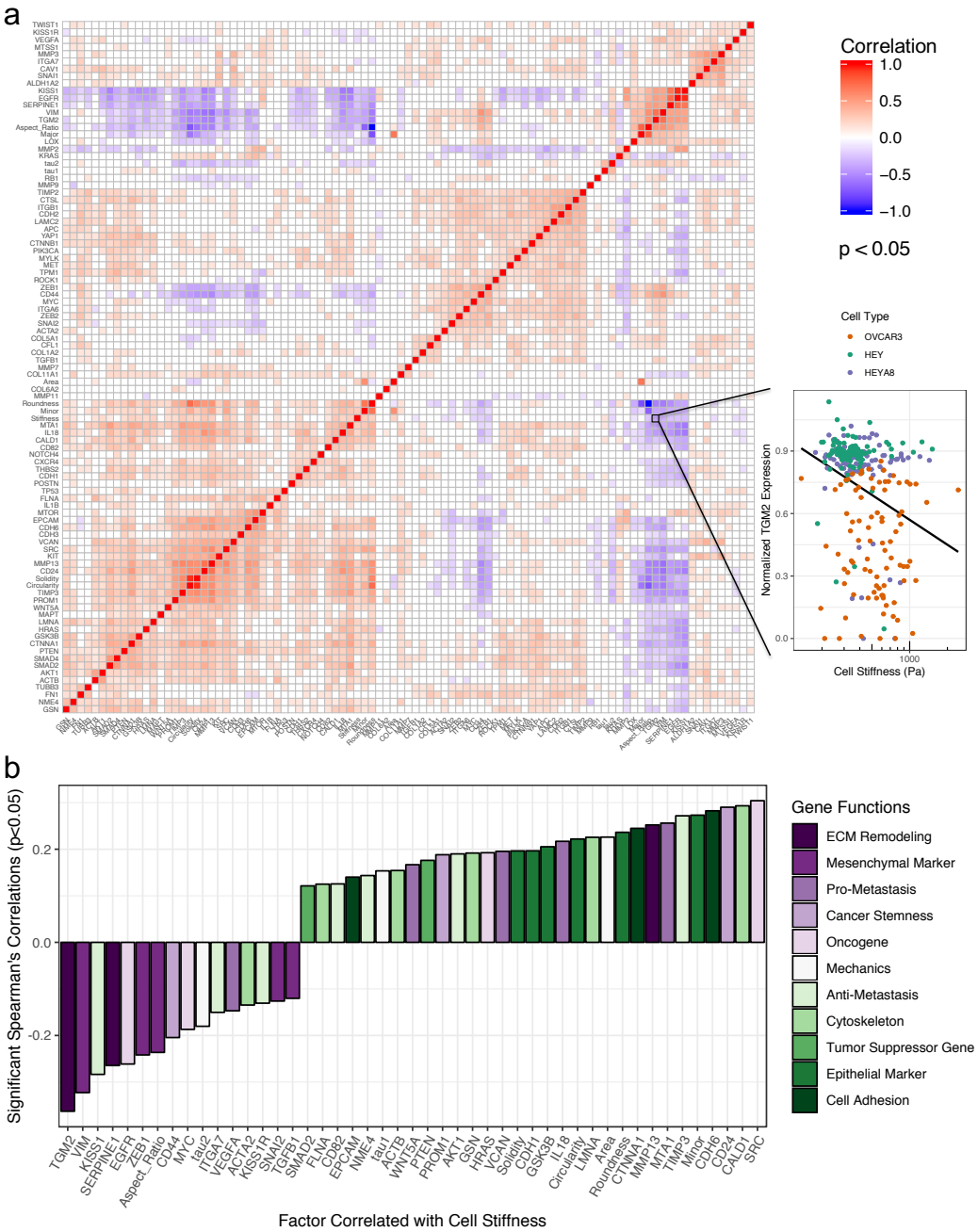

Figure 17 – Single cell correlations between genetic, morphological and mechanical parameters – a) Correlation matrix comparing the Spearman's pairwise correlations between each combination of single cell genetic, morphological, and mechanical data. Only statistically significant ($p < 0.05$) correlations are plotted. The inset shows the single cell values for cell stiffness and normalized *TGM2* expression. b) Significant correlations between cell stiffness and genetic, morphological and mechanical parameters. Bars are colored by nominal function. Data can be explored further with interactive plots at https://kyoung74.github.io/PlotlyPlots/.

Counterintuitively, the genes that are most highly correlated with cell stiffness are not directly related to the cytoskeleton, but rather drive various processes important for promoting or preventing metastasis. The gene most strongly negatively correlated with cell stiffness is *TGM2* which codes for transglutaminase 2, an ECM remodeling protein. The gene most strongly positively correlated with cell stiffness is *SRC*, an oncogene that has been associated with stress fiber assembly and increased proliferation. We also repeated the correlation analysis for the three cell types separately. From this analysis, we were able to identify additional cell type specific correlations between genes of interest and cell stiffness (Figure 18).

a OVCAR3

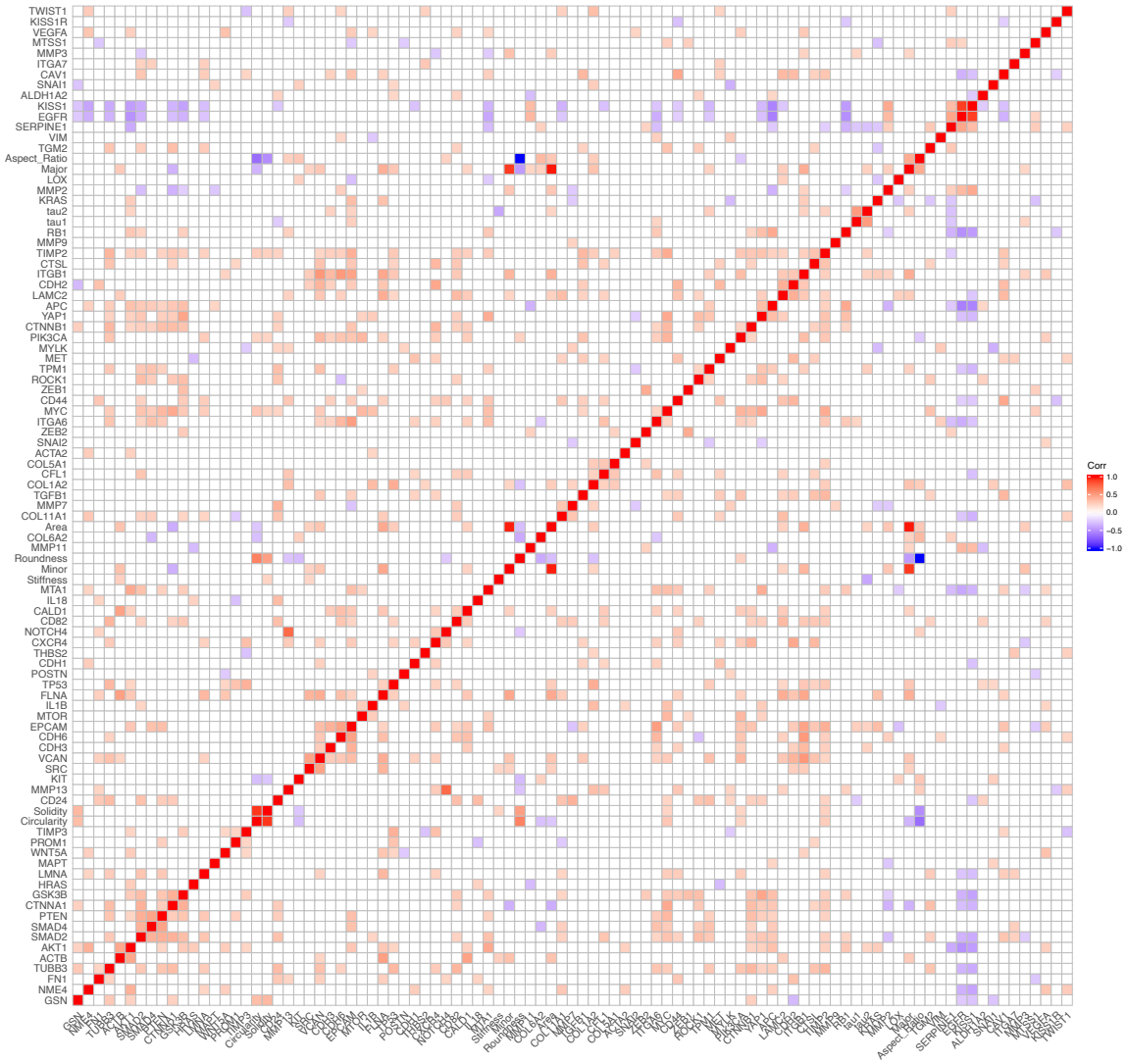

Figure 18 – Single cell correlations between genetic, morphological and mechanical parameters for each cell type – Correlation matrices comparing the Spearman's pairwise correlations between each combination of single cell genetic, morphologic and mechanical data for a) OVCAR3 cells, b) HEY cells, and c) HEY A8 cells. Only statistically significant ($p<0.05$) correlations are plotted.

b HEY

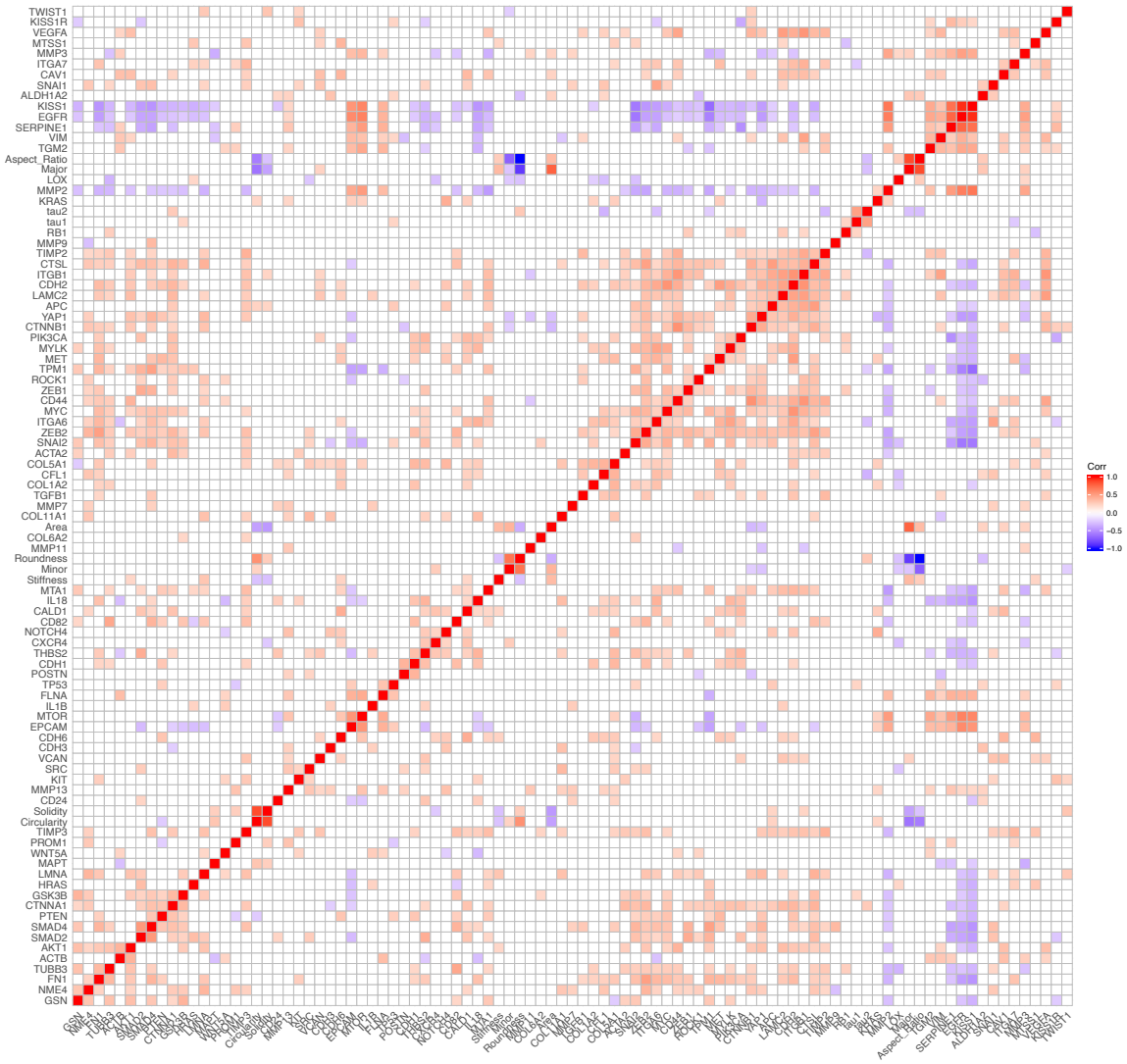

Figure 18 (continued)

c HEY A8

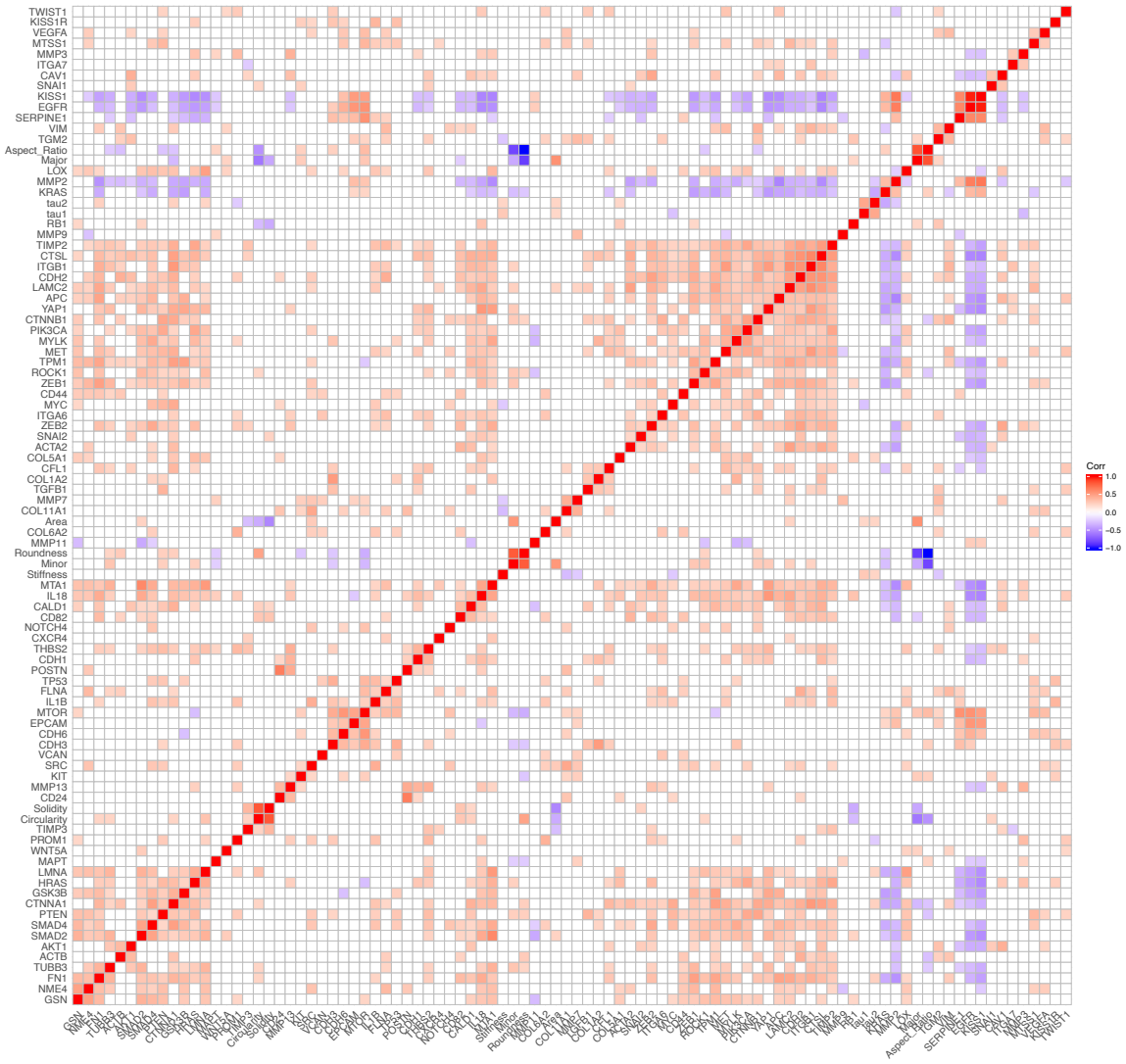

Figure 18 (continued)

3.4.4 Single data type measurements insufficient to distinguish between cell types

Principal component analysis (PCA) was used to reduce the dimensionality of the genetic, morphological, and mechanical data separately to group cells into clusters associated with a cell type and, by proxy, metastatic potential. Surprisingly, the use of single cell expression of 85 genes was insufficient to effectively separate by cell type (Figure 19a). We found that morphological (Figure 19b) and mechanical data (Figure 19c) alone were also inadequate to separate by cell type. We quantified the success of each PCA clustering scheme using the Davies-Bouldin (DB) index (see 3.3.10) (Figure 19h). A lower DB index represents a lower ratio of intra-cluster to inter-cluster variation and a more optimal clustering scheme. We found that the low inter-cluster variation between the HEY and HEY A8 populations, which were derived from the same cell line with different migratory potential, dominated the DB index and resulted in poor clustering of cell types when only considering gene expression. Thus, a single data type is insufficient to classify closely related HEY and HEY A8 cell types that differ in metastatic potential.

3.4.5 Combining gene expression, mechanical, and morphological data types improves cell type clustering

The DB index for cell clustering is substantially improved (that is reduced) by combining the gene expression, morphological, and mechanical data collected

for each single cell using partial least squares (PLS) analysis (see 3.3.10). Combining the morphological and mechanical data reduces the DB index below that of gene expression data alone showing that using multiple data types to cluster cells is more effective than using a single data type (Figure 19d). Cell clustering was further improved through the combinations of gene expression data with imaging data (Figure 19e) and with mechanical data (Figure 19f), providing superior clustering, surpassing a conservative assessment of an optimal DB index[112] (Figure 19h). Distinguishing between the closely related HEY and HEY A8 populations was only achieved when all three data types were combined (Figure 19g), which demonstrates the ability to cluster cells based on their metastatic potential.

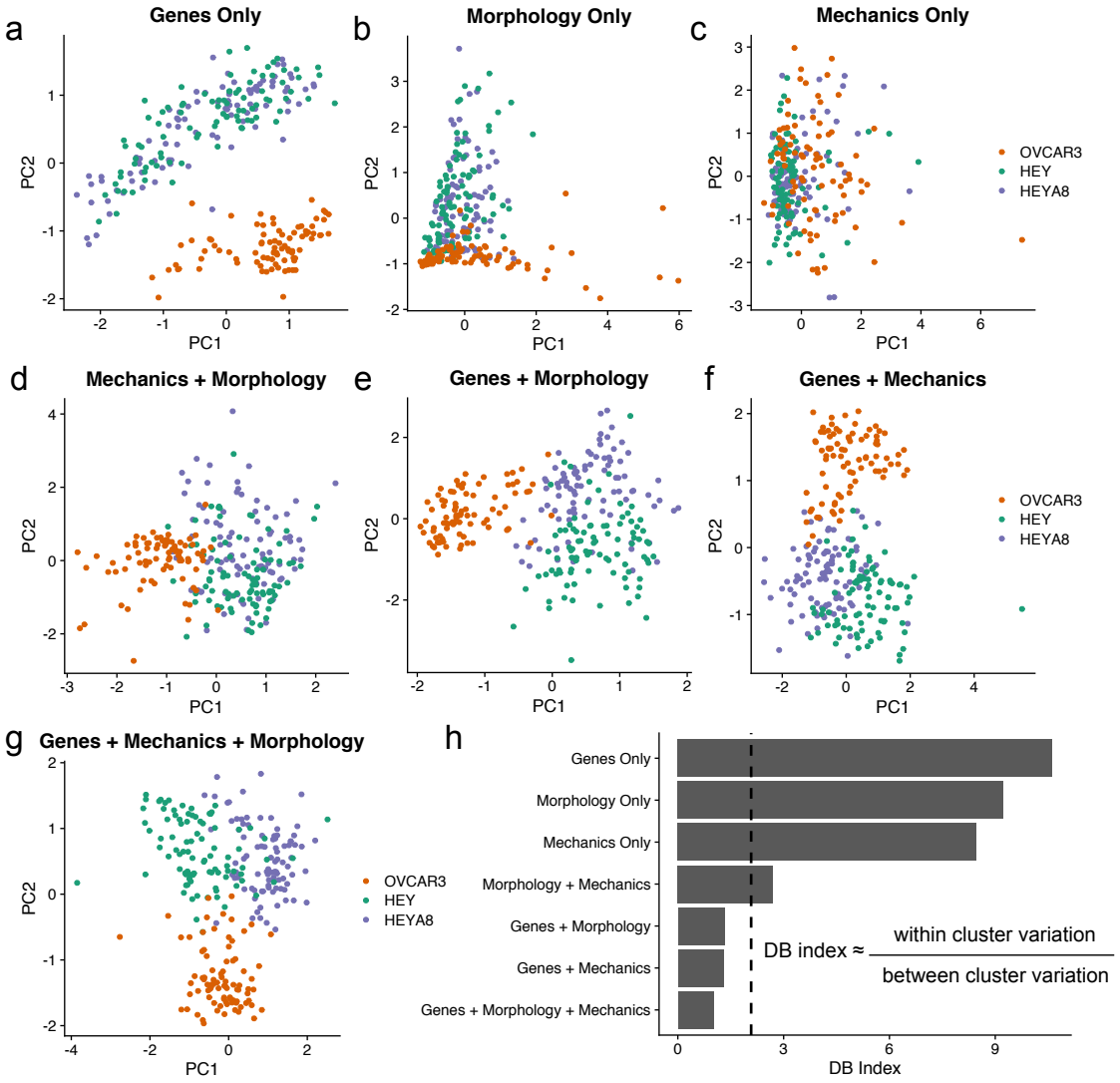

Figure 19 – Single data type measurements insufficient but combining data types improves cell type clustering – PCA cell clustering with single data type using single cell gene expression (a), morphological parameters (b) or mechanical parameters (c). d) PCA clustering using both morphological and mechanical data. e) PCA clustering using both morphological and genetic data. f) PCA clustering using both genetic and mechanical data. g) PCA clustering using all three data types, genetic, morphological, and mechanical data. h) Comparison of the Davies-Bouldin index for each clustering pattern, which is a ratio of within-cluster variation and between-cluster variation. Thus, a minimized DB index is associated with a more optimal clustering scheme. The dashed line refers to the to the highest published optimal value of the DB index[112].

3.5 – Discussion

This study has identified several genes that are significantly correlated with cell mechanical properties. Of particular interest include negative correlations between cell stiffness and *TGM2*, a crosslinking protein involved with ECM remodeling and EMT in ovarian cancer[13], the intermediate filament protein vimentin, a mesenchymal marker and mediator of cytoskeletal organization[113], and *ZEB1*, a transcription factor implicated in the EMT and metastatic processes[111]. *TGM2* crosslinks collagen, stiffening the matrix around cells, resulting in changes to their contractile and proliferative responses[114,115]. Interestingly, increased matrix stiffness has also been associated with induction of the EMT process through the TWIST1-G3BP2 mechanotransduction pathway[116], possibly relating increased *TGM2* expression to a softer cell mechanotype and mesenchymal phenotype through its mechanism of stiffening the surrounding microenvironment. These negatively correlated genes related to ECM remodeling and a more mesenchymal phenotype support an association of a softer phenotype with more migratory, metastatic behavior. This claim is further supported by the recent work of Li *et al.* where they identified a positive relationship between cell deformability (which is inversely related to cell stiffness) and a mesenchymal state[117].

Of note from the positive correlations are the metastasis suppressor and metalloproteinase inhibitor *TIMP3*, nuclear structure protein lamin A, which protects against DNA damage and provides a major barrier to cell invasion[98] and

E Cadherin, an adhesion protein and epithelial marker, implying a relationship between stiffer cells and a more epithelial and less migratory phenotype. Additionally, there are positive correlations between stiffness and *SRC,* an oncogene that causes increased stress fiber assembly and focal adhesion formation[118], and *AKT1,* an oncogene that has been associated with both metastasis promotion and suppression[78]. The associations of increased stiffness with genes related to proliferation and an epithelial-like state could support a dichotomy between a cell's ability to proliferate and to migrate, known as the "go or grow" hypothesis[119]. For example, during collective cell migration, phenotypic differences result in leader and follower tumor cell subpopulations in which leader cells are highly migratory with lower proliferative ability and follower cells represent the converse[120]. Further work examining the mechanics of these leader and follower subpopulations could elucidate the relationship between cell stiffness, proliferation, and migration states. Additionally, recent work has confirmed the correlation of E-Cadherin expression in cells with a weakly migratory phenotype; however, they interestingly identified these cells as more metastatic which brings up the question of dissecting the role of cell mechanics on the separate processes of cell migration and the multi-step metastatic cascade[121].

These studies represent the first exploration of combining cell mechanical data and gene expression data at the single cell level. While starting to gain a mechanistic understanding of the mechanical regulation of the metastatic process, we do recognize several limitations to our current study as well as

potential future lines of experimentation. Our current work to validate this new method focused on the use of cancer cell lines grown on rigid glass and tissue culture plastics coated with ECM materials. To improve the translatability of the work, the method could be applied to dissociated primary tumor cells or collected circulating tumor cells attached to tissue-stiffness-matched hydrogels, although that soft substrate would need to be accounted for during AFM mechanical measurements. Additionally, the current method could be expanded from targeted RT-qPCR to single cell RNA sequencing, using a system such as SmartSeq2, to broaden the scope of the genes explored, as we are certain there are other interesting relationships between a cell's genotype, mechanotype, and phenotype that we have not yet observed. Finally, as noted above, metastasis is a multi-step process that often relies on collective action of multiple tumor cells to successfully colonize a metastatic site. Our study explores the intrinsic properties of single cells, but we recognize that cell migration and metastasis also involve important interactions between multiple cells and their environment, which is beyond the scope of this study and this method.

In the future, this method could also be applied to other cancer types and dissociated primary tumor cells as well as to other biological problems where cellular mechanics can play a role in differences between normal and diseased state, including chemoresistance, angiogenesis, and stem cell differentiation[122-125]. Although this study has focused on the role of cellular mechanics in the context of cancer and metastasis, because the cytoskeletal makeup and motility

machinery is conserved across cell types, we expect that this method could be used to investigate the correlation between a softer mechanotype with a more motile phenotype in both diseased and healthy tissues.

With this new genomechanical method we have explored important connections between a cell's mechanotype, genotype, and phenotype. Studying cells at a single cell level has allowed us to form new hypotheses about the association of a mesenchymal phenotype and soft mechanotype with ECM remodeling pathways and epithelial and proliferative phenotypes with a stiff mechanotype as well as draw conclusions about the molecular factors associated with the metastatic process. Because of the use of our novel technique, we have produced an extremely rich dataset that can be explored further to understand inter- and intra- cell line variability and the various gene networks that may be governing a single cell's metastatic potential.

CHAPTER 4 – SCALING COMPLEX MICROFLUIDICS BY MULTIPLEXING WITH PASSIVE FLOW CONTROL FOR IMPROVED THROUGHPUT

4.1 – Abstract

Microfluidics can bring unique functionalities to cell processing, but the small channel dimensions often limit the throughput for cell processing that prevents scaling necessary for key applications. While the processing throughput can be addressed by an increase of cell concentration or flow rate, both parameters can also negatively affect the successful operation of the device. Designing parallel channels is another solution to linearly increase the throughput with channel number, but for complex microfluidics with multiple inlets and outlets, the design of the channel architecture with more channels can result in cumbersome channel pathways and different flow parameters in parallel channels. We demonstrate an approach to use multiple parallel channels for complex microfluidic designs that use two innovations. First, we linearize the inlets and outlets to align with a 96-well plate pitch to facilitate liquid transfer. Second, we incorporate a second manifold layer to connect three inlets and five outlets per channel in a manner that balances flow properties through each channel. The flow balancing was accomplished through an analytical analysis followed by a computational finite element analysis to account for the different pathlengths that result from the linearized outlets and inlets. We validated these analyses by

measuring the volumetric flow as well as measuring the cell flow velocity profile in each multiplexed channel. We demonstrate eight-channel operation of a label-free mechanical separation that retains the accuracy of a single channel separation. Using the parallelized device and a model biomechanical cell system for sorting of cells based on their viability, we processed over 16 million cells total over three replicates at a rate of 5.3 million cells per hour. Thus, parallelization of complex microfluidics can enable higher throughput processing with label-free approaches important for rare cell isolation, cell therapy manufacturing, and genome-scale hypothesis testing.

4.2 – Introduction

Microfluidics can harness microscale physics to enable new processing capabilities of cells. The precision of microscale fabrication has enabled manipulation of single cells with identical forces at a high rate for a variety of applications in cell sparations[122,126–128], transfections[129–131], and various point-of-care diagnostics and treatment[132,133]. Many microfluidic platforms have leveraged this principle to enable cell separations according to different cell properties[134–137], single-organism analysis[138,139], and micro-cultures[140,141] that all rely on precise channel geometry and flow profile. Complex microfluidics have also been developed that use multiple inlets and outlets to separate cells, for example, through differences in mechanics that include stiffness, viscosity, adhesion, and size[142–144,61,64,63,145].

The small processing volumes that are inherent to microfluidic channels can result in increased accuracy, yet the dimensions of a single channel inherently limit the rate of throughput to applications with small volumes in the diagnostics or research setting. Scaling to larger processing volumes is required for key applications, such as genomic analyses[146,147] or processing in a clinical setting[148-150]. The challenges of scaling microfluidic throughput can be addressed by increasing the concentration of cells processed or by increasing the fluid flow rate. Often these approaches have upper bounds limited by the distortion of the physical phenomena being implemented (Figure 20a).

Designing multiple channels in parallel can increase throughput linearly with the number of channels (Figure 20b)[151-158]. However, parallelization faces a challenge in the case of complex architectures that have more than a single inlet or outlet. Increasing the number of processing channels for complex microfluidics also results in increase in the number of inlet and outlet paths, particularly for sorting approaches that leverage fractionated outlet flows[134,135]. Previous microfluidic approaches to mechanical sorting have shown processing rates on the order of 10[159], 20[160], or 100[128,161] cells per second, or 1-10 mL of volume per minute[134]. Replicating the flow parameters of each approach would include an increase in inlets an outlets that scales with the number of replicate channels. In the case of five outlet channels, a linear increase in channels results in a five-fold increase in outlet connections, which becomes an untenable layout for single layer microfluidics in which paths must not cross. Moreover, a large number of collection

ports introduces increased difficulty for sample handling, which could easily lead to the loss of processed material. Finally, the complexity of the design leads to greater difficulty in ensuring each channel is operated at similar flow parameters. Therefore, in order to parallelize complex channels for increased microfluidic output, we need to develop a design approach that simplifies the inlet and outlet geometry in a manner that maintains identical flow parameters across multiple channels.

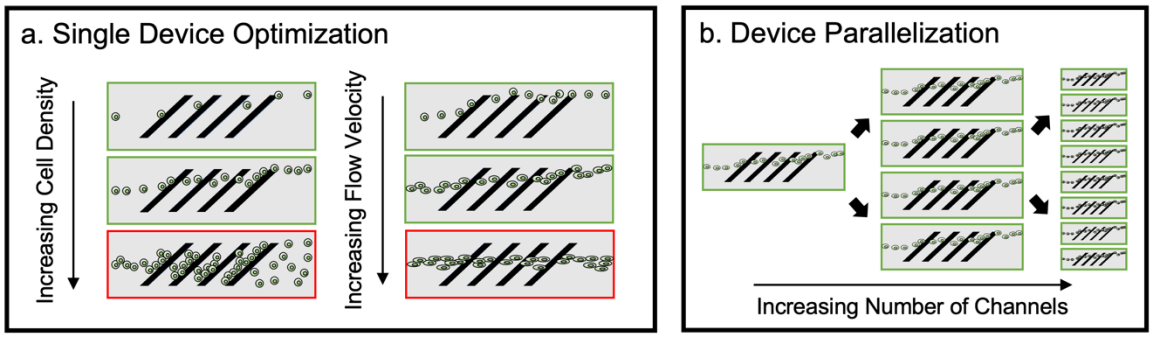

Figure 20 – Device parallelization allows for linear improvement of processing throughput – a) Throughput of microfluidic cell sorting devices can be increased by increasing the cell density and flow velocity, but only to a limit. At high cell density, cell-cell interactions disrupt the translations of cells at each ridge. At high flow velocity, the hydrodynamic forces outweigh the normal forces associated with cell deformation at the ridges and cells are not deflected sufficiently. b) Increasing the number of parallel channels in a device results in a linear improvement of processing throughput. This improvement requires all channels to be operated at the same flow conditions.

In this chapter, we describe a scalable approach for multiplexing complex microfluidics. This approach is especially applicable to microfluidic platforms with multiple inlets or outlets. First, we convert the set of inlets and outlets to a

linearized design that aligns with a 96-well plate to ease sample collection and recombination (Figure 21). Next, an analytical flow resistance model[162] is implemented to set the flow resistance through each channel as identical, despite the different path lengths associated with inlets and outlets. We then refine the design using finite element modeling[157] to estimate the flow resistance across the device and balance fluid flow to each outlet. Finally, we experimentally compare the designs through measurement of volumetric output. Due to the complexity of connecting channels with multiple outlets and inlets within a single layer, we created a second manifold layer connected by vias to distribute and recombine fluid of similar inlets and outlets from eight sorting channels. This approach employs passive flow control to dramatically reduce the need for 24 inlet ports and 40 outlet ports for eight channels to three inlet ports and five outlet ports. We demonstrate the ability to improve the throughput of microfluidic cell sorting device by over 8-fold to over 5 million cells per hour while maintaining the accuracy of separation compared to a single channel.

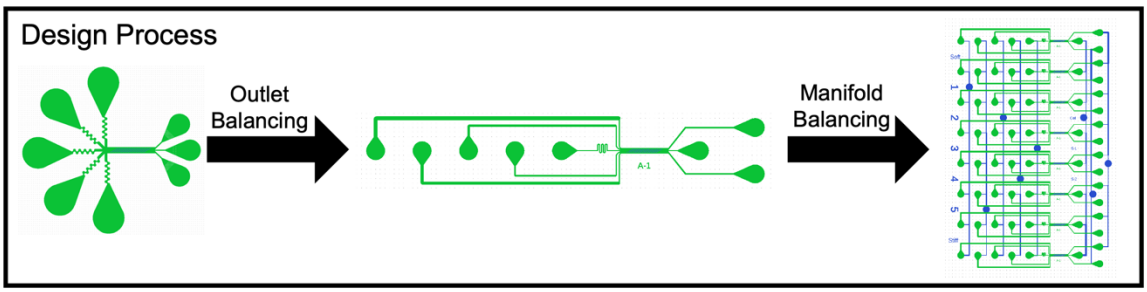

Figure 21 – Design process for linearizing and parallelizing microfluidic stiffness-based sorting device for increased throughput.

4.3 – Materials and Methods

4.3.1 Modeling and analytical calculations

A key aspect of maintaining similar flow conditions for each parallel channel is to balance both outlet channel resistances and the manifold layer channel resistances to achieve equal fluid distribution and recombination rather than relying on matching channel length and width. Fluid distribution networks for the linearized channel layer and the manifold layer were first designed using an analytical flow resistance model. For a rectangular channel, Equation 1 and Equation 2 describe the pressure drop, ΔP, and flow resistance, R, respectively, where Q is volumetric flow rate, μ is dynamic viscosity, L is channel length, h is channel height, and w is channel width.

$$\Delta P = R \times Q \qquad \text{Equation 1}$$

$$R = \frac{1}{1-0.63\left(h/w\right)}\frac{12\mu L}{h^3 w} \qquad \text{Equation 2}$$

Equation 2 assumes a high aspect ratio for the channel in which the channel width is substantially larger than the height. For the linearized devices, the outlet channel ratios ranged from 4:1 in the shorter channels to 20:1 in the longer channels. In the narrower channels, there is potential for over or under estimation of the channel resistance using this approach. To create the balanced channel designs, resistance of each outlet channel must be equal. By equating Equation 2 of two channel geometries, the relationship of channel width and length can be expressed using Equation 3, where L_1, L_2, w_1, and w_2 are the lengths and widths of two different outlet channels. The channel height, h, is the same for both

channels because the fabrication method requires the channel to maintain the same height for parallel channels.

$$w_1 = 0.63h\left(1 - {}^{L_1}/_{L_2}\right) + w_2\left({}^{L_1}/_{L_2}\right) \qquad \text{Equation 3}$$

Finite element analysis (FEA) was then performed to balance volumetric flow more accurately to each of the five outlet channels. A 2D mesh was formed in COMSOL based upon a computer aided design (CAD) of the channel layout and FEA was performed using the laminar flow package and an estimate of channel width. The flow rate to each outlet or manifold was calculated using the built-in integral functions to sum velocity values over each outlet channel. The resulting flow rate measurements were used to adjust the channel designs and iteratively test the flow rates until the differences between channels were less than 5% of the average value.

A similar resistance framework and FEA analysis was applied to model the resistances required to balance the manifold layer used to combine inlets and outlets of the linearized sorting design. In the resistance model, the width of both the main channel and each leg connecting the main channel and each port were adjusted to both balance the pressure drop between each individual port and the combined channel and to maintain minimum and maximum channel widths for manufacturability. Each inlet and outlet manifold was individually modeled since the combined outlets are in different locations and therefore required different channel geometries to maintain equal flow. The total pressure drop across each combination channel were matched so that there was no difference between

outlet flow rates. The resulting design was the starting point for the FEA modeling. From that initial design, the channel widths were adjusted until the output flow rates for each channel were equal.

4.3.2 Microfluidic fabrication

The previously described "tree" microfluidics[163] were molded using two-step SU-8 molding process. The first gap layer was fabricated by spinning SU-8 2005 (Kayaku Advanced Materials) on a silicon wafer (University Wafer) at 1500 rpm to form a 9 μm gap. The wafer was prebaked at 95°C for 10 minutes and exposed with 365 nm light (MA-6 mask aligner, Karl Suss). The exposed wafer was then baked at 95°C and developed in SU-8 developer (Kayaku Advanced Materials). Fabrication for the second channel layer followed the same process using SU-8 2010 spun onto the wafer at 2000 rpm to form a total channel height of approximately 25 μm. The completed wafer was hard baked at 95°C for at least 10 minutes.

The current microfluidic approach requires two PDMS layers. The first layer is the parallel linearized sorting channels. Similar to the "tree" design, this silicon mold was fabricated with two layers, a gap layer and a channel layer. Unlike the "tree" design, the new mold was made using reactive ion etching (RIE). For each layer, SC1827 or SC1813 photoresist (Microposit) was spun onto bare silicon wafers (University Wafer) depending on the etch depth required. SC1827 was used for any etch deeper than 10 μm. The resist was soft baked at 115°C. The

layer design was exposed using an MLA150 mask writer with 405 nm wavelength light. The resist was developed with MF-319 (Microposit) and hard baked for a minimum of 20 min at 100°C. The wafer went through a 30 sec descum process using an HRM ICP plasma etcher (Surface Tech Sys) before etching with a Bosche process. The etch depth was measured using a stylus profilometer (P15, Tencore). Further etching steps were done to reach the desired channel depth. The remaining resist was stripped in an acetone bath with sonication. The process was repeated for the second thickness of the sorting channel. A single etch step was used to create the second PDMS mold at a thickness of 75 μm. After the etching process was completed, each mold was exposed to Trichloro(1H,1H,2H,2H-perfluorooctyl)silane (Sigma-Aldrich) to form a hydrophobic surface on the silicon to assist with demolding cured PDMS.

Polydimethylsiloxane (PDMS) (Fisher Scientific) was mixed at a 10:1 polymer to crosslinker ratio and degassed to remove bubbles. Approximately 25 mL of PDMS was cast over each of the molds to a thickness of approximately 5 mm and cured at 80°C for at least 1.5 hours. The PDMS was then demolded from the wafer and cut to size. A 1.2 mm dermal punch (VWR) was used to create inlets and outlets for the single devices and manifold layer while a 1 mm dermal punch was used to create the vias on the sorting layer to connect the two fluid networks. Then dust was removed from the bottom side of the sorting layer cast with Scotch tape and exposed to air plasma (Harrick Plasma) along with a Scotch tape-cleaned 50x75 mm microscope slide (Sigma-Aldrich) for approximately 45

seconds. Similarly, single channel devices were constructed by bonding a single device to a 3x1 in microscope slide (VWR). The PDMS cast and glass slide were bonded together and then baked for at least 10 min at 80°C. After using Scotch tape to carefully clean all dust from each surface, the top side of the resulting device was plasma treated and bonded to the bottom side of the manifold layer. The manifolds and formed vias were aligned by visual inspection and brought into contact to form a completed device. The final device was then baked for at least 10 min at 80°C to set the bond fully.

4.3.3 Cell culture

The HEY A8 ovarian cancer cell line that features a Cas9-GFP cassette (see 5.3.1) was cultured in complete media consisting of RPMI-1640 (Sigma-Aldrich) supplemented with 10% v/v fetal bovine serum (Atlanta Biologicals) and 1% v/v penicillin-streptomycin (Sigma-Aldrich). Cells were cultured at 37°C at 5% CO_2.

For the flow rate optimization experiments and high-speed video analysis, cells were prepared for processing by trypsinization and resuspension in flow buffer (complete media, either 20% v/v Percoll (Sigma-Aldrich) or 10% v/v OptiPrep (Sigma-Aldrich), and 0.1% v/v Pluronic F-127 (Millipore Sigma)) with 1 mg/mL DNAse I (Sigma-Aldrich) at approximately 1-2 million cells/mL. The formulation of either Percoll or OptiPrep in the flow buffer was optimized to create a neutrally buoyant solution to prevent cell settling in the device or tubing. In short, cells were resuspended in solutions with different concentrations of each

density gradient medium and centrifuged at 300xg for 10 minutes. The concentration at which a cell pellet first began to form was selected as the ideal buffer density. Cells were strained using a 20 μm pore filter (PluriSelect) and loaded into a syringe (VWR) for microfluidic processing.

To validate our biomechanical separation ability, we used a heat-treated cell viability model. Separate flasks of cells were first stained using either 2 μM Cell Tracker Green CMFDA (ThermoFisher) or 500 nM Cell Tracker Deep Red (ThermoFisher) in serum-free media. After incubating in the dark for 30 minutes at 37°C, media was replaced with complete media and cells incubated for at least an additional 30 minutes. Directly before microfluidic processing, cells were trypsinized and transferred to conical tubes. A tube of red-dyed cells was placed in a water bath at 65°C for 10 minutes to kill and stiffen the cells. Both the green- and red-dyed cells were resuspended in the flow buffer at 1-2 million cells per mL and strained through a 20 μm filter. A portion of each individually dyed cell solution was retained for flow cytometry analysis and the rest of each sample was mixed at a 1:1 ratio so that the initial inlet population of cells would be approximately 50% red, dead, stiff cells and approximately 50% green, live, soft cells. A portion of the mixed samples was reserved for flow cytometry analysis. In practice, initial population percentages ranged from 33-65% live cells and 28-60% dead cells as validated with flow cytometry. The prepared cell samples were loaded into a syringe for injection into the microfluidic chips using a vertically aligned syringe pump. For each single device trial, two confluent T75 flasks (VWR)

of cells were prepared for processing (1 red, 1 green). For each multiplex device trial, six confluent T75 flasks were prepared for processing (3 red, 3 green).

4.3.4 AFM and force curve analysis

To confirm a stiffness difference between live and heat-treated cells, we used force spectroscopy to obtain force-indentation curves with an atomic force microscope (Asylum Research) with an integrated optical microscope (Nikon) on a vibration isolation table. To improve the contact geometry, a 7.32 µm spherical polystyrene particle was attached to a tipless silica nitride cantilever (Bruker Probes) using a two-part epoxy (JB Weld). The cantilever was calibrated using the Sader method[164] to determine the deflection inverse optical lever sensitivity and spring constant. The measured stiffness constant was approximately 30 pN/nm.

Cells were seeded onto glass coverslips (Fisher Scientific) coated with 3.5 $\mu g/cm^2$ Cell-Tak (Corning) according to the manufacturer's instructions. Coverslips with cells were centrifuged at 300 xg for 10 minutes to attach the cells to the coated glass which were then submerged in media in a glass bottom FluoroDish (World Precision Instruments) for force curve collection. For measurements, the cantilever probe was visually aligned with the cell center and moved with a velocity of 2 µm/s to indent the cell with increasing compressive force until a force trigger of 5 nN was reached. The cantilever was held in position

for 10 seconds, dwelling towards the surface, to record viscous relaxation of the cell before retraction. We collected 50 cellular measurements per condition.

We analyzed the force curves by applying the Hertzian contact model, which describes non-adhesive elastic contact between two bodies to calculate the cellular Young's modulus using custom code written in R (https://github.com/nstone8/Rasylum)[25]. The contact point was estimated by the intersection of the flat, undeformed region of the force curve with a line fit to the force curve region where the cantilever was in contact with the cell. Next, we identified the true contact point by iteratively testing the points around the estimated contact point with the minimal residual difference between the measured force curve and a nonlinear fit described by the governing equation Hertz used to describe the contact between an elastic sphere and an elastic half space. The population measurements were compared using a t-test with a significance level of α=0.05.

4.3.5 Microfluidic device cell separation

The microfluidic device was set up on the stage of an inverted optical microscope (Nikon) for the monitoring of cell trajectories. High-speed videos of the cells were recorded using a Phantom camera at 2500-3000 frames per second to monitor cell trajectories and velocity after interactions with the diagonal ridges. The device was first primed by flowing flow buffer through the device to remove all air bubbles. Flow was controlled using two syringe pumps (Harvard Apparatus)

with 0.02 in inner diameter and 0.06in outer diameter Tygon tubing (Cole Parmer) connecting the sheath flow syringes of flow buffer to the inlets of the left and right sheath channels. The two independent sheath flows allow for the control of cell focusing at the entrance of the sorting channel. The tubing fits directly into the 1.2 mm punch without need for adapters. All tubing and needles used in the experiment were cleaned prior to use with deionized water. Tubing was also fit into the 5 outlet ports and placed in a conical tube for sorted cell collection. Once the device was prepared, the syringe of cells in flow buffer with DNAse were connected to the cell inlet of the device with tubing using a third syringe pump. After sorting, the volume of fluid collected at each outlet was measured for comparison of volumetric flow output variability between outlets.

4.3.6 High-speed video analysis – cell trajectories and cell velocity

To measure cell trajectories, ImageJ was used to extract an image stack from each video and a Z-projection was used to identify the background of each image. The calculator plus function was used to subtract the background from the image stack so that only moving cells would remain. Using the TrackMate[165,166] plugin in ImageJ[167,168], cells were identified in each frame and linked together into tracks tracing each cell's movement through the device. This produced approximately 500 tracks per video. Custom python software (https://github.com/nstone8/heimdall) was used to analyze collected cell trajectories. The tracks of live and dead cell populations were analyzed to

determine deflection and interaction time with each ridge. The cumulative deflection of the live and dead populations are shown for each of the three flow rates in Figure 25. Velocity measurements were taken from TrackMate outputs.

4.3.7 Microfluidic flow rate optimization

Cell trajectory videos were collected at 3 total flow rates – 25 μL/min, 50 μL/min, and 75 μL/min. All three flow rates include a left sheath inlet, cell inlet, and right sheath inlet with a 2.5:1:1.5 ratio respectively. This sheath flow focused the cells at the entrance of the sorting channel with a bias towards the soft outlet side. High-speed video was collected at each of the prescribed flow rates and the sorted cells were tracked. The tracked cells were used to plot the cumulative deflection of the live and dead cell populations to determine the difference in trajectory of the two populations at each of the flow rates.

4.3.8 Sorting evaluation and flow cytometry

Sorting experiments were conducted at the optimized flow rate of 50 μL/min total flow rate. Cells were collected from the five outlets in conical tubes and stored on ice before analysis with flow cytometry using an Accuri C6 Plus. Using the inlet mixed population and two one-color cell controls, gates on the forward scatter and side scatter plot were set to separate cells from debris as well as the fluorescence gates for green, live cells (FL1) and red, dead cells (FL4). The event count and amount of fluid processed were used to identify cell

concentrations and ratios before and after sorting of both the live and dead cell populations. Analysis of flow cytometry data was completed using FlowJo software.

4.3.9 Enrichment, purity, cell yield, and throughput analysis

Enrichment for live and dead cells, purity, cell yield, and throughput were calculated for each sample using Equations 4, 5, 6, 7, and 8 respectively.

$$Live\ Enrichment = (\%\ Green/\%\ Red)_{Sorted\ Outlet}/(\%\ Green/\%\ Red)_{Inlet} \quad \text{Equation 4}$$

$$Dead\ Enrichment = (\%\ Red/\%\ Green)_{Sorted\ Outlet}/(\%\ Red/\%\ Green)_{Inlet} \quad \text{Equation 5}$$

$$Purity = \left({}^{Target\ Cell\ Count}/_{Total\ Cell\ Count}\right)_{Sorted} \quad \text{Equation 6}$$

$$Cell\ Yield = {}^{Target\ Cell\ Count_{Sorted\ Outlet}}/_{Target\ Cell\ Count_{All\ Outlets}} \quad \text{Equation 7}$$

$$Throughput = Inlet\ Cell\ Concentration \times Flow\ Rate \quad \text{Equation 8}$$

Purity was calculated for live and dead cells for combinations of outlets 1&2 and outlets 4&5. Cell yield was calculated for live and dead cells for combinations of outlets 1&2 and outlets 3,4&5.

4.4 – Results

4.4.1 Linearized inlets and outlets require modeling to balance volumetric output to each outlet

Inlets and outlets to microfluidic channels frequently feature a symmetric layout to balance the fluidic resistance (see for example the "tree" design in Figure 21). We ensure that the five outlets are equidistant from the exit of the sorting channel to balance the exit flows of fractionated cells for each mechanical subtype[163]. We observed the even distribution of volumetric output to each outlet in the "tree" design across multiple experiments, with the normalized output ranging from 0.946 to 1.124 (no statistical difference in output to any of the five outlets, one-way ANOVA, $F>0.1$, Figure 22a). The symmetric layout interfered with efficient liquid handling since the outlets are not aligned with the pitch of microwell plates. Therefore, we first designed a linear arrangement to align the pitch of the three inlets and five outlets to a 96-well plate to facilitate simpler liquid handling. However, we needed to adjust the resistance of each outlet to minimize hydrodynamic variation and balance the volumetric output to each outlet to account for the different channel lengths.

We implemented two steps to balance outlet resistances to and from each separation channel. First, we applied analytical calculations of channel resistance to estimate channel widths and introduce serpentine channels to short fluid paths. With Equation 3, the width of each channel can be easily calculated by using the channel lengths required by the linear design and a starting channel width. We chose the shortest channel to have a width of 100 μm and calculated other channel widths from that defined channel. Second, we employed finite element modeling to determine fluid pressure drops and flow (Figure 22b). We tested the

resistance balanced linear device and the FEA balanced linear device and observed similar normalized volumetric flow to each outlet, with output ranging from 0.869 to 1.063 and 0.917 to 1.068, respectively. In experimental measurements of volumetric flow, we found outlet 3 of the resistance balanced linear device to have a statistically lower output compared to all other channels, using a Tukey HSD post-hoc test, $p < 0.01$ (Figure 22c). For the FEA balanced design, outlet 5 had a statistically lower output compared to outlets 1 and 2, using a Tukey HSD post-hoc test, $p < 0.05$ (Figure 22d). Comparing the average standard deviation between normalized volumetric output for each outlet, both the resistance balanced and FEA balanced linear devices saw reduction in outlet variability compared to the “tree” design (Figure 22e). We found the FEA model designed device demonstrated slightly lower variability compared to the analytical model.

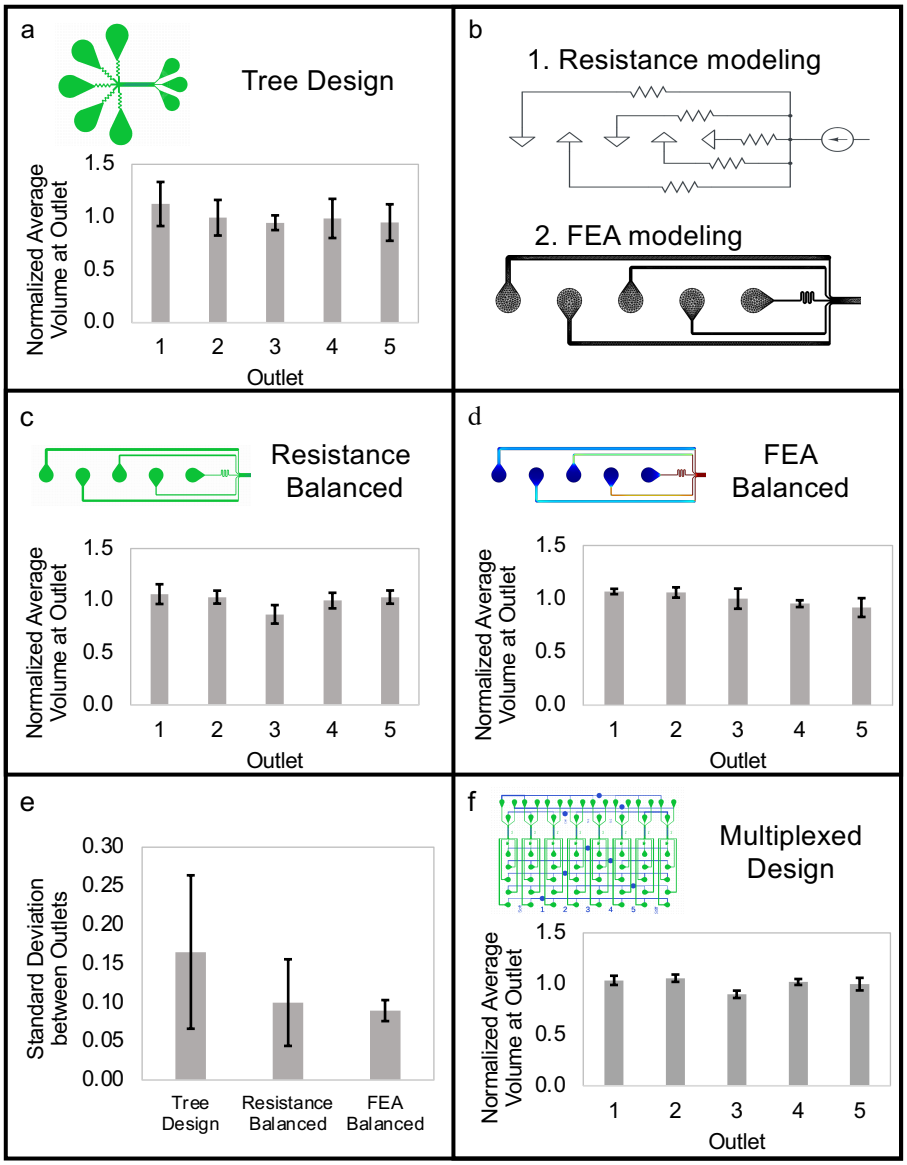

Figure 22 – Modeling microfluidic device enables balancing of volumetric output to each outlet – a) The normalized average volumetric output at each outlet for the original tree sorting device design, n = 7. b) Schematics depicting the two methods for balancing channel resistances for the linear device design – 1) An analytical approach modeling the device as a fluidic circuit and 2) A finite element analysis of the device geometry. c) The normalized average volumetric output at each outlet for the resistance balanced linear device, n = 11. d) The normalized average volumetric output at each outlet for the FEA balanced linear device, n = 4. e) Comparison of the average standard deviation between the normalized volumetric output of outlets 1 to 5 for the three single device designs. f) The normalized average volumetric output at each outlet for the resistance balanced linear device, n = 12. All error bars depict standard deviation.

4.4.2 Top manifold layer evenly splits fluid flow to bottom multiplex device layer

We chose to use the analytically balanced design due to the reduced volumetric flow to outlets 4 and 5 of the FEA model design, which contained the fractions of cells most deflected by the ridges, which are the target cells for our sorting application. The reduced flow rate in the center channel can be attributed to slight deformation of the larger channels when under pressure[169]. This optimized resistance-balanced linear design was duplicated for eight channels in a device to enable high-throughput sorting (in green, Figure 23a). To simplify the liquid handling, the outlets associated with each biomechanical fraction channel were combined. Yet, it was not possible to combine the outlets from distinct channels without having the fluid paths cross. Therefore, we implemented a second manifold layer connected by vias to the stacked sorting layer. The manifold top layer, shown in blue, Figure 23a, was used to distribute cells and recombine the appropriate outlets in the sorting layer. The manifold was placed on top of the sorting channel to maintain visibility of the sorting channels for microscopy. The FEA approach was used to adjust the manifold channel widths to evenly distribute and recombine the cell solution with the lowest variation between channels. Figure 23b shows the different channel widths used in both layers to balance the flow throughout the equivalent paths.

The five outlets of the eight sorting channels should have equal flow rates at each of the five combined outlets to ensure all cell paths through each channel are equivalent. Measuring the volumetric flow rate at each of the five combined outlets, we did see consistent normalized volumetric output to all five outlets with output ranging from 0.897 to 1.055. Outlet 3 had a statistically lower output compared to all other channels and outlet 5 had a statistically lower output compared to outlet 2 (Tukey HSD post-hoc test, $p < 0.05$, Figure 22f). Using video tracking, we determined the average velocity of cells in each of the eight channels during operation. We observed a slight variation of flow velocity (mean: 47.0 mm/sec, standard error: 15.5%) in all channels with the fastest flow in the middle channels and the slowest flow in the outer channels (Figure 23c). The variation in velocity corresponds to a volumetric flow rate between 40 and 65 μL/min. Comparing this variation to the tested flow rates from our flow rate optimization experiment (Figure 25), this velocity range is acceptable for effective sorting between the viable and non-viable cell populations. However, we expect that the outer channels will show greater sensitivity to cell mechanics than the center channels due to the lower flow velocities.

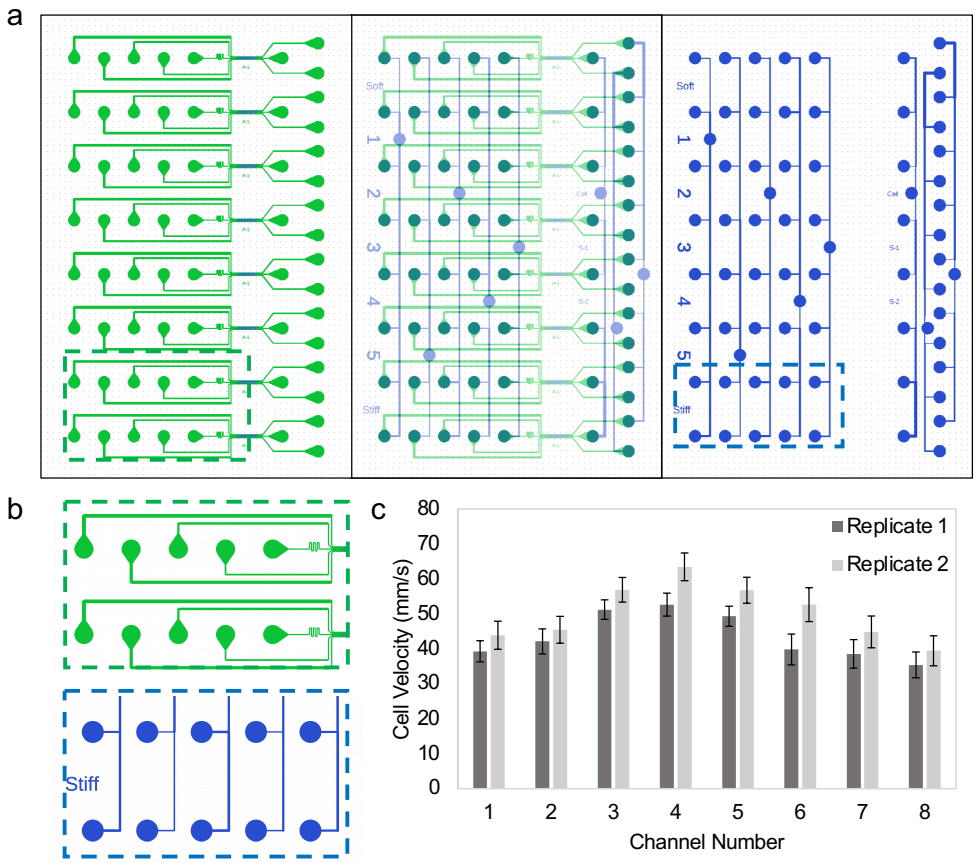

Figure 23 – Top manifold layer evenly splits fluid flow to bottom multiplex device layer – a) The multi-layer multiplex device consists of two layers – a bottom sorting layer (left, green) with 8 parallel sorting devices and a top manifold layer (right, blue) for fluid distribution and recombination. The middle panel shows the alignment of the two layers which are connected by vias where the two layers overlap. The blue circles that do not overlap with the green layer are where the total device inlets and outlets are connected. b) Detail image shows how differing channel widths are used to balance the fluid flow. c) High-speed video cell tracking was used to determine the velocity of fluid in each channel of the multiplex device. The data from two replicates is displayed with an average of 100 cells tracked per channel. The error bars depict standard deviation.

4.4.3 Sorting enrichment, purity, and cell yield maintained when multiplexing, but throughout and processing time are greatly improved

The heat treatment cell stiffening model was used to evaluate the sorting ability of the designs. Necrotic and apoptotic cells after heat treatment are significantly stiffer than live cells[163] (Figure 24). After determining the optimal flow parameters for operation of the single tree device which resulted in maximal deflection of the non-viable population at the highest flow rate (Figure 25), we observed up to 16-fold enrichment of the live cells in the soft outlets and up to 69-fold enrichment of non-viable cells in the stiff outlets (Figure 26). The performance of the single linear device was similar with up to 6-fold enrichment of the live cells and 37-fold enrichment of the non-viable cells in their respective outlets (Figure 26). In the multiplex device, we observed up to 58-fold enrichment of non-viable cells in the stiff outlets (Figure 26). However, we did observe a reduced enrichment of live cells of 1.3-fold in the soft outlets. To explain the reduction in enrichment in the eight-channel design, we note an overall increased channel resistance and longer path length in the linear design. The channels operate at a nominal pressure drop of 0.2 bar, which includes the recombination manifold resistance. It is possible that the different channel widths result in variations in channel deformations at this applied pressure, leading to changes in the flow rate for each channel[170].

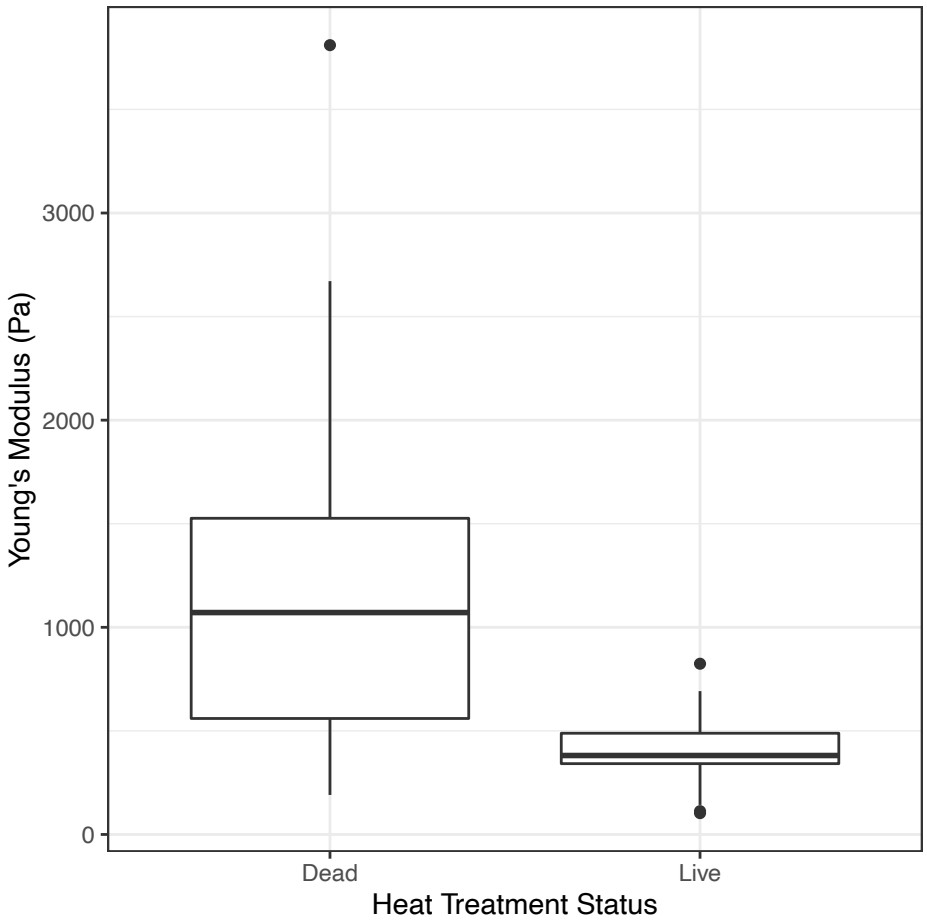

Figure 24 – Heat treatment of cells used as model system for separating soft and stiff cells – AFM measurements show significant difference between live HEY A8 Cas9 GFP cells and heat-treated dead cells (Welch two sample t-test, $p < 0.0001$).

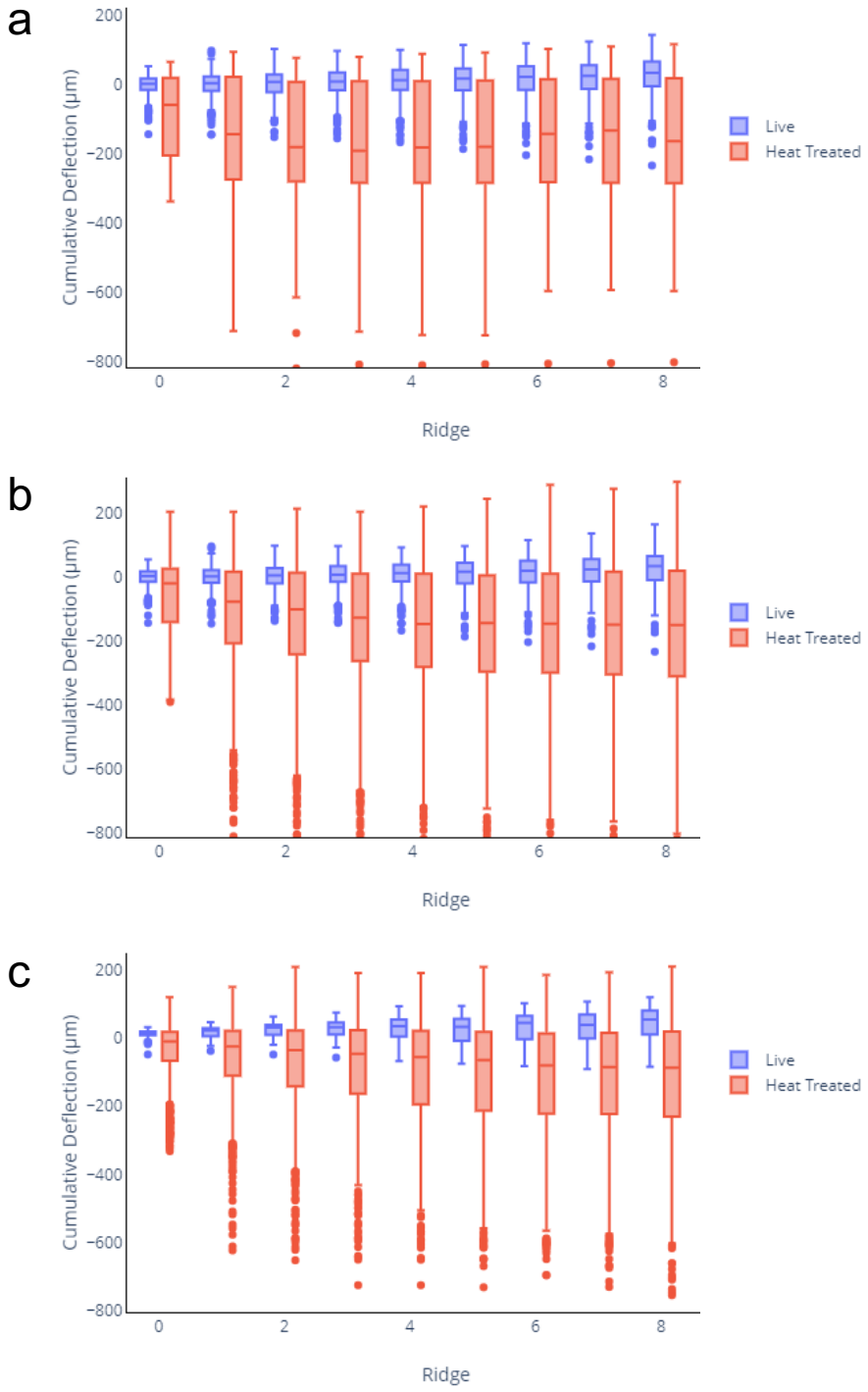

Figure 25 – Flow rate optimization using cell trajectory analysis for single device – Cumulative deflection in the microfluidic device from cell trajectories for live and heat-treated cells at a total flow rate of a) 25 μL/min, b) 50 μL/min, and c) 75 μL/min.

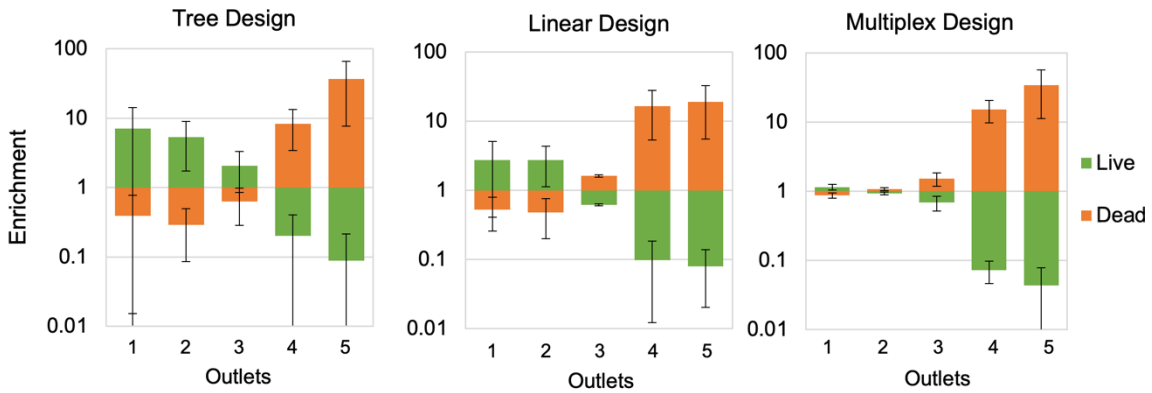

Figure 26 – Sorting enrichment maintained when multiplexing – Sorting enrichment comparison for live and dead cells sorted with both the tree and linear single devices and the multiplex device. Please note the log scale axis. Error bars depict standard deviation, n = 4 for single devices and n = 3 for multiplex device.

We also recorded the purity and yield of target cells for each design. Across the single tree, single linear, and multiplex linear designs, we maintained highly pure samples of stiffened cells in the stiff outlets (87%, 93%, and 91% purity of dead cells when combining outlets 4 and 5 for the tree, linear, and multiplex designs respectively) (Figure 27a). We observed the highest yield of live cells being sorted to the soft outlets as expected for all designs (82%, 97%, and 83% of live cells going to outlets 1 and 2 for the tree, linear, and multiplex design) (Figure 27b). The decreased enrichment of live cells in the linear and multiplex designs is due to a significant number of non-viable cells that were directed to the soft outlets (41%, 79%, and 66% of dead cells going to outlets 1 and 2 for the tree, linear, and multiplex devices). The live cell purity in the multiplexed device could be improved by iterating the manifold layer to produce a more balanced distribution in cell velocity in each of the multiplex channels.

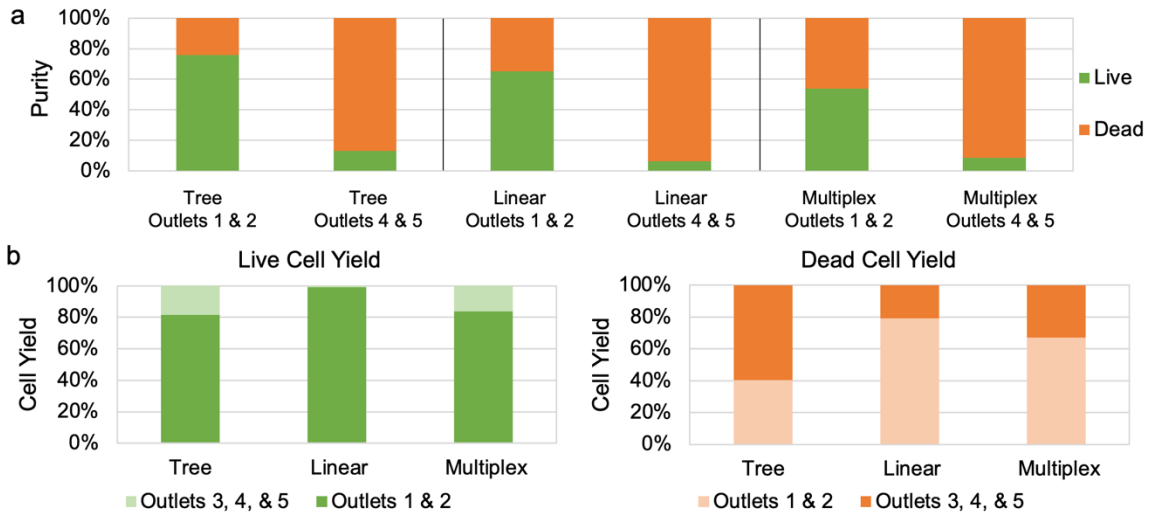

Figure 27 – Sorting purity and cell yield maintained when multiplexing – a) Comparison of average cell purity in combined outlets (soft – 1 & 2, stiff – 4 & 5) for the tree and linear single device designs and the multiplex design. b) Comparison of live and dead cell yield in combined outlets (soft – 1 & 2, middle to stiff – 3, 4, & 5) for the tree and linear single device designs and the multiplex design.

The processing throughput of a single channel was approximately 240,000 cells/hour. By introducing the multiple parallel channels to our design, we were able to increase the throughput over 8-fold to process over 5.3 million cells/hour in a single multiplex device (Figure 28a).

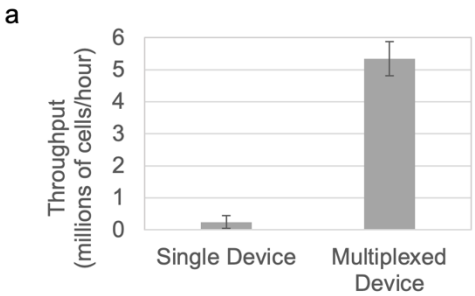

b

Number of Cells to Process	Single Device Processing Time	Multiplex Device Processing Time
500,000	2.1 hours	5.6 minutes
5,000,000	20.6 hours	56.2 minutes
50,000,000	8.6 days	9.4 hours

Figure 28 – Throughput and processing time are greatly improved with multiplexing – a) Comparison of throughput in millions of cells per hour between the single devices and the multiplexed devices. Error bars depict standard

deviation. b) Comparison of the processing time required to process increasing number of cells for different applications between the single device and multiplexed device.

4.5 – Discussion

We have shown the ability to combine linearized inlets and outlets to produce highly enriched subpopulations at a much-reduced processing time. In this study, we have described a method to scale complex microfluidic channels by including a stacked manifold layer for the even distribution and recombination of fluid in each of the inlets and outlets that were linearly aligned. We have shown that eight parallel sorting channels can be fabricated, increasing the overall throughput of processing by over 8-fold. We used two models to produce equivalent volumetric flow to each of the outlets. Based on previous work leveraging the relationship of cellular mechanics to cellular phenotype, we can now approach the same applications with higher throughput and possibly enable further discoveries in the role of cell mechanics in cell viability, response to chemotherapy, differentiation state, and malignancy[122,125,163,171–173].

We showed that while the two fluid balancing approaches estimated equal flow rates between channels, there are always differences between modeled and experimental results. Based on the experimental results, we were able to choose the combination of approaches that was, although more variable, biased toward deflecting cells. There are applications in which it is desirable to collect highly enriched, stiffer, more adhesive, larger, or less viscous cells, such as separating

cancer cells from liquid biopsy samples, investigating gene expression of mechanically stiffened cells, or identifying more differentiated stem cells[122,172,173]. In these cases, the cells of interest are rarer, and our sorting would suffer from the loss of volumetric output to the outlets containing these rare cells of interest. The resistance balanced design offers symmetric flow rates between the soft and stiff outlets, and thus was desirable for maximizing the collection of deflected cells. When we used an FEA model to adjust outlet resistances, the resulting device did have a lower variation in volumetric output to each channel. This process of iterative and modular design could be used to further reduce the variation in flow and maximize desired cellular fractionation, and we suggest the use of this combination of analytical and computational modeling for other microfluidic parallelization efforts as well.

By controlling the inlet and outlet layout, incorporating fluid resistance into the design, and adding a balanced manifold layer to the device, channels can be run in parallel with the same complexity of control system as a single channel. This has benefits both in the lab and potentially in a clinical setting. By improving the throughput but maintaining the simplicity the control system, devices such as this one could more feasibly be used in a clinical setting where larger patient samples would need to be processed in a simple and time-effective manner. Because of the linear nature of throughput improvement with each additional channel, we could envision further increase of processing ability by adding more channels in

parallel as well as exploring the possibility of vertical stacking of the multiplexed device using via connections between each sorting layer.

Improving the throughput of the device while maintaining our ability to enrich cells in subpopulations based on their mechanics is an enabling technology for applications involving large numbers of cells. This method for parallelization and multiplexing can also act as an enabling step for other microfluidic systems that also include multiple outlets and rely on flow parameters for successful operation. For example, the use of a flow-balanced manifold for inlet and outlet flow control could also be applied to other cell separation devices such as deterministic lateral displacement channels, pinched flow fractionation microchannels, and inertial separation spiral and serpentine microfluidics[152–155,151].

We have shown the ability to maintain sorting efficiency across multiple design iterations, but the largest difference in our sorting metrics between the single devices and the multiplex devices is our increase of processing throughput rate and reduction of required processing time. This throughput increase allows us to imagine a number of use cases for new applications for mechanical sorting of cells (Figure 28b). The increased throughput can be leveraged to either increase the number of cells being processed or drastically reduce the processing time. For small volume applications, the multiplexed platform could be used to reduce processing time and the time cells spend out of their ideal culture environment. If you need a mid-range number of cells processed such as 5,000,000 cells for a small cell dose for a cell therapy, like a mesenchymal stem

cell transplantation[174], the multiplexed device converts an experiment that would be incredibly cumbersome (over 20 hours with a single device) to very doable (less than 1 hour). Finally, if you need a large number of cells processed such as 50,000,000 cells for rare cell separations (like isolation of circulating tumor cells that are present at a concentration of 1-10 cells/mL of blood[175]), large cell therapy doses (like CAR-T therapy which requires over 3 million cells/kg for each dose[176]), or for large linked dataset generation (like the GeCKO mechanical screen described in chapter 5 that requires a coverage of 500 cells per sgRNA[146]), the multiplexing process actually becomes enabling, turning an impossible project (almost 9 days with a single device) to an achievable experiment time (9 hours). These are theoretical numbers and times, but they show the limitations that throughput can place on a microfluidic technology which often keeps technologies confined to an academic setting and prevents commercialization[177]. Our multiplexing approach greatly improves microfluidic throughput while preserving the physical functionality and control system complexity of the original design.

CHAPTER 5 – GECKO MECHANICS: GENOME-SCALE CRISPR KNOCKOUT SYSTEM TO EXPLORE GENOMECHANICAL RELATIONSHIPS

5.1 – Abstract

Cell mechanics can serve as an important biomarker for cell state and phenotype such as metastatic ability. While some molecular mechanisms underlying cell mechanical properties have been investigated through targeted analyses, a genome-wide study of genes and gene networks that modulate cell biophysical properties has not been attempted. In this work, we combined a microfluidic stiffness-based sorting device with a genome-scale CRISPR knockout (GeCKO) screen in order to investigate the effect of single gene knockouts on cell stiffening and cell softening across the entire protein-coding genome. We processed approximately 150 million Cas9-expressing ovarian cancer cells that had been transduced with a library of 76,000 single guide RNAs (sgRNAs) against the 19,000 protein-coding genes in the genome, sorting the cells into 5 mechanical subsets. We identified 7 gene knockouts that were significantly depleted in the softer subsets and over 700 gene knockouts that were significantly enriched in the stiffer subsets. This study was the first to explore the relation between gene expression and cell mechanics at the genome-scale to understand the intersection between cell genotype, mechanotype, and phenotype for metastatic cancer cells. The method could also be applied to study the effect

of genes on other biophysical cell processes as well as for identifying universal pathways for the control of cellular mechanics across many cell types.

5.2 – Introduction

The process of metastasis, which causes 90% of all cancer-related deaths, involves the collection of mutations that allow primary tumor cells to modify their adhesion and mechanics, undergo EMT, break away from their tumor, degrade the extracellular matrix (ECM), migrate to neighboring tissues, and undergo mesenchymal-to-epithelial transition (MET) to form a new metastatic tumor. EMT causes cells to change from being polarized and epithelial-like to being spindly, solitary, motile, and mesenchymal-like[11]. This transition occurs with the loss of cell-cell interactions, the activation of certain transcription factors, changes in surface protein expression, a reordering of the internal cytoskeleton, and production of enzymes to degrade the extracellular matrix[12–15].

Many of the changes described above, including the invasion and migration of metastatic cells, are associated with the mechanical properties of a cell. The processes of EMT and MET rely heavily on the reorganization of a cell's cytoskeleton, the proteins within a cell which provide structural support and allow for cell motility[1,12]. Beyond the mechanical processes of EMT/MET, cancer cells undergo other mechanical processes that allow them to affect their extracellular microenvironment in addition to the mechanics of the cell itself. Cell softening has been demonstrated in many motile cell types and it has been shown that for many

cancer types, as metastatic potential increases, cell stiffness will decrease[1,2,21,22]. In addition to the importance of mechanics in cancer cell behavior, we have also studied the role of mechanics in cell viability, chemoresistance, sickle cell transport, leukocyte demargination, endothelial tube formation, stem cell differentiation, liver fibrosis, and fibrogenesis[27–36]. Because of the relationship between disease state and cell mechanics, cell stiffness has been suggested as an important biomarker that could be used as a correlate of cell migratory or invasive capacity. There is currently a gap in our understanding of the molecular and network mechanisms driving this phenomenon. Understanding how cell mechanics integrate the signals of many molecular pathways may enable its use as a better biomarker and possible targets for therapeutics.

While certain genes that affect cell mechanics have been studied, a genome-wide study of genes and gene networks that modulate cell biophysical properties has not been attempted. The use of genome-wide CRISPR knockout (GeCKO) pooled screens has allowed researchers to start exploring the connection between a cell's genotype and various phenotypes, including chemoresistance, gene essentiality, *in vivo* metastasis, and immune activation[45,52–55]. The GeCKO process involves delivering a pooled lentiviral library of single guide RNAs targeted to over 19,000 genes (approximately every protein-coding gene in the human genome) to a Cas9-expressing cell line at a low multiplicity of infection so that statistically each cell will only contain one CRISPR knockout[52]. Cells with the single gene knockouts are screened for the phenotype of interest and sequencing is

used to compare the sgRNA distribution before and after the screen to identify which genes are related to the applied screening pressure. To understand gene networks that control cell mechanics and their role in metastatic potential, we used a high-throughput mechanical screen in conjunction with a genome-scale CRISPR knockout strategy to uncover the genetic and molecular mechanisms that allow cells from an inherently heterogeneous tumor population to change their mechanical properties to successfully form a metastatic tumor (Figure 29). Not only will this work play a significant role in the understanding metastasis, which leads to approximately 8 million deaths annually worldwide, but the development of this new method and uncovering the molecular mechanisms of cell migration will also lead to a biomechanical understanding of several other processes, including stem cell differentiation, immune cell development and activation, mechanotransduction, and wound healing.

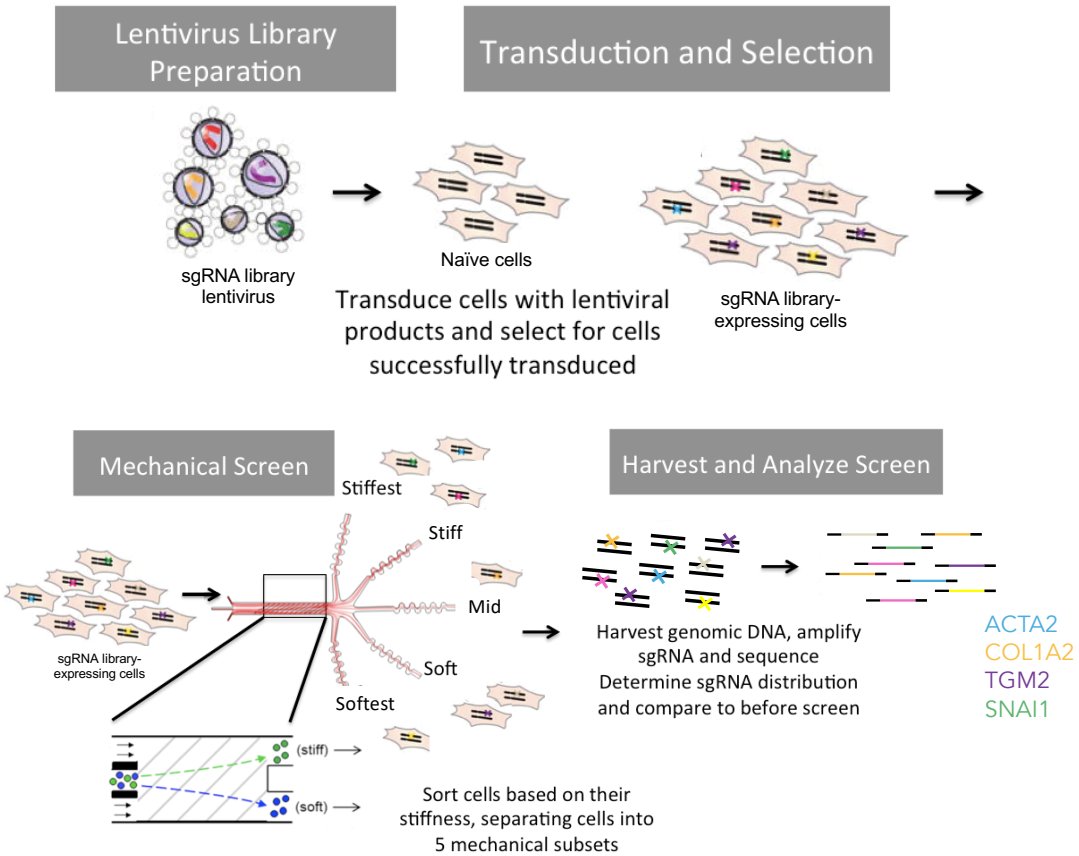

Figure 29 – Schematic overview of GeCKO mechanical screen – In brief, cells expressing Cas9 are transduced with a lentiviral library containing sgRNAs across the entire protein-coding genome at a low MOI to allow for single gene knockouts. Antibiotic selection ensures only cells with gene knockouts are included in mechanical screen. Next, the library of cells with single gene knockouts are processed with a microfluidic stiffness-based cell sorting device into 5 mechanical subsets. Genomic DNA is harvested, the sgRNA regions are amplified and sequenced, and the distribution of sgRNAs before and after the mechanical screen is used to determine which gene knockouts are correlated with each mechanical subset.

5.3 – Materials and Methods

5.3.1 – Development of Cas9-expressing cell line

We have developed an ovarian cancer cell line that expresses Cas9 allowing for delivery of sgRNA to knock out particular genes of interest. HEK293T cells

(provided by Lena Gamboa in Dr. Gabe Kwong's lab) were cultured on poly-L-lysine (Sigma Aldrich) coated petri dishes (VWR) and transfected at 80-95% confluence with a lentiviral transfer vector containing Cas9 from *Streptococcus pyogenes* and GFP for detection of vector integration, psPAX2, VSV-G, TransIT-LT1transfection reagent (Mirus Bio), and Opti-MEM (ThermoFisher). Three days after transfection, viral particles were harvested and concentrated using overnight incubation at 4 °C with PEG-it (System Biosciences) and centrifugation at 1500xg for 30 minutes. Viral particles were resuspended in PBS and stored at -80°C until use. Ovarian cancer cell HEY A8 cells (provided by Dr. John McDonald) were transduced with the varying amounts of the concentrated lentiviral particles (0, 10, 20, 40, and 60 μL per confluent 24-well), removing the virus the following day. Each well was trypsinized and resuspended for single cell sorting with FACS (BD FACS Aria) into a 96 well plate. Cells transduced with 0 μL of virus were used to create a GFP-negative gate. We additionally applied a high-GFP and mid-GFP gate, selecting the mid-GFP gate for the single cell sort, because we wanted to select cells that had GFP (and thus Cas9) integrated into their genome, but not too frequently (because of unwanted issues with the locations the vector integrates into the genome). Single cells deposited in 96-well plates were expanded into clonal populations over two weeks.

To test the efficacy of the expressed Cas9, we transfected the HEY A8-Cas9-GFP cells with 1 μg/μL sgRNA against GFP (sgGFP sequence: GGGCGAGGAGCTGTTCACCG) with Lipofectamine 2000 (ThermoFisher) in

OptiMEM (ThermoFisher) for 24 hours. Five days after transfection, flow cytometry (BD Accuri) was used to compare the FL1 expression of HEY A8-Cas9-GFP cells with and without the addition of sgGFP. Additionally, DNA from the transfected cells was extracted using Quick Extract (Lucigen) and the GFP region was amplified with PCR. Gel electrophoresis was used to confirm an amplified GFP region and PCR products were sent for Sanger sequencing (Eton) to determine the insertion-deletion rate after Cas9 editing using Tracking of Indels by Decomposition (TIDE) analysis (https://tide.nki.nl).

5.3.2 – Cell culture and sample preparation

The HEY A8-Cas9-GFP ovarian cancer cell line was cultured in complete media consisting of RPMI-1640 (Sigma-Aldrich) supplemented with 10% v/v fetal bovine serum (Atlanta Biologicals) and 1% v/v penicillin-streptomycin (Sigma-Aldrich). HEK293T cells were cultured in complete media consisting of DMEM (ThermoFisher) with 10% v/v fetal bovine serum (Atlanta Biologicals) and 1% v/v penicillin-streptomycin (Sigma-Aldrich). Cells were cultured at 37°C at 5% CO_2.

For the GeCKO mechanics microfluidic sort, cells were prepared for processing by trypsinization and resuspension in flow buffer (complete media, 10% v/v OptiPrep (Sigma-Aldrich) and 0.1% v/v Pluronic F-127 (Millipore Sigma)) with 1 mg/mL DNAse I (Sigma-Aldrich) at approximately 1-2 million cells/mL. The formulation of OptiPrep in the flow buffer was optimized to create a neutrally buoyant solution to prevent cell settling in the device or tubing. In short, cells

were resuspended in solutions with different concentrations of each density gradient medium and centrifuged at 300xg for 10 minutes and the concentration at which a cell pellet first began to form was selected as the ideal buffer density. Cells were strained using a 20 μm pore filter (PluriSelect) and loaded into a syringe (VWR) for microfluidic processing.

5.3.3 – GeCKO viral library transduction

The human CRISPR Brunello lentiviral pooled library was designed to optimize on-target activity and reduce off-target effects (Addgene 73178-LV)[53]. This library targets 19,114 human genes with 76,441 total gRNAs, with 3-4 gRNAs targeting each gene. The 2-vector system was selected where the Cas9 component and guide library are delivered in different viral vectors. This allows for the reduction of noise in the knockout screen, a higher-titer guide lentivirus for a more efficient transduction, and a recombinant system that is safer for use in the lab. To maintain coverage of approximately 315 cells with each sgRNA knockout after transduction, approximately 60 million cells were transduced with the lentiviral library. Cells were seeded at a high concentration of 3 million cells per 12-well in RMPI supplemented with 10% v/v heat-inactivated FBS, 1 μg/μL polybrene (Sigma Aldrich) and 300 μL of the lentiviral library (2.88E6 TU/mL). Transducing the Cas9-expressing cells with a low MOI (0.3-0.5) ensures that statistically most cells will only receive at most one knockout[178]. The GeCKO infection protocol was optimized by transducing the HEY A8-Cas9-GFP cells with

varying amounts of the lentiviral library (0, 50, 100, 300, and 500 μL). Puromycin was used as selection agent to isolate the cells that successfully received a single gene knockout. We used 0.5 μg/mL puromycin as the minimal antibiotic dose that killed all cells after 1 week of treatment. After 1 week of puromycin selection, 40% of the cells that had been transduced with 300 μL of lentiviral library survived when compared with cells that did not undergo puromycin selection, the optimal infection efficiency. For the GeCKO sort, the cells that were transduced with the lentiviral library and underwent puromycin selection were expanded so that there was at least 40 million cells for microfluidic processing to maintain coverage of all sgRNAs.

5.3.4 – AFM and force curve analysis

To investigate the effect of transduction of the GeCKO library on cell mechanics, we used force spectroscopy to obtain force-indentation curves with an atomic force microscope (Asylum Research) with an integrated optical microscope (Nikon) on a vibration isolation table. For improved contact area between the cantilever and cell, a 7.32 μm spherical polystyrene particle was attached to a tipless silica nitride cantilever (Bruker Probes) using a two-part epoxy (JB Weld). Before taking measurements, the cantilever was calibrated to determine the deflection inverse optical lever sensitivity and spring constant (k was approximately 30 pN/nm).

Cells were seeded after trypsinization in a glass bottom FluoroDish (World Precision Instruments) and allowed to attach before force curve collection. For measurements, the cantilever probe was visually aligned with the cell center and moved with a velocity of 2 µm/s to indent the cell with increasing compressive force until a force trigger of 10 nN was reached. The cantilever was held in position for 5 seconds, dwelling towards the surface, allowing for viscous relaxation of the cell before reversing the direction of its velocity. We collected 150 cellular measurements per cell type.

We used custom code written in R (https://github.com/nstone8/Rasylum) relying on the Hertzian contact model, which describes non-adhesive elastic contact between two bodies, to calculate the cellular reduced Young's modulus[25]. The contact point was estimated by the intersection of the flat, undeformed region of the force curve with a line fit to the force curve region where the cantilever was in contact with the cell. Next, we identified the true contact point by iteratively testing the points around the estimated contact point with the minimal residual difference between the measured force curve and a nonlinear fit described by the governing equation Hertz used to describe the contact between an elastic sphere and an elastic half space.

5.3.5 – High-speed video analysis

High-speed videos were taken of the cells passing through a single channel sorting device operating at 30 μL/min total flow rate using a Phantom camera at

2500-3000 frames per second to monitor cell trajectories and velocity after interactions with the diagonal ridges. To measure cell trajectories, ImageJ was used to extract an image stack from each video and a Z-projection was used to identify the background of each image. The calculator plus function was used to subtract the background from the image stack so that only moving cells would remain. Using the TrackMate[165,166] plugin in ImageJ[167,168], cells were identified in each frame and linked together into tracks tracing each cell's movement through the device. This produced approximately 100 tracks per video. Custom python software (https://github.com/nstone8/heimdall) was used to analyze collected cell trajectories. The tracks of transduced and non-transduced cell populations were analyzed to determine deflection and interaction time with each ridge.

5.3.6 – Microfluidic mechanical screen

The library of single gene knockout cells was processed through the multiplexed microfluidic cell mechanical sorting device described in chapter 4. The microfluidic device was set up on the stage of an optical microscope (Nikon) to monitor cell sorting. First, the device was primed by flowing flow buffer through the device to remove all air bubbles. Flow was controlled using two syringe pumps (Harvard Apparatus) with 0.02 in inner diameter and 0.06 in outer diameter Tygon tubing (Cole Parmer) connecting the sheath flow syringes of flow buffer to the inlet ports of the left and right sheath channels. The two independent sheath flows allow for the control of cell focusing at the entrance of the sorting channel. The

tubing fits directly into the 1.2 mm punch without need for adapters. All tubing and needles used in the experiment were cleaned prior to use with deionized water. Tubing was also fit into the five outlet ports and placed in a conical tube for sorted cell collection. Once the device was prepared, the syringe of cells in flow buffer with DNAse were connected to the cell inlet of the device with tubing using a third syringe pump. The flow parameters were optimized (see 4.3.7) for sorting of the ovarian cancer cells based on stiffness, with 50 μL/min total flow rate per channel, or 200 μL/min and 120 μL/min sheath flows, and 80 μL/min cell inlet flow for the entire multiplex device. The optimal device gap size was 9.5 μm with 14 diagonal ridges. After distribution, cell sorting, and recombination of fluid in the multiplexed device, cells were separated into five subsets – softest, softer, median, stiffer, and stiffest cells. Cells were collected in conical tubes and kept on ice until the sort was complete. After recording the volume and concentration of cells collected at each outlet, cells were pelleted and flash frozen at -80°C for genomic DNA extraction. The GeCKO mechanical screen was repeated 4 times with 4 biological replicates.

5.3.7 – Isolation and purification of genomic DNA

Genomic DNA was isolated and purified using the Wizard Genomic DNA Purification Kit (Promega). In short, pelleted cells were washed in PBS and lysed using a nuclei lysis solution with RNAse. After incubation for 15 minutes at 37°C, a protein precipitation solution was added and DNA from the supernatant layer

was transferred to a clean tube. The addition of isopropanol (Sigma Aldrich) precipitated the DNA which was washed with 70% ethanol (Fisher Scientific), pelleted, and air dried before resuspension in a DNA rehydration solution. DNA was stored at 4°C and a Nanodrop spectrophotometer (ThermoFisher) was used to determine the quantity and quality of DNA from each sample.

5.3.8 – Genomic DNA sequencing

Next generation sequencing (NGS) was used to confirm the sgRNA distribution after the screen. First, we prepared our library for sequencing using PCR to amplify the sgRNA target region (P5 primer: ACACTCTTTCCCTACACGACG CTCTTCCGATCTTTGTGGAAAGGACGAAACACC*G, P7 primer: GACTGGAGTTCAGA CGTGTGCTCTTCCGATCTTCTACTATTCTTTCCCCTGCACTG*T, product size: 354 nucleotides) of gDNA from each sample (five outlets and one inlet for each of the four bio-replicates) with a second PCR step to add Illumina adaptor sequences and barcodes for batch NGS. Next, the PCR products were purified and quantified using a Bioanalyzer (Agilent) before combining and sequencing the indexed samples for sgRNA distribution on a NovaSeq 6000 (Illumina) using the SP 100 cycle kit with 122 cycles of read 1 (forward) and 8 cycles of index 1 with a coverage of at least 100 reads per sgRNA in the library (650-800 million reads total).

5.3.9 - Screen analysis

The web-based Basespace Sequencing Hub (Illumina) was used to generate FASTQ files from the raw NovaSeq data which were then input into a fully-interactive analysis and documentation suite for pooled CRISPR screens, CRISPRAnalyzeR (https://github.com/boutroslab/CRISPRAnalyzeR). This web-based, interactive analysis suite took the input of the NGS raw data and a description of the Brunello pooled CRISPR sgRNA library and output the data quality, read count distribution, replicate quality and sample comparison, and sgRNA statistics. After passing this screen quality step, the software completed six differential analysis methods (Wilcox, DESeq2, MAGeCK, sgRSEA, EdgeR, and Z Ratio) and two Bayesian analysis methods (BAGEL and ScreenBEAM) comparing sgRNA distributions of each outlet to the inlet distribution. I focused my analysis on the DESeq2 method which uses the summed read counts of all 4-6 sgRNAs per gene and tests for differential effects between the inlet and outlet distributions using a negative binomial distribution model[179]. The total read count per gene is normalized, size-factors are estimated, and variance is stabilized with a parametric test. A Wald test is used to compare the difference in fold changes in the inlet and outlet distributions to determine whether the gene was enriched or depleted. We used an adjusted p-value threshold of 0.001 to determine significance for the DESeq2 method.

5.4 – Results

5.4.1 – Successful integration of Cas9-GFP cassette in ovarian cancer cell line

To use the 2-vector lentiviral system for the GeCKO screen, we first needed to establish an ovarian cancer cell line that expressed Cas9. We confirmed the successful integration of a gene cassette containing Cas9 and GFP by introducing a sgRNA against GFP. Using flow cytometry to compare the GFP expression level of HEY A8-Cas9-GFP cells after transfection of sgGFP, we observed a significant reduction in the number of GFP+ cells after the addition of 50, 150, and 250 ng of sgGFP (Figure 30a). Additionally, we observed a significant reduction in the mean fluorescence intensity of the transduced cells (Figure 30b). Together, this data confirms the successful integration of the Cas9 cassette that is able to functionally edit genes when transduced with sgRNA. As final confirmation, we sequenced the GFP region of the cells after gene editing and observed a 25-60% total insertion-deletion efficiency at the cut site as determined using TIDE analysis (Figure 30c). Additionally, the cells maintained GFP expression (and thus we also assume Cas9 expression) after cells were continually cultured and stored in liquid nitrogen for over two years.

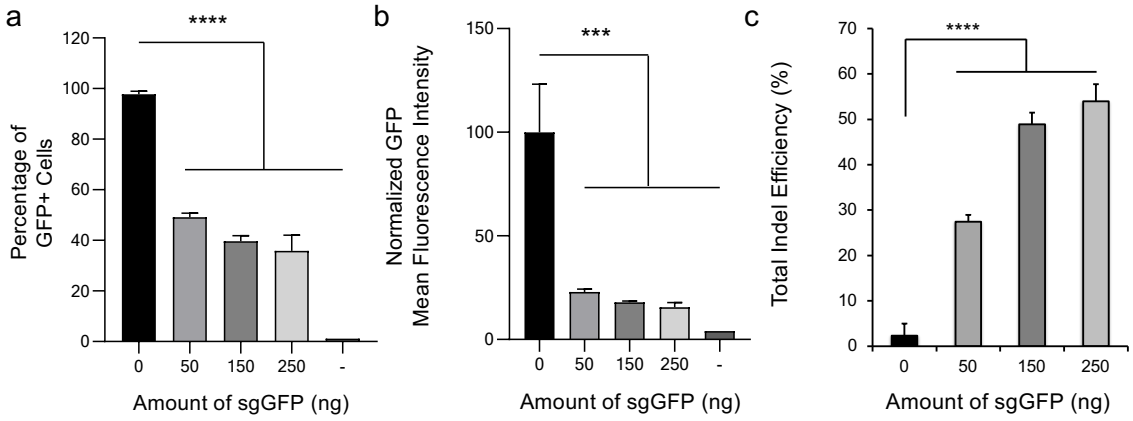

Figure 30 – Cas9-expressing cells capable of gene editing – a) The addition of sgGFP to Cas9 and GFP expressing HEY A8 cells results in the significant reduction GFP+ cells as measured by flow cytometry (Tukey HSD post-hoc test, ****, $p < 0.0001$). – cells are HEY A8 cells that do not express Cas9 and GFP. b) The addition of sgGFP to HEY A8-Cas9-GFP cells also results in significant reduction of mean fluorescent intensity (MFI) of each sample implying successful knockout of GFP region (Tukey HSD post-hoc test, ***, $p < 0.001$). – cells are HEY A8 cells that do not express Cas9 and GFP. c) TIDE analysis was used to determine the insertion-deletion efficiency significantly increases after the addition of varying amounts of sgGFP to HEY A8-Cas9-GFP cells (Tukey HSD post-hoc test, ****, $p < 0.0001$).

5.4.2 – Stiffness-based sorting microfluidic device capable of separating GeCKO transduced cells

After establishing our Cas9 cell line, we tested the feasibility that single gene knockouts could result in detectable changes in cell mechanics that could be sorted in the microfluidic device. We transduced cells with the GeCKO lentiviral sgRNA library and took AFM measurements comparing the cell stiffness of cells with single gene knockouts and non-transduced Cas9-expressing cells. There was a significant difference between these two populations ($p=0.0029$, $n=150$ for each condition) with 5% of the GeCKO cells exhibiting measured stiffness higher

than the maximum control cell stiffness (Figure 31a). As a reminder, if this 5% of stiffened cells is representative of the entire library of GeCKO transduced cells, it would imply there are over 3,800 sgRNAs or 950 gene knockouts that could potentially increase the cell stiffness. Additionally, there was an increase spread of the single gene-knockout cell group compared to the control cell population, implying the GeCKO transduction process results in increased heterogeneity of cell mechanics that could potentially be detected by our microfluidic device. To test the behavior of these transduced cells in our device, we used high-speed video analysis custom software to track the locations of cells deflected at each diagonal ridge. Cells with single gene knockouts had increased amount of deflection in the device, an increased spread of deflection, increased interaction time with each ridge, and an increased spread of interaction times, also confirming the feasibility of sorting GeCKO transduced cells by biomechanical properties in our microfluidic device (Figure 31b and Figure 31c).

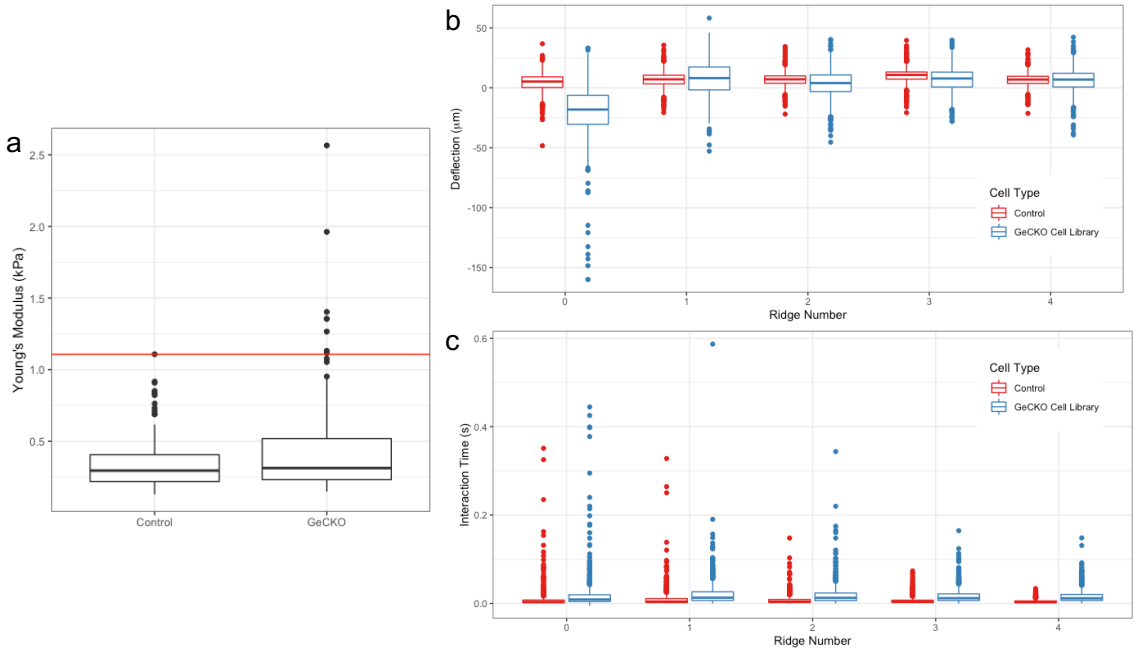

Figure 31 – Cell mechanical changes due to single gene knockouts could be sorted by microfluidic device – a) AFM measurements show GeCKO transduction leads to statistically different cell populations with a wider range of observed stiffnesses ($p < 0.01$, Welch two sample t-test, $n = 150$ per sample). The red line denotes the highest Young's modulus value of the control cell population; 5% of the GeCKO transduced cells fell above this maximal stiffness line. b) High-speed video analysis was used to track the deflection of the control and GeCKO-transduced cells in our microfluidic device at each ridge. The GeCKO cells show a wider variation in cell trajectories with more cells deflected at the first ridge compared to the control cells. c) High-speed video analysis was used to observe the interaction of control and GeCKO-transduced cells in our microfluidic device with each ridge. The GeCKO cells show a wider variation in interaction time as well as increased interaction time as compared to the control cells.

5.4.3 – Approximately 150 million GeCKO transduced cells mechanically sorted across four bio-replicates

Four separate GeCKO mechanical screens were conducted with 20 – 67 million transduced cells collected per experiment. In total, approximately 150 million cells were processed and collected in five mechanical subsets. The majority

of the cells followed the fluid streamlines through the device ending in the soft outlets, outlet 1 and outlet 2. Approximately 3% of the transduced were deflected to the stiff outlets, outlet 4 and outlet 5 (Figure 32). This figure is consistent with our prediction above that approximately 5% of cells would receive a single gene knockout that might result in cell stiffening that could be used for cell separation in our microfluidic device. On average, we processed cells at a rate of 6.2 million cells/hour, and the duration of processing time ranged from 4.75 hours to 11.5 hours. Sorted cell subpopulations were stored on ice until cells were pelleted and flash frozen before gDNA extraction.

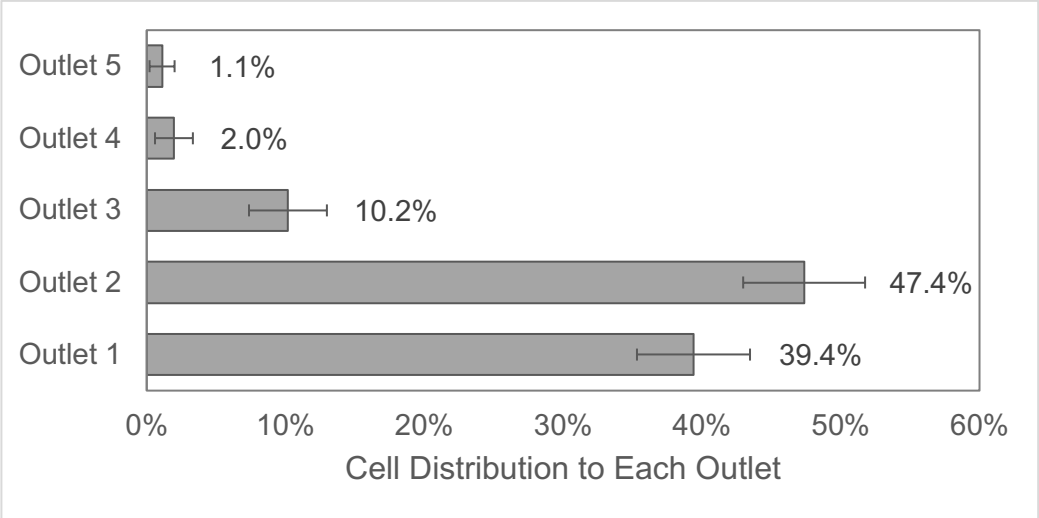

Figure 32 – Cell distribution to each outlet for GeCKO mechanical sort bio-replicates – This graph depicts the average percentage of total sorted cells that were deflected to each outlet over four bio-replicate sorts. Outlet 1 indicates the softest subset. Error bars denote standard deviation between the replicates.

5.4.4 – DESeq2 analysis reveals hundreds of genes enriched in the different mechanical subsets

After extracting the gDNA from all samples and using next generation sequencing to determine the pre- and post-screen distribution of each sgRNA, we identified hundreds of genes differentially distributed in each of the different mechanical subsets as compared to the inlet distributions. For the softest outlet, outlet 1, 4 gene knockouts were significantly depleted (Figure 33a). For the soft outlet, outlet 2, 3 gene knockouts were significantly depleted (Figure 33b). For the median outlet, outlet 3, 111 gene knockouts were significantly enriched and 2 gene knockouts were significantly depleted (Figure 33c). For the stiff outlet, outlet 4, 362 gene knockouts were significantly enriched and 4 gene knockouts were significantly depleted (Figure 33d). For the stiffest outlet, outlet 5, 348 gene knockouts were significantly enriched (Figure 33e). Because of the sorting efficiency of the multiplex device (see 4.4.3), it is understandable that we would observe more enriched genes in outlets 3 through 5, where we observed high enrichment and purity of the stiffened cells.

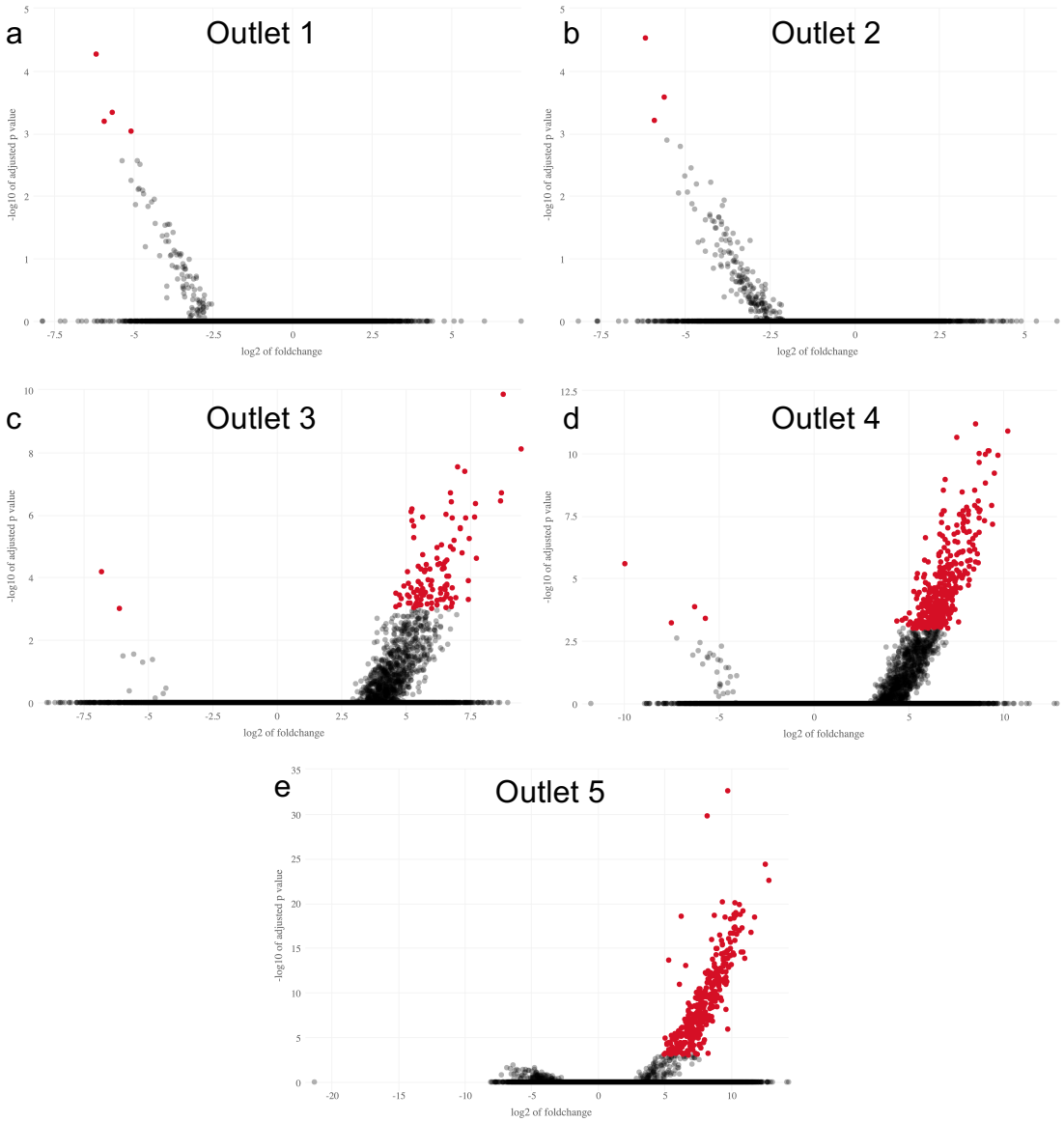

Figure 33 – DESeq2 analysis reveals hundreds of genes enriched in mechanically sorted subpopulations – Ratio of log-2 transformed fold change and log-10 transformed fold change adjusted p-value for each gene evaluated by DESeq2 differential effect test for a) Outlet 1, b) Outlet 2, c) Outlet 3, d) Outlet 4, and e) Outlet 5 of GeCKO mechanical screen. Each red dot represents a significantly enriched or depleted gene in the outlet compared to the inlet sgRNA distribution (adjusted p-value threshold = 0.001). All black dots represent non-significant genes.

5.5 – Discussion

Using the multiplex microfluidic cell sorting device described in chapter 4, I was able to complete and replicate the first ever GeCKO mechanical screen. Sorting approximately 150 million cells with single gene knockouts spanning the entire protein-coding genome into five mechanical subsets has resulted in a large linked dataset correlating gene knockouts to the cell softening and cell stiffening processes. There are hundreds of significant genes that were enriched or depleted in the five mechanical subsets, providing hundreds of hypotheses for future testing of potential genetic control points for cell mechanotype and phenotype. The next step in processing this large dataset will be to investigate the functional annotation for each significant gene. This could be completed using the PANTHER Classification System (http://www.pantherdb.org) or the Database for Annotation, Visualization and Integrated Discovery (DAVID). Because of the results linking cell mechanotype with a metastatic gene expression profile as noted in chapter 3, I expect to see enrichment of terms related to metastatic processes in the mechanically enriched genes. However, if this is not the case, we could potentially also uncover relationships between cell mechanics and other molecular processes in the cell.

One potential gene of interest that was significantly depleted in Outlet 1 was *DNAI1*. *DNAI1* encodes for a member of the dynein intermediate chain family, which is a part of the dynein complex in ciliated cells. Interestingly, defects in the primary cilium of ovarian surface epithelium have been implicated in tumorigenesis

and ovarian cancer cells displayed reduced numbers of primary cilia[180]. *DNAI1* was identified as depleted in the Outlet 1 subpopulation. To explain further, because the sgRNAs against *DNAI1,* and thus cells with *DNAI1* knockouts, were found in greater abundance in the Outlet 1 population as compared to the inlet population, we can hypothesize the loss of *DNAI1* is associated with cell softening. This makes sense as the dynein structure generates the force responsible for the motion of axonemes in ciliated cells, supporting a hypothesis linking cell force generation, cell motion, and mechanics[181]. To further explore this link, we could use sgRNAs against *DNAI1* to knockout this gene and characterize the mechanical and migratory properties of these knockout cells. This is just one example of hundreds of potential genes that could be explored in the same way that were enriched and depleted in the multiple mechanical subpopulations.

There are a couple limitations to the GeCKO mechanics method that could be further explored and amended in the future. As mentioned previously, using a low MOI for the lentiviral transduction results in most cells receiving at most one gene knockout. However, the number of cells receiving two or more integrants could be close to 20% of all infected cells when using an optimized infection efficiency of 40%[178]. With the current sequencing protocol, we are unable to determine whether the sgRNA that ends up in each outlet was the only integrant in a cell or a multi-integrant. However, because of the redundancy of using ~500 cells per sgRNA, 4-6 sgRNAs per gene, and 4 bio-replicates, we can say with more confidence that the genes that appear significantly enriched in an outlet are most

likely due to the knockout of that specific gene and not a combination of genes. Additionally, the GeCKO mechanics method should be viewed primarily as a hypothesis generator and all potential genes correlated with each mechanical subset need to be validated. Another limitation of this method is related to our specific ability to create enriched and highly pure samples of stiffened cells, without enriching softened cells. We saw the effect of this differential enrichment in the increased number of significantly enriched and depleted genes in the stiff outlets compared to the soft outlets. We could improve our ability to enrich softened cells by further optimization of cell concentration and flow parameters as well as ensuring equal sorting in all eight parallel channels. As discussed in chapter 4, the slight variation in the flow velocity across the channels could result in reduced sorting in some channels.

Finally, there are a number of interesting and exciting directions this work could take next as this method is applied to other areas of research. This same method could be used to mechanically screen for genes of interest in other cell types. Do mechanically correlated genes differ between different cancer types? What about between cancer cell lines of different metastatic potential? Would the mechanical screen results differ between a cancer cell line and a healthy fibroblast line? Exploring these questions could help the field establish universal genes that are associated with the mechanical properties of all cells. Additionally, there are a number of other GeCKO libraries that have already been developed that could also be substituted for the Brunello library we used in this study. For example, there

are libraries of sgRNAs to knock out epigenetic regulators and lncRNAs as well as libraries that activate, instead of knock out, genes of interest. This procedure could be repeated with different combinations of cell types and sgRNA libraries of interest to generate more testable hypotheses about the connection between cell phenotype, genotype, and mechanotype.

CHAPTER 6 – HYPOTHESIS TESTING TO EXPLORE PHENOTYPIC AND MECHANOTYPIC IMPORTANCE OF GENES OF INTEREST

6.1 – Abstract

Cell mechanical properties, such as cell stiffness and viscous behavior, have been proposed as biomarkers for the diseased state of cells. Moreover, the molecular pathways that modify cell mechanical properties may also be potential novel targets for managing lethal malignancies by specifically changing the mechanical phenotype of cancer cells. In this chapter, we used a large linked dataset to explore the correlations between cell mechanical properties (Young's modulus and two viscous time constants), gene expression, and functional migration. Using a network analysis, we identified potential master regulators that could control the expression of multiple genes that are correlated with cell mechanics. We investigated the up- and down-regulation of 7 potential regulators (*MIR183*, 17-ODYA, *MIR520c*, lacidipine, *AKT2*, *ITGB6*, and AG879) and measured the effect of the modulation of these regulators on both cell stiffness and gene expression across multiple ovarian cancer cell types. We have identified a number of regulators that work in cell-type specific manners to soften and stiffen cells that can also change functional aspects of the cell, such as migratory ability.

6.2 – Introduction

Ovarian cancer is a lethal gynecological malignancy with low survival rates largely due to late-stage diagnoses. About 60% of all ovarian cancer cases from 2007-2013 were diagnosed at an advanced stage after malignant cells had already spread beyond their organ of origin, resulting in low five-year survival rates and reduced treatment options for many patients[182]. As we have started to reach the limit of chemotherapeutics for the management of this disease, researchers have turned to molecular agents to target new pathways associated with aberrant signaling for the processes of apoptosis, survival and proliferation, angiogenesis, and migration and invasion[183]. Another targetable disease biomarker that integrates several signaling pathways is cellular mechanics, which is of particular interest because the intrinsic mechanical properties of cells have been shown to affect both the cell's response to its microenvironment and the progression of ovarian cancer[21,184,185]. While the specific role of the expression of a number of cytoskeletal proteins on cancer cell mechanics has been studied before[186–189], there are many other gene and protein signaling pathways that affect cancer cell mechanics that are unknown. As described in chapters 3 and 5, we have developed methods for investigating the intersection between cell mechanotype, phenotype, and genotype. We have used these methods to identify new gene expression pathways associated with cell mechanics. These genomechanical relationships can help us identify potential control nodes in the pathways that link cell mechanics

and metastatic ability. These control nodes could act as therapeutic targets for better management or prevention of cell migration and metastatic disease.

The focus of this chapter is to test a number of hypotheses generated in chapter 3 that connect genes of interest and cell mechanical properties. Because decreasing cell stiffness and cell viscosity are both associated with increasing ovarian cancer malignancy[190], we explore the genetic regulation of both of these mechanical properties. Using a genomic network analysis, we identified several potential master regulators to control the expression of genes significantly correlated with cell stiffness, the fast viscous time constant (tau1), and the slow viscous time constant (tau2). We tested the effect of up- and down-regulation of several potential regulators in multiple ovarian cancer cell lines, while observing the cells' changes in mechanical properties, gene expression, and migratory ability. We have successfully discovered a number of regulators that modify complex mechanics and migration in a cell-type specific manner.

6.3 – Materials and Methods

6.3.1 – Single cell genomechanics dataset

From the data sets generated in chapter 3, we identified 39 genes significantly correlated with cell stiffness, 12 genes correlated with viscous parameter tau1, and 32 genes correlated with viscous parameter tau2 ($p < 0.05$, Spearman's correlation test). As a brief reminder, the data sets were acquired from single cell AFM measurements taken on 273 ovarian cancer cells (91 HEY A8

cells, 95 HEY cells, 87 OVCAR3 cells). We extracted cell stiffness and viscous properties by applying a Hertzian contact mechanics model and a Maxwell viscoelastic model. Each single cell was isolated using micropipette aspiration for downstream analysis of 96 genes of interest related to cytoskeletal proteins, cancer pathways, cell mechanics, and metastatic processes. After normalizing each cell's expression to its housekeeping gene expression, we examined the correlative relationships between the mechanical properties and the genes probed at the single cell level using a Spearman's pairwise correlation.

6.3.2 – Gene network analysis

We applied Causal Network Analysis[191] from the Ingenuity Pathway Analysis package using the genes significantly correlated with both cell stiffness and cell viscous properties to identify potential upstream regulators, including master regulators that control expression of several of these genes. For genes correlated with cell stiffness, the fast viscous time constant, and the slow viscous time constant, the analysis resulted in 37, 30, and 39 predicted causal networks, respectively, with a network-corrected p-value<0.01 (right-tailed Fisher's exact test) and absolute Z-scores ≥ 2. The overlap p-value can be interpreted as a probability that a given master regulator is associated with downstream genes correlated with each cell mechanical property by chance. In addition, network bias-corrected p-values can be calculated, which correct overlap p-values for bias introduced by downstream genes with "hub character", i.e., downstream genes

that are regulated by many master regulators[191] . For master regulators *CD82*, *MIR183*, *MIR520c*, lacidipine, *AKT2*, *ITGB6*, and AG879, the network bias-corrected p-values are $9x10^{-4}$, $1.4x10^{-3}$, $4x10^{-3}$, $3.8x10^{-3}$, $6.4x10^{-2}$, $3.16x10^{-2}$, and $1.42x10^{-2}$, respectively, and imply very low probability of associations of each of these regulators with mechanics-regulated genes only by chance.

6.3.3 Ovarian cell culture

The ovarian cancer cell lines HEY, its derivative cell line HEY A8, and OVCAR3 were cultured in RPMI-1640 media (Sigma-Aldrich) supplemented with 10% fetal bovine serum (Atlanta Biologicals) and 1% penicillin-streptomycin (Sigma-Aldrich). Cells were cultured at 37°C at 5% CO_2. All three cell lines were provided by Dr. John McDonald. For AFM experiments, approximately 50,000 cells were seeded in a glass bottomed FluoroDish (World Precision Instruments) for 24-hour treatment protocols. For RNA extraction, approximately 250,000 cells were seeded in a T25 flask (VWR) for 24-hour treatment protocols.

6.3.4 – Master regulator perturbations

We tested the effect of modulation of multiple types of potential master regulators of cell mechanics and gene expression, including microRNAs (MIR183-5p and MIR520c-3p), genes (*CD82*, *AKT2,* and *ITGB6)*, and small molecule inhibitors (lacidipine and AG879).

MIR183-5p and MIR520c-3p were overexpressed in cells via transfection with mirVana miRNA mimic for hsa-MIR183-5p or hsa-MIR520c-3p (ThermoFisher), respectively. Alternatively, cells were transfected with a negative control mimic miRNA (ThermoFisher). Additionally, we transfected cells with either a mirVana miRNA inhibitor for hsa-MIR183-5p or a negative control inhibitor miRNA at a ratio of 1:5 mimic to inhibitor. We determined optimal transfection conditions to be 2 µL of Lipofectamine RNAiMAX Transfection Reagent (Life Technologies) and 30 pmol of miRNA per 1 mL of media as well as the optimal incubation time post-transfection. After 6 hours, the transfection media was exchanged for fresh media and cell stiffness was measured 72 hours post-transfection with atomic force microscopy as described below.

CD82 up-regulation was induced by treatment of cells with 50 µM 17-octadecynoic acid (17-ODYA)(Cayman Chemical) reconstituted in DMSO (Sigma Aldrich). An equivalent amount of DMSO was used as a vehicle control. 17-ODYA is an inhibitor of *CYP2J2,* an inhibitor of CD82 expression; therefore, 17-ODYA upregulates the expression of CD82[192]. After 24 hours of treatment, as recommended, cell stiffness was measured with AFM as described below.

Lacidipine was used as a regulator of genes correlated with tau1. Cells were treated with 10 µM lacidipine (Sigma Aldrich) reconstituted in DMSO. An equivalent amount of DMSO was used as a vehicle control. After 24 hours of treatment, as recommended, cell viscosity was measured with AFM as described below.

AKT2 down-regulation was induced by treatment of cells with 10 μM BAY11259676 (MedChemExpress) reconstituted in DMSO. An equivalent amount of DMSO was used as a vehicle control. After 24 hours of treatment, as recommended, cell viscosity was measured with AFM as described below.

ITGB6 knockdown was induced by treatment of cells via transfection with *ITGB6* siRNA Silencer assay 144658 or Silencer Select Negative Control No. 1 siRNA (ThermoFisher). We determined optimal transfection conditions to be 1.7 μL of Lipofectamine RNAiMAX Transfection Reagent (Life Technologies) and 33 nmol of siRNA per 1 mL of media as well as the optimal incubation time post-transfection. Cell viscosity was measured 48 post-transfection with AFM as described below.

AG879 was used as a regulator of genes correlated with tau2. HEY A8, HEY, and OVCAR3 cells were treated with 10 μM Tyrphostin AG 879 (Sigma Aldrich) reconstituted in DMSO. An equivalent amount of DMSO was used as a vehicle control. After 24 hours of treatment, as recommended, cell viscosity was measured with AFM as described below.

6.3.5 – AFM and force curve analysis

For better global stiffness measurements of the cell, 5.24 μm spherical silica particles were attached to tipless silica nitride cantilevers (Bruker Probes) using a two-part epoxy. To characterize the mechanical properties of each cell, we used force spectroscopy to obtain force-indentation curves with an atomic

force microscope (Asylum Research) with an integrated optical microscope (Nikon) on a vibration isolation table. Each cantilever was calibrated to determine the deflection inverse optical lever sensitivity and spring constant (k is approximately 10 – 25 pN/nm). For measurements, the cantilever probe was visually aligned with the cell center and moved with a velocity of 2 μm/s to indent the cell with increasing compressive force until a force trigger of 5 nN was reached. The cantilever was held in position for 10 seconds, dwelling towards the surface, allowing for viscous relaxation of the cell before reversing the direction of its velocity.

We used custom code written in R (https://github.com/nstone8/Rasylum) relying on the Hertzian contact model, which describes non-adhesive elastic contact between two bodies, to calculate the cellular Young's modulus[25]. The contact point was estimated by the intersection of the flat, undeformed region of the force curve with a line fit to the force curve region where the cantilever was in contact with the cell. Next, we identified the true contact point by iteratively testing the points around the estimated contact point with the minimal residual difference between the measured force curve and a nonlinear fit described by the governing equation Hertz used to describe the contact between an elastic sphere and an elastic half space. We additionally used the Rasylum custom R package to fit the dwell region of the force curve to a biexponential decay curve to identify the fast (tau1) and slow (tau2) viscous time constants[26].

6.3.6 – RNA Extraction and RT-qPCR

To compare the gene expression of each cell line after perturbation of each master regulator, we used qPCR with SsoAdvanced Universal SYBR Green Supermix (BioRad) and cDNA reverse transcribed from mRNA Trizol (ThermoFisher) extracted and purified from T-25 flasks of HEY, HEY A8, and OVCAR3 cells (approximately 2 million cells each). Amplification curves from the ABI StepOne Plus qPCR machine were analyzed using LinRegPCR (https://www.medischebiologie.nl/files/) to determine a cycle threshold (C_t) for each sample-assay pair. The $\Delta\Delta C_t$ method was used to compare the fold-change expression differences between each treatment and control group. In short, we took difference between the C_t value of the geometric mean expression of housekeeping genes, *GAPDH* and *RPL32,* and the gene of interest's C_t value. Next, we took the difference between the normalized values of the control and treatment groups. Finally, we calculated the relative fold gene expression values using the expression $2^{-\Delta\Delta Ct}$. miRNA expression was measured using RT-qPCR with TaqMan fluorescent probes (Life Technologies) with UNG activation and normalization to *RNU6B* expression.

6.3.7 – Migration assay

To test the migratory properties of HEY A8 cells after 17-ODYA treatment, we used the Cultrex 24-well transwell migration assay (Trevigen), where 100,000 cells of each cell population were seeded in serum free media (RPMI-1640) in an

8-micron pore well insert, leading to a well filled with complete media (RPM1-1640 media supplemented with 10% FBS and 1% penicillin-streptomycin). After 8 hours of incubation, cells that migrated through the pores and were detached, lysed, and fluorometrically dyed with Calcein-AM fluorescent dye. The amount of fluorescence per well was read with a plate reader at 480 nm/520 nm (BioTek). A standard curve was performed to determine the relationship between fluorescence and number of cells.

6.3.8 – Gene ontology

The Database for Annotation, Visualization and Integrated Discovery (DAVID) is a tool widely used for gene functional classification, annotation, and ID conversion[193]. The bioinformatics analysis tool generates clusters of enriched annotations associated with a given gene list. DAVID ranks the biological significance of gene groups based on enriched functional genomic annotations by an overall Expression Analysis Systematic Explorer (EASE) score[194]. In order to test for significance, DAVID uses a hypergeometric test method, which compares the probability of k successes (random draws for which the gene drawn is associated with the specified functional annotation) in n draws without replacement from a finite population. We investigated enriched pathways from the Kyoto Encyclopedia of Genes and Genomes (KEGG) with Benjamini corrected p-values less than 0.05.

6.4 – Results

6.4.1 - Network analysis can generate hypotheses to test putative targets that affect cell stiffness

Given the broad assortment of identified metastatic genes that correlate with mechanical properties, we speculate there exist genes that could serve as cell stiffness-related control points. We applied a network analysis (see 6.3.2) to the genes significantly correlated with cell stiffness to identify potential upstream targets that affect the expression of the correlated genes. The analysis resulted in 37 master regulators predicted to significantly affect cell stiffness, 11 of which represent easily targetable transcription factors, miRNAs, or regulatory genes (Table 3 and Figure 34). Regulators with positive activation z-scores are associated with the increase of expression of genes positively correlated with stiffness or the decrease of expression of genes negatively correlated with stiffness; regulators with negative activation z-scores are expected to produce the opposite effect on genes of interest.

Table 3 – Network analysis reveals master regulators that could control cell stiffness – Network analysis of genes correlated with stiffness revealed 37 significant potential master regulators, 11 of which are listed here. Bolded potential regulators were experimentally tested.

Master Regulator	Molecule Type	Activation z-score	Network bias-corrected p-value
RECK	Other	2.828	6.00E-04
MRTFA	Transcription Regulator	2.500	8.60E-03
AR	Ligand Dependent Nuclease	2.111	1.00E-03
CD82	Other	2.065	9.00E-04
SPEN	Transcription Regulator	2.065	7.40E-03
miR520c	microRNA	2.000	4.00E-03
miR183	microRNA	-2.000	1.40E-03
EGFR	Kinase	-2.000	5.00E-04
ETV5	Transcription Regulator	-2.333	2.00E-04
YAP1	Transcription Regulator	-2.449	4.10E-03
TWIST2	Transcription Regulator	-2.449	9.00E-04

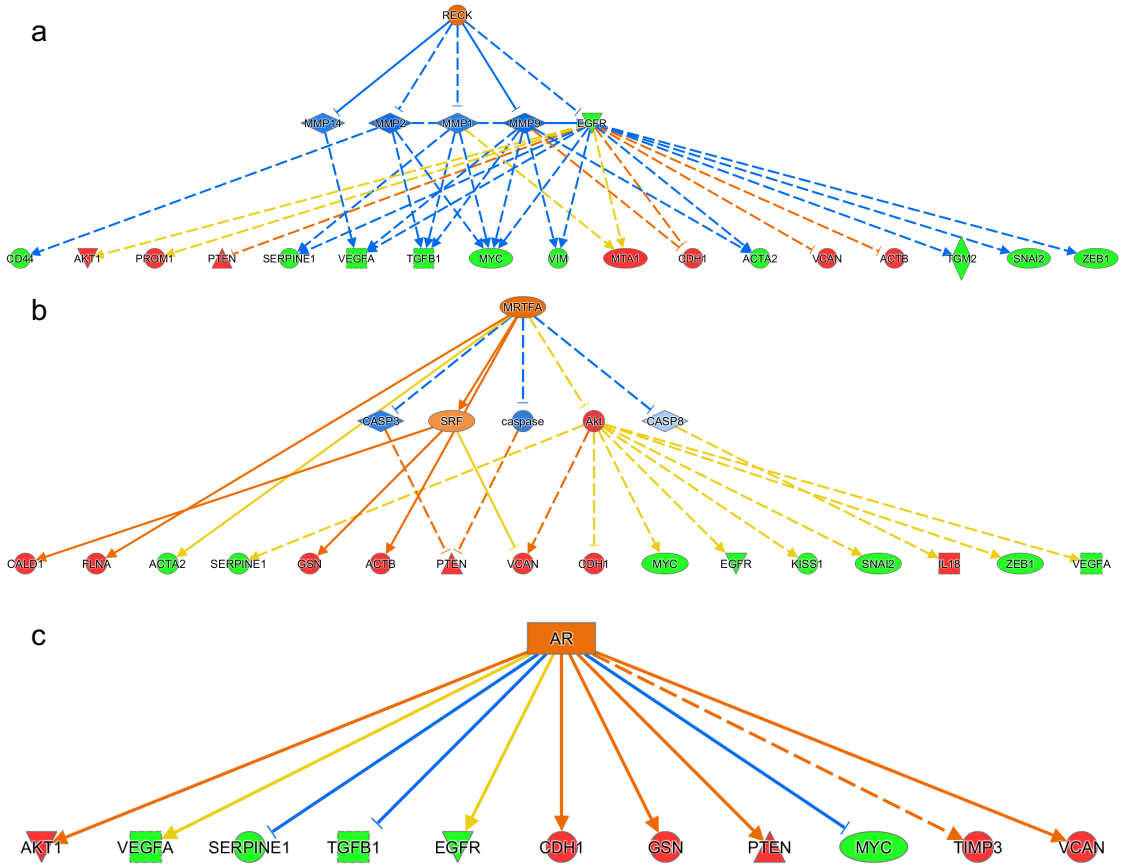

Figure 34 – Network of genes predicted to be under the control of stiffness master regulators – Network relationships for master regulators a) *RECK*, b) *MRTFA*, c) *AR*, d) *CD82* and 17-ODYA activator, e) *SPEN*, f) *MIR515*, g) *MIR183*, h) *EGFR*, i) *ETV5*, j) *YAP1* and k) *TWIST2*. Blue nodes represent regulators predicted to result in cell softening. Orange nodes represent regulators predicted to result in cell stiffening. Green nodes represent genes negatively correlated with cell stiffness and red nodes represent genes positively correlated with cell stiffness. Yellow lines represent relationships where a regulator is predicted to increase stiffness actually increases the expression of genes negatively correlated with stiffness or decreases expression of positively correlated stiffness genes as well as the opposite for predicted cell softening regulators.

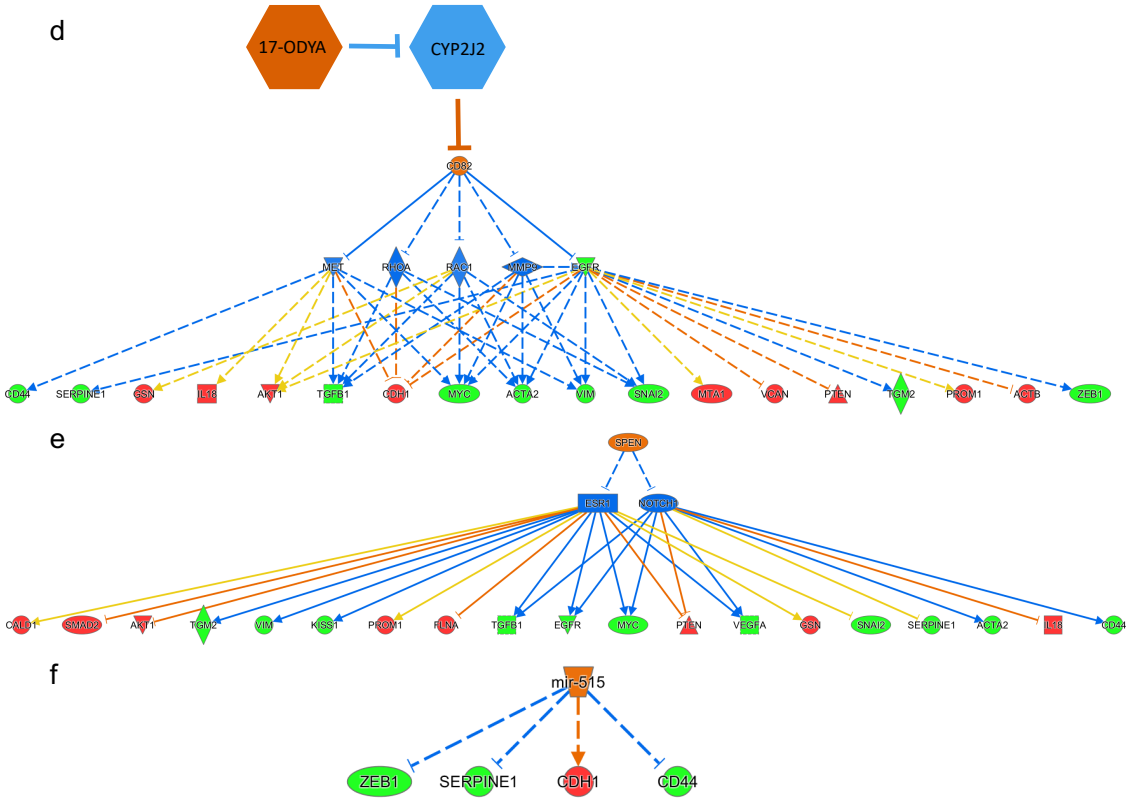

Figure 34 (continued)

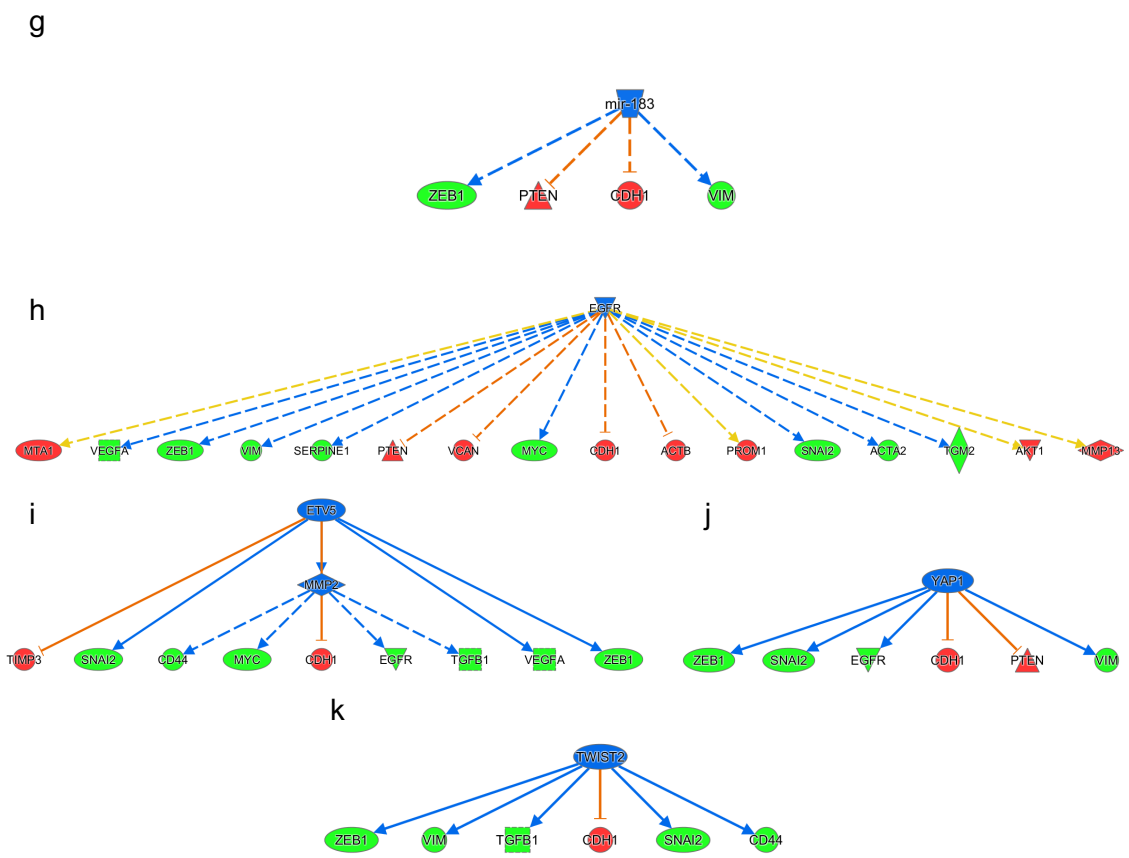

Figure 34 (continued)

To test the expected effect of the modulation of *MIR183* on cell mechanics, we transfected HEY A8 cells with combinations of a miRNA mimic and a miRNA inhibitor for *MIR183*. *MIR183* is a master regulator with a negative activation z-score predicted to lead to a decrease in cell stiffness. HEY A8 cells transfected with the *MIR183* mimic for 72 hours had a large increase of *MIR183* (41,866-fold change compared to cells transfected with negative control mimics and inhibitors, Table 4) and were significantly softer than cells transfected with the negative controls as predicted ($p < 0.05$, post-hoc Tukey HSD) (Figure 35a). Cells transfected with the *MIR183* inhibitor for 72 hours demonstrated a 1.3-fold

decrease in *MIR183* levels compared to cells transfected with both negative controls (Table 4) and were significantly stiffer than the *MIR183* mimic transfected cells as expected ($p < 0.0001$, post-hoc Tukey HSD). When we transfected cells with both a *MIR183* mimic and *MIR183* inhibitor, cell stiffness remained unchanged (Figure 35a). Interestingly, *MIR183* levels for the cells treated with both the mimic and inhibitor for *MIR183* were reduced as compared to cells treated with the *MIR183* mimic alone, but they were still highly elevated compared to cells that were transfected with both negative controls for the mimic and inhibitor (Table 4). Additionally, when this same experiment was repeated with the HEY and OVCAR3 cell lines, we observed changes in cell stiffness that were not consistent with the predicted mechanical regulation that was observed in the HEY A8 cell line (Figure 35b and Figure 35c). While the inhibitor increased cell stiffness for the HEY and OVCAR3 cells as expected, the mimic did not decrease cell stiffness in these cell lines.

Table 4 – miR183 expression levels after transfection – A miR183 mimic and miR183 inhibitor were used to overexpress and inhibit the expression of *MIR183* in three ovarian cancer cell lines. Fold expression is calculated with the $\Delta\Delta C_t$ method normalizing RT-qPCR C_t values to housekeeping gene *RNU6B* expression and *MIR183* levels of samples that were transfected with both the negative control miRNA (miRNC) mimic and inhibitor.

Cell Line	miR183 mimic + miRNC inhibitor – miR183 Fold Change	miRNC mimic + miR183 inhibitor – miR183 Fold Change	miR183 mimic + miR183 inhibitor – miR183 Fold Change
HEY A8	41,866.400	0.777	13,312.299
HEY	620.540	0.312	578.150
OVCAR3	2,594.437	5.180	4,495.697

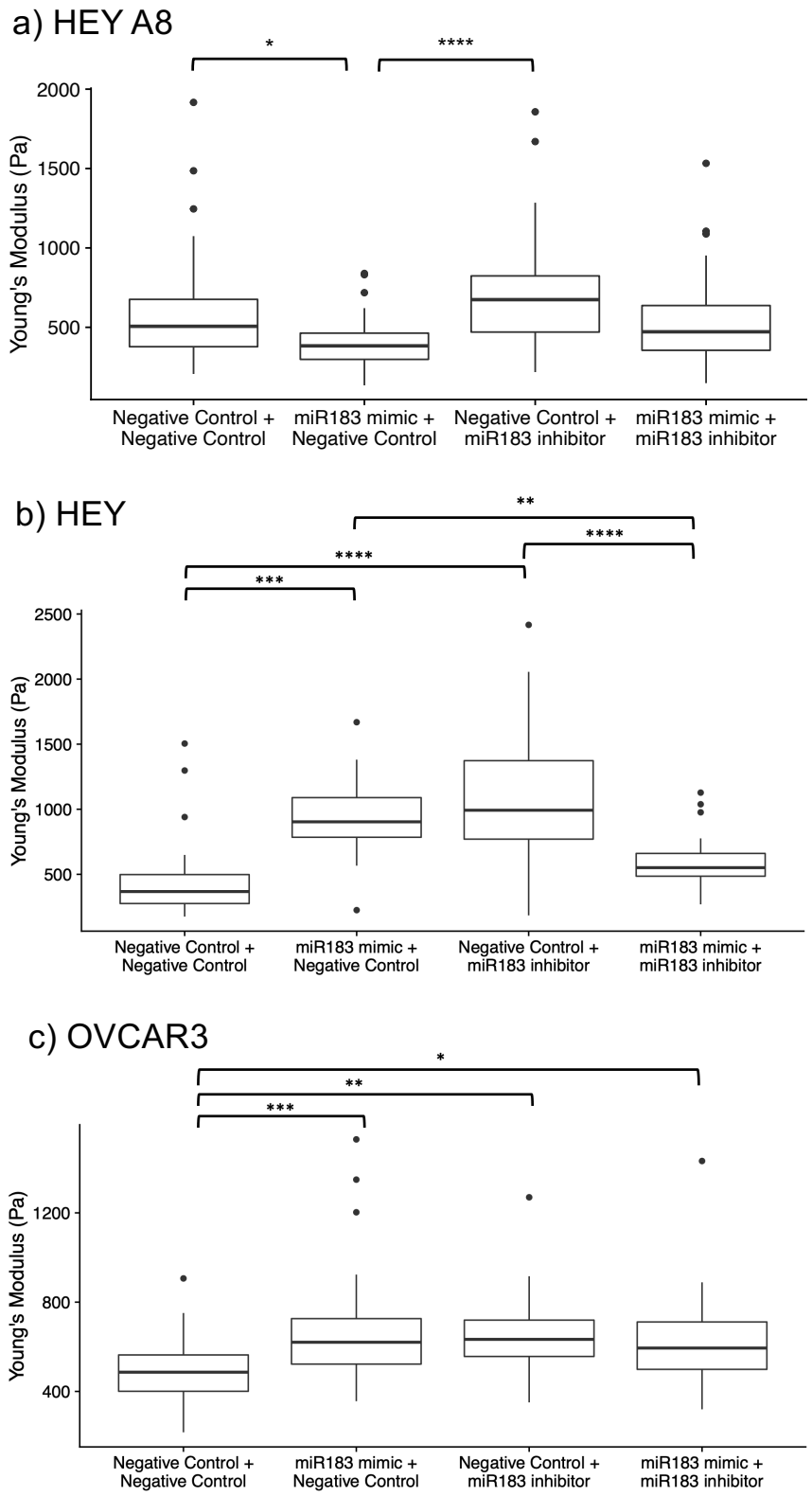

Figure 35 – Changes in *MIR183* expression result in cell stiffness changes in cell type specific manner – Boxplots comparing the Young's modulus of a) HEY A8, b) HEY, and c) OVCAR3 cells treated with combinations of negative control miRNC

mimic, negative control miRNC inhibitor, *MIR183* mimic, and *MIR183* inhibitor for 72 hours. N = 40 for each treatment condition. In HEY A8 cells, *MIR183* mimic decreased cell stiffness while the *MIR183* inhibitor increased cell stiffness. *MIR183* mimic and inhibitor transfection resulted in different responses in HEY and OVCAR3 cell lines (post-hoc Tukey HSD, *, $p < 0.05$, **, $p < 0.01$, ***, $p < 0.001$, ****, $p < 0.0001$)

Although we did observe the stiffness changes in the HEY A8 cell line expected after transfection with the *MIR183* mimics and inhibitors, the expression of the downstream genes associated with this microRNA (*CDH1*, *PTEN*, *VIM*, and *ZEB1*) were not regulated in accordance with the predictions from the network analysis (Figure 34g and Figure 36). For example, we observed a greater than 2-fold increase of *CDH1* expression in the HEY A8 cells when the network analysis predicted *MIR183* was associated with a decrease of *CDH1*. Also, we observed a greater than 2-fold decrease of *VIM* expression in OVCAR3 cells when it was expected to increase. Therefore we demonstrated confirmation of the mechanical regulation hypothesis of *MIR183* as a cell softener, but only in the HEY A8 cell line and not through the hypothesized gene regulation.

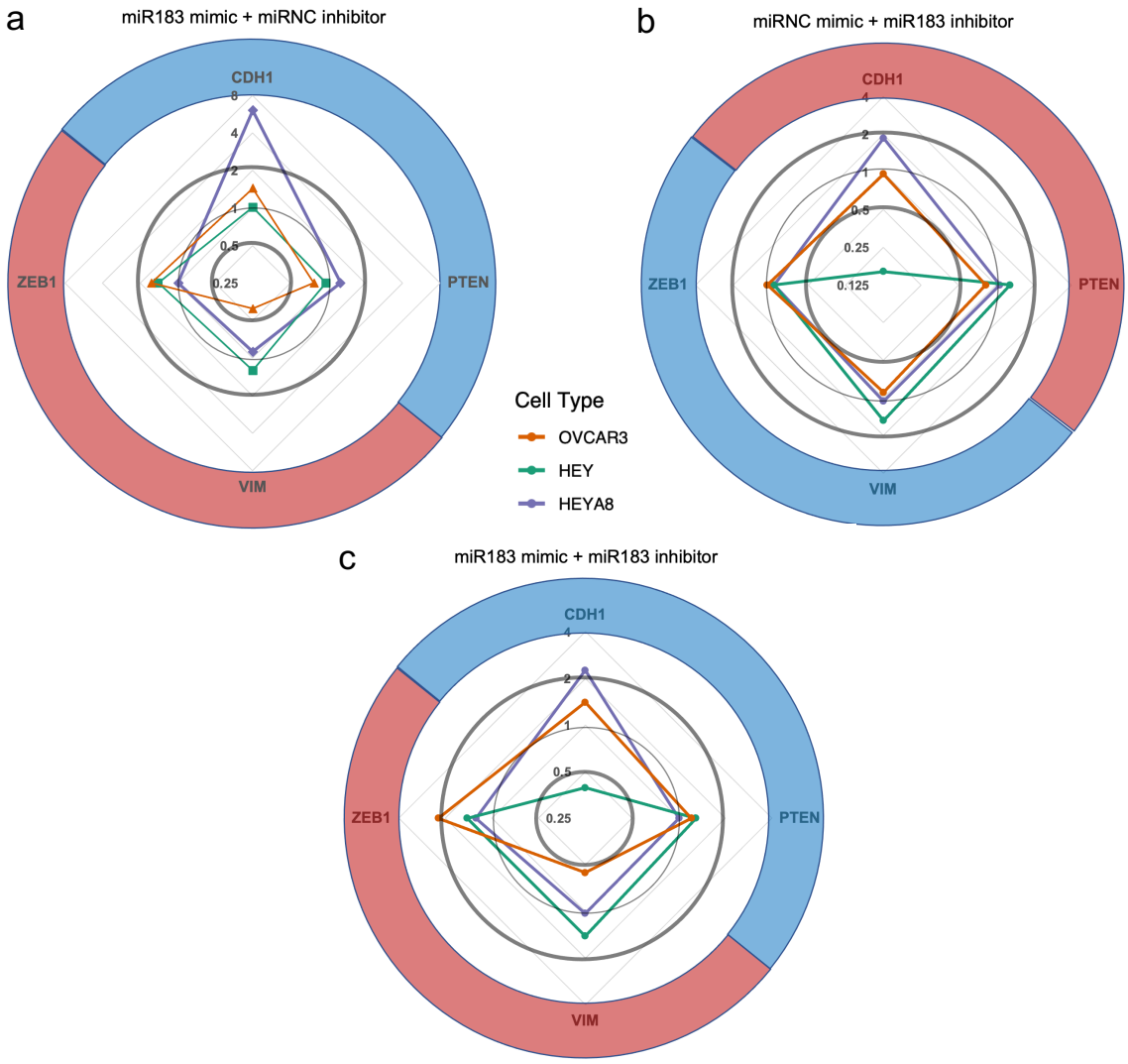

Figure 36 – Gene expression did not change as expected with *MIR183* overexpression and inhibition – Cells were transfected with a) *MIR183* mimic and a negative control miRNA inhibitor, b) *MIR183* inhibitor and a negative control miRNA mimic, or c) both *MIR183* mimic and inhibitor. RT-qPCR was used to detect the fold change differences of expression of predicted gene targets when normalized to housekeeping genes *GAPDH* and *RPL32* and expression levels of cells treated with both mimic and inhibitor negative controls. Genes highlighted in red were predicted to increase with increased *MIR183* expression and genes highlighted in blue were predicted to decrease with increased *MIR183* expression. The two thick circles indicate a 2-fold expression change threshold increase and decrease.

To test another master regulator, we treated HEY A8, HEY, and OVCAR3 cells with the small molecule 17-octadecynoic acid (17-ODYA), an inhibitor of *CYP2J2*, to overexpress the potential master regulator *CD82* with a positive activation z-score that was hypothesized to result in cell stiffening. After 24 hours of treatment with 17-ODYA, all three cell lines demonstrated an increase of *CD82* expression (Figure 37b) and both the HEY A8 and HEY cell lines treated with 17-ODYA were significantly stiffer than cells treated with a DMSO vehicle control ($p = 0.0066$, Welch two sample t-test) (Figure 37a). However, the treated OVCAR3 cells did not experience a significant change in mechanical properties. Investigating the downstream gene targets of 17-ODYA can help explain some of this cell type specificity. For the HEY and HEY A8 cell types, the downstream genes were regulated in the manner hypothesized by the network analysis with an increase of *CD82* expression and decreased expression of *EGFR, MET, MMP9,* and *TGFB* (Figure 37b). However, for OVCAR3 cells, we did not observe the same major reduction in *MMP9* expression, supporting one explanation for the different mechanical response of OVCAR3 cells to 17-ODYA treatment. Finally, we also wanted to investigate the functional effect of 17-ODYA on cell migration. After treatment with 17-ODYA, HEY A8 cells were significantly less migratory than cells treated with a DMSO vehicle control ($p = 0.0033$, Welch two sample t-test) (Figure 37c). This helps support the hypothesis that there is a link between cell softening and a mesenchymal, migratory phenotype.

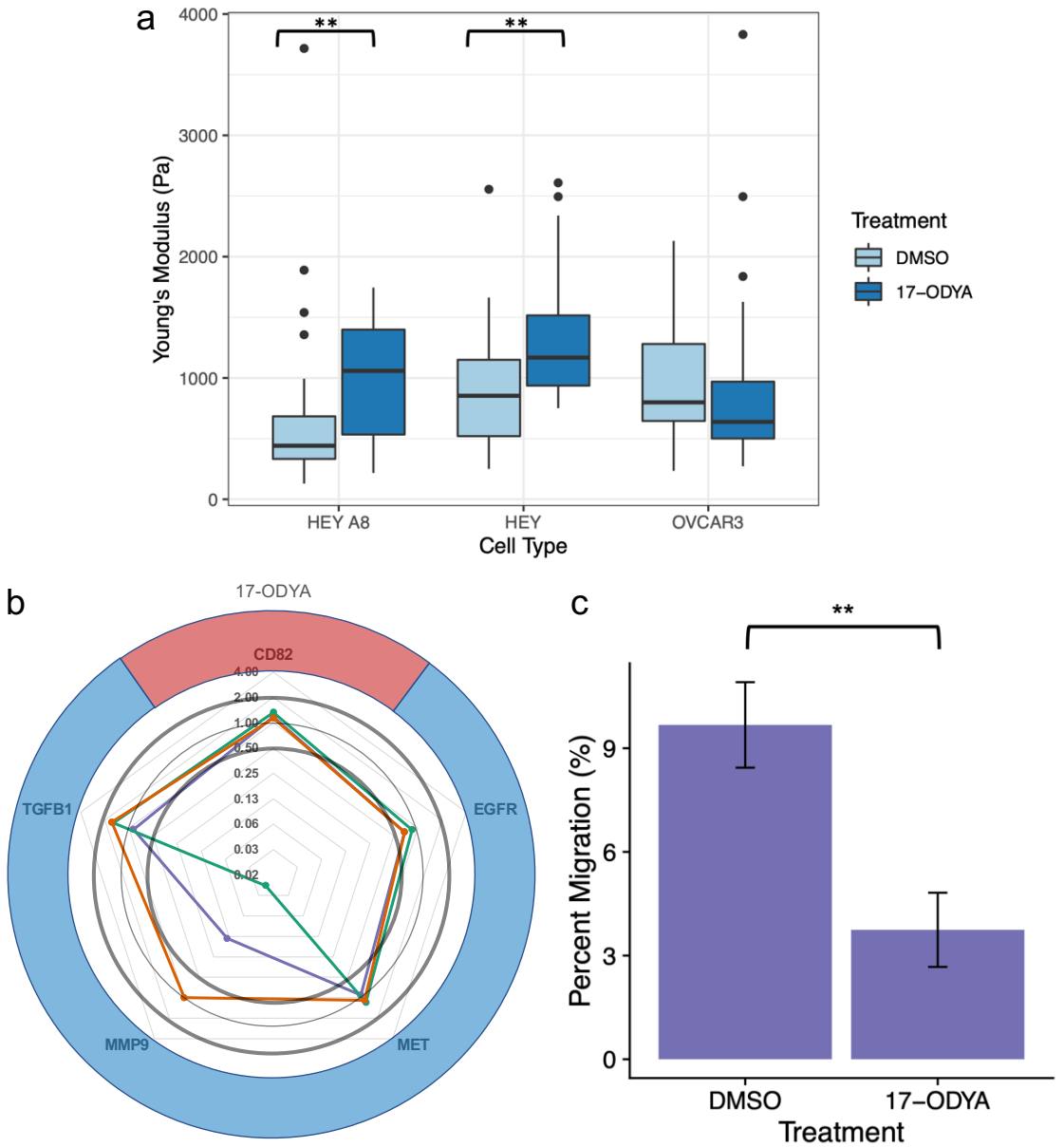

Figure 37 – Cell stiffening 17-ODYA treatment results in gene expression changes that are slight, but consistent with predictions and reduces cell migration – a) Boxplots comparing the Young's modulus of cells treated with a negative control DMSO vehicle and of those treated with small molecule inhibitor and CD82 up-regulator 17-ODYA. n = 40 for each treatment condition. 17-ODYA increased cell stiffness (Welch two sample t-test, **, $p < 0.01$) for HEY A8 and HEY cell lines, but not for the OVCAR3 cell line. b) Cells were treated with 10 μM 17-ODYA for 24 hours and RT-qPCR was used to detect the fold change differences of expression of predicted gene targets when normalized to housekeeping genes *GAPDH* and *RPL32* and expression levels of cells treated with DMSO vehicle control. Genes highlighted in red were predicted to increase with 17-ODYA

treatment and genes highlighted in blue were predicted to decrease with 17-ODYA treatment. The two thick circles indicate a 2-fold expression change threshold increase and decrease. c) Transwell migration assay data demonstrate the decreased migratory ability of the HEY A8 cells treated with 17-ODYA compared to the HEY A8 cells treated with a negative control DMSO vehicle (Welch two sample t-test, **, $p < 0.01$). Cells that migrated through the transwell were fluorescently quantified and normalized using a standard curve.

While we did observe the predicted effect of *MIR183* and 17-ODYA on cell mechanics of some cell types, when we overexpressed *MIR520c*, which was predicted to lead to cell stiffening, we observed the opposite effect for all three cell lines (Figure 38a). Interestingly, when we used qPCR to investigate the expression of the predicted targets of *MIR520c*, we did observe the predicted decrease of *CD44, SERPINE1,* and *ZEB1* expression and an increase in *CDH1* expression the HEY A8 and HEY cell lines (Figure 38b). These individual genes perturbed in isolation may have a smaller effect on cell stiffness than hypothesized or the transfection of *MIR520c* may result in changes of expression of other genes which may dominate the effect on cell stiffness. Interestingly, the OVCAR3 cells displayed a different gene expression change pattern (e.g. an increase in *SERPINE* expression) from the HEY and HEY A8 cell lines and we also observed a smaller change in cell stiffness after treatment with *MIR520c.* While *MIR520c* did not act as a cell stiffener as expected, it does seem to have a generalizable cell softening effect on both the mesenchymal HEY derived cell lines as well as the epithelial OVCAR3.

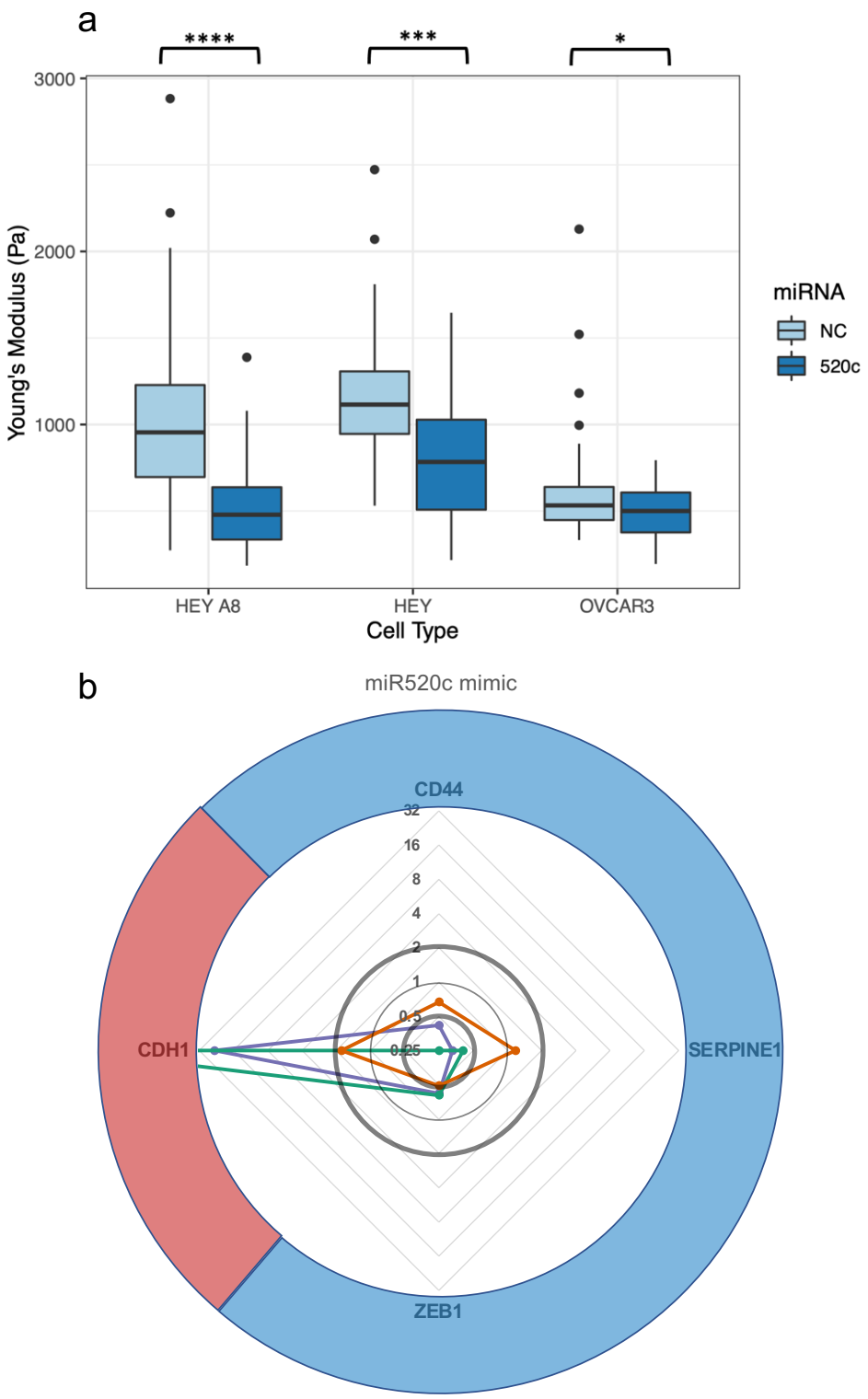

Figure 38 – *MIR520c* acts as a cell softener contrary to prediction, but the gene expression changes are consistent with predicted changes – a) Boxplots comparing the Young's modulus of cells treated with a negative control miRNC and of those treated with miR520c for 72 hours. n = 30-40 for each treatment

condition. *MIR520c* decreased cell stiffness (Welch two sample t-test, *, $p < 0.05$, ***, $p < 0.001$, ****, $p < 0.0001$) for all three cell lines. b) Cells were transfected with *MIR520c* mimic and RNA was extracted from cells 72 hours post-transfection. RT-qPCR was used to detect the fold change differences of expression of predicted gene targets when normalized to housekeeping genes *GAPDH* and *RPL32* and expression levels of cells treated with miRNA mimic negative control. Genes highlighted in red were predicted to increase with *MIR520c* transfection and genes highlighted in blue were predicted to decrease with *MIR520c* transfection. The two thick circles indicate a 2-fold expression change threshold increase and decrease. *CDH1* fold-expression change for HEY cells was greater than 32-fold.

6.4.2 - Network analysis results in hypothesis generation and testing of putative targets that affect cell viscosity

We expanded the use of the single cell correlation dataset to investigate which master regulators could potentially affect the expression of genes significantly correlated with cell viscous properties in order to control cell mechanical properties. We applied a network analysis (see 6.3.2) to the genes significantly correlated with cell viscous time constants, tau1 and tau2, to identify potential upstream targets that affect the expression of these genes. The analysis resulted in 30 and 34 significant predicted master regulators for tau1 and tau2, respectively, 24 of which represent easily targeted transcription factors, enzymes, kinases, growth factors, and other regulatory molecules (Table 5, Table 6, Figure 39, and Figure 40). Regulators with positive activation z-scores are associated with the increase of expression of genes positively correlated with tau1 or tau2 or the decrease of expression of genes negatively correlated with tau1 or tau2; regulators with negative activation z-scores should produce the opposite effect on genes of interest. Interestingly, relying on functional annotations, we

discovered genes positively correlated with tau1 were associated with the functional pathways of cell development and apoptosis while the negatively correlated tau1 genes were associated with cell proliferation. Genes positively correlated with tau2 were associated with cell movement, growth inhibition, and cell signaling, while the negatively correlated tau2 genes were associated with hematological cancers. To investigate whether the predicted regulators could affect the viscous properties as expected, we chose four regulators to test: lacidipine, predicted to increase tau1, *AKT2*, predicted to decrease tau1, *ITGB6*, predicted to increase tau2, and AG879, predicted to decrease tau2.

Table 5 – Network analysis reveals master regulators that could control cell fast viscous time constant (tau1) – Network analysis of genes correlated with cell viscous time constant, tau1, revealed 30 significant potential master regulators, 9 of which are listed here. Bolded potential regulators were experimentally tested.

Tau 1 Master Regulator	Molecule Type	Activation z-score	Network bias-corrected p-value
Lacidipine	Small Molecule	2.449	3.80E-03
NDRG1	Kinase	2.000	8.00E-03
PAX5	Transcription Regulator	2.000	6.00E-04
CCN5	Growth Factor	2.000	5.80E-03
AKT2	Kinase	-2.000	6.40E-02
MMP9	Peptidase	-2.000	4.97E-02
TBX3	Transcription Regulator	-2.000	3.78E-02
WNT5A	Cytokine	-2.236	1.90E-02
CREB3	Transcription Regulator	-2.646	1.86E-02

Table 6 – Network analysis reveals master regulators that could control cell slow viscous time (tau2) – Network analysis of genes correlated with cell viscous time constants, tau2, revealed 34 significant potential master regulators, 15 of which are listed here. Bolded potential regulators were experimentally tested.

Tau 2 Master Regulator	Molecule Type	Activation z-score	Network bias-corrected p-value
ERBB3	Kinase	2.449	1.43E-02
YAP1	Transcription Regulator	2.236	4.64E-02
ITGB6	Other	2.236	3.16E-02
WWTR1	Transcription Regulator	2.121	2.67E-02
mir-221	miRNA	2.111	4.10E-02
SPDEF	Transcription Factor	-2.000	2.19E-02
miR-17-5p	miRNA	-2.000	1.67E-02
miR-450a-5p	miRNA	-2.000	6.70E-03
CADM1	Other	-2.309	1.69E-02
mir-223	miRNA	-2.324	3.00E-02
AG879	Small Molecule	-2.357	1.42E-02
HOXA4	Transcription Regulator	-2.449	2.04E-02
TEAD2	Transcription Regulator	-2.449	1.62E-02
CCN5	Growth Factor	-2.646	2.00E-04
Estrogen Receptor	Transcription Regulator	-2.714	1.00E-04

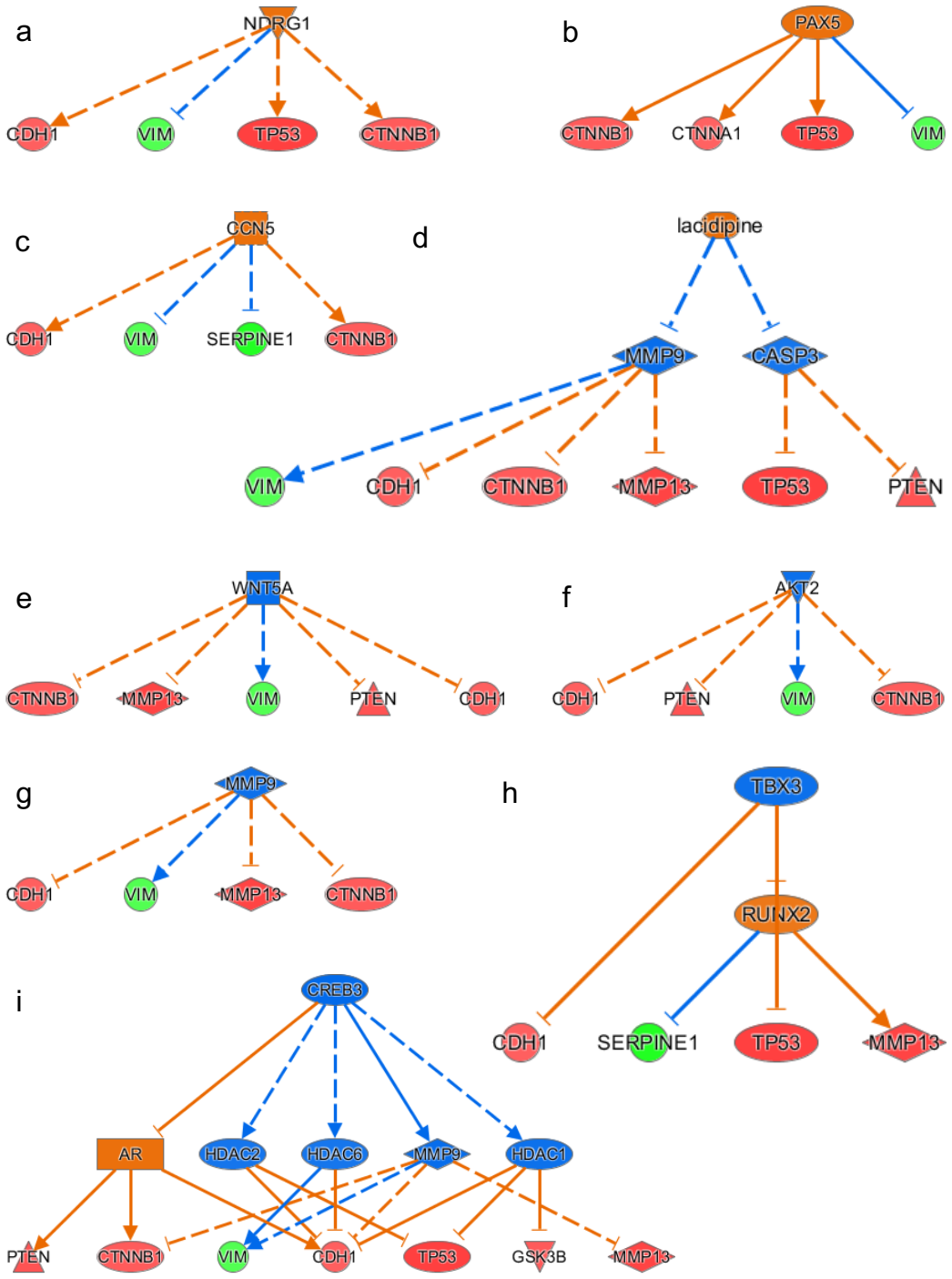

Figure 39 – Network of genes predicted to be under the control of tau1 master regulators – a) *NDRG1*, b) *PAX5*, c) *CCN5*, d) lacidipine, e) *WNT5A*, f) *AKT2*, g) *MMP9*, h) *TBX3*, and i) *CREB3*. Blue nodes represent regulators predicted to increase tau1. Orange nodes represent regulators predicted to decrease tau1. Green nodes represent genes negatively correlated with tau1 and red nodes represent genes positively correlated with tau1.

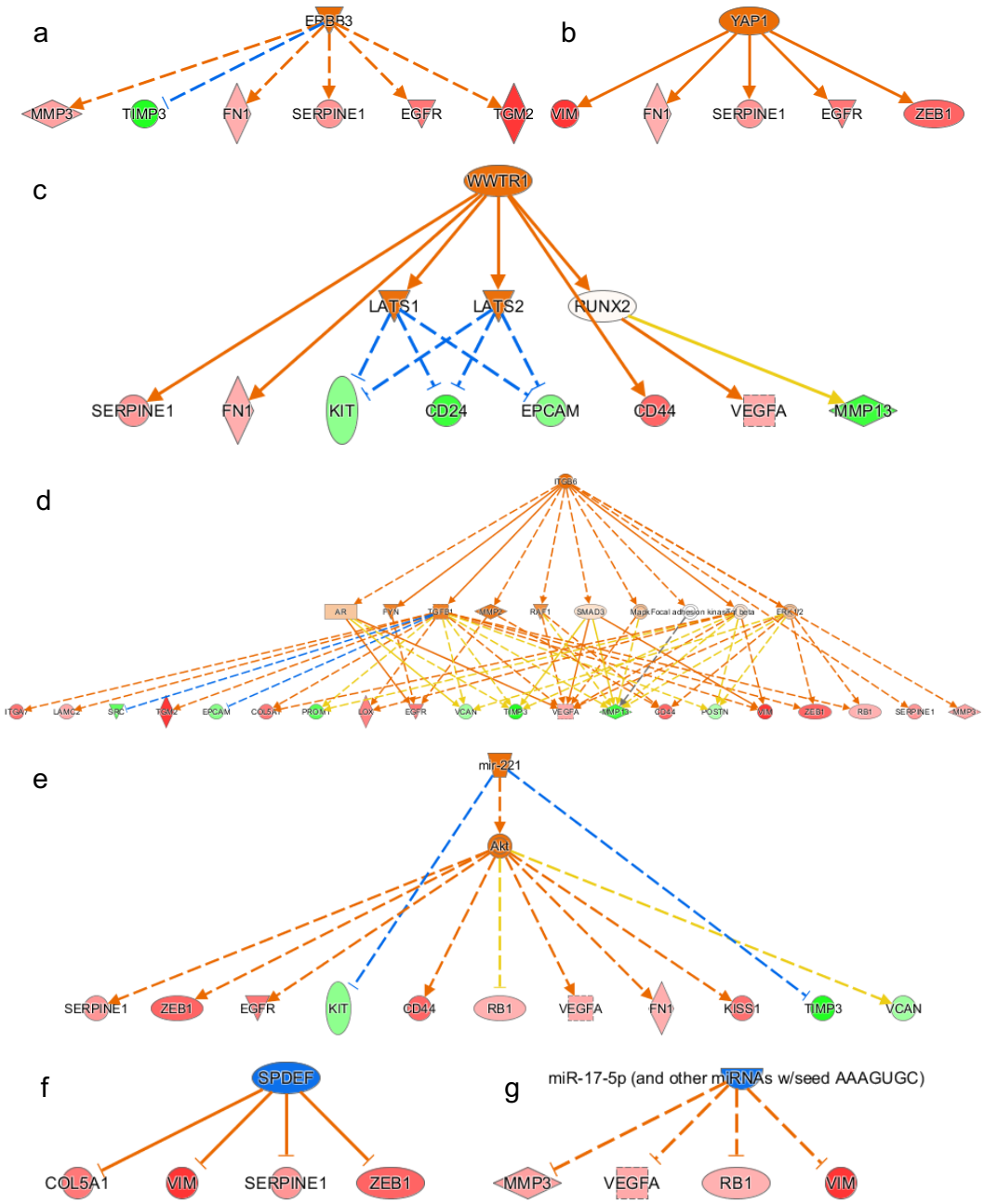

Figure 40 – Network of genes predicted to be under the control of tau2 master regulators – a) *ERBB3*, b) *YAP1*, c) *WWTR1*, d) *ITGB6*, e) mir-221, f) *SPDEF*, g) miR-17-5p, h) *CADM1*, i) mir-223, j) AG879, k) *CCN5*, l) *TEAD2*, and m) estrogen receptor. Blue nodes represent regulators predicted to increase tau2. Orange nodes represent regulators predicted to decrease tau2. Green nodes represent genes negatively correlated with tau2 and red nodes represent genes positively correlated with tau2. Yellow lines represent relationships where a regulator predicted to increase tau2 actually increases the expression of genes negatively correlated with tau2 or decreases expression of positively correlated tau2 genes as well as the opposite for predicted tau2 inhibitor regulators.

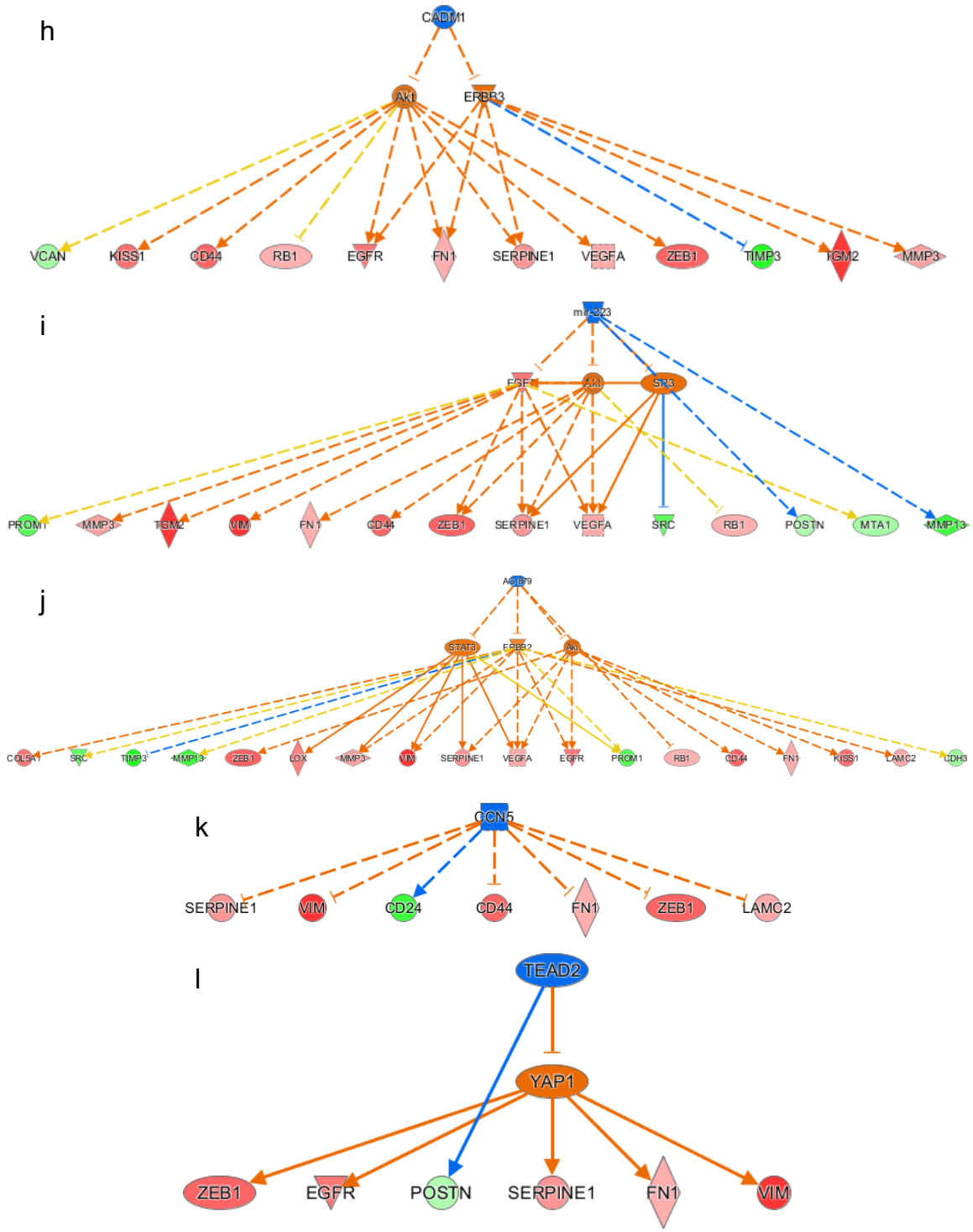

Figure 40 (continued)

m

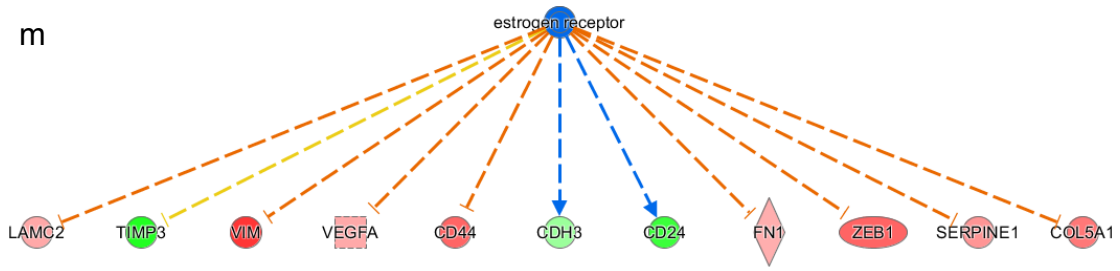

Figure 40 (continued)

The network analysis predicted a decrease in *AKT2* expression would result in an increase of tau1. We treated HEY A8, HEY, and OVCAR3 cells with 10 μM of the small molecule chemical drug BAY11259676 for 24 hours to induce *AKT2* inhibition[195] followed by AFM measurement of the cell viscous properties. After *AKT2* inhibition, we did observe an increase in tau1 as expected in all three cell lines (although the increase in the HEY cell line was not statistically significant) (Figure 41a). There was not a large change in the expression of the majority of the genes correlated with cell viscosity predicted to be associated with *AKT2*, but we did see a large fold-expression change in *CDH1* as expected implying this correlated gene may play a role in connecting cell mechanotype and genotype during *AKT2* inhibition (Figure 41b).

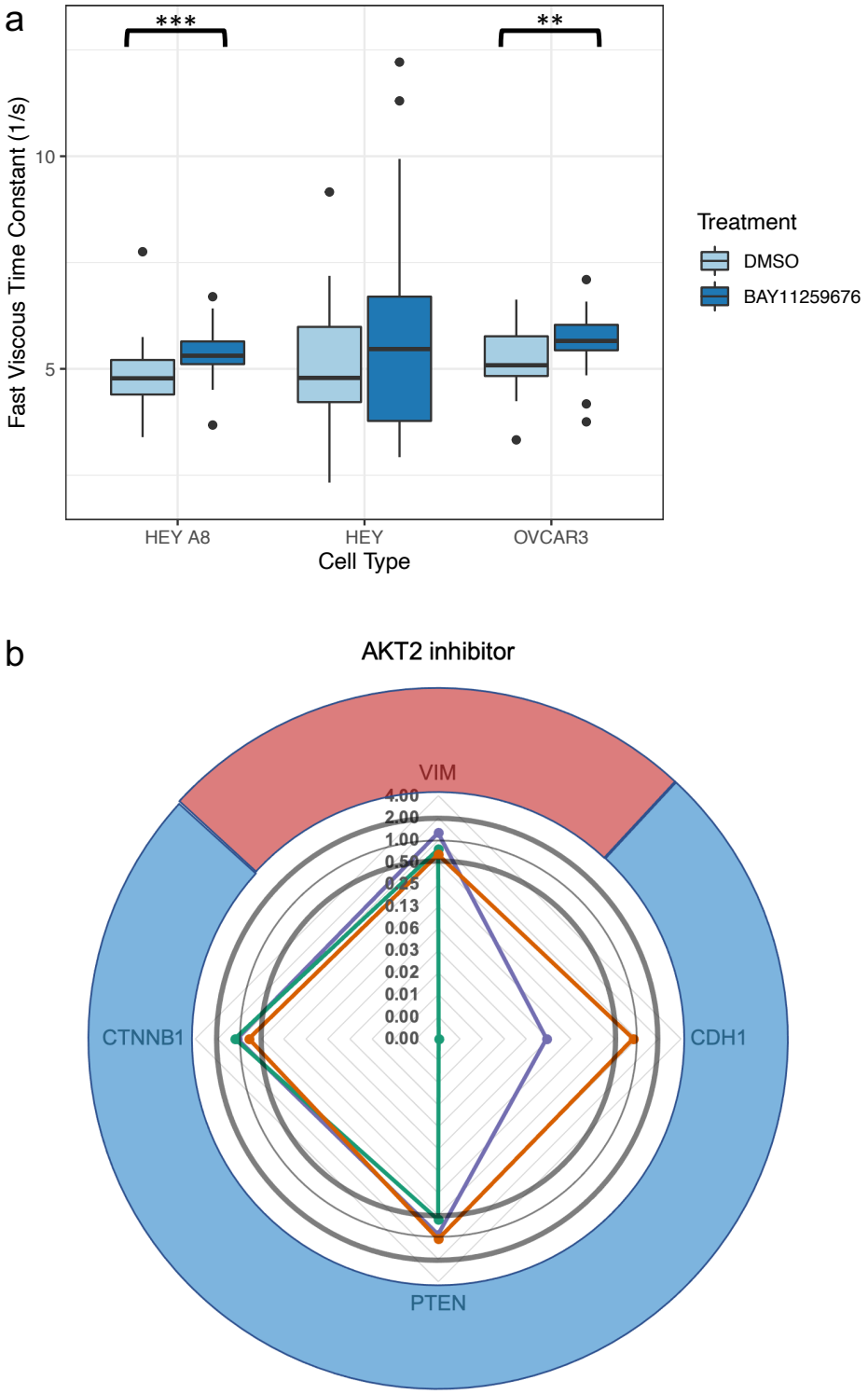

Figure 41 – *AKT2* inhibition results in increase of tau1 as predicted – a) Boxplots comparing the fast viscous time constant, tau1, of cells treated with *AKT2* inhibitor BAY11259676 for 24 hours. n = 40 for each treatment condition. *AKT2* inhibition significantly increased tau1 for HEY A8 and OVCAR3 cells (Welch two

sample t-test, **, $p < 0.01$, ***, $p < 0.001$). b) Cells were treated with BAY11259676 and RNA was extracted from cells 24 hours post-treatment. RT-qPCR was used to detect the fold change differences of expression of predicted gene targets when normalized to housekeeping genes *GAPDH* and *RPL32* and expression levels of cells treated with a vehicle negative control. Genes highlighted in red were predicted to increase with *AKT2* inhibition and genes highlighted in blue were predicted to decrease with *AKT2* inhibition. The two thick circles indicate a 2-fold expression change threshold increase and decrease.

The network analysis predicted the small molecule chemical drug lacidipine treatment would result in an increase of tau1. We treated HEY A8, HEY, and OVCAR3 cells with 10 μM of lacidipine for 24 hours followed by AFM measurement of the cell viscous properties. While we did see a slight, non-significant increase in tau1 in the HEY and OVCAR3 cell lines as predicted, we also observed a significant decrease in tau1 in the HEY A8 cell line, contrary to the predicted effect (Figure 42a). There was further misalignment between the predicted cell behavior and the experimental validation as several genes of interest were not affected as predicted by the IPA pathway (Figure 42b). For example, while we did observe a greater than 2-fold decrease of *MMP9* expression in HEY A8 cells and of *VIM* in OVCAR3 cells as expected, as well as a greater than 2-fold increase of *TP53* for OVCAR3 cells, we also recorded large gene expression changes that occurred in a manner opposite to the prediction, as well as genes that had little fold-change observed at all.

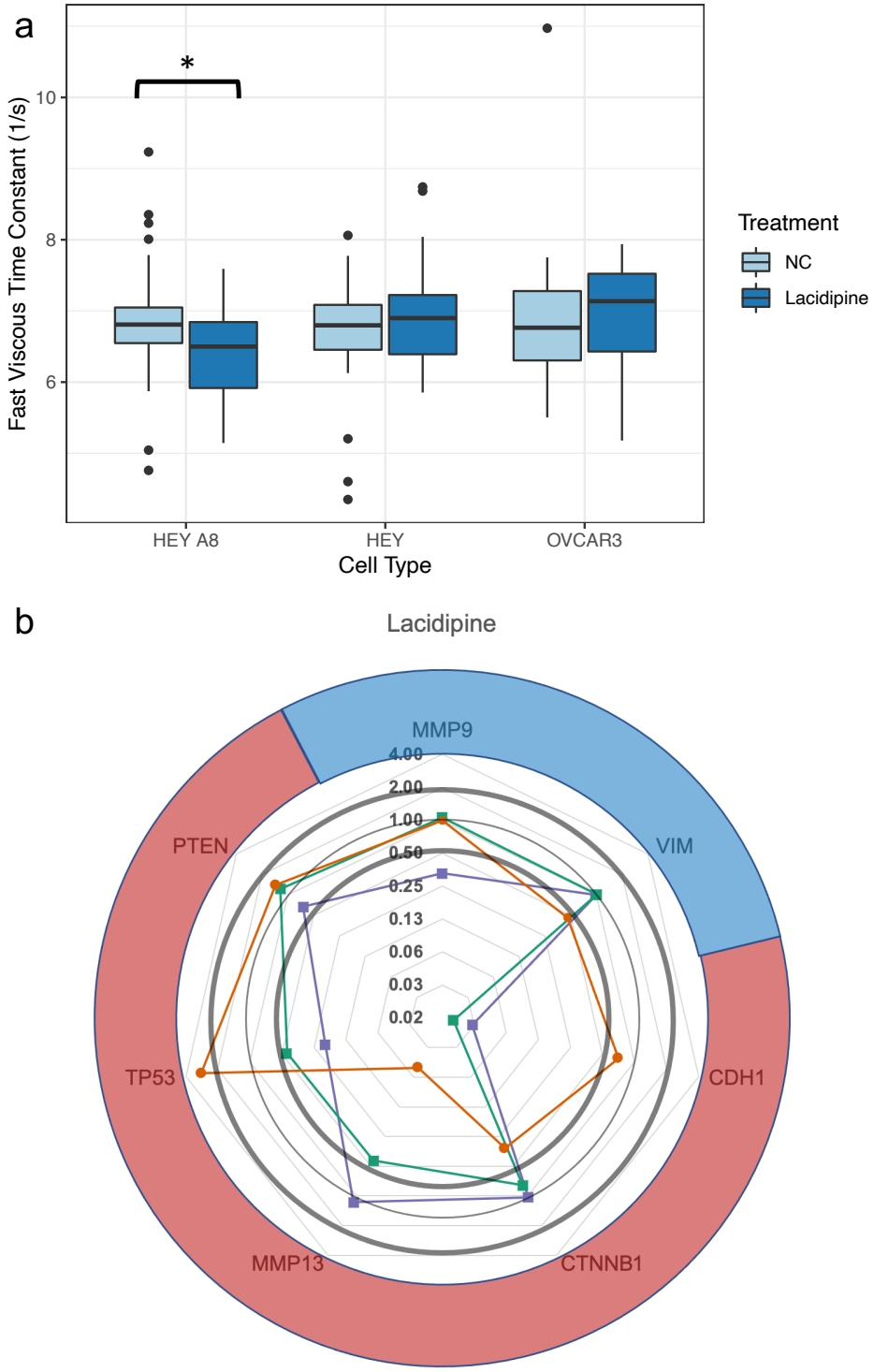

Figure 42 – Lacidipine does not increase tau1 as predicted – a) Boxplots comparing the fast viscous time constant, tau1, of cells treated with a vehicle negative control and lacidipine for 24 hours. n = 30 for each treatment condition. Lacidipine decreased tau1 for HEY A8 cells, but only resulted in a slight, non-significant increase of tau1 for HEY and OVCAR3 cells (Welch two sample t-test,

*, $p < 0.05$). b) Cells were treated with lacidipine and RNA was extracted from cells 24 hours post-treatment. RT-qPCR was used to detect the fold change differences of expression of predicted gene targets when normalized to housekeeping genes *GAPDH* and *RPL32* and expression levels of cells treated with a vehicle negative control. Genes highlighted in red were predicted to increase with lacidipine treatment and genes highlighted in blue were predicted to decrease with lacidipine treatment. The two thick circles indicate a 2-fold expression change threshold increase and decrease.

The network analysis predicted a decrease in *ITGB6* expression would result in the decrease of tau2. We transfected HEY A8, HEY, and OVCAR3 cells with siRNA against *ITGB6* for 48 hours followed by AFM measurement of the cell viscous properties. The knockdown of this integrin resulted in a decrease in tau2 as expected for all three cell lines, although the change was not statistically significant (Figure 43a). While we did see alignment of fold-expression changes for some genes of interest in some cell lines (such as down-regulation of *ITGB6, CD44, TGM2,* and *RB1,* and up-regulation of *SRC*), there were also genes that significantly changed in a manner opposite to the predicted effect of *ITGB6* (such as *EPCAM* down-regulation and up-regulation of *ITGA7*, *LAMC2,* and *MMP3*) (Figure 43b).

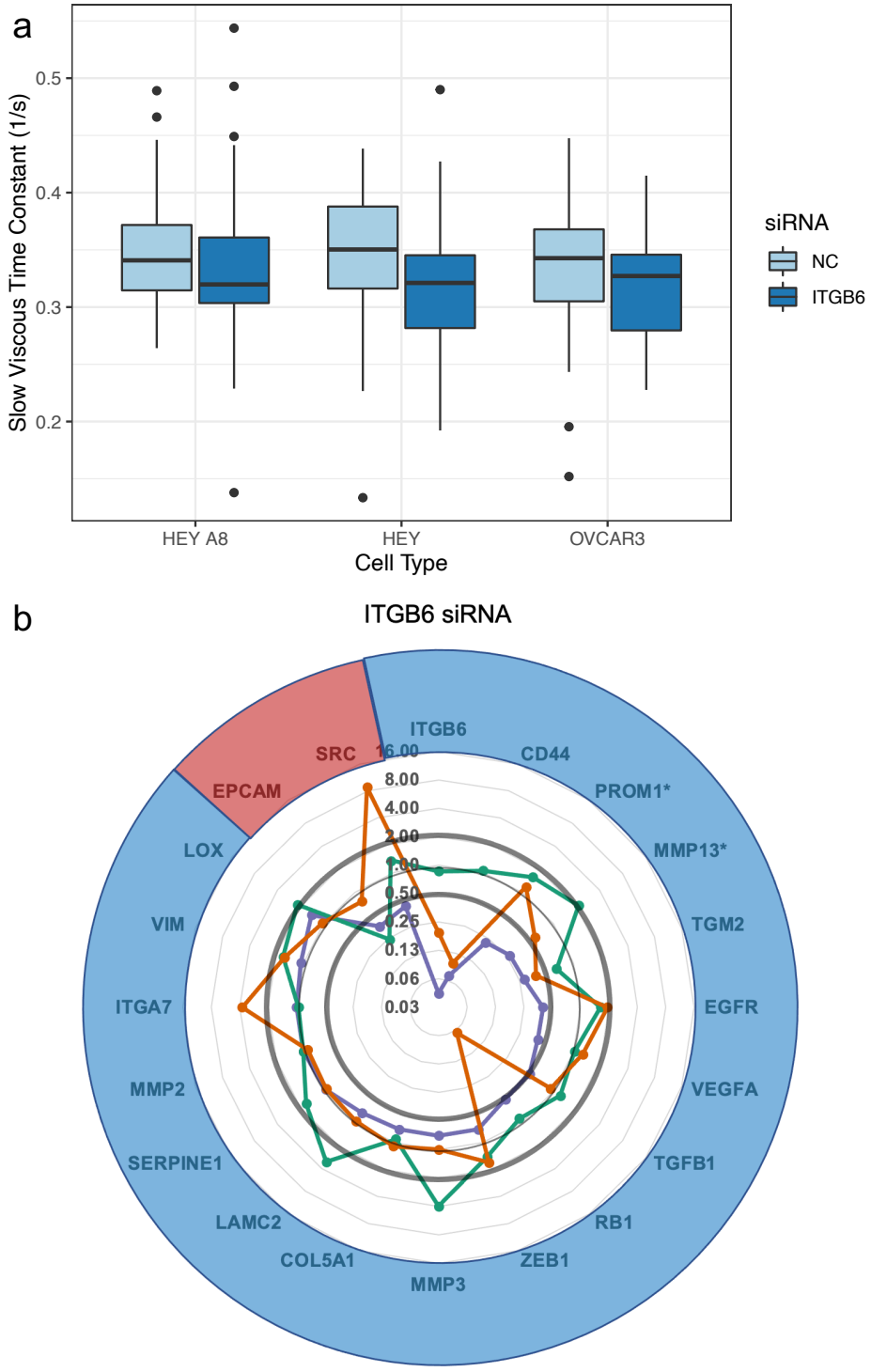

Figure 43 – *ITGB6* knockdown leads to slight, but not significant, decrease in tau2 as predicted – a) Boxplots comparing the slow viscous time constant, tau2, of cells transfected with siRNA against *ITGB6* for 48 hours. n = 40 for each treatment condition. *ITGB6* knockdown resulted in a slight, but not significant decrease in tau2 as predicted (Welch two sample t-test, $p > 0.05$). b) Cells were transfected

with siRNA against ITGB6, and RNA was extracted from cells 48 hours post-transfection. RT-qPCR was used to detect the fold change differences of expression of predicted gene targets when normalized to housekeeping genes *GAPDH* and *RPL32* and expression levels of cells treated with a vehicle negative control. Genes highlighted in red were predicted to increase with *ITGB6* inhibition and genes highlighted in blue were predicted to decrease with *ITGB6* inhibition. The two thick circles indicate a 2-fold expression change threshold increase and decrease. Asterisks next to gene names denote genes negatively correlated with tau2 that were predicted to be downregulated.

The network analysis predicted AG879 treatment would result in a decrease of tau2. We treated HEY A8, HEY, and OVCAR3 cells with 10 μM of the small molecule chemical drug AG879 for 24 hours followed by AFM measurement of the cell viscous properties. We observed a significant decrease in tau2 as predicted in HEY A8 cells, while we also saw a slight tau2 decrease in HEY cells, but little change in mechanics for the OVCAR3 cells after treatment (Figure 44a). This may be partially explained by the gene expression change results in which we saw a number of genes in the HEY A8 and HEY cells decrease in expression as predicted, while OVCAR3 cells had an increase in expression in those particular genes, such as *RB1* and *KISS1* (Figure 44b). Interestingly, although the network predicted a few genes that are negatively correlated with tau2, such as *SRC, PROM1,* and *MMP13,* would be downregulated by AG879, the predicted tau2 inhibitor, when we experimentally tested the expression of these genes, we saw their expression increase. While the molecular expression does not align with the network prediction, we did observe a reduction in tau2 as predicted.

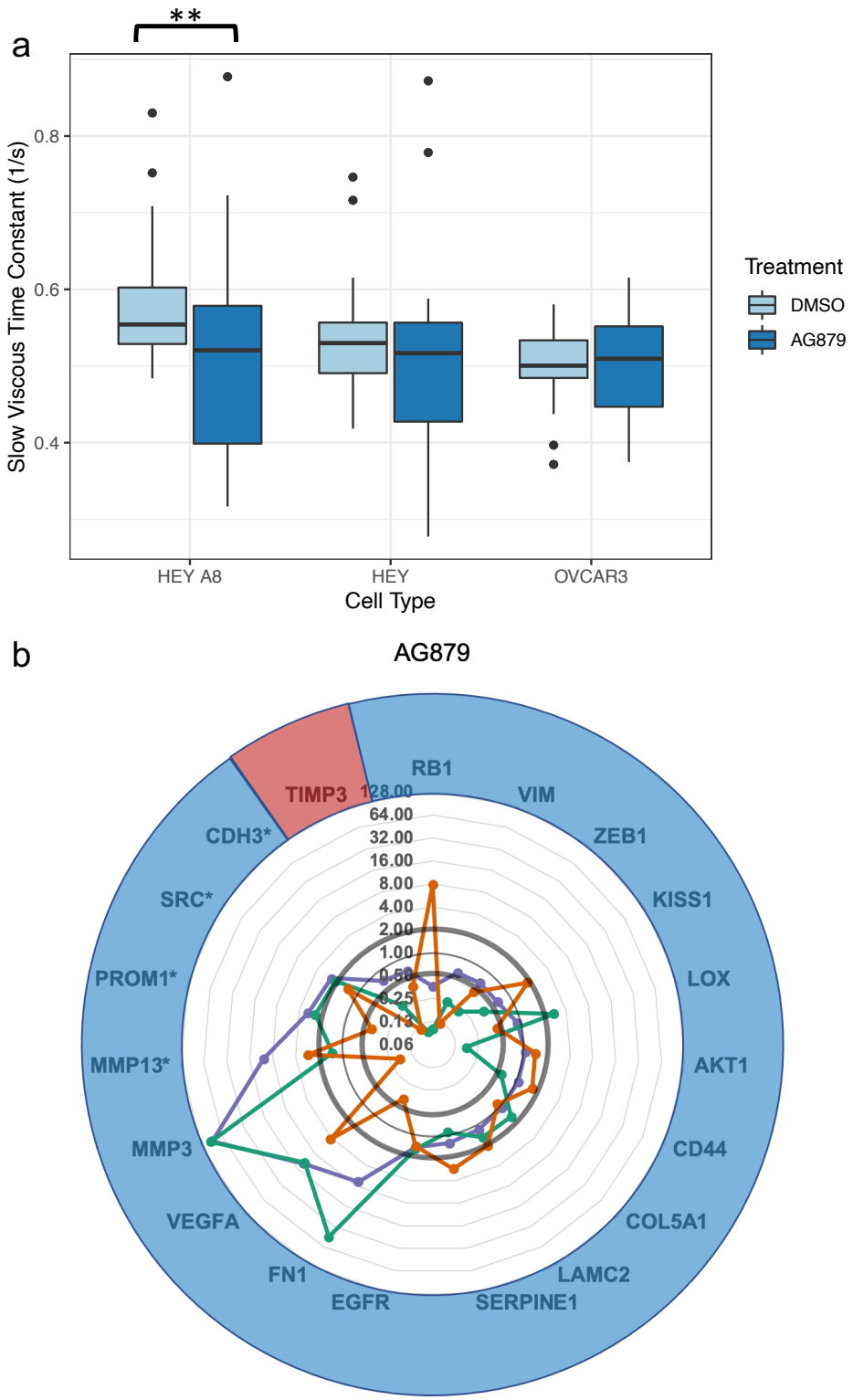

Figure 44 – AG879 decreases tau2 as predicted for the HEY A8 cell line – a) Boxplots comparing the slow viscous time constant, tau2, of cells treated with small molecule chemical drug AG879. n = 40 for each treatment condition. AG879 resulted in a significant decrease in tau1 as predicted for the HEY A8 cell line

(Welch two sample t-test, **, $p < 0.01$). There was a non-significant decrease in tau1 observed in the HEY cells, and little change observed in the OVCAR3 cell line. b) Cells were treated with AG879 and RNA was extracted from cells 24 hours post-transfection. RT-qPCR was used to detect the fold change differences of expression of predicted gene targets when normalized to housekeeping genes *GAPDH* and *RPL32* and expression levels of cells treated with a vehicle negative control. Genes highlighted in red were predicted to increase with AG879 treatment and genes highlighted in blue were predicted to decrease with AG879 treatment. The two thick circles indicate a 2-fold expression change threshold increase and decrease. Asterisks next to gene names denote genes negatively correlated with tau2 that were predicted to be downregulated.

6.5 – Discussion

From the network analysis, we identified several putative gene targets that affect multiple genes significantly correlated with cell stiffness and with cell viscous properties. We found that the overexpression of *MIR183* would lead to cell softening in the HEY A8 cell line. *MIR183* has been found to be overexpressed in most breast cancers and has been categorized as an oncogene in multiple cancer types for its contribution to increased cell proliferation and migration[196-198]. Additionally, in ovarian cancer, downregulation of the microRNA has been shown to inhibit cell proliferation, migration and invasion[199]. However, the role of *MIR183* in metastasis is complex, with some groups identifying the microRNA as a tumor suppressor in osteosarcoma and lung cancer, with observation that overexpression of the miR resulted in transition to a more epithelial and less metastatic phenotype[200,201]. Interestingly, the change in cell stiffness seems to not be mediated through the exact genes predicted by the network analysis. We anticipate that the biological effect of miRNAs can be cell line dependent since

the network is based upon reported data from many different cell types. Moreover, the expression of genes is time dependent; while we chose each analysis timepoint when change in expression could reasonably be expected to occur, it is possible the relevant changes were missed by our measurements. Finally, the action of miRNA can be both dose dependent and non-monotonous, therefore alterations in dosing may change the observations[202]. Our work demonstrating *MIR183*'s role in cell softening in the metastatic, mesenchymal HEY A8 cell line supports the connection between a soft mechanotype, expression of genes in the EMT pathway and a more metastatic phenotype.

Additionally, we identified 17-ODYA as a cell stiffening small molecule inhibitor through its minor up-regulation of *CD82* for the mesenchymal cell lines HEY and HEY A8. The metastasis suppressor gene *CD82* has been implicated in several cancers to inhibit cell migration through restricting cell protrusion and retraction[203,204]. Both *CD82* and *MMP9* expression increase with the treatment of the epoxygenase inhibitor 17-ODYA which has also been associated with inhibition of cell migration and invasion[192]. We do note the lack of mechanical effect of 17-ODYA treatment on the epithelial OVCAR3 cell line. One explanation may involve the cell state and nascent gene expression levels prior to treatment. For example, 17-ODYA resulted in large increases of *CDH1* in the HEY and HEY A8 cell lines. However, E-Cadherin is already highly expressed in the epithelial OVCAR3 cell line (Figure 11) so 17-ODYA perturbation would be expected to produce less of a practical effect on this cell line. The ability of 17-ODYA to stiffen the mesenchymal

cell lines and reduce their migratory phenotype suggests this inhibitor represents a potential therapeutic agent for metastasis prevention through a genomechanical pathway.

This study was the first to explore the relationship between the viscosity of cells and the underlying molecular mechanisms that affect cell mechanics. The gene annotation software, DAVID, was used to explore the functions of genes correlated with the slow and fast viscous time constants, tau1 and tau2. We investigated the following KEGG pathways for tau2-correlated genes: focal adhesion formation and *PI3K-AKT* signaling[205]. We wanted to identify upstream regulators that modulated several of the genes significantly correlated with tau2. In the focal adhesion pathway, we observed that changing the interaction of two molecules, *FAK* and *SRC*, could impact the promotion of cell migration. Specifically targeting *SRC* would downregulate the pathway as it is required for *FAK* proteolysis and focal adhesion disassembly during v-*Src* transformation[206]. *FAK* could be a key component that can be regulated to cause significant change to cell mechanics, cell motility, and metastasis. *FAK* also controls multiples downstream genes which, if knocked down, would cause a significant decrease in gene expression of pathways related to cell motility and migration. Integrin alpha and beta are heterodimers that together control *FAK*, which made *ITGB6* particularly interesting as a putative master regulator. The downregulation of *ITGB6* could cause a decrease in *FAK* activity and other downstream migration-related genes. While we did see a slight reduction in cell viscous properties after

knockdown of *ITGB6,* we may see even greater effect on mechanics and possibly also migratory phenotypes if we targeted both components of the integrin heterodimer. One study found that the heterodimer of *ITGAV* and *ITGB6* are required for neoplastic invasion of epidermal squamous cell carcinoma[207]. The *PI3K-AKT* pathway involved the viscosity-correlated genes *PTEN, TP53,* and *GSK3B*. *GSK3B* was identified as an important regulator of cancer invasion, chemoresistance, and tumor cell stemness[208]. Upregulating the tau2-correlated genes could help affect the downstream genes in the *PI3K* pathway. *AKT2* inhibition showed great promise for increasing cell viscosity as measured by the tau1 parameter in multiple cell lines. Evaluating whether these viscosity changes have functional relevance in cell migration could be further explored. *AKT2* shares the same effect on *FAK* in the focal adhesion pathway, causing a significant decrease in tumor growth and metastasis. *AKT2* knockdown was observed in mice to accelerate tumor development by *p53* and *PTEN* pathways, therefore we may anticipate that increased viscosity would correlate with increased migratory capacity[209]. Yet we can anticipate the mechanical alterations will be affected by a number of additional factors, as studies of isoform-specific inhibitors via microRNAs show altered activities of downstream signals from the Akt family, including *AKT1, AKT2,* and *AKT3*[210]*.* Thus, the individual or combined knockdown of the Akt kinase could be combined to achieve heterogenous tumor response[209,211].

Overall, this study tested several hypotheses linking cell mechanical properties to the expression of genes that play a role in ovarian cancer metastasis. We identified a number of cell line specific regulation points that have an effect on cell stiffness (like *MIR183* and 17-ODYA) and on cell viscous properties (like *AKT2, ITGB6*, and AG879). Further study into why these regulators have different effects in different cell lines remains. Alternatively, different models for the network analysis may result in alternative predicted relationships that more accurately reflect mechanical and gene expression measurements. This chapter represents just a start of the exploration of the rich linked dataset generated in chapter 3.

CHAPTER 7 – EXPLORING THE RELATIONSHIP BETWEEN CELL PHENOTYPE AND MECHANOTYPE BEYOND THE METASTATIC CONTEXT

7.1 – Introduction

While the previous 4 chapters have specifically investigated the relationship between cell genotype, phenotype, and mechanotype in the context of ovarian cancer cell lines of varying metastatic potential, cell mechanics play an important role in a number of different biological processes. In this chapter, I will explore the relationship between cell mechanical properties and cell behavior in many different contexts, specifically broken down into three groups: 1) healthy cell behaviors, 2) cell behaviors associated with a diseased state, and 3) behaviors of cells undergoing various types of cell death. A few of these topics relate back directly to the investigations described in the previous 4 chapters, and all support the importance of cell mechanics to our better understanding of cellular processes and the development of therapeutics that could specifically target the intersection of cell mechanics, molecular mechanisms, and cell behavior.

7.2 – Mechanical Properties of Healthy Cells

7.2.1 Viscous properties of cells under rapid compression

In addition to using ridged microfluidic devices for the sorting of cells based on mechanical properties as described in chapters 4 and 5, the Sulchek Lab has

also investigated the use of similar ridged devices at much higher flow rates to induce a rapid compression of cells. Under rapid compression (deformation onset of 10–100 μs and duration of ≈1 ms), cells demonstrate a viscoelastic behavior that actually results in cell volume loss and recovery which can be utilized for cargo delivery referred to as volume exchange for convective transfection (VECT)[131,212] (Figure 45). Cell viscous properties vary between cell types and play an important role in cell volume loss, and thus transfection efficiency, using the VECT device. Because a more viscous cell is unable to expand as quickly under compression, it was hypothesized and observed to exhibit larger volume loss than a less viscous cell.

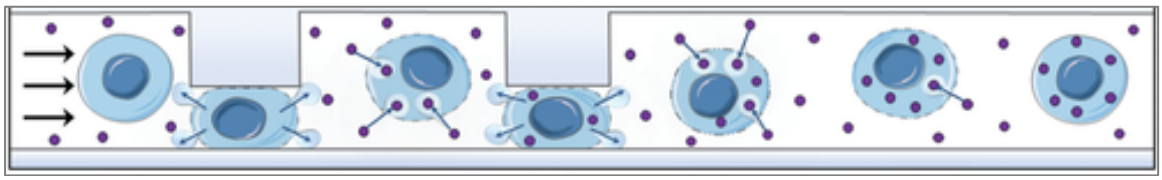

Figure 45 – Schematic of cell permeabilization and volume loss, subsequent recovery, and repeated volume exchange with compressions[212]

To investigate the relationship between cell volume loss under rapid compression and cell viscoelastic properties, we used AFM to measure the viscous rate constant of multiple cell lines (both leukocyte and epithelial cell types) (Figure 46). This AFM data, together with high-speed video cell compression data of different cell types in the VECT device, was used to parameterize the relationship between cell viscosity and elasticity during deformation. The dimensionless

Ericksen number describes the ratio between viscous forces and elastic forces of the cell, Equation 9. The cell is modeled as a Maxwell viscoelastic material with dynamic viscosity $\mu = T_v E$, where E is the Young's Modulus and T_v is the viscous time constant as measured by AFM. Viscous force is dependent on cell compression velocity ($V = \Delta L T_c^{-1}$ where T_c is the compression time measured by video analysis) and a characteristic length (L is the relaxed cell diameter, $\Delta L = L$ – compression gap). The elastic force is defined by Young's Modulus and A, cell area.

$$Ericksen\ number = \frac{Viscous\ Force}{Elastic\ Force} = \frac{\mu V L}{EA} = \frac{T_v}{T_c}\frac{L\Delta L}{A} \qquad \text{Equation 9}$$

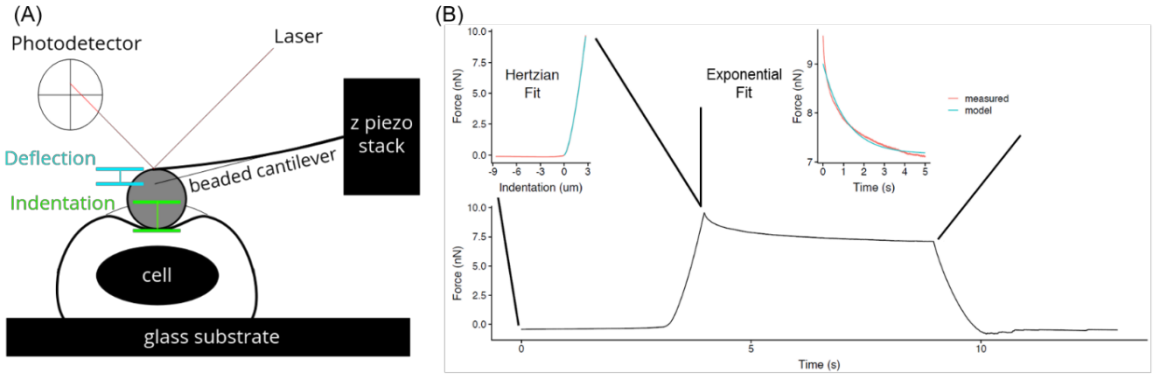

(C)	K562[25]	K562F[22,25]	HL-60[25]	HEY	OVCAR
Mean viscous rate constant T_v^{-1} [s^{-1}]	17.7	47.5	8.91	0.99	0.77
Viscous rate constant SD [s^{-1}]	13.7	27.9	4.6	0.11	0.11
Number of cells measured	69	42	63	100	90
Mean viscous time constant T_v [s]	0.056	0.021	0.112	1.01	1.3
Mean Young's modulus [kPa]	0.40	23	0.86	0.38	0.60
Young's modulus SD [kPa]	0.22	13	0.22	0.20	0.31

Figure 46 – AFM measurement of leukocyte and epithelial cell mechanical properties – a) Schematic of AFM detection of a laser reflected off a deflected cantilever. The cantilever bends when brought in contact with a sample, causing the laser spot on the photodetector to move. Cell indentation can be extracted

by subtracting the amount of deflection by the position of the back of the cantilever. b) The initial approach portion of the force curve was fit to the Hertzian contact model to calculate cell Young's modulus. The dwell portion of the force curve was fit to an exponential decay curve to extract the viscous rate constant. c) Table of AFM measurements taken for HEY and OVCAR cells. Values for K562, K562F, and HL-60 cells were taken from published AFM data[143,144].

Comparing this Ericksen number across multiple cell types with the observed volume change of cells revealed a sigmoidal relationship where highly viscous cells experience higher volume loss compared to cells with a low ratio of viscous to elastic forces (Figure 47). Under rapid deformation where $T_c \ll T_v$, cells have to compress at a time scale too fast for active remodeling of the cytoskeleton and the attached cellular membrane, resulting in an increase of internal fluid pressure, membrane permeabilization, and volume exchange. This cell deformation behavior is governed by the viscoelastic properties of the whole cell and not individual cytoskeletal or membrane components. By understanding the mechanical properties of different cell types of interest, we could predict the transfectability of certain cell types and adjust our device operation parameters to maximize the ratio of viscous and elastic forces on the cells and total cell volume exchange.

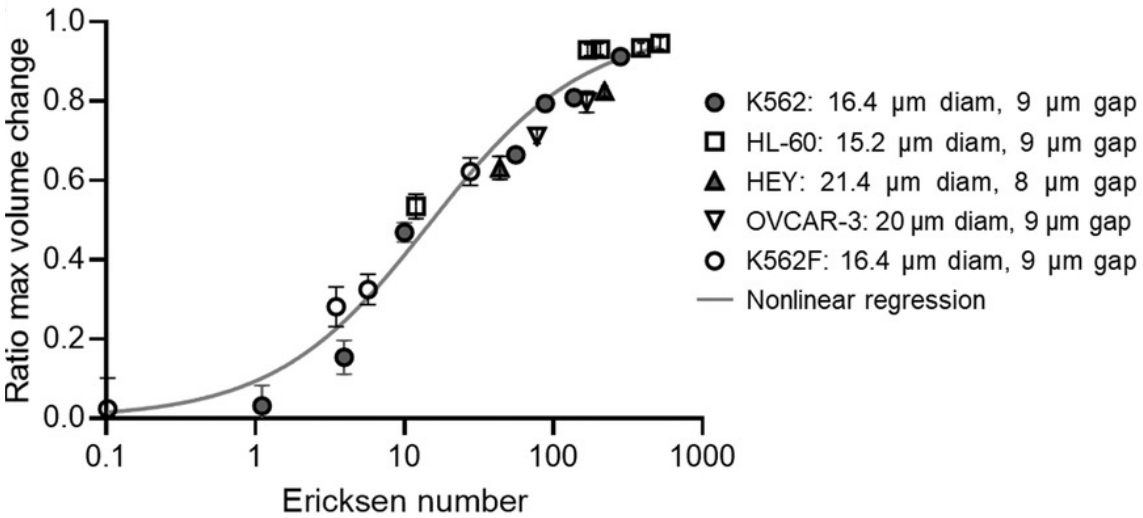

Figure 47 – Relationship between cell viscoelastic properties and volume loss – A plot of volume change for multiple cell types shows sigmoidal relation with Ericksen number (*Er*). Cell types include leukocyte cell lines K562, HL-60, and formaldehyde-treated K562F, and epithelial cell lines HEY and OVCAR-3. n ≥ 25, bars represent standard error.

7.2.2 Mechanical characterization for peripheral blood mononuclear cell sorting

With the rapid expansion in use of immunotherapies to treat many cancer types, such as CAR-T and other adoptive cell therapies, technology development to isolate, identify, and preserve therapeutic cells is becoming a critical need to support the development of these treatments. A label-free and reagent-free approach to T cell isolation would simplify scaleup steps required while maintaining the integrity of the cells. Peripheral blood mononuclear cells (PBMCs) are a common source of immune cells that consist of monocyte and lymphocyte cell types. The separation of lymphocytes from PBMCs is a necessary step to prepare blood specimens for diagnostic assays or isolate immune cells for autologous cell

therapies. Our group has worked on using the stiffness-based sorting platform described in chapters 4 and 5 to separate these cell types for further downstream applications. Lymphocytes were found to be significantly stiffer (p = 0.0051, Welch two sample t-test) than monocytes with mean Young's Modulus values of $1495 \pm 569\, Pa$ and $931 \pm 890\, Pa,$ respectively (Figure 48a and Figure 48f). However, lymphocytes were also determined to be significantly smaller (p = 1.75×10^{-12}, Welch two sample t-test) than monocytes with cell diameters of $7.6 \pm 0.75\, \mu m$ and $9.3 \pm 0.77\, \mu m$, respectively (Figure 48b and Figure 48f). Because of the large difference in cell size, we chose to sort lymphocytes and monocytes by size instead of cell stiffness. Furthermore, we observed a difference in adhesion force between each cell type and a negatively charged polystyrene bead with monocytes being significantly more adhesive than lymphocytes (Figure 48c). However, no visible difference was observed in cell adhesion to the PDMS device or glass surfaces during device operation. We observed no difference in cell viscous properties for the monocyte and lymphocyte populations (Figure 48d and Figure 48e). Using this mechanical characterization, we were able to optimize the operation parameters for our device to achieve a 5-fold enrichment for monocytes and a 4.5-fold enrichment for lymphocytes. This process could be further optimized and expanded using the principles of multiplexing described in chapter 4 to allow for high-throughput isolation of either lymphocytes or monocytes from PBMCs for downstream therapeutic applications.

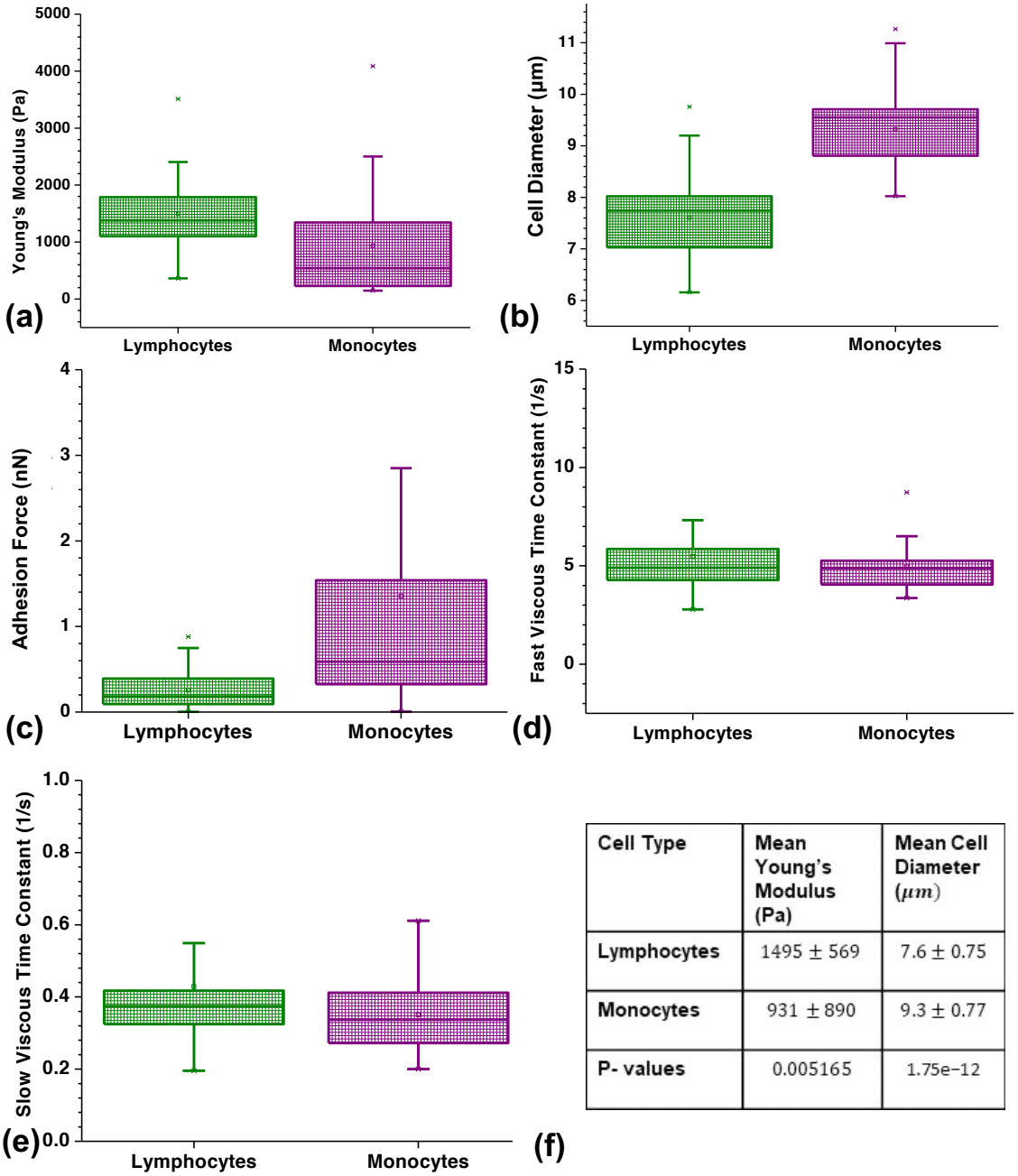

Cell Type	Mean Young's Modulus (Pa)	Mean Cell Diameter (μm)
Lymphocytes	1495 ± 569	7.6 ± 0.75
Monocytes	931 ± 890	9.3 ± 0.77
P- values	0.005165	1.75e−12

Figure 48 – Biophysical properties of PBMCs characterized using AFM – a) Boxplots depicting the comparison of each cell type's Young's modulus, b) cell diameter, c) adhesion force, d) fast viscous time constant, and e) slow viscous time constant. f) Table showing the most significant differences in mechanical properties to be used for sorting.

7.2.3 – Embryonic stem cells stiffen as they differentiate

For tissue engineering and regenerative medicine applications, the ability to use cells with pluripotent and proliferative properties is highly sought after. However, embryonic stem cell (ESC) cultures can be quite heterogenous containing both pluripotent and differentiated cell types. We have proposed the use of cell biomechanics as a marker for stem cell differentiation[24,213-215]. Using a mouse embryonic stem cell line and a LIF removal differentiation protocol, our group observed a significant increase of cell stiffness after just 1 day of differentiation (Figure 49)[125]. We also observed increase in cell size and decrease in cell circularity with stem cell differentiation.

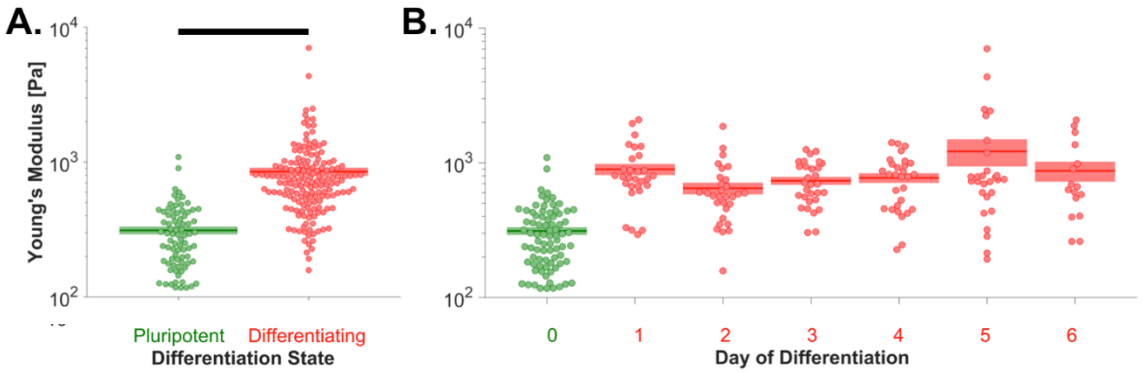

Figure 49 – Embryonic stem cells become stiffer during differentiation – a) Pluripotent ESCs were significantly softer than the pool of all differentiating cells ($p<10^{-6}$). b) Cellular Young's modulus increased after 1 day of differentiation, and no substantial subsequent change was observed through 6 days of differentiation, indicating the potential utility of Young's modulus as an early marker of ESC differentiation[125].

To further understand the observed morphology changes, cells after 0–6 days of differentiation were stained for F-actin and DNA, revealing three distinct morphology types: rounded cells, sheet-like actin, and polarized, fiber-rich actin (Figure 50a). Cells during days 0–1 of differentiation were characterized by the rounded cell morphology, followed by a transition to the sheet-like actin morphology during days 2–5, and finally to the polarized, fiber-rich actin morphology on day 6 (Figure 50b). The observed changes to the actin cytoskeleton align with the observed change from round to spindle-shaped morphology during differentiation.

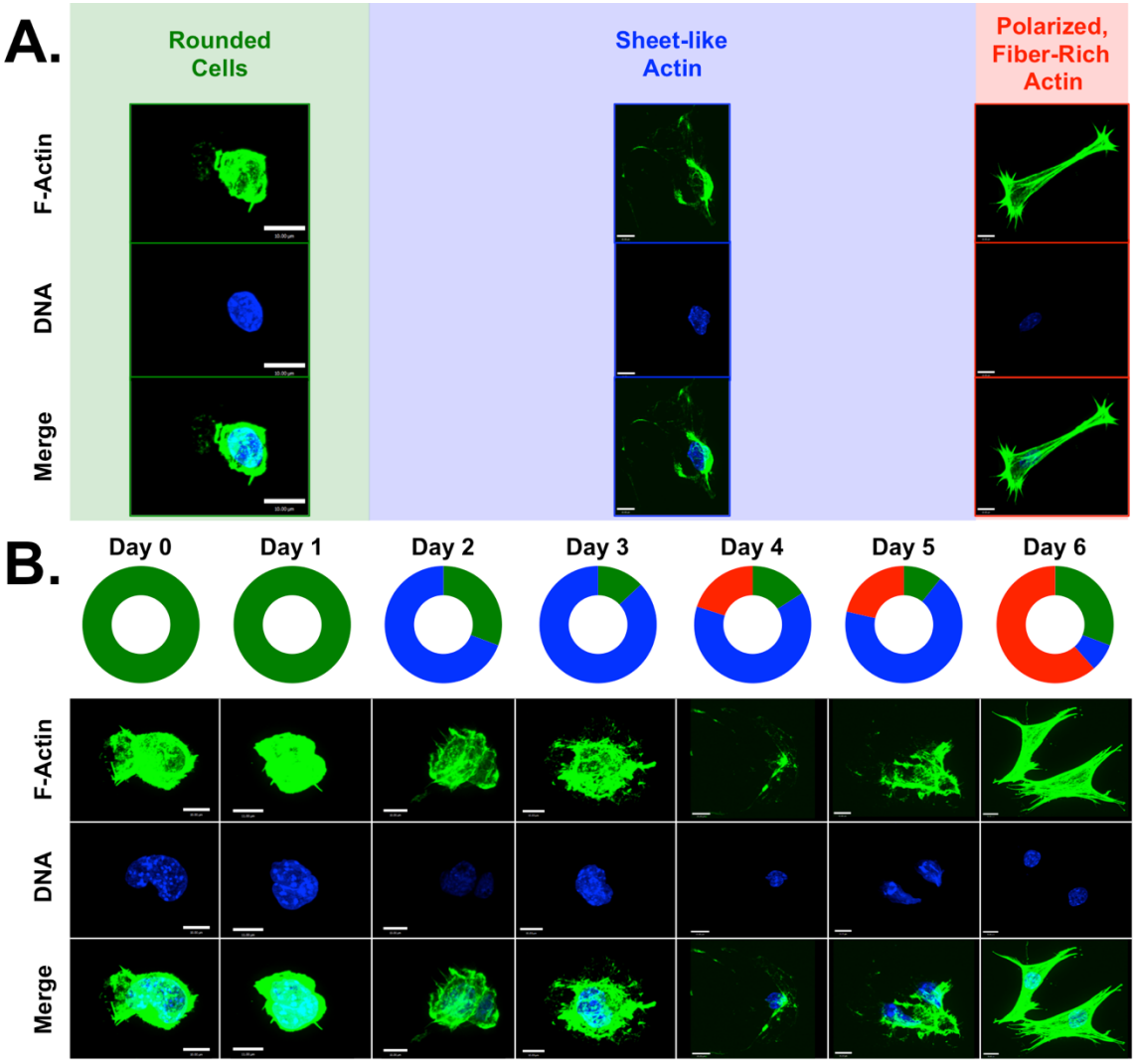

Figure 50 – Cytoskeleton remodeling during differentiation – a) Cells were stained for F-actin (fluorescent green) using phalloidin and for DNA (fluorescent blue) using Hoechst 33342. Cell morphologies were categorized as one of three types: rounded cells (left), sheet-like actin (middle), or polarized, fiber-rich actin (right). b). As shown in the doughnut plots, the dominant morphology type changed from rounded cells (green) on days 0–1 to sheet-like actin (blue) on days 2–5 and finally to polarized, fiber-rich actin (red) on day 6. Representative images were selected from the majority morphological type for each day of differentiation. Scale bars indicate 10 μm[125].

Similar to the work presented in chapter 3, 5, and 6, we investigated the intersection between genotype, mechanotype, and phenotype for stem cells during differentiation and after mechanical sorting using the microfluidic device we used in chapters 4 and 5. The expression of housekeeping genes (*Gapdh*, *Rps18*), pluripotency genes (*Nanog*, *Pou5f1*, *Sox2*), differentiation genes (*Isl1*, *Map2*), and structural genes (*Actn1*, *Lmna*, *Map2*) was investigated both over the course of differentiation and for the soft, middle, and stiff biophysical subsets. *Actn1* (α-actinin-1) crosslinks and bundles F-actin filaments, increases the stiffness of the actin filament network, and is known to increase as ESCs differentiate to cardiac progenitor cells[214,216,217]. Expression of *Lmna* (lamin A/C) is associated with stiff nuclei[218] and differentiated mouse embryonic tissue[24,219,220]. *Map2* (microtubule-associated protein 2) expression is associated with both ectoderm differentiation and microtubule assembly[221,222]. In comparison to the work in chapter 3, I also investigated the role of cytoskeletal remodeling proteins (*Cald1, Cfl1, Flna, Gsn, Mtss1, Mylk, Rock1, Tpm1),* lamin A/C, and microtubule-associated proteins (*Mapt*) as related to cell stiffness, seeing a positive relationship between cell stiffness and *Flna, Gsn, Lmna,* and *Cald1* expression (see Figure 17).

After sorting ESCs by their stiffness and investigating the gene expression of cells from each outlet, the expression of *Actn1* continuously increased from the soft to middle to stiff outlet, indicating that F-actin crosslinking may play a role in stiffness differences between the biophysical subsets, which is

corroborated by evidence that *Actn1* is responsible for stiffening both actin filament networks and entire cells[223,224]. The apparent connection between cellular spread area, roundness, and *Actn1* expression reflects a previous finding that *Actn1* controls cellular shape plasticity and the reaction to mechanical cues[224]. Furthermore, pluripotent ESCs have reduced levels of lamin A/C, resulting in an open chromatin state and irregular nuclear shape[219] that is linked to decreased cell stiffness[218]. Previous reports have also suggested a role of chromatin condensation in ESC stiffening during differentiation[24]. The overlapping genes and cell processes of interest across biological phenomena further suggests the connection between cell mechanotype, phenotype, and genotype.

7.2.4 – Mechanical characterization of cardiac progenitor cells early in differentiation

Human induced pluripotent stem cells (hiPSCs) are a promising source of cells for tissue engineering and cell-based therapies because of our ability to expand a cell type of interest *in vitro* and the ability to differentiate cells into whichever cell type is needed, including cardiomyocytes[225]. From a cell manufacturing standpoint, it would be incredibly beneficial to understand which cells have high potential to differentiate into a desired cell state at an early time point in order to remove poor differentiators and enrich good differentiators in the culture. Because of our expertise in mechanically sorting cells based on their differentiation status (see 7.2.3), we collaborated with the Palecek lab to

mechanically characterize three cell lines of known differentiation potential at an early time point to determine whether cardiac progenitor cells that are more likely to become cardiomyocytes could be isolated and enriched in a culture. The three cultures we investigated were all derived from the hiPSC parent cell line WTC-11 and were all on day 5 of a cardiac progenitor cell differentiation process[226]. Previous experimentation had established these three cell lines as good differentiators (60-90% of cells differentiate into cardiomyocytes), intermediate differentiators (45-50% of cells differentiate into cardiomyocytes), and bad differentiators (25-40% of cells differentiate into cardiomyocytes).

In parallel, cells were grown on Matrigel coated vessels for early AFM measurements the day after seeding and for further differentiation to confirm differentiation efficiency 11 days after seeding. The cells that continued to differentiate did indeed move toward the cardiomyocyte fate as spontaneous beating was observed in the good differentiator colonies 7 days post cell seeding (12 days into the differentiation process). The majority of the poor differentiators did not survive the differentiation process and the intermediate differentiators did have an intermediate response with half the cells surviving and limited spontaneous beating observed. Forty cells of each differentiation potential were mechanically tested to determine the adhesion force between the cell and silica bead, cell viscous properties, and cell stiffness. The good differentiators were statistically less adhesive than the intermediate differentiators ($p < 0.05$, Tukey HSD post-hoc test). We have observed cells that cells that are dying often have

an increase in cell adhesion (see 7.4), so one hypothesis is that cells that are not surviving the stem cell differentiation process may also demonstrate elevated adhesiveness, even at this early time point (Figure 51). When comparing cell population stiffness and viscosity measurements, we observed no differences between each cell line (ANOVA, $F > 0.05$) (Figure 52a). However, looking at the single cell AFM measurements, we noticed potential subpopulations in all three cell lines with a threshold of 650 Pa separating the groups. When only looking at single cell measurements less than 650 Pa, we noticed a decreasing trend of cell stiffness from good to poor differentiation status (good differentiators were stiffer than poor differentiators, $p < 0.1$, Tukey HSD post-hoc test) (Figure 52b). This aligns with our observations in 7.2.3 where cell stiffness increases with stem cell differentiation. A larger sample size, combining single cell AFM measurements with single cell fluorescent read outs, and testing cell stiffness at different time points may further elucidate a relationship between early cell mechanics and differentiation potential that could be used to enrich good CPC differentiators.

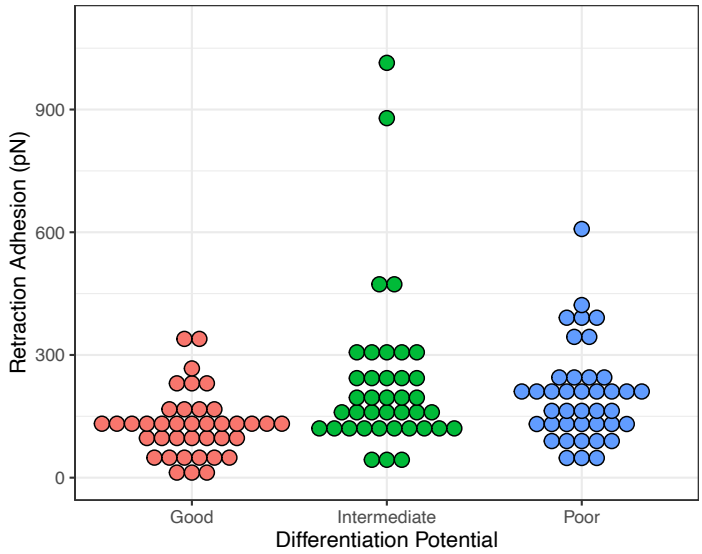

Figure 51 – Good CPC differentiators are less adhesive – Retraction adhesion force measured by AFM between cell and silica bead. n=40 for each CPC line. Good differentiators are statistically less adhesive than intermediate differentiators ($p<0.05$, Tukey HSD post-hoc test). No other statistically significant comparisons were observed.

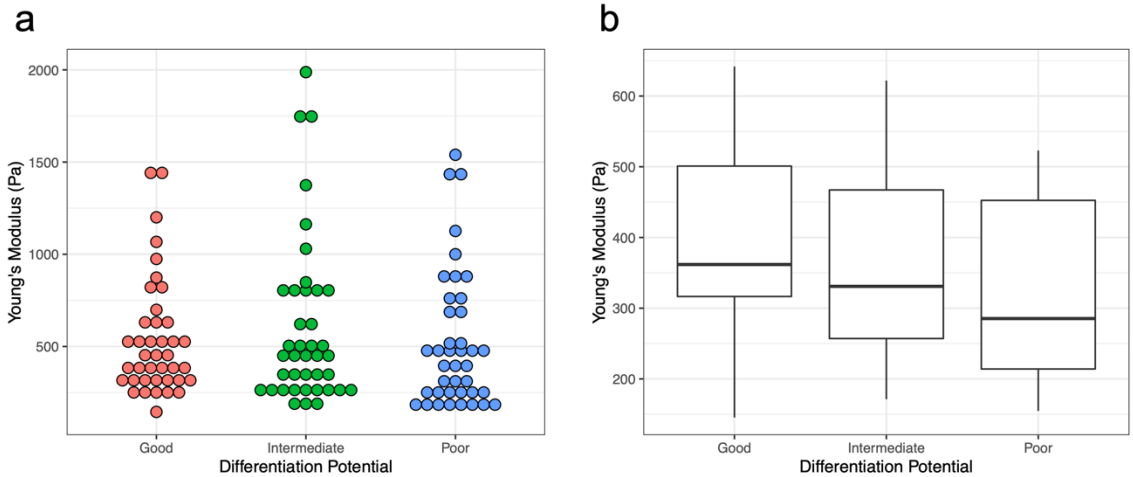

Figure 52 – As differentiation potential decreases, stiffness of soft subpopulation of cells decreases – Cell stiffness was measured with AFM. n = 40 cells for each CPC line. a) When looking at all measurements, there was no statistical difference (ANOVA, $F > 0.05$) between any group's stiffness. b) Using 650 Pa as a threshold to define a soft subpopulation in each line, we observed a relationship between differentiation potential and cell stiffness. The good cell line is stiffer than poor cell line ($p < 0.1$, Tukey HSD post-hoc test)

7.3 – Mechanical Properties of Diseased Cells

7.3.1 – Loss of Ptpn21decreases hematopoietic stem cell stiffness

Missense mutations and frameshift truncating mutations in *PTPN21*, which codes for a tyrosine phosphatase protein that binds to and regulates the actin cytoskeleton, have been identified in chronic lymphocytic leukemia (IntOGen—mutational cancer drivers database) and colon cancer[227-229], respectively. This phosphatase is highly expressed in hematopoietic stem cells (HSC) as compared to differentiated leukocytes and it was hypothesized to play an important role in HSC quiescence and maintenance of retention in the bone marrow microenvironment[124]. To explore this role, our collaborators isolated several different cell types from the bone marrow of *Ptpn21*$^{+/+}$ and *Ptpn21*$^{-/-}$ mice; Lin^{-} cells are bone marrow cells that do not express any lineage-specific markers (for myeloid cells, lymphocytes, and erythrocytes), LSK cells are early progenitor cells that are Lin^{-}Sca-1^{+}c-Kit^{+} and HSCs are defined as Lin^{-}Sca-1^{+}c-Kit^{+}CD150^{+}CD48^{-}. We measured the stiffness of HSCs, LSK, and Lin^{-} cells with AFM and found that *Ptpn21*$^{-/-}$ knockout mice bone marrow cells were significantly softer than their WT counterparts for all three cell types (Figure 53a) and more motile. AFM measurements additionally confirmed that for healthy mice, their HSCs, LSK cells, and Lin^{-} cells were stiffer than Lin^{+} cells such as CD3^{+} T cells, B220^{+} B cells and Mac-1^{+}Gr-1^{+} myeloid cells (Figure 53b) as well as less motile. Although no significant difference in cell stiffness between healthy quiescent (in the G_0 phase) and healthy activated HSCs (in the G_1/S/G_2/M phases) was detected (Figure 53c),

cell tension quickly decreased upon HSC differentiation in culture (Figure 53d), consistent with the data obtained from human early progenitor cells[230]. AFM measurements of cell stiffness showed that *Ptpn21*-deleted leukemic cells were softer than control leukemic cells (Figure 53e), similar to the phenotypes of "normal" *Ptpn21*$^{-/-}$ hematopoietic cells. The soft mechanotype for *Ptpn21* knockout cells is correlated with stem cell egress from the bone marrow niche which results in impaired hematopoiesis. It is also interesting to note the stiffness difference between healthy progenitor cells and differentiated cells is opposite to that observed with the mouse embryonic stem cells in 7.2.3. This may be attributed to the fact that the differentiated blood cells migrate more frequently than their progenitor and HSC counterparts, and the need to traffic is intricately connected to whole-cell stiffness.

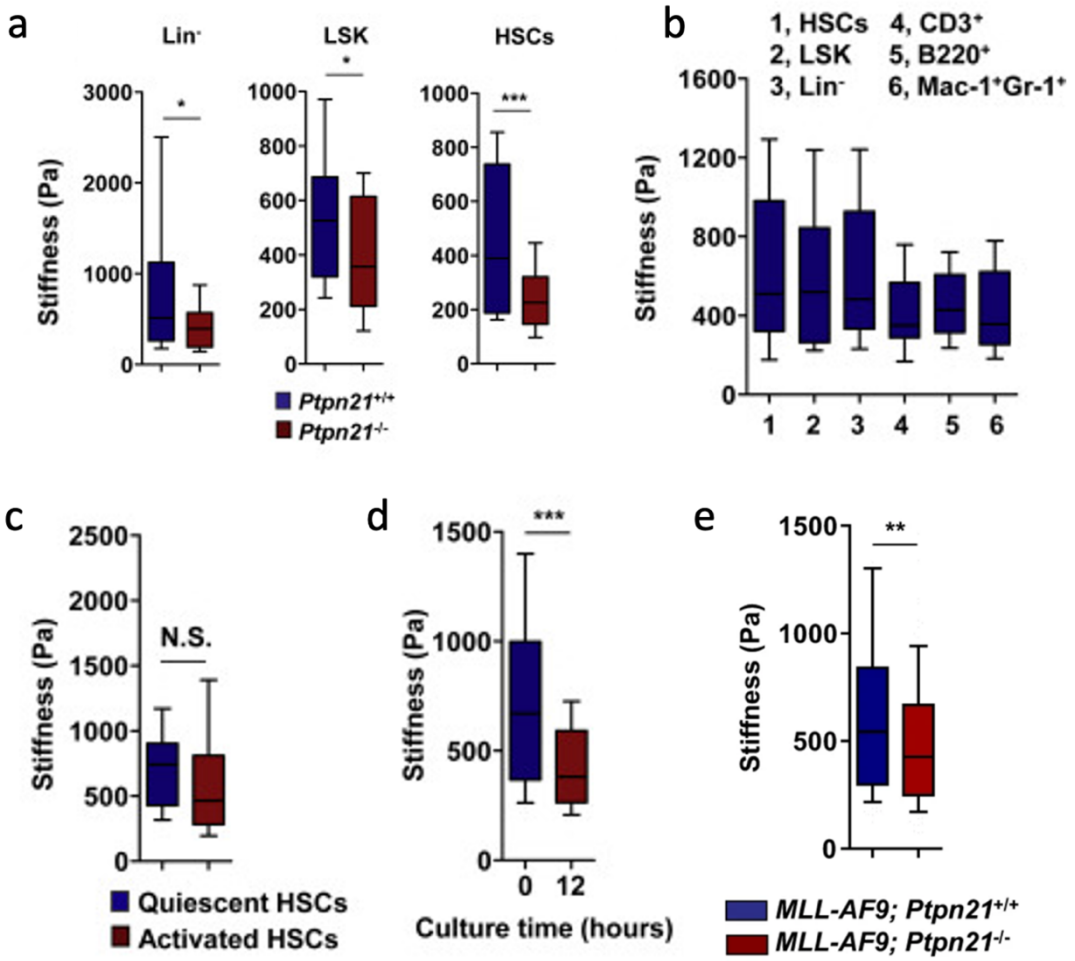

Figure 53 – Loss of Ptpn21 Decreases Cell Stiffness and Increases Mobility in HSCs – a) Lin⁻ cells, LSK cells, and HSCs isolated from *Ptpn21*$^{-/-}$ and *Ptpn21*$^{+/+}$ mice (n = 3–7 per genotype; 28 cells examined per mouse sample) were measured for stiffness by atomic force microscopy (AFM). Data are presented as the mean ± SD of biological replicates. *, $p < 0.05$; ***, $p < 0.001$ (unpaired, two-tailed Student's t test). b) HSCs, LSK, Lin⁻, CD3⁺, B220⁺, and Mac1⁺Gr-1⁺ cells isolated from healthy C57BL/6 mice (n = 4 mice; 26 cells examined per mouse sample) were mechanically assessed by AFM. c) HSCs in the G_0 (quiescent) and $G_1/S/G_2/M$ (activated) phases were sorted separately and measured for cell stiffness (n = 4 mice; 29 cells examined per mouse sample). d) HSCs sorted from healthy C57BL/6 mice were cultured in 50 ng/mL SCF, 50 ng/mL Flt3L, 20 ng/mL interleukin-3 (IL-3), and 20 ng/mL IL-6-containing medium for 12 h. Cells were then collected and measured for cell stiffness (n = 3 mice; 40 cells examined per mouse sample). Data are presented as the mean ± SD of biological replicates. ***, $p < 0.001$. N.S., not significant (unpaired, two-tailed Student's t test). e) Leukemic cells isolated were measured for mechanical stiffness by atomic force microscopy (*n* = 3 mice per genotype; 108 cells examined per mouse sample)[124,231].

7.3.2 – Loss of CCM protein expression in endothelial cells results in increase of cell stiffness with knockdown of KRIT and CCM2 but not PDCD10

Cerebral cavernous malformations (CCMs) are a class of vascular disease that is marked by enlarged endothelial channels in the central nervous system which increases the risk of brain hemorrhage. This disease state is the result of mutation in one of three genes, *Krit1* (*Ccm1*), *Ccm2*, or *Pdcd10* (*Ccm3*). Cells with each of these gene knockdowns (KDs) were manufactured using shRNA against each gene of interest. Through computational modeling, our collaborators predicted that changes in cytoskeletal tension and cellular responses to external force in CCM KD cells would have a dramatic effect on endothelial tubule formation, specifically through dysregulated RhoA function. To test this hypothesis, AFM measurements were taken from 30–50 cells in each of the experimental groups at 24 hours after plating. The results of three independent experiments showed significantly higher stiffness of *KRIT1* KD ($p = 0.00053$, Tukey HSD post-hoc test) and *CCM2* KD ($p = 0.00014$, Tukey HSD post-hoc test) cells as compared with WT cells. However, the stiffness of *PDCD10* KD cell was not different from that of WT cultures, $p = 0.23$, Tukey HSD post-hoc test (Figure 54a and Figure 54b). It was hypothesized that unexpectedly low stiffness of *PDCD10* cells might be due to specifics of the architecture of actin cytoskeleton in these cells. Interestingly, the area of high F-actin activity was dramatically reduced in *PDCD10* KD cells, indicating a lack of cell connectivity of stress fibers.

Analysis of F-actin distribution showed that *KRIT1* and *CCM2* KD cell cytoskeleton had a higher contrast of actin bundles and was characterized by less homogeneity of staining as compared with WT and *PDCD10* KD cells[123]. The characteristics of actin cytoskeleton organization may contribute to differences in biomechanical properties of KD cells, the patterns of vascular networks, and the response of KD cultures to ROCK inhibition.

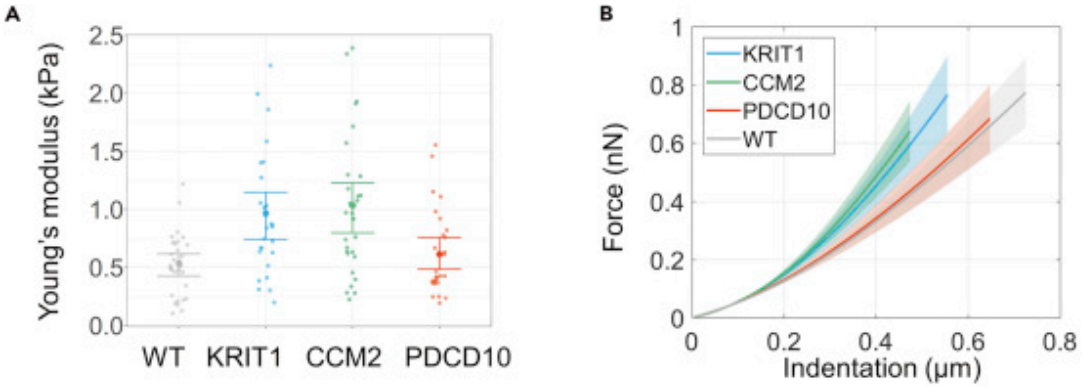

Figure 54 – Changes in actomyosin cytoskeleton associated with loss of CCM protein expression result in increased stiffness of cells with knockdown of *KRIT1* and *CCM2* but not *PDCD10* – a) AFM stiffness measurement results for single PLKO.1 (WT) cells and single cells with knockdown of *KRIT1*, *CCM2*, and *PDCD10*. The graph shows mean values and standard deviations of measurements from up to 30 cells in each group. Note higher stiffness of *KRIT1* and *CCM2* KD but not *PDCD10* KD cells when compared with WT. The data shown are from one representative of three independent experiments. b) The graph shows representative force curves of WT cells and cells with loss of CCM protein expression recorded by AFM, with shaded area representing ±2 SEM.[123]

7.3.3 – Netarsudil reduced steroid-induced trabecular meshwork stiffening

While topical glucocorticoids are often used after eye surgery, they unfortunately frequently result in ocular hypertension that can progress to steroid-induced glaucoma. Glucocorticoids can cause pro-fibrotic changes in the outflow pathway mediated through rho-associated protein kinase (ROCK) activity. A ROCK inhibitor netarsudil (NT) has recently been approved for clinical use to treat ocular hypertension in glaucoma patients. To better define NT's mechanism of restorative, anti-fibrotic action in treating steroid-induced ocular hypertension, we investigated the effect of the treatment on the tissue stiffness of mouse glaucoma model eyes. Mechanical stiffness of the trabecular meshwork (TM), a key tissue in the conventional outflow pathway, was shown to be increased by GC treatment, negatively correlating with outflow facility[232]. In order to obtain a direct measurement of TM stiffness in a cohort of NT-treated mouse eyes, we used AFM on cryosectioned tissue[233]. Ocular hypertension was induced by delivering dexamethasone nanoparticles bilaterally for 3 weeks to mice before starting unilateral delivery of either NT or a placebo (PL). We observed that NT significantly reduced TM tissue stiffness by 23% compared to contralateral eyes treated with a placebo (1.54 ± 0.19 vs. 2.00 ± 0.13 kPa, $p=0.007$, Figure 55). In contrast, PL did not affect TM tissue stiffness compared to contralateral eyes (1.39 ± 0.12 vs. 1.73 ± 0.20 kPa, $p=0.39$). When stiffness measurements of PL and NT groups were normalized to untreated contralateral eyes, a trend toward NT-induced

softening was observed but was not significant perhaps due to small sample size ($p = 0.15$, Welch two sample t-test). We consider it noteworthy that NT appears to have restored normal TM biomechanical properties in the steroid-induced ocular hypertension model after only 4 days of treatment, and that this restoration was accompanied by significant morphological changes in the ECM of the TM. While AFM allows for the direct measurement of the compressive mechanical properties of outflow tissues in different locations with high resolution, this method is limited to *ex vivo*, cryosectioned tissues and most likely reflect ECM stiffness as opposed to cellular stiffness.

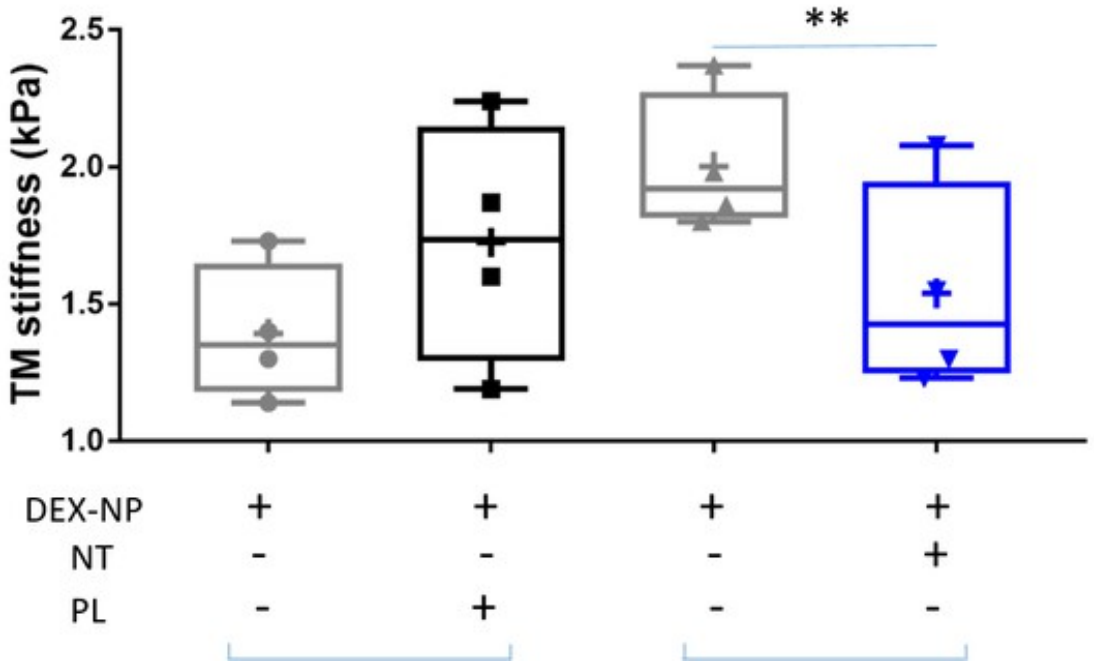

Figure 55 – Netarsudil (NT) reduced steroid-induced trabecular meshwork (TM) stiffening measured directly by atomic force microscopy (AFM) – At day 5, eyes were collected and processed for atomic force measurements of TM stiffness (Young's modulus). We observed that NT softened the TM vs. control eyes.

Brackets indicate paired eyes. An average of 135 measurements were made from three quadrants on four biological samples for both cohorts, $p = 0.007$[234].

7.3.4 – Pointwise modulus AFM force mapping for distinguishing mechanics of perinuclear and cytoplasmic regions in multiple cancer cell lines

Conventional AFM force mapping utilizes the possibly nonlinear portions of force curves to extract Young's moduli, which can obfuscate the comparison of local material properties. We used a new technique called linear elastography that explicitly uses only the linear portion of the force curve to determine a 2-D map of Young's modulus. We determine the linear elastography of cells by combining standard force mapping and the pointwise Hertzian method. This new technique systematically addresses the inherent nonlinearity of cellular mechanical measurements by finding and recording only the linear elasticity region for the purpose of stiffness mapping. The result is an enhanced contrast of key features for determining cell mechanical variations within cells.

Using the pointwise modulus linear elastography, we took measurements of ovarian cancer and breast cancer cells of varying metastatic potential. At a population level, HEY A8 ovarian cancer cells have been identified as softer and more migratory than their HEY counterparts (both used in chapter 3)[21]. Similarly, MCF10-CA breast cancer cells are the more metastatic derivative of the MCF10-A parent cell line[235]. Figure 56a shows the enhanced contrast image of individual cells, in which the edge of the nucleus appears as dark contrast and pseudopod

extensions are visible. Figure 56b shows the topography of each cell measured during force mapping. The elastography in Figure 56c reveals spatial variations in cell stiffness, including regions of increased stiffness in the cytoskeletal region and with significantly softer perinuclear regions in the case of metastatic cell types. Force-indentation curves measured at the cell surface with atomic force microscopy reflect the underlying cell structure and because of the coupling of the nucleus and intracellular actin structures to the cell surface, indentations translate into compression of all components underneath the probe[25,236]. We therefore infer that heterogenous mechanical properties measured across the cell are related to the properties of the cells' internal structures. The elastographies display clear spatial variations and indicate that mechanical stiffness of cells can be highly heterogeneous along lateral dimensions. The central region corresponding to the nucleus shows lower Young's moduli than the cytoplasm.

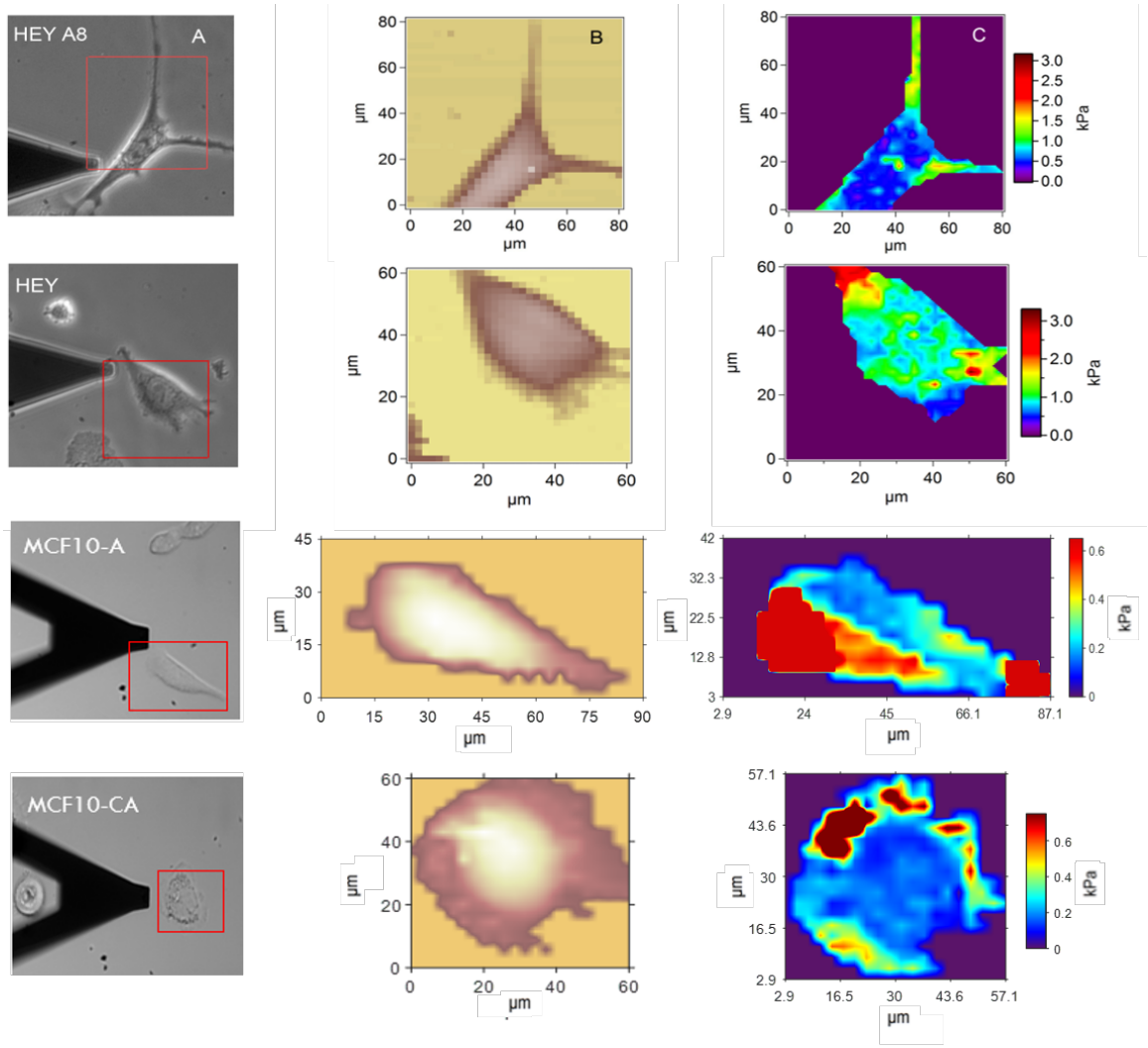

Figure 56 – Images and linear elastographies of ovarian cancer cell lines (HEY A8, HEY), and breast cancer cell lines (MCF10-A, MCF10-CA) – a) Enhanced contrast microscopy shows the cell boundary and edge of the nucleus. b) The region defined by the red box was scanned to show a 2-D representation of the topography. c) The corresponding elastographies show linear elasticity distribution of the cells, in which the nuclear region is softer than the surrounding cytoplasm in invasive HEYA8 and MCF10-CA cells. In contrast, noninvasive cancer cells from HEY and MCF10-A do not show a softer nuclear region.

It is worth noting that within the nuclear region of the elastography, the stiffness distribution is also heterogeneous. These stiffer locations may result from heterogeneities within the nucleus, such as tightly packed chromatin or

heterochromatin [237,238]. The cytoplasmic region surrounding the nucleus was seen to have higher moduli than the perinuclear region for the invasive HEY A8 cells but not for less invasive HEY cells (Figure 57). The elastographies of the MCF10 cell line display a stiffening of the lamellipodia region in the invasive MCF10-CA cells (454 ± 56 Pa) when compared to the less-invasive MCF10-A cells (246 ± 60 Pa) (Figure 57). Moreover, the Young's Modulus averages a 1.5-fold increase in stiffness between the lamellipodia and perinuclear regions for the metastatic MCF10-CA cells (Figure 57). The Young's modulus of the cell also exhibits less variation in the perinuclear region of the cells (differing by less than 2 kPa).

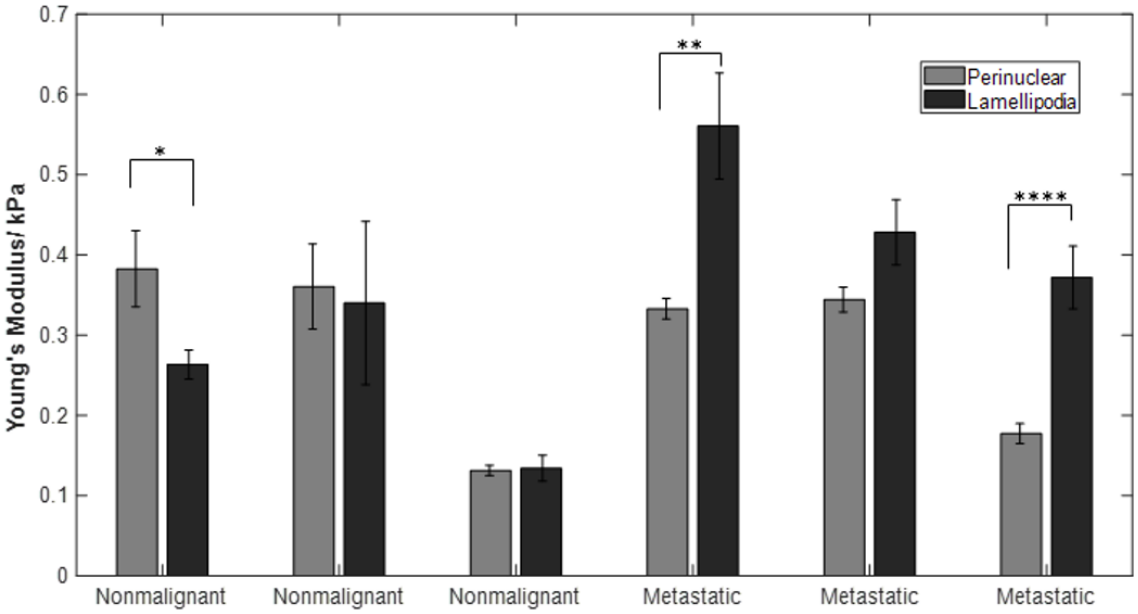

Figure 57 – Modulus values of the perinuclear region and lamellipodia region for three MCF10-A cells (non-malignant) and three MCF10-CA cells (metastatic) – Statistical differences between the two regions were compared using a t-test for each cell. Error bars denote standard error of the mean.

Various techniques have demonstrated the importance of nuclear mechanics in cancer cell migration[239–242]. We hypothesize that the softening we observed in the perinuclear region is primarily attributed to the cell's nucleus. However, the difference may also be due changes in perinuclear actin[243]. Perinuclear actin, consisting of both an actin cap and dorsal actin cables, is important for assistance in cancer cell migration through tight constrictions by aiding in nuclear movement and positions after accumulation during migration[244–246]. Our direct measurement of mechanical properties with spatial resolution of intact nuclei and cytoplasmic region of invasive cells provides insight to the mechanical and structural properties important to migration. The fact that the nucleus of invasive HEY A8 and MCF10-CA cell types is at least as soft as the surrounding cytoplasm is consistent with the role of the nucleus as a key limiting factor in cancer cell migration[247,248]. The nuclei in cancer cells can display a ruptured and less organized structure[242] resulting in a decreased mechanical stiffness upon malignancy. Since the deformation of the nucleus is a critical step in cell transport in physiological scenarios, and possibly the rate-limiting factor[241,249,250] of cancer cell migration[248,251], cells with more deformable nuclei more easily migrate through small confines and are thus more invasive.

7.3.5 – Mechanically sorting cells from ovarian cancer patients' ascites samples

The microfluidic device described in chapters 4 and 5 can also be used to obtain more highly purified ovarian cancer cell samples from patient fluid samples such as ascites. Higher purity samples will then result in accelerated cancer biology research and improved treatments by clinicians through more accurate and sensitive outcomes of analytical techniques. Ovarian cancer is a particularly important pathology to apply enrichment techniques, considering the general poor quality of existing biomarkers[252–254]. For example, one marker used to assess malignancy in ovarian cancer is *TGM2*, but unfortunately the resulting protein TG2 is expressed in a wide variety of tissues and detectible in all organs[255].

To determine if microfluidic sorting is capable of separating cell populations of clinical interest from heterogeneous specimens, we obtained ascites from two patients with advanced metastatic ovarian cancer from Northside Hospital in Atlanta, GA under an informed consent IRB protocol (H16135). Cells were resuspended in flow buffer and subjected to biomechanical sorting. The sorted fractions were collected from each of the five output ports and were stained for TG2, a protein whose overexpression has been shown to be a feature of ovarian cancer[256]. This sorting resulted in cell fractions enriched for high-TG2 cells, consistent with an enrichment of metastatic cancer cells (Figure 58a). In addition, NGS libraries were prepared to enable deep sequencing of the TP53 gene, mutations in which are commonly observed in ovarian cancer[257]. As shown in

Figure 58b, the proportion of mutant reads and TG2 florescence intensity in the sorted populations change at different device outlets indicating separation of the heterogeneous input into biologically relevant subpopulations. Mutations in P53 were enriched at stiff outlets 1 and 2 (note the numbering convention is switched from chapters 4 and 5) whereas in soft outlets 4 and 5, cells containing P53 mutations were substantially removed, indicating a transfer of cancer cells to outlets of 1 and 2. These results were consistent for both patients and indicate that the microfluidic cell sorting device is capable of selectively enriching cells with *TP53* mutations associated with ovarian cancer cells in a label-free manner.

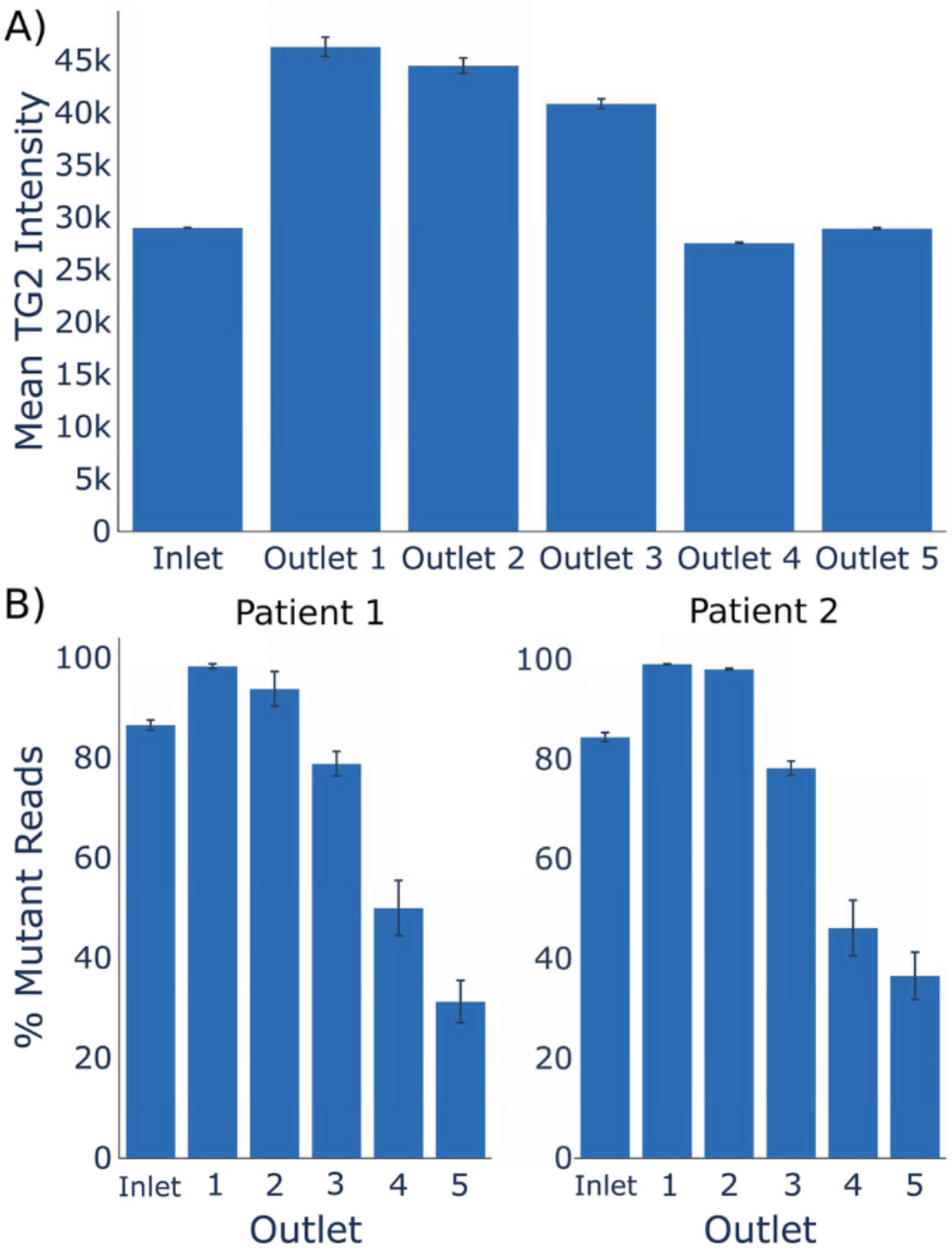

Figure 58 – Sorting of primary ascites samples – To assess the usefulness of our platform in a clinical setting, we used our device to sort metastatic cells from patient ascites samples. Enrichment of putative cancer cells (*TP53* mutant, high TG2 intensity) was achieved in outlet 1 and 2 for (a) one patient as quantified via immunocytology and (b) two separate patients as quantified via sequencing[173].

7.3.6 – Exploring the relationship with both *MYLK* expression and nuclear actin filament formation with cellular stiffness

Because our group identified a negative population level relationship between myosin light chain kinase (*MYLK*) expression and ovarian cancer cell line metastatic potential (with HEY A8 cells demonstrating a two-fold decrease in expression compared to HEY cells)[21], we were contacted by Dr. Primal de Lanerolle about investigating the cellular mechanics of three human breast cancer cell lines which demonstrated the same relationship between *MYLK* expression and aggressiveness. They have shown that *MYLK* expression is decreased in human tumor tissue compared to surrounding normal tissue[258]. Also, human breast cancer cells express less *MLCK* and this correlates with their aggressiveness. MCF10A cells, which are transformed but not tumorigenic, express robust levels of non-muscle *MYLK*. MCF7 cells, which are tumorigenic but non-metastatic when injected into immunodeficient mice, express less of non-muscle *MYLK* and smooth muscle *MYLK*. MCF10CA cells, which are isogenic with MCF10A cells, are both highly tumorigenic and metastatic. These cells express low levels of smooth muscle *MYLK*. Our hypothesis is that a decrease in *MYLK* is related to a decrease in breast cancer cytoskeletal stiffness, making cells softer and better able to negotiate the ECM and survive the shear forces in the circulation. Both tumorigenic cell lines, MCF10CA and MCF7, were statistically softer than then non-tumorigenic cell line MCF10A ($p < 0.001$, Tukey HSD post-hoc test), supporting the same relationship between *MYLK* expression, cell stiffness, and metastatic potential (Figure 59).

Interestingly, we did not observe a statistical correlation between *MYLK* expression and cell stiffness on the single ovarian cancer cell level (Figure 17).

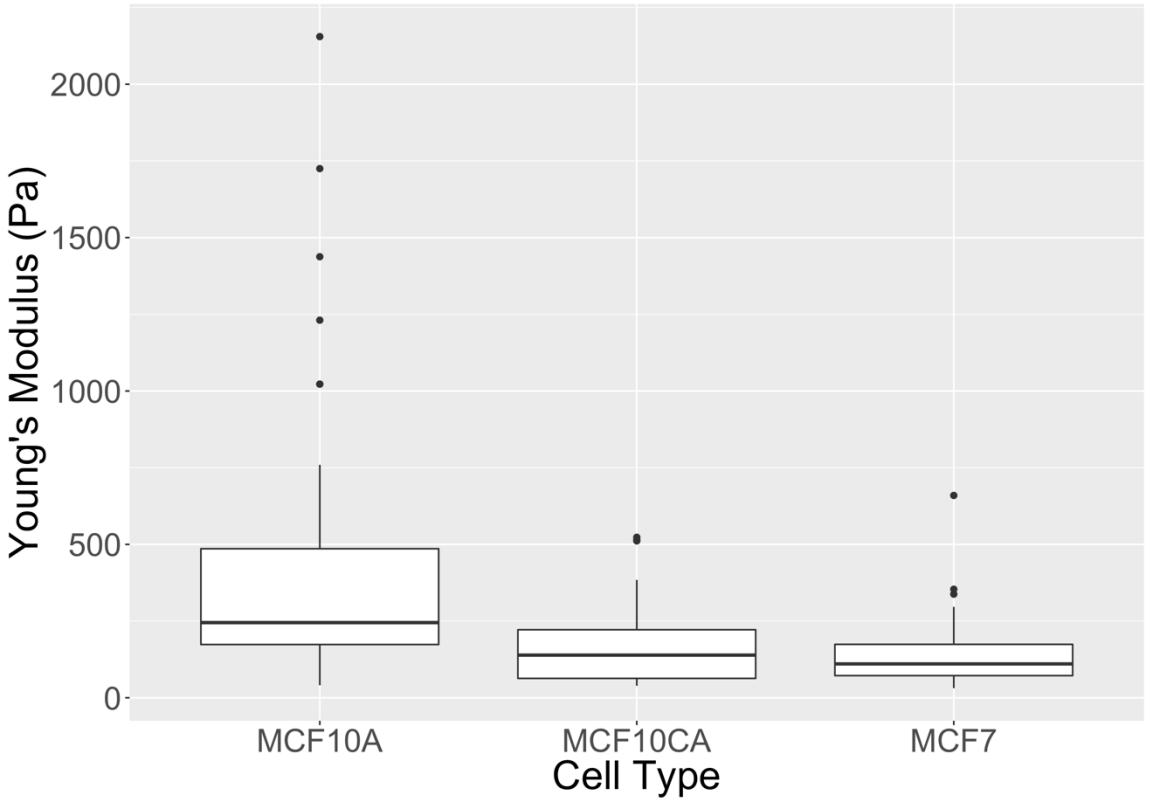

Figure 59 – Breast cancer cell stiffness negatively correlated with *MYLK* expression and cell aggressiveness – AFM measurements (n = 50 per cell line) demonstrate negative correlation between cell stiffness and cell aggressiveness. MCF10A cells are transformed breast epithelial cells that are non-tumorigenic and express high levels of *MYLK* and both MCF10CA and MCF7 cells are tumorigenic and express low levels of *MYLK*. Both MCF10CA and MCF7 cells are statistically softer than MCF10A cells ($p < 0.001$, Tukey HSD post-hoc test).

Beyond studying the effect of *MYLK*, which promotes actin-activated myosin motor activity and cytoskeletal tension generation, we were also interested in investigating the role of actin specifically in the nucleus on cell

stiffness. Through the process of mechanotransduction, signals from the extracellular matrix are transmitted through the cytoplasm into the nucleus and eventually to transcription machinery. Actin plays an important role in the transduction of the external signals and when actin is forced into the nucleus to form nuclear actin filaments, transcription is inhibited through RNA polymerase I[259]. Interestingly, when comparing nuclear stiffness measurements, isolated nuclei are softer than nuclei *in situ* in cells and other groups have claimed that nuclear stiffening is not triggered by nuclear actin, but rather by the nuclear lamina[260,261]. (As a reminder, *LMNA* expression is positively correlated with single cell stiffness measurements - Figure 17). One explanation to these observations is that nuclear actin must be connected to cytoskeletal actin to exert force within the nucleus. The nucleus is a major barrier to metastatic cell invasion, so one explanation could be that metastatic cells are more invasive because of a softer cytoskeleton that is related to a decrease in *MYLK* and results in a downregulation of nuclear stiffness. To further explore, the role of nuclear actin as well as nuclear actin filament formation on cell mechanics, we transfected cells with various constructs that would affect nuclear actin. An EYFP-actin plasmid was used to label cytoplasmic actin while a GFP-NLS-actin plasmid was used to target actin to the nucleus to result in nuclear actin filaments. A V163M-α-actin plasmid was also used to stabilize nuclear actin filaments (V163M is a naturally occurring point mutation that causes intranuclear rod myopathy marked by nuclear actin filament formation)[259] (Figure 60a). Surprisingly, after transfection with the V163M

plasmid to drive nuclear actin filament formation as well as transfection with the plasmid that targets the actin to the nucleus, we actually saw a slight reduction in cell stiffness compared to non-transduced cells or cells transfected with EYFP-actin, respectively ($p > 0.05$) (Figure 60b and Figure 60c). Both of these comparisons were made with small sample sizes and the AFM measurement method was limited – for nuclear measurement, the cantilever was visually aligned to the nucleus and we were not able to use an objective with the proper magnification to distinguish the formation of nuclear actin filaments. In an effort to improve the resolution of mechanical measurement and correlate it to actin filament formation, we took a force map a cell transfected with the V163M actin plasmid (Figure 61a). Using the cell height to only include data points from a single cell, we were able to compare the fluorescence intensity at each force curve location with the stiffness data at that location (Figure 61b, Figure 61c, and Figure 61d). We identified a statistically significant correlation between fluorescence intensity and cell stiffness (Pearson correlation = -0.525, $p<0.05$), implying that the regions with more labelled actin are softer (Figure 61e). This trend seems to hold with the single cell measurements that imply non-transfected cells are stiffer than the transfected cells, although it is still important to note the inability to resolve the presence of nuclear actin filaments in the fluorescent image. Additionally, from the study in 7.3.4, we have observed elevated stiffness in lamellipodial regions, which might bias this data as we would expect the stiff lamellipodia to exhibit a low fluorescence signal.

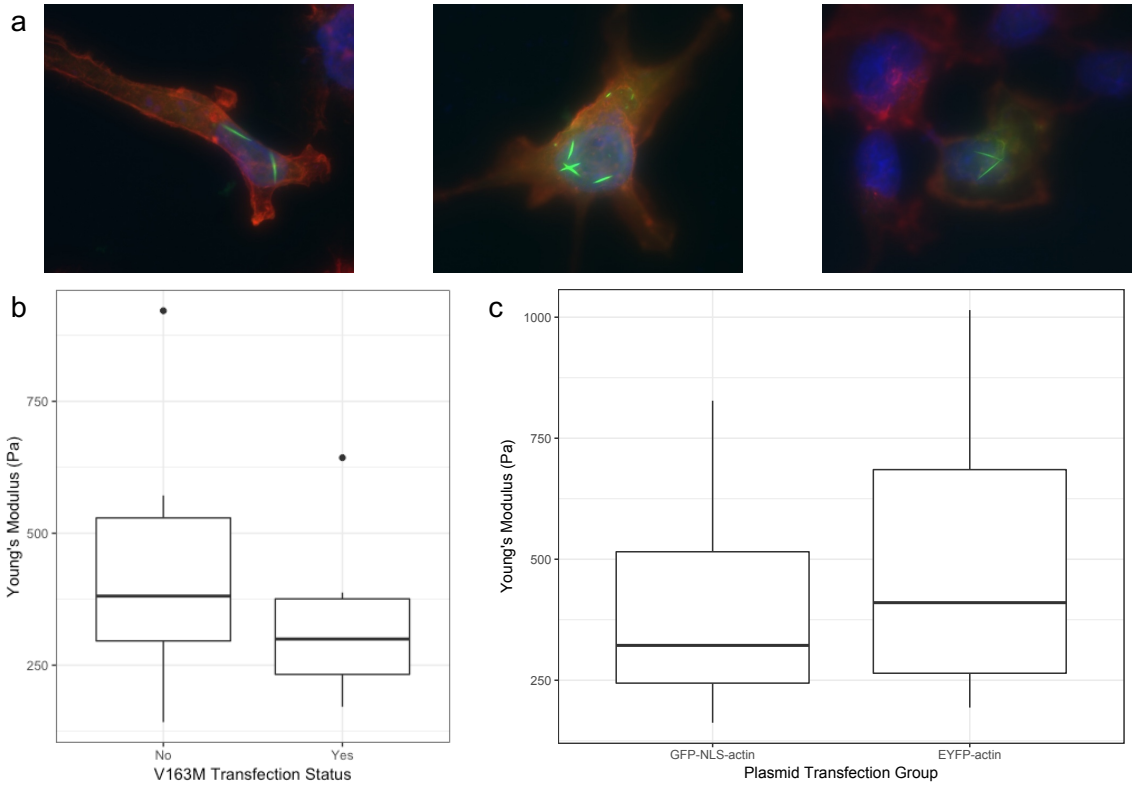

Figure 60 – Nuclear actin filament formation possibly associated with cell softening – a) Three fluorescent images of COS7 cells transfected with V163M-α-actin. Blue channel is Hoechst 33342 nuclear stain, green channel is V163M-α-actin, and red channel is Alexa Fluor 546 Phalloidin f-actin stain. 63x magnification with a Zeiss LSM 700 laser scanning confocal microscope. b) Boxplot depicting the slight, but non-significant, difference in stiffness between cells after transfection with V163M-α-actin (n=11 for non-transfected cells, n=5 for V162M transfected cells). c) Boxplot depicting the slight, but non-significant, difference in stiffness between cells transfected with EYFP-actin and GFP-NLS-actin plasmids (n=20 for each cell population).

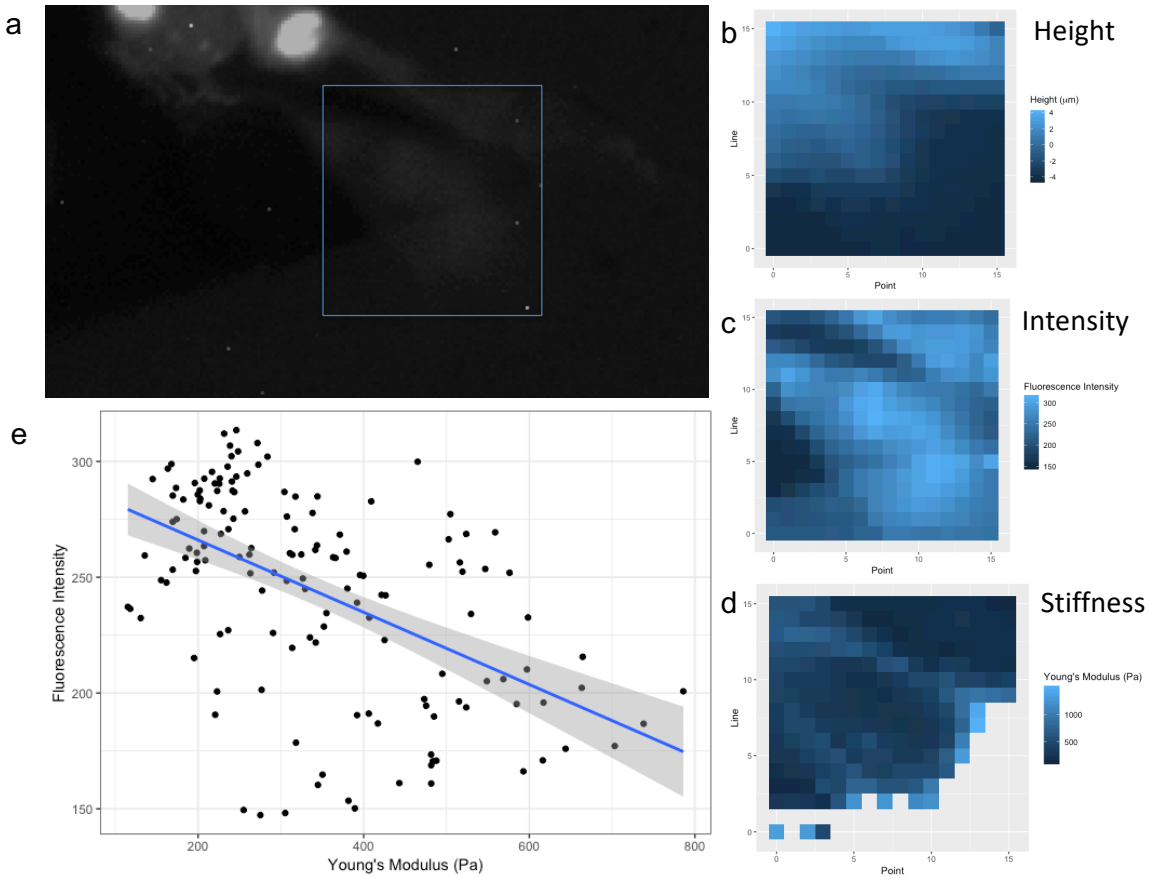

Figure 61 – Force mapping reveals negative correlation between stiffness measurements and fluorescent intensity of labelled actin – a) Fluorescent image of COS7 cell transfected with V163M-α-actin. Blue box depicts region for force map, a 40 μm x 40 μm area. b) Cell height as determined by AFM force mapping. c) Fluorescence intensity (GFP channel) that corresponds with force map region. d) Cell stiffness determined by Hertzian contact mechanics model at each cell location, a 16 x 16 point map. e) Scatterplot showing negative correlation between cell stiffness and fluorescence intensity for single cell force map (Pearson's correlation = -0.525, $p < 0.05$).

We had expected that nuclear actin filaments would increase nuclear stiffness as they pull inward on the lamina and nuclear envelope. One possibility that might explain the preliminary data that is pointing to a decrease in measured stiffness with nuclear actin filament formation is that these stress fibers link with

the cortical cytoskeleton and polymerization of actin affects both stress fibers and the cortical cytoskeleton. Consequently, changes in actin are distributed throughout the cell. Nuclear actin filaments may only have very local effects on the nuclear envelope, and it is possible that filament formation in the nucleus may result in more disorganized actin structures in the rest of the nucleus and cell. Before drawing more definitive conclusions from this study, we would need improve the method to allow for visualization of nuclear actin filaments and higher resolution nuclear stiffness measurements that could be correlated with exact filament location.

7.4 – Mechanical Properties of Dying Cells

7.4.1 – Temporal dynamics of mechanical properties of cells undergoing necrosis and apoptosis after heat treatment

Cell death is often defined using morphological criteria. The two most well-known cell death mechanisms are necrosis and apoptosis. Both mechanisms can be induced via heat shock depending on the duration and degree of exposure to a high external temperature. Necrosis usually occurs seconds to minutes after the application of an injury and is characterized by the loss of cell membrane integrity and cell swelling. Apoptosis is an internal process where the cell systematically dissembles and degrades its structural components to induce cell death[262]. A past study on osteoblasts has shown that heat shock at a temperature of 48 °C correlates to an increase in the number of necrotic cells by 15-20% after only a

few minutes[263]. Another study conducted on Jurkat cells showed similar results. The cells treated at a lower temperature (42 °C) for 30 minutes underwent apoptosis. Meanwhile, the cells treated at a higher temperature (46 °C) for 60 minutes underwent necrosis[264]. Therefore, heat treating cells at 42 °C is expected induce apoptosis. Similarly, a higher temperature, such as 65 °C, would be expected to cause necrosis.

Understanding and measuring cell viability is essential since the presence of nonviable cells in *in vitro* cell culture can negatively affect cell productivity or functionality. Furthermore, low viability can affect the clinical outcome of cell therapies[163]. Although most viability testing is currently conducted using immunocytochemistry assays, such as the Trypan blue, Propidium iodide, and MTT assays, biomechanics has shown potential as an early detector of cell death. Apoptosis is the commonly accepted mechanism for chemotherapy-induced cell death. Past studies have identified an increase in cell stiffness in apoptotic cells due to changes in the actin cytoskeleton, a decrease in cytoplasmic components, and the cross linking of the membrane to cytoskeletal components[122]. The understanding of the mechanical changes of cells undergoing apoptosis post-chemotherapy or heat treatment is crucial for early recognition of chemo-resistant cell behavior.

When we exposed Jurkat T-cell leukemia cells to varying durations of 65°C heat treatment (from 5 minutes to 5.5 hours), we observed a drastic cell stiffening responses for even the shortest amount of heat treatment (Figure 62a).

Early stages of apoptosis (such as initiation of caspase cascades) occur within 30 minutes of apoptosis initiation, but often cells do not exhibit signs of apoptotic death for multiple hours. However, cells can undergo necrosis in short time frames. Therefore, we were interested in observing which type of cell death cells undergoing 65°C experienced. Staining for Annexin V, an early apoptotic marker, and 7-AAD, a marker for late apoptosis or necrosis, we identified 65°C heat resulted in necrotic cell death. This process resulted in a large change in cellular mechanics which was utilized in other chapters of this thesis for the purposes of cell viability sorting (chapter 4 and 7.4.4).

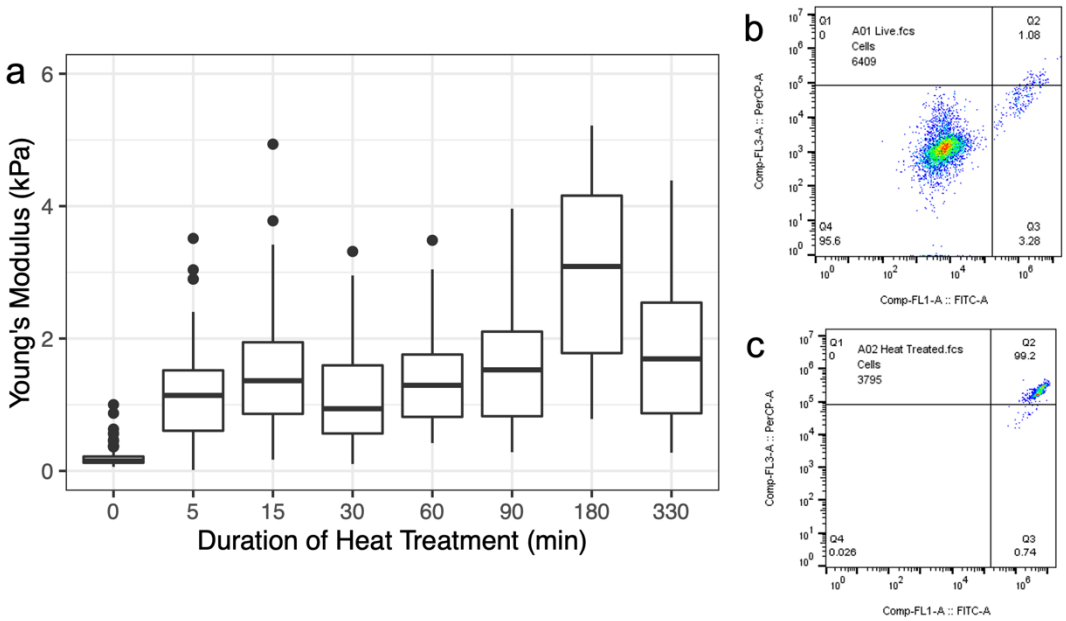

Figure 62 – Large stiffness changes observed in necrotic cells after 5 minutes of 65°C heat treatment – a) Jurkat T-cell leukemia cells were exposed to different durations of 65°C heat treatment and AFM was used to measure the stiffness of cells after heat treatment. Live (b) and heat treated cells (c) were stained with FITC-labelled Annexin V and 7-AAD (detected in the FL3 channel) to identify whether cells were in early stage apoptosis or necrosis.

Beyond necrotic cell death, we were also interested in investigating the effect of apoptotic cell death on cell mechanics. To minimize the time between a 42°C heat treatment and AFM stiffness measurements, we utilized an AFM stage heater which could heat the fluidic environment of cells during AFM measurements. Using this system, we observed an increase in cell stiffness directly after the cells reached 42°C (Figure 63a). The rolling average stiffness value also continued to rise as cells were exposed to heat during the course of the experiment. When testing for apoptotic stage after 2 hours post heat treatment, we observed 21% of cells in the early apoptotic phase and 39% of cells in the late apoptotic/necrotic phase (Figure 63b and Figure 63c). This data suggests cell stiffness could potentially be used as an early apoptotic marker as we start to see differences in cell mechanics much earlier than we are able to detect apoptosis by conventional, fluorescently labelled methods such as immunocytochemistry.

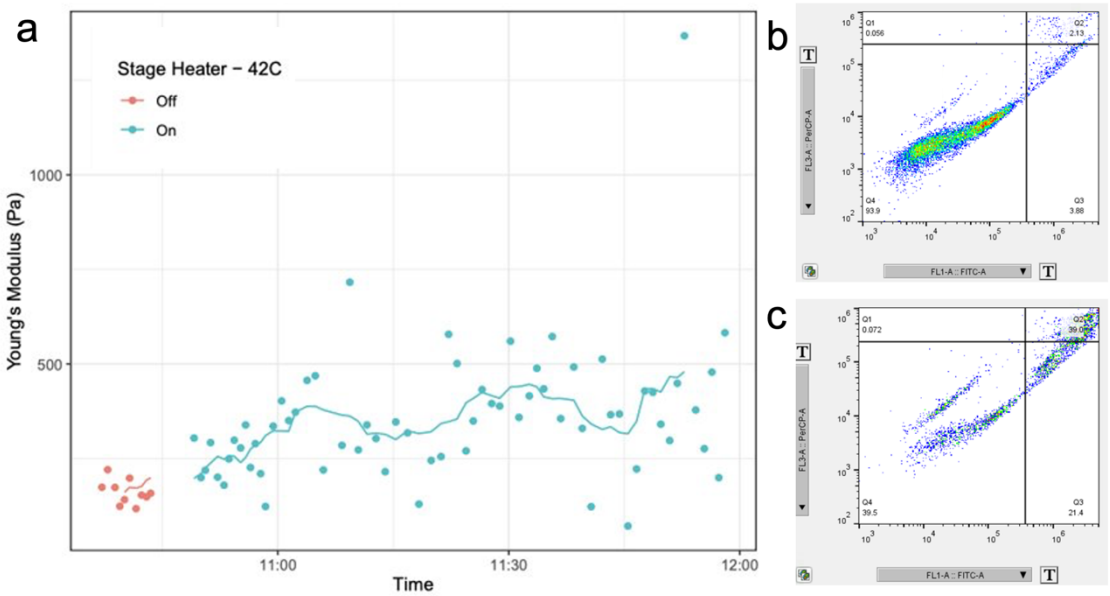

Figure 63 – Fast stiffness change response also observed in apoptotic cells heated to 42°C on AFM stage – a) Jurkat T-cell leukemia cells were exposed to 42°C heat treatment on AFM stage for measurement of cell stiffness during the heat treatment process. Live (b) and heat-treated cells (c) were stained with FITC-labelled Annexin V and 7-AAD (detected in the FL3 channel) to identify whether cells were in early-stage apoptosis or necrosis.

7.4.2 – Mechanical characterization of cells treated with chemotherapy

Beyond heat-treatment to induce necrosis and apoptosis, we also used chemotherapeutics to induce cancer cell death to observe the temporal relationship between cell death and cell mechanics. SU-DHL-4, a B cell lymphoma cell line, cells were treated with varying amounts of the chemotherapeutic agent doxorubicin. We took AFM measurements after 1 day of treatment as well as 3 days after a 1-day course of doxorubicin treatment. We observed significant stiffness changes in cells after one day of treatment at high doses (over 0.6 μg/mL) while medium to low doses of chemotherapeutics did not result in major

cell stiffness changes (Tukey HSD, $p < 0.01$) (Figure 64a). However, 4 days after the start of chemotherapeutic treatment, we observed significant changes in stiffness in doses as low as 0.05 μg/mL (Tukey HSD, $p < 0.05$) (Figure 64b). Further study of how cell mechanics change over time during chemotherapeutic regimens could help further understanding of the cell dying process and possible early identification of chemo resistant cells in culture.

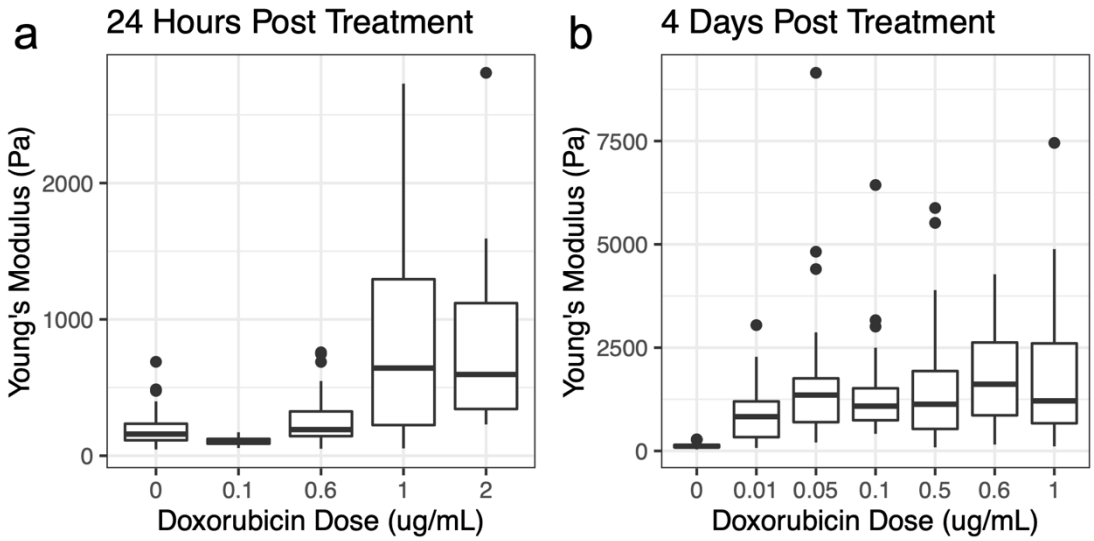

Figure 64 – Temporal dynamics of mechanical changes observed in chemotherapeutic-treated cells – SU-DHL-4 B-cell lymphoma cells were treated with different concentrations of the chemotherapeutic Doxorubicin and AFM was used to measure cell stiffness after a) 24 hours and b) 4 days post-treatment.

7.4.3 – Mechanical characterization of cell undergoing pyroptosis

Recently, the world has observed the quick spread of severe acute respiratory syndrome coronavirus 2 (SARS-CoV-2). The clinical manifestations of

SARS-CoV-2 can vary; however, acute respiratory distress syndrome is found in most patients[265]. Acute respiratory distress syndrome (ARDS) is described as a progressive, uncontrolled inflammation of lung tissue[266]. A common characteristic of ARDS is alveolar injury due to epithelial cell death. Evidence points to pyroptosis, a highly inflammatory form of programmed cell death, as a possible cause of the observed epithelial damage. Li D. et al. suggested that pyroptosis of macrophages plays an important role in the pathogenesis of ARDS[267]. Pyroptosis is a highly inflammatory cell death that results in the release of the infected cell's inflammatory contents. In patients with severe ARDS, there is no resolution of acute inflammation. Instead, they show a persistent response to the pathogens, which results in an accumulation of proinflammatory cytokines causing uncontrolled lung edema[267]. A better understanding of the pyroptosis mechanism could lead to the development of better treatments for SARS-CoV-2. Currently, there is no detailed knowledge on how this phenomenon alters the physical properties of compromised cells. Recently, Man et al. identified that the immune response to control Salmonella infection causes polymerization of actin in macrophages, which results in increased cellular stiffness[268]. We hypothesize that cellular stiffness is increased in pyroptotic cells.

We optimized a procedure that would allow us to initiate pyroptosis in differentiated macrophages. THP1 monocytes into macrophages using a treatment of 50 ng/mL PMA for three days. Cells were then primed with 1 μg/mL LPS for three hours and 20 μM nigericin for 30 minutes was used to trigger the

NLPR3 inflammasome and initiate pyroptosis. With this method, we observed over 60% of the treated cells undergoing pyroptosis (Figure 65a-d). The presence of inflammasomes was confirmed by using a FAM-FLICA Caspase-1 assay, which allowed the assessment of caspase-1 activation by detecting the fluorescent signal emitted after it binds to FLICA reagent. The assay served as a direct measure of caspase-1 and helped confirm pyroptosis initiation in THP1 cells. We then initiated pyroptosis in a population of cells and used Fluorescence Activated Sorting (FACS) to sort cells based on their Caspase-1 activity. We measured mechanical changes of the pure pyroptotic population using AFM. There was a slight, but non-significant increase of cell stiffness in the FLICA-Caspase1 positive cells (ANOVA, $p > 0.05$, n=50 per cell type) (Figure 65e). While this increase in stiffness is small, it is possible we could optimize a microfluidic procedure for separating cells in a label-free manner based off of this stiffness difference for further study of cells in a pre-pyroptotic phase.

This project aimed to better understand the biophysical and mechanical changes in immune cells' experience after being compromised. SARS-COV-2 causes an uncontrolled inflammatory response, and pyroptosis is involved in its pathology. Our studies have highlighted the importance of a better understanding of the mechanical and physical changes immune cells experience when undergoing this process. Being able to characterize and separate the different cell populations is key to developing better treatments of diseases that involve pyroptosis.

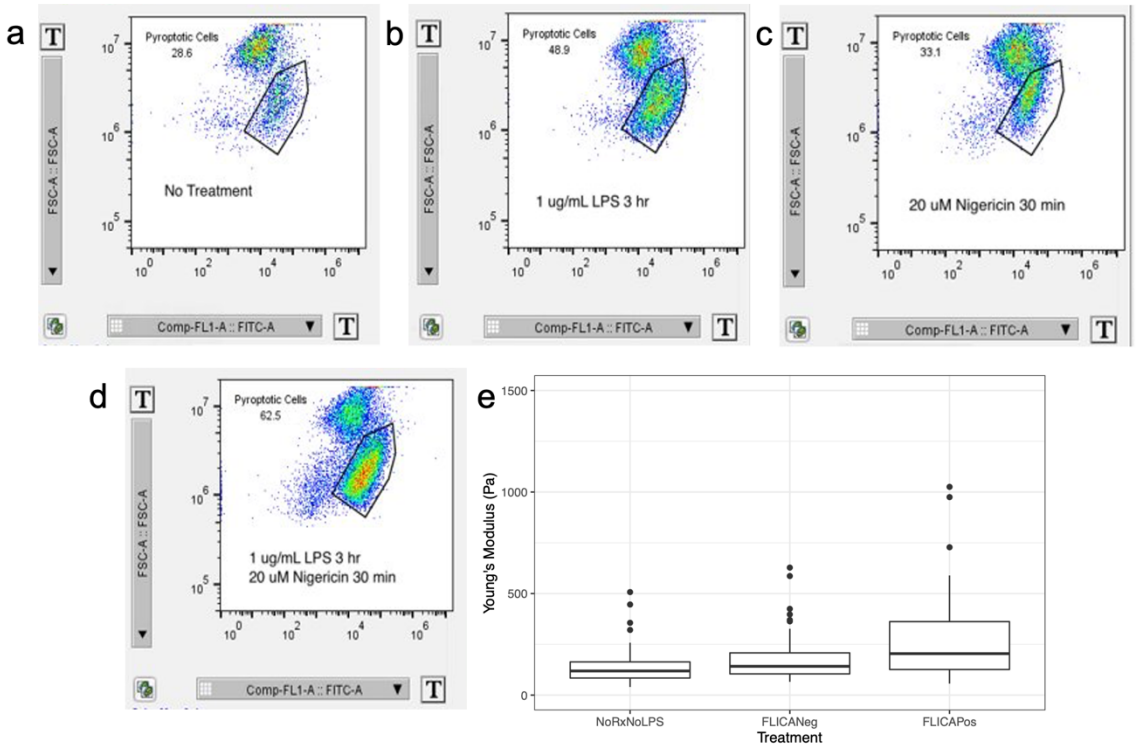

Figure 65 – Pyroptosis induced cells show significant increase in cell stiffness – Flow cytometry plots show the effect of LPS priming and nigericin treatment of PMA-differentiated THP1 macrophage on the induction of pyroptosis as measured by Caspase-1 activity labelled with FAM-FLICA (a-d). e) FACS was utilized to separate Caspase-1 positive and negative cells after LPS priming and nigericin treatment and AFM was used to measure the cell stiffness of each population. The FLICA-Caspase1 positive cells are significantly stiffer than the FLICA negative cells (Tukey HSD, $p < 0.05$, n=50 per cell type).

7.4.4 – Mechanical sorting of cells by viability

The knowledge of cell viability is critical to understand and predict cell culture health and therapeutic responses to pharmacological agents[269,270]. To address the need to monitor and purify cells for viability, we highlight the use of physical changes that occur to cells after a loss of viability that could be leveraged in a label-free manner to sense and sort viable cells to substantially benefit cell manufacturing. AFM analysis of both viable and nonviable cell populations was

conducted to quantify the biomechanical properties. The average Young's modulus was found to be 0.2 kPa for viable cells and 1.92 kPa for nonviable cells ($p < 10^{-11}$, Welch two sample t-test), indicating a significant increase of nearly one order of magnitude (Figure 66a). The dramatic increase in cell stiffness with cell death is a result of several structural changes to the cell, including the dynamic changes of actin fibers, the presence of stress fibers, cell wall modification, and changes of cortical actin organization under the cell membrane[271–274]. We conducted an analysis of the viscoelastic properties of viable and nonviable cells by calculating viscoelastic time constants using the Maxwell–Weichert model. To best fit the data, two Maxwell elements were chosen: the slow and the fast relaxation time constants. The slow viscous time constant was found to be 0.41 s^{-1} for viable cells and 0.31 s^{-1} for nonviable cells ($p < 10^{-11}$, Welch two sample t-test) (Figure 66b), and the fast time constant was 5.75 s^{-1} for viable cells and 6.10 s^{-1} for nonviable cells ($p < 0.24$, Welch two sample t-test, data not shown). This result shows that the slow viscous time constant of viable and nonviable Jurkat cells is also significantly different and thus, it can be considered as a viability marker.

We also measured the adhesion force of both viable and nonviable cell populations by examining the attraction between the cell and the AFM probe upon cell contact. The magnitude of the adhesion force was found to be 0.22 nN for viable cells and 1.05 nN for nonviable cells ($p < 0.0001$, Welch two sample t-test) (Figure 66c). This result shows that nonviable cells are more adhesive to the silica

bead of the AFM tip than viable cells. Furthermore, the same observation is noticeable during the experiments in which nonviable cells interact with the PDMS and glass surfaces of a microfluidic channel. The increased attractive interaction of the nonviable cells in comparison to viable cells could lead to adhesion to the ridges, an inhibition of continuous flow, or a modification to the trajectory of flow[275]. The cell size was the final biomechanical property that we evaluated from the analysis of optical images taken during AFM measurements. The average diameter was found to be 15.5 μm for viable cells and 13.83 μm for nonviable cells ($p < 10^{-7}$, Welch two sample t-test) (Figure 66d). These size differences are in agreement with what was reported as a change in cell size during apoptosis and necrosis[272,276], though we note that cell size can vary over the course of apoptosis. Overall, both stiffness and adhesion properties provide opportunities for sortable viability markers due to the large differences between viable and nonviable cells. Thus, the enrichment and separation between the two cell populations in microfluidic separation device likely rely on difference in these properties.

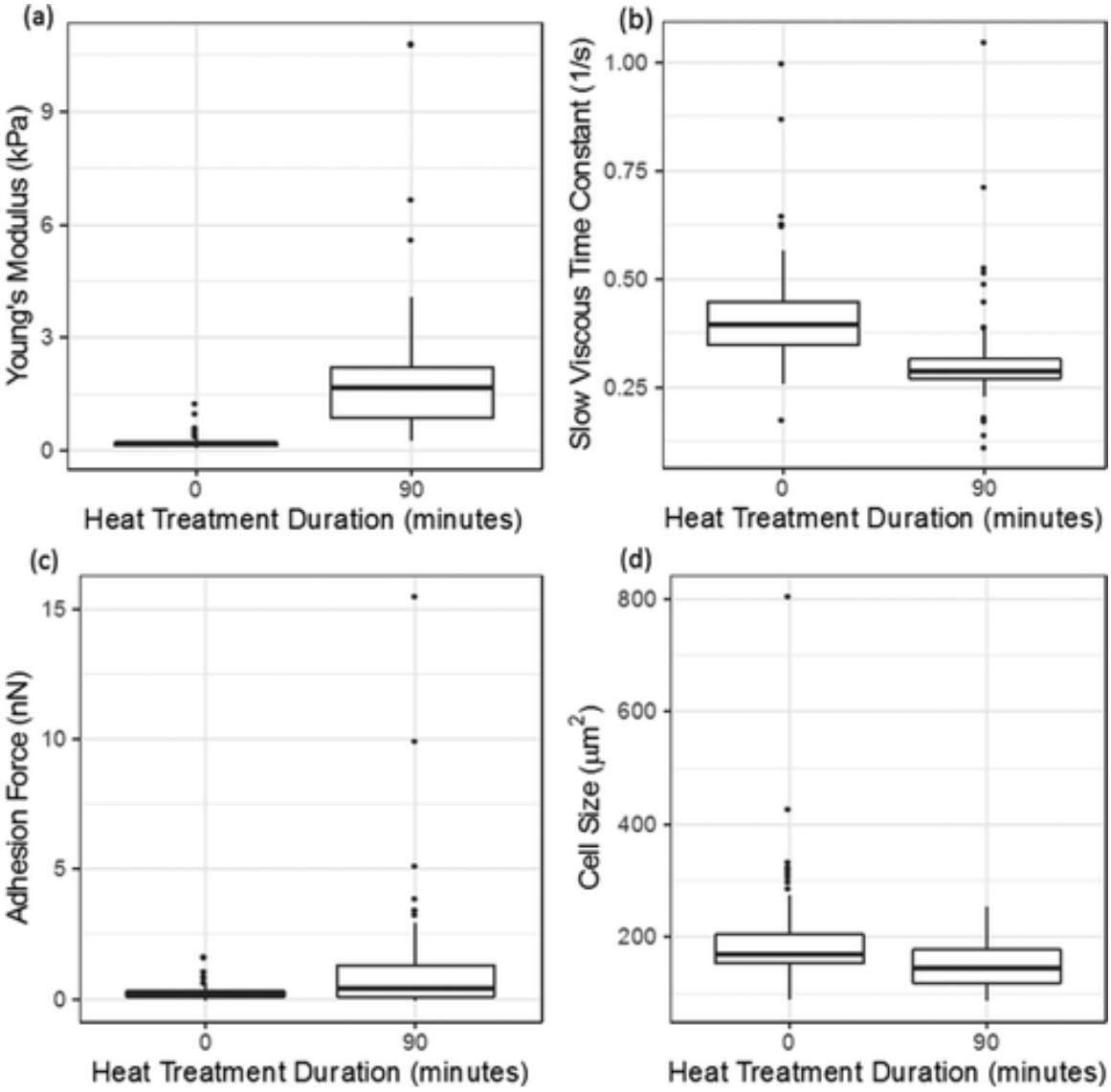

Figure 66 – Mechanical properties of viable and nonviable Jurkat cells after heat treatment from AFM measurement – a) Young's modulus (Welch two sample t-test, $p < 0.0001$), b) slow viscous time constant (Welch two sample t-test, $p < 0.0001$), c) adhesion force (Welch two sample t-test, $p < 0.0001$), and d) cell size (Welch two sample t-test, $p < 0.0001$). Number of cells, $n = 268$.

We used a cell mechanics-based microfluidic sorting device similar to the one described in chapters 4 and 5 to sort cells by viability and used high-speed video tracking analysis of each cells' cumulative deflection to use the microfluidic device as a sensor. Since the cumulative deflection reduces several cell-specific

variables to a single parameter, there could be even more benefit in examining the trajectories of cells with more detail to determine the cell viability. We therefore used the cell size, deflection (Dx), and interaction time (Tx) at each ridge (x) as input variables to perform a dimensionality reduction using a principal component analysis (PCA) to further explore the clustering of viable and nonviable cell populations. We reduced the 11 variables to two dimensions (Figure 67). A clustering of the viable cell population with the PCA showed no overlap with the clustering from the nonviable cell population, suggesting that the detection could be even more accurate than sensing on cumulative deflection alone. The principal components PC1 and PC2, respectively, explain 23 and 19.8% of the total variance. From the loading of each of the variables in the reduced data space, we notice that the interaction time with a ridge correlates with the deflection on the next ridge; for example, $T1$ correlates with $D2$ and $T2$ correlates with $D3$. It is also observed that viable cells cluster to a single location, while the nonviable cells cluster to three regions of the plot by the ridge where they deflect. It should be noted that all three clusters of the nonviable cells ended at the same outlet. However, PCA can be used to identify different routes of cell translation and possibly subsets of nonviable cells that are not distinguished by collecting from outlets.

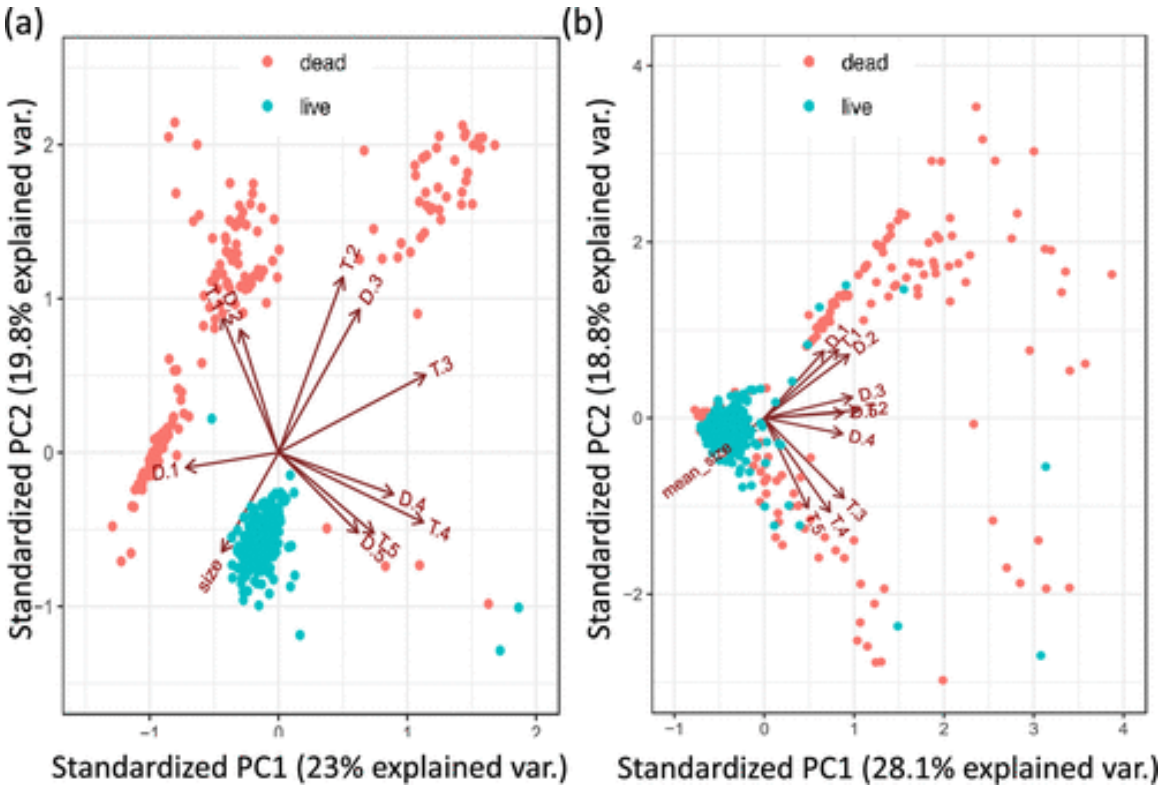

Figure 67 – PCA analysis of nonviable and viable cells based on cell trajectory features in microfluidic device – The cell deflection at each ridge, cell interaction time at each ridge, and cell size for a) Jurkat and b) SU-DHL-4 cells in the microfluidic sensing device were used to cluster cells on viability status. A total of 489 Jurkat cells and 650 SU-DHL-4 cells were analyzed.

7.5 – Conclusions

In summary, cell mechanics play an important role as a biomarker that can be utilized for separating cells by their healthy or diseased states. For example, we have proposed the sorting of nucleated blood cells for lymphocyte isolation, sorting of embryonic stem cells to select for more pluripotent cells, sorting of cardiac progenitor cells for enrichment of cells more likely to differentiate into desired cardiomyocyte cells, sorting liquid biopsy samples from ovarian cancer patients to isolate metastatic cancer cells, and sorting cells based on their viability

to help the health of a cell culture, identify chemo resistant cells or study cells in a pre-pyroptotic phase. In addition to the applications in cell sorting, studying cell mechanics also allows us to better understand different disease states of cells. For example, the cell stiffening process in leukemic hematopoietic stem cells is important for the retention and proper maturation of developing blood cells. Cell stiffness and adhesion play an important role in endothelial tube formation and investigating the mechanics of different CCM mutations allows us to better understand the disease. Studying the stiffness of the trabecular meshwork of diseased and treated glaucoma model eyes allows to better understand both the disease and the mechanism of treatment for a new therapeutic. This chapter has also described advances in methods, such as the use of linear elastography as well as the combination of fluorescence microscopy and AFM force mapping to better understand the role of nuclear mechanics for metastatic and non-metastatic cells. Overall, studying cell mechanical properties allows for a richer understanding of cell biology, both in healthy and diseased paradigms.

CHAPTER 8 – CONCLUSIONS

8.1 – Summary

The long-term goal of this body of work was to explore the molecular and mechanical mechanisms driving metastasis that could lead to the discovery of new diagnostics and therapeutic targets to find and stop key processes of metastatic cells. To reach this goal, I developed a new method to correlate mechanical, morphological and genetic data for the same single cells (chapter 3). Additionally, I leveraged a novel microfluidics approach (designed in chapter 4) for cell sorting based upon biophysical properties in combination with single gene knockouts across the entire genome for the high-throughput discovery of genes linked to cell mechanics and metastasis (chapter 5). I used these approaches to determine how cellular mechanics are regulated within the context of networks of cytoskeletal and structural proteins in addition to various transcription factors and signaling proteins associated with increased metastatic potential (chapter 6). Beyond the process of metastasis, I have also shown that cell mechanics plays an important role in distinguishing between many cell states, acting as a phenotype marker for healthy, diseased, and dying cell behaviors (chapter 7).

Through this work I have investigated the hypothesis that there is a link between cell softening and mesenchymal, migratory phenotypes that is controlled by the expression of a network of genes of interest. These studies represent the first attempt to evaluate the entire genome for its role in directing cell mechanics

to understand the connection between cancer cell genotype, phenotype and mechanotype both across the whole genome and on the single cell level. Being able to collect information about the combination of gene expression data and cell stiffness measurements in a high throughput fashion and an in-depth exploration of genes related to mechanics and metastatic potential is contributing to great advancement of our understanding of the metastatic cascade with potential application in many other fields where cell mechanics play a role in disease state.

8.2 – Next Steps, Future Work, and Further Applications

8.2.1 – Single Cell Genomechanics

The single cell genomechanics method described in chapter 3 represents the first exploration of combining cell mechanical data and gene expression data at the single cell level. While it started to paint a picture of a mechanistic understanding of the mechanical regulation of the metastatic process, we do recognize several limitations to the current study as well as potential future lines of experimentation. The current methodology focused on the use of cancer cell lines grown on rigid glass and tissue culture plastics coated with ECM materials, which does not accurately represent the microenvironment of tumor cells and is likely affecting the results of the cell mechanical measurements. To improve the translatability of the work, the method could be applied to dissociated primary tumor cells or collected circulating tumor cells attached to tissue-stiffness-

matched hydrogels, although that soft substrate would need to be accounted for during AFM mechanical measurements. Additionally, the current method could be expanded from targeted RT-qPCR to single cell RNA sequencing, using a system such as SmartSeq2, to broaden the scope of the genes explored, as we are certain there are other interesting relationships between a cell's genotype, mechanotype, and phenotype that we have not yet observed, some of which were explored in chapters 5, 6, and 7. Finally, our study explores the intrinsic properties of single cells, but we recognize that cell migration and metastasis also involves important interactions between multiple cells and their environment, which is beyond the scope of this study and this method.

In the future, this method could also be applied to other cancer types and dissociated primary tumor cells as well as to other biological problems where cellular mechanics can play a role in differences between normal and diseased state, including chemoresistance, angiogenesis, and stem cell differentiation[122–125]. Although the study has focused on the role of cellular mechanics in the context of cancer and metastasis, because the cytoskeletal makeup and motility machinery is conserved across cell types, we expect that this method could be used to investigate the correlation between a softer mechanotype with a more motile phenotype in both diseased and healthy tissues.

8.2.2 – Multiplexing Microfluidics

Improving the throughput of the Sulchek Lab microfluidic mechanics-based sorting device was an enabling step that not only made the GeCKO mechanical screen described in chapter 5 possible, but also opens up the possibility for this technology to be applied to many other fields such as cell manufacturing or clinical sample processing. In the cell manufacturing space, large quantities of cells (tens of millions) are needed for therapeutic doses of cell therapies such as stem cell or immunotherapies. We greatly improved the processing time which transformed a 9-day experiment into a 9-hour experiment, which allowed us to generate a new, large linked dataset between cell mechanotype and phenotype that was previously impossible to collect. This method for parallelization and multiplexing can also act as an enabling step for other microfluidic systems that also include multiple outlets and rely on flow parameters for successful operation. For example, the use of a flow-balanced manifold for inlet and outlet flow control could also be applied to other cell separation devices such as deterministic lateral displacement channels, pinched flow fractionation microchannels, and inertial separation spiral and serpentine microfluidics.

Even though we were able to demonstrate a twenty-fold increase of cell throughput, there is still room for further improvement of the device through iterative design. For example, using the volumetric flow output data from both the analytical model and FEA model linearized device designs, we could further equalize the volumetric output to each outlet to ensure proper fractionation of

cell samples. Additionally, we could adjust the resistances of each outlet to allow for biased distribution of each outlet, which may be useful for samples with rare subpopulations that we would specifically like to collect. Through this process, we could also further equalize the flow velocity to each sorting channel from the manifold layer to allow for identical and optimized sorting in each channel. Along these same lines, there is room for further optimization of the specific flow parameters used to sort cells based on their stiffness. For our model heat-treatment system, this may allow for improved soft cell enrichment as well as a reduced yield of stiffened cells in the soft outlet. An additional change that would help reduce stiffened cell yield in the soft outlets would be to work to deconvolute the size and stiffness parameters in the sorting process. This could be accomplished by using multi-stage sorting, separating cells first by size followed by stiffness to distinguish between small, stiff cells and large, soft cells. Finally, throughput could be further improved by adding more channels in parallel as well as exploring the possibility of vertical stacking of the multiplexed device using via connections between each sorting layer.

8.2.3 – GeCKO Mechanics

The GeCKO mechanical screen is the first of its kind to investigate the effect of gene knockouts across the entire genome on cell mechanical properties. For our study, we focused on using a knockout sgRNA library in a metastatic ovarian cancer cell line. Developing this methodology opens the door to many

other lines of experimentation. For example, this screen could be repeated for other cell types, including ovarian cells of different metastatic potential, different cancer types, different stem cell lines, or even a generic fibroblast cell. By observing the overlapping gene knockouts that are enriched in the softened and stiffened subsets, we could compile a list of genes universally associated with cell mechanics across healthy and diseased cell types. Additionally this experiment could be expanded to also include GeCKO libraries against epigenetic genes, lncRNAs, or a genome-scale activation schema instead of knockout. Finally, any optimization suggested in 8.2.2 would also benefit our sorting ability that was described in chapter 5. Currently, our device is more effective at enriching for stiffened cells than softened cells, limiting our focus to gene knockouts that result in cell stiffening. By adjusting the flow parameters and outlet resistances, we could envision a device that has improved sensitivity to soft subpopulations that would better allow us to explore both ends of the spectrum of shifting cell mechanics.

8.2.4 – Hypothesis Testing

Because of the large datasets generated in aims 1 and 2 of this work, there are many, many more hypotheses that were generated about the intersection of mechanotype, genotype, and phenotype than we were able to explore in this work. The understanding of tested stiffness and viscosity regulators could be expanded by following up with more migration assays. This will allow us to link the role of cell mechanics and metastatic potential more clearly, especially for the less-

studied property of cell viscosity. The different responses of different cell lines to each proposed mechanics regulator leads to the questions of cell line specificity in the relationship between mechanics and gene expression as well as the role of cell state in changes to cell behavior and properties. Seeing as many genes were not associated as predicted with the genes in the network analyses, changing models for the network analysis may result in more accurately predicted relationships between master regulators and downstream genes of interest. This work could also be expanded further by choosing to perturb individual genes correlated with cell stiffness and viscosity to see their effect on cell mechanotype and phenotype. Finally, in addition to exploring further the relationships between cell mechanics and cell gene expression as identified in chapters 3 and 5, the large linked single cell data set also includes many gene-gene relationships that could be investigated further.

REFERENCES

1. Rianna, C. & Radmacher, M. Cell mechanics as a marker for diseases: Biomedical applications of AFM. in *AIP Conf. Proc.* **1760,** 020057 (AIP Publishing, 2016).

2. Maxwell, C. & Roskelley, C. *Genomic Instability and Cancer Metastasis: Mechanisms, Emerging Themes, and Novel Therapeutic Strategies*. (Springer, 2014).

3. Mehlen, P. & Puisieux, A. Metastasis: a question of life or death. *Nat. Rev. Cancer* **6,** 449–458 (2006).

4. Morgan-Parkes, J. H. Metastases: mechanisms, pathways, and cascades. *Am. J. Roentgenol.* **164,** 1075–1082 (1995).

5. Luzzi, K. J., MacDonald, I. C., Schmidt, E. E., Kerkvliet, N., Morris, V. L., Chambers, A. F. & Groom, A. C. Multistep Nature of Metastatic Inefficiency. *Am. J. Pathol.* **153,** 865–873 (1998).

6. Sleeman, J. P., Christofori, G., Fodde, R., Collard, J. G., Berx, G., Decraene, C. & Rüegg, C. Concepts of metastasis in flux: The stromal progression model. *Semin. Cancer Biol.* **22,** 174–186 (2012).

7. Azzi, S., Hebda, J. K. & Gavard, J. Vascular Permeability and Drug Delivery in Cancers. *Front. Oncol.* **3,** (2013).

8. Simpson, C. D., Anyiwe, K. & Schimmer, A. D. Anoikis resistance and tumor metastasis. *Cancer Lett.* **272,** 177–185 (2008).

9. Guo, P., Cai, B., Lei, M., Liu, Y. & Fu, B. M. Differential arrest and adhesion of tumor cells and microbeads in the microvasculature. *Biomech. Model. Mechanobiol.* **13,** 537–550 (2014).

10. Talmadge, J. E. & Fidler, I. J. AACR centennial series: the biology of cancer metastasis: historical perspective. *Cancer Res.* **70,** 5649–5669 (2010).

11. Martin, T. A., Ye, L., Sanders, A. J., Lane, J. & Jiang, W. G. *Cancer Invasion and Metastasis: Molecular and Cellular Perspective*. (Landes Bioscience, 2013). at <https://www.ncbi.nlm.nih.gov/books/NBK164700/>

12. Shankar, J. & Nabi, I. R. Actin Cytoskeleton Regulation of Epithelial Mesenchymal Transition in Metastatic Cancer Cells. *PLoS ONE* **10,** (2015).

13. Shao, M., Cao, L., Shen, C., Satpathy, M., Chelladurai, B., Bigsby, R. M., Nakshatri, H. & Matei, D. Epithelial-to-Mesenchymal Transition and Ovarian Tumor Progression Induced by Tissue Transglutaminase. *Cancer Res.* **69,** 9192–9201 (2009).

14. Chen, Z.-Y., Wang, P.-W., Shieh, D.-B., Chiu, K.-Y. & Liou, Y.-M. Involvement of gelsolin in TGF-beta 1 induced epithelial to mesenchymal transition in breast cancer cells. *J. Biomed. Sci.* **22,** (2015).

15. Mezencev, R., Matyunina, L. V., Jabbari, N. & McDonald, J. F. Snail-induced epithelial-to-mesenchymal transition of MCF-7 breast cancer cells: systems analysis of molecular changes and their effect on radiation and drug sensitivity. *BMC Cancer* **16,** (2016).

16. Hanahan, D. & Weinberg, R. A. Hallmarks of Cancer: The Next Generation. *Cell* **144,** 646–674 (2011).

17. Monteiro, J. & Fodde, R. Cancer stemness and metastasis: therapeutic consequences and perspectives. *Eur. J. Cancer Oxf. Engl. 1990* **46,** 1198–1203 (2010).

18. Hennessy, B. T., Gonzalez-Angulo, A.-M., Stemke-Hale, K., Gilcrease, M. Z., Krishnamurthy, S., Lee, J.-S., Fridlyand, J., Sahin, A., Agarwal, R., Joy, C., Liu, W., Stivers, D., Baggerly, K., Carey, M., Lluch, A., Monteagudo, C., He, X., Weigman, V., Fan, C., Palazzo, J., Hortobagyi, G. N., Nolden, L. K., Wang, N. J., Valero, V., Gray, J. W., Perou, C. M. & Mills, G. B. Characterization of a naturally occurring breast cancer subset enriched in epithelial-to-mesenchymal transition and stem cell characteristics. *Cancer Res.* **69,** 4116–4124 (2009).

19. Heerboth, S., Housman, G., Leary, M., Longacre, M., Byler, S., Lapinska, K., Willbanks, A. & Sarkar, S. EMT and tumor metastasis. *Clin. Transl. Med.* **4,** (2015).

20. Pastushenko, I., Brisebarre, A., Sifrim, A., Fioramonti, M., Revenco, T., Boumahdi, S., Keymeulen, A. V., Brown, D., Moers, V., Lemaire, S., Clercq, S. D., Minguijón, E., Balsat, C., Sokolow, Y., Dubois, C., Cock, F. D., Scozzaro, S., Sopena, F., Lanas, A., D'Haene, N., Salmon, I., Marine, J.-C., Voet, T., Sotiropoulou, P. A. & Blanpain, C. Identification of the tumour transition states occurring during EMT. *Nature* **556,** 463 (2018).

21. Xu, W., Mezencev, R., Kim, B., Wang, L., McDonald, J. & Sulchek, T. Cell Stiffness Is a Biomarker of the Metastatic Potential of Ovarian Cancer Cells. *PLOS ONE* **7,** e46609 (2012).

22. Guck, J., Schinkinger, S., Lincoln, B., Wottawah, F., Ebert, S., Romeyke, M., Lenz, D., Erickson, H. M., Ananthakrishnan, R., Mitchell, D., Käs, J., Ulvick, S. & Bilby, C. Optical Deformability as an Inherent Cell Marker for Testing Malignant Transformation and Metastatic Competence. *Biophys. J.* **88,** 3689–3698 (2005).

23. Kuznetsova, T. G., Starodubtseva, M. N., Yegorenkov, N. I., Chizhik, S. A. & Zhdanov, R. I. Atomic force microscopy probing of cell elasticity. *Micron* **38,** 824–833 (2007).

24. Pillarisetti, A., Desai, J. P., Ladjal, H., Schiffmacher, A., Ferreira, A. & Keefer, C. L. Mechanical phenotyping of mouse embryonic stem cells: increase in stiffness with differentiation. *Cell. Reprogramming* **13,** 371–380 (2011).

25. Haase, K. & Pelling, A. E. Investigating cell mechanics with atomic force microscopy. *J. R. Soc. Interface* **12,** 20140970 (2015).

26. Moreno-Flores, S., Benitez, R., Vivanco, M. dM & Toca-Herrera, J. L. Stress relaxation and creep on living cells with the atomic force microscope: a means to calculate elastic moduli and viscosities of cell components. *Nanotechnology* **21,** 445101 (2010).

27. Islam, M., Brink, H., Blanche, S., DiPrete, C., Bongiorno, T., Stone, N., Liu, A., Philip, A., Wang, G., Lam, W., Alexeev, A., Waller, E. K. & Sulchek, T. Microfluidic Sorting of Cells by Viability Based on Differences in Cell Stiffness. *Sci. Rep.* **7,** 1997 (2017).

28. Islam, M., Mezencev, R., McFarland, B., Brink, H., Campbell, B., Tasadduq, B., Waller, E. K., Lam, W., Alexeev, A. & Sulchek, T. Microfluidic cell sorting by stiffness to examine heterogenic responses of cancer cells to chemotherapy. *Cell Death Dis.* **9,** 239 (2018).

29. Carden, M. A., Fay, M., Sakurai, Y., McFarland, B., Blanche, S., DiPrete, C., Joiner, C. H., Sulchek, T. & Lam, W. A. Normal saline is associated with increased sickle red cell stiffness and prolonged transit times in a microfluidic model of the capillary system. *Microcirc. N. Y. N 1994* **24,** (2017).

30. Fay, M. E., Myers, D. R., Kumar, A., Turbyfield, C. T., Byler, R., Crawford, K., Mannino, R. G., Laohapant, A., Tyburski, E. A., Sakurai, Y., Rosenbluth, M. J., Switz, N. A., Sulchek, T. A., Graham, M. D. & Lam, W. A. Cellular softening

mediates leukocyte demargination and trafficking, thereby increasing clinical blood counts. *Proc. Natl. Acad. Sci. U. S. A.* **113,** 1987–1992 (2016).

31. Chernaya, O., Zhurikhina, A., Hladyshau, S., Pilcher, W., Young, K. M., Ortner, J., Andra, V., Sulchek, T. A. & Tsygankov, D. Biomechanics of Endothelial Tubule Formation Differentially Modulated by Cerebral Cavernous Malformation Proteins. *iScience* **9,** 347–358 (2018).

32. Bongiorno, T., Kazlow, J., Mezencev, R., Griffiths, S., Olivares-Navarrete, R., McDonald, J. F., Schwartz, Z., Boyan, B. D., McDevitt, T. C. & Sulchek, T. Mechanical stiffness as an improved single-cell indicator of osteoblastic human mesenchymal stem cell differentiation. *J. Biomech.* **47,** 2197–2204 (2014).

33. Bongiorno, T., Gura, J., Talwar, P., Chambers, D., Young, K. M., Arafat, D., Wang, G., Jackson-Holmes, E. L., Qiu, P., McDevitt, T. C. & Sulchek, T. Biophysical subsets of embryonic stem cells display distinct phenotypic and morphological signatures. *PLOS ONE* **13,** e0192631 (2018).

34. Bongiorno, T., Chojnowski, J. L., Lauderdale, J. D. & Sulchek, T. Cellular Stiffness as a Novel Stemness Marker in the Corneal Limbus. *Biophys. J.* **111,** 1761–1772 (2016).

35. Brown, A. C., Fiore, V. F., Sulchek, T. A. & Barker, T. H. Physical and chemical microenvironmental cues orthogonally control the degree and duration of fibrosis-associated epithelial-to-mesenchymal transitions. *J. Pathol.* **229,** 25–35 (2013).

36. Kumar, P., Smith, T., Raeman, R., Chopyk, D. M., Brink, H., Liu, Y., Sulchek, T. & Anania, F. A. Periostin promotes liver fibrogenesis by activating lysyl oxidase in hepatic stellate cells. *J. Biol. Chem.* **293,** 12781–12792 (2018).

37. White, A. K., VanInsberghe, M., Petriv, O. I., Hamidi, M., Sikorski, D., Marra, M. A., Piret, J., Aparicio, S. & Hansen, C. L. High-throughput microfluidic single-cell RT-qPCR. *Proc. Natl. Acad. Sci.* **108,** 13999–14004 (2011).

38. Ziegenhain, C., Vieth, B., Parekh, S., Reinius, B., Guillaumet-Adkins, A., Smets, M., Leonhardt, H., Heyn, H., Hellmann, I. & Enard, W. Comparative Analysis of Single-Cell RNA Sequencing Methods. *Mol. Cell* **65,** 631-643.e4 (2017).

39. Gross, A., Schoendube, J., Zimmermann, S., Steeb, M., Zengerle, R. & Koltay, P. Technologies for Single-Cell Isolation. *Int. J. Mol. Sci.* **16,** 16897–16919 (2015).

40. Zhang, M., Matyunina, L. V., Walker, L. D., Chen, W., Xiao, H., Benigno, B. B., Wu, R. & McDonald, J. F. Evidence for the importance of post-transcriptional regulatory changes in ovarian cancer progression and the contribution of miRNAs. *Sci. Rep.* **7,** 8171 (2017).

41. Maier, T., Güell, M. & Serrano, L. Correlation of mRNA and protein in complex biological samples. *FEBS Lett.* **583,** 3966–3973 (2009).

42. Easwaran, H., Tsai, H.-C. & Baylin, S. B. Cancer Epigenetics: Tumor Heterogeneity, Plasticity of Stem-like States, and Drug Resistance. *Mol. Cell* **54,** 716–727 (2014).

43. Genshaft, A. S., Li, S., Gallant, C. J., Darmanis, S., Prakadan, S. M., Ziegler, C. G. K., Lundberg, M., Fredriksson, S., Hong, J., Regev, A., Livak, K. J., Landegren, U. & Shalek, A. K. Multiplexed, targeted profiling of single-cell proteomes and transcriptomes in a single reaction. *Genome Biol.* **17,** 188 (2016).

44. Angermueller, C., Clark, S. J., Lee, H. J., Macaulay, I. C., Teng, M. J., Hu, T. X., Krueger, F., Smallwood, S. A., Ponting, C. P., Voet, T., Kelsey, G., Stegle, O. & Reik, W. Parallel single-cell sequencing links transcriptional and epigenetic heterogeneity. *Nat. Methods* **13,** 229–232 (2016).

45. Dixit, A., Parnas, O., Li, B., Chen, J., Fulco, C. P., Jerby-Arnon, L., Marjanovic, N. D., Dionne, D., Burks, T., Raychndhury, R., Adamson, B., Norman, T. M., Lander, E. S., Weissman, J. S., Friedman, N. & Regev, A. Perturb-seq: Dissecting molecular circuits with scalable single cell RNA profiling of pooled genetic screens. *Cell* **167,** 1853-1866.e17 (2016).

46. Shalem, O., Sanjana, N. E. & Zhang, F. High-throughput functional genomics using CRISPR–Cas9. *Nat. Rev. Genet.* **16,** 299–311 (2015).

47. Shah, S., Lubeck, E., Zhou, W. & Cai, L. In Situ Transcription Profiling of Single Cells Reveals Spatial Organization of Cells in the Mouse Hippocampus. *Neuron* **92,** 342–357 (2016).

48. Ståhl, P. L., Salmén, F., Vickovic, S., Lundmark, A., Navarro, J. F., Magnusson, J., Giacomello, S., Asp, M., Westholm, J. O., Huss, M., Mollbrink, A., Linnarsson, S., Codeluppi, S., Borg, Å., Pontén, F., Costea, P. I., Sahlén, P., Mulder, J., Bergmann, O., Lundeberg, J. & Frisén, J. Visualization and analysis of gene expression in tissue sections by spatial transcriptomics. *Science* **353,** 78–82 (2016).

49. Cadwell, C. R., Palasantza, A., Jiang, X., Berens, P., Deng, Q., Yilmaz, M., Reimer, J., Shen, S., Bethge, M., Tolias, K. F., Sandberg, R. & Tolias, A. S. Electrophysiological, transcriptomic and morphologic profiling of single neurons using Patch-seq. *Nat. Biotechnol.* **34,** 199–203 (2016).

50. Cadwell, C. R., Scala, F., Li, S., Livrizzi, G., Shen, S., Sandberg, R., Jiang, X. & Tolias, A. S. Multimodal profiling of single-cell morphology, electrophysiology, and gene expression using Patch-seq. *Nat. Protoc.* **12,** 2531–2553 (2017).

51. Kimmerling, R. J., Prakadan, S. M., Gupta, A. J., Calistri, N. L., Stevens, M. M., Olcum, S., Cermak, N., Drake, R. S., Pelton, K., De Smet, F., Ligon, K. L., Shalek, A. K. & Manalis, S. R. Linking single-cell measurements of mass, growth rate, and gene expression. *Genome Biol.* **19,** 207 (2018).

52. Joung, J., Konermann, S., Gootenberg, J. S., Abudayyeh, O. O., Platt, R. J., Brigham, M. D., Sanjana, N. E. & Zhang, F. Genome-scale CRISPR-Cas9 knockout and transcriptional activation screening. *Nat. Protoc.* **12,** 828–863 (2017).

53. Doench, J. G., Fusi, N., Sullender, M., Hegde, M., Vaimberg, E. W., Donovan, K. F., Smith, I., Tothova, Z., Wilen, C., Orchard, R., Virgin, H. W., Listgarten, J. & Root, D. E. Optimized sgRNA design to maximize activity and minimize off-target effects of CRISPR-Cas9. *Nat. Biotechnol.* **34,** 184–191 (2016).

54. Chen, S., Sanjana, N. E., Zheng, K., Shalem, O., Lee, K., Shi, X., Scott, D. A., Song, J., Pan, J. Q., Weissleder, R., Lee, H., Zhang, F. & Sharp, P. A. Genome-wide CRISPR screen in a mouse model of tumor growth and metastasis. *Cell* **160,** 1246–1260 (2015).

55. Shen, J. P., Zhao, D., Sasik, R., Luebeck, J., Birmingham, A., Bojorquez-Gomez, A., Licon, K., Klepper, K., Pekin, D., Beckett, A., Sanchez, K., Thomas, A., Kuo, C.-C., Du, D., Roguev, A., Lewis, N. E., Chang, A. N., Kreisberg, J. F., Krogan, N., Qi, L., Ideker, T. & Mali, P. Combinatorial CRISPR-Cas9 screens for de novo mapping of genetic interactions. *Nat. Methods* **14,** 573–576 (2017).

56. Mills, G. B., May, C., Hill, M., Campbell, S., Shaw, P. & Marks, A. Ascitic fluid from human ovarian cancer patients contains growth factors necessary for intraperitoneal growth of human ovarian adenocarcinoma cells. *J. Clin. Invest.* **86,** 851–855 (1990).

57. Hotulainen, P., Paunola, E., Vartiainen, M. K. & Lappalainen, P. Actin-depolymerizing factor and cofilin-1 play overlapping roles in promoting rapid

F-actin depolymerization in mammalian nonmuscle cells. *Mol. Biol. Cell* **16,** 649–664 (2005).

58. Moseley, J. B., Okada, K., Balcer, H. I., Kovar, D. R., Pollard, T. D. & Goode, B. L. Twinfilin is an actin-filament-severing protein and promotes rapid turnover of actin structures in vivo. *J Cell Sci* **119,** 1547–1557 (2006).

59. An, S. S., Laudadio, R. E., Lai, J., Rogers, R. A. & Fredberg, J. J. Stiffness changes in cultured airway smooth muscle cells. *Am. J. Physiol. Cell Physiol.* **283,** C792-801 (2002).

60. Wang, G., Mao, W., Byler, R., Patel, K., Henegar, C., Alexeev, A. & Sulchek, T. Stiffness Dependent Separation of Cells in a Microfluidic Device. *PLOS ONE* **8,** e75901 (2013).

61. Wang, G., Turbyfield, C., Crawford, K., Alexeev, A. & Sulchek, T. Cellular enrichment through microfluidic fractionation based on cell biomechanical properties. *Microfluid. Nanofluidics* **19,** 987–993 (2015).

62. Wang, G., Crawford, K., Turbyfield, C., Lam, W., Alexeev, A. & Sulchek, T. Microfluidic cellular enrichment and separation through differences in viscoelastic deformation. *Lab. Chip* **15,** 532–540 (2014).

63. Tasadduq, B., Lam, W., Alexeev, A., Sarioglu, A. F. & Sulchek, T. Enhancing size based size separation through vertical focus microfluidics using secondary flow in a ridged microchannel. *Sci. Rep.* **7,** 17375 (2017).

64. Tasadduq, B., McFarland, B., Islam, M., Alexeev, A., Sarioglu, A. F. & Sulchek, T. Continuous Sorting of Cells Based on Differential P Selectin Glycoprotein Ligand Expression Using Molecular Adhesion. (2017). doi:10.1021/acs.analchem.7b02878

65. Luo, Q., Kuang, D., Zhang, B. & Song, G. Cell stiffness determined by atomic force microscopy and its correlation with cell motility. *Biochim. Biophys. Acta BBA - Gen. Subj.* **1860,** 1953–1960 (2016).

66. Swaminathan, V., Mythreye, K., O'Brien, E. T., Berchuck, A., Blobe, G. C. & Superfine, R. Mechanical Stiffness Grades Metastatic Potential in Patient Tumor Cells and in Cancer Cell Lines. *Cancer Res.* **71,** 5075–5080 (2011).

67. Gawad, C., Koh, W. & Quake, S. R. Single-cell genome sequencing: current state of the science. *Nat. Rev. Genet.* **17,** 175–188 (2016).

68. Cheon, D.-J., Tong, Y., Sim, M.-S., Dering, J., Berel, D., Cui, X., Lester, J., Beach, J. A., Tighiouart, M., Walts, A. E., Karlan, B. Y. & Orsulic, S. A Collagen-Remodeling Gene Signature Regulated by TGF-β Signaling Is Associated with Metastasis and Poor Survival in Serous Ovarian Cancer. *Clin. Cancer Res.* **20,** 711–723 (2014).

69. Foster, R., Buckanovich, R. J. & Rueda, B. R. Ovarian cancer stem cells: Working towards the root of stemness. *Cancer Lett.* **338,** 147–157 (2013).

70. Cheaib, B., Auguste, A. & Leary, A. The PI3K/Akt/mTOR pathway in ovarian cancer: therapeutic opportunities and challenges. *Chin. J. Cancer* **34,** 4–16 (2015).

71. Lawson, D. A., Bhakta, N. R., Kessenbrock, K., Prummel, K. D., Yu, Y., Takai, K., Zhou, A., Eyob, H., Balakrishnan, S., Wang, C.-Y., Yaswen, P., Goga, A. & Werb, Z. Single-cell analysis reveals a stem-cell program in human metastatic breast cancer cells. *Nature* **526,** 131–135 (2015).

72. Fife, C. M., McCarroll, J. A. & Kavallaris, M. Movers and shakers: cell cytoskeleton in cancer metastasis. *Br. J. Pharmacol.* **171,** 5507–5523 (2014).

73. Dupont, S., Morsut, L., Aragona, M., Enzo, E., Giulitti, S., Cordenonsi, M., Zanconato, F., Le Digabel, J., Forcato, M., Bicciato, S., Elvassore, N. & Piccolo, S. Role of YAP/TAZ in mechanotransduction. *Nature* **474,** 179–183 (2011).

74. Wu, Z., Wu, L., Weng, D., Xu, D., Geng, J. & Zhao, F. Reduced expression of lamin A/C correlates with poor histological differentiation and prognosis in primary gastric carcinoma. *J. Exp. Clin. Cancer Res. CR* **28,** 8 (2009).

75. Davies, D. L. & Bouldin, D. W. A Cluster Separation Measure. *IEEE Trans. Pattern Anal. Mach. Intell.* **PAMI-1,** 224–227 (1979).

76. Lee, H. W., Park, Y. M., Lee, S. J., Cho, H. J., Kim, D.-H., Lee, J.-I., Kang, M.-S., Seol, H. J., Shim, Y. M., Nam, D.-H., Kim, H. H. & Joo, K. M. Alpha-smooth muscle actin (ACTA2) is required for metastatic potential of human lung adenocarcinoma. *Clin. Cancer Res.* clincanres.1181.2013 (2013). doi:10.1158/1078-0432.CCR-13-1181

77. Guo, C., Liu, S., Wang, J., Sun, M.-Z. & Greenaway, F. T. ACTB in cancer. *Clin. Chim. Acta* **417,** 39–44 (2013).

78. Rao, G., Pierobon, M., Kim, I.-K., Hsu, W.-H., Deng, J., Moon, Y.-W., Petricoin, E. F., Zhang, Y.-W., Wang, Y. & Giaccone, G. Inhibition of AKT1 signaling

promotes invasion and metastasis of non-small cell lung cancer cells with K-RAS or EGFR mutations. *Sci. Rep.* **7,** 7066 (2017).

79. Wang, Y., Shao, F. & Chen, L. ALDH1A2 suppresses epithelial ovarian cancer cell proliferation and migration by downregulating STAT3. *OncoTargets Ther.* **11,** 599–608 (2018).

80. Lee, M.-S., Lee, J., Kim, J. H., Kim, W. T., Kim, W.-J., Ahn, H. & Park, J. Overexpression of caldesmon is associated with tumor progression in patients with primary non-muscle-invasive bladder cancer. *Oncotarget* **6,** 40370–40384 (2015).

81. Celus, W., Di Conza, G., Oliveira, A. I., Ehling, M., Costa, B. M., Wenes, M. & Mazzone, M. Loss of Caveolin-1 in Metastasis-Associated Macrophages Drives Lung Metastatic Growth through Increased Angiogenesis. *Cell Rep.* **21,** 2842–2854 (2017).

82. Li, W., Ma, H., Zhang, J., Zhu, L., Wang, C. & Yang, Y. Unraveling the roles of CD44/CD24 and ALDH1 as cancer stem cell markers in tumorigenesis and metastasis. *Sci. Rep.* **7,** 13856 (2017).

83. Tonoli, H. & Barrett, J. C. CD82 metastasis suppressor gene: a potential target for new therapeutics? *Trends Mol. Med.* **11,** 563–570 (2005).

84. Mrozik, K. M., Blaschuk, O. W., Cheong, C. M., Zannettino, A. C. W. & Vandyke, K. N-cadherin in cancer metastasis, its emerging role in haematological malignancies and potential as a therapeutic target in cancer. *BMC Cancer* **18,** (2018).

85. Gugnoni, M., Sancisi, V., Gandolfi, G., Manzotti, G., Ragazzi, M., Giordano, D., Tamagnini, I., Tigano, M., Frasoldati, A., Piana, S. & Ciarrocchi, A. Cadherin-6 promotes EMT and cancer metastasis by restraining autophagy. *Oncogene* **36,** 667–677 (2017).

86. Yang, Z.-L., Miao, X., Xiong, L., Zou, Q., Yuan, Y., Li, J., Liang, L., Chen, M. & Chen, S. CFL1 and Arp3 are biomarkers for metastasis and poor prognosis of squamous cell/adenosquamous carcinomas and adenocarcinomas of gallbladder. *Cancer Invest.* **31,** 132–139 (2013).

87. Yoshida, R., Kimura, N., Harada, Y. & Ohuchi, N. The loss of E-cadherin, alpha- and beta-catenin expression is associated with metastasis and poor prognosis in invasive breast cancer. *Int. J. Oncol.* **18,** 513–520 (2001).

88. Kao, S.-H., Wang, W.-L., Chen, C.-Y., Chang, Y.-L., Wu, Y.-Y., Wang, Y.-T., Wang, S.-P., Nesvizhskii, A. I., Chen, Y.-J., Hong, T.-M. & Yang, P.-C. GSK3β controls epithelial-mesenchymal transition and tumor metastasis by CHIP-mediated degradation of Slug. *Oncogene* **33,** 3172–3182 (2014).

89. Zhang, W., Wang, S., Wang, Q., Yang, Z., Pan, Z. & Li, L. Overexpression of cysteine cathepsin L is a marker of invasion and metastasis in ovarian cancer. *Oncol. Rep.* **31,** 1334–1342 (2014).

90. Chatterjee, S., Azad, B. B. & Nimmagadda, S. The Intricate Role of CXCR4 in Cancer. *Adv. Cancer Res.* **124,** 31–82 (2014).

91. Sasaki, T., Hiroki, K. & Yamashita, Y. The role of epidermal growth factor receptor in cancer metastasis and microenvironment. *BioMed Res. Int.* **2013,** 546318 (2013).

92. van der Gun, B. T. F., Melchers, L. J., Ruiters, M. H. J., de Leij, L. F. M. H., McLaughlin, P. M. J. & Rots, M. G. EpCAM in carcinogenesis: the good, the bad or the ugly. *Carcinogenesis* **31,** 1913–1921 (2010).

93. Savoy, R. M. & Ghosh, P. M. The dual role of filamin A in cancer: can't live with (too much of) it, can't live without it. *Endocr. Relat. Cancer* **20,** R341–R356 (2013).

94. Fujita, H., Okada, F., Hamada, J., Hosokawa, M., Moriuchi, T., Koya, R. C. & Kuzumaki, N. Gelsolin functions as a metastasis suppressor in B16-BL6 mouse melanoma cells and requirement of the carboxyl-terminus for its effect. *Int. J. Cancer* **93,** 773–780 (2001).

95. Lewis, A. M., Varghese, S., Xu, H. & Alexander, H. R. Interleukin-1 and cancer progression: the emerging role of interleukin-1 receptor antagonist as a novel therapeutic agent in cancer treatment. *J. Transl. Med.* **4,** 48 (2006).

96. Blake, A., Dragan, M., Tirona, R. G., Hardy, D. B., Brackstone, M., Tuck, A. B., Babwah, A. V. & Bhattacharya, M. G protein-coupled KISS1 receptor is overexpressed in triple negative breast cancer and promotes drug resistance. *Sci. Rep.* **7,** 46525 (2017).

97. Cho, S., Kitadai, Y., Yoshida, S., Tanaka, S., Yoshihara, M., Yoshida, K. & Chayama, K. Deletion of the KIT gene is associated with liver metastasis and poor prognosis in patients with gastrointestinal stromal tumor in the stomach. *Int. J. Oncol.* **28,** 1361–1367 (2006).

98. Irianto, J., Pfeifer, C. R., Ivanovska, I. L., Swift, J. & Discher, D. E. Nuclear lamins in cancer. *Cell. Mol. Bioeng.* **9,** 258–267 (2016).

99. Liu, J., Ping, W., Zu, Y. & Sun, W. Correlations of lysyl oxidase with MMP2/MMP9 expression and its prognostic value in non-small cell lung cancer. *Int. J. Clin. Exp. Pathol.* **7,** 6040–6047 (2014).

100. Wang, H., Fan, L., Wei, J., Weng, Y., Zhou, L., Shi, Y., Zhou, W., Ma, D. & Wang, C. Akt Mediates Metastasis-Associated Gene 1 (MTA1) Regulating the Expression of E-cadherin and Promoting the Invasiveness of Prostate Cancer Cells. *PLoS ONE* **7,** (2012).

101. Li, B., Xu, W. W., Lam, A. K. Y., Wang, Y., Hu, H.-F., Guan, X. Y., Qin, Y. R., Saremi, N., Tsao, S. W., He, Q.-Y. & Cheung, A. L. M. Significance of PI3K/AKT signaling pathway in metastasis of esophageal squamous cell carcinoma and its potential as a target for anti-metastasis therapy. *Oncotarget* **8,** 38755–38766 (2017).

102. Luxen, D., Gielen, G. H., Waha, A., Isselstein, L., Müller, T., Koch, P., Hammes, J., Becker, A., Simon, M., Wurst, P., Endl, E., Pietsch, T., Gessi, M. & Waha, A. MTSS1 is epigenetically regulated in glioma cells and inhibits glioma cell motility. *Transl. Oncol.* **10,** 70–79 (2016).

103. Gordon, C. A., Gulzar, Z. G. & Brooks, J. D. NUSAP1 expression is upregulated by loss of RB1 in prostate cancer cells. *The Prostate* **75,** 517–526 (2015).

104. Zheng, B., Liang, L., Wang, C., Huang, S., Cao, X., Zha, R., Liu, L., Jia, D., Tian, Q., Wu, J., Ye, Y., Wang, Q., Long, Z., Zhou, Y., Du, C., He, X. & Shi, Y. MicroRNA-148a Suppresses Tumor Cell Invasion and Metastasis by Downregulating ROCK1 in Gastric Cancer. *Clin. Cancer Res.* **17,** 7574–7583 (2011).

105. Sang, Y., Chen, M.-Y., Luo, D., Zhang, R.-H., Wang, L., Li, M., Luo, R., Qian, C.-N., Shao, J.-Y., Zeng, Y.-X. & Kang, T. TEL2 suppresses metastasis by down-regulating SERPINE1 in nasopharyngeal carcinoma. *Oncotarget* **6,** 29240–29253 (2015).

106. Kang, Y., Ling, J., Suzuki, R., Roife, D., Chopin-Laly, X., Truty, M. J., Chatterjee, D., Wang, H., Thomas, R. M., Katz, M. H., Chiao, P. J. & Fleming, J. B. SMAD4 regulates cell motility through transcription of N-cadherin in human pancreatic ductal epithelium. *PloS One* **9,** e107948 (2014).

107. Padua, D. & Massagué, J. Roles of TGFbeta in metastasis. *Cell Res.* **19,** 89–102 (2009).

108. Lin, H., Zhang, Y., Wang, H., Xu, D., Meng, X., Shao, Y., Lin, C., Ye, Y., Qian, H. & Wang, S. Tissue inhibitor of metalloproteinases-3 transfer suppresses malignant behaviors of colorectal cancer cells. *Cancer Gene Ther.* **19,** 845–851 (2012).

109. Hu, L., Lau, S. H., Tzang, C.-H., Wen, J.-M., Wang, W., Xie, D., Huang, M., Wang, Y., Wu, M.-C., Huang, J.-F., Zeng, W.-F., Sham, J. S. T., Yang, M. & Guan, X.-Y. Association of Vimentin overexpression and hepatocellular carcinoma metastasis. *Oncogene* **23,** 298–302 (2004).

110. Borcherding, N., Kusner, D., Kolb, R., Xie, Q., Li, W., Yuan, F., Velez, G., Askeland, R., Weigel, R. J. & Zhang, W. Paracrine WNT5A Signaling Inhibits Expansion of Tumor-Initiating Cells. *Cancer Res.* **75,** 1972–1982 (2015).

111. Nagaishi, M., Nakata, S., Ono, Y., Hirata, K., Tanaka, Y., Suzuki, K., Yokoo, H. & Hyodo, A. Tumoral and stromal expression of Slug, ZEB1, and ZEB2 in brain metastasis. *J. Clin. Neurosci. Off. J. Neurosurg. Soc. Australas.* **46,** 124–128 (2017).

112. Matias-Guiu, J. A., Díaz-Álvarez, J., Ayala, J. L., Risco-Martín, J. L., Moreno-Ramos, T., Pytel, V., Matias-Guiu, J., Carreras, J. L. & Cabrera-Martín, M. N. Clustering Analysis of FDG-PET Imaging in Primary Progressive Aphasia. *Front. Aging Neurosci.* **10,** (2018).

113. Liu, C.-Y., Lin, H.-H., Tang, M.-J. & Wang, Y.-K. Vimentin contributes to epithelial-mesenchymal transition cancer cell mechanics by mediating cytoskeletal organization and focal adhesion maturation. *Oncotarget* **6,** 15966–15983 (2015).

114. Spurlin, T. A., Bhadriraju, K., Chung, K.-H., Tona, A. & Plant, A. L. The treatment of collagen fibrils by tissue transglutaminase to promote vascular smooth muscle cell contractile signaling. *Biomaterials* **30,** 5486–5496 (2009).

115. Lee, J., Condello, S., Yakubov, B., Emerson, R., Caperell-Grant, A., Hitomi, K., Xie, J. & Matei, D. Tissue Transglutaminase Mediated Tumor-Stroma Interaction Promotes Pancreatic Cancer Progression. *Clin. Cancer Res. Off. J. Am. Assoc. Cancer Res.* **21,** 4482–4493 (2015).

116. Wei, S. C., Fattet, L., Tsai, J. H., Guo, Y., Pai, V. H., Majeski, H. E., Chen, A. C., Sah, R. L., Taylor, S. S., Engler, A. J. & Yang, J. Matrix stiffness drives

Epithelial-Mesenchymal Transition and tumour metastasis through a TWIST1-G3BP2 mechanotransduction pathway. *Nat. Cell Biol.* **17,** 678–688 (2015).

117. Li, F., Cima, I., Vo, J. H., Tan, M.-H. & Ohl, C. D. Single Cell Hydrodynamic Stretching and Microsieve Filtration Reveal Genetic, Phenotypic and Treatment-Related Links to Cellular Deformability. *Micromachines* **11,** 486 (2020).

118. Sreenivasappa, H., Chaki, S. P., Lim, S.-M., Trzeciakowski, J. P., Davidson, M. W., Rivera, G. M. & Trache, A. Selective regulation of cytoskeletal tension and cell–matrix adhesion by RhoA and Src. *Integr. Biol.* **6,** 743–754 (2014).

119. Cheung, K. J., Gabrielson, E., Werb, Z. & Ewald, A. J. Collective Invasion in Breast Cancer Requires a Conserved Basal Epithelial Program. *Cell* **155,** 1639–1651 (2013).

120. Konen, J., Summerbell, E., Dwivedi, B., Galior, K., Hou, Y., Rusnak, L., Chen, A., Saltz, J., Zhou, W., Boise, L. H., Vertino, P., Cooper, L., Salaita, K., Kowalski, J. & Marcus, A. I. Image-guided genomics of phenotypically heterogeneous populations reveals vascular signalling during symbiotic collective cancer invasion. *Nat. Commun.* **8,** 1–15 (2017).

121. Hapach, L. A., Carey, S. P., Schwager, S. C., Taufalele, P. V., Wang, W., Mosier, J. A., Ortiz-Otero, N., McArdle, T. J., Goldblatt, Z. E., Lampi, M. C., Bordeleau, F., Marshall, J. R., Richardson, I. M., Li, J., King, M. R. & Reinhart-King, C. A. Phenotypic Heterogeneity and Metastasis of Breast Cancer Cells. *Cancer Res.* **81,** 3649–3663 (2021).

122. Islam, M., Mezencev, R., McFarland, B., Brink, H., Campbell, B., Tasadduq, B., Waller, E. K., Lam, W., Alexeev, A. & Sulchek, T. Microfluidic cell sorting by stiffness to examine heterogenic responses of cancer cells to chemotherapy. *Cell Death Dis.* **9,** 1–12 (2018).

123. Chernaya, O., Zhurikhina, A., Hladyshau, S., Pilcher, W., Young, K. M., Ortner, J., Andra, V., Sulchek, T. A. & Tsygankov, D. Biomechanics of Endothelial Tubule Formation Differentially Modulated by Cerebral Cavernous Malformation Proteins. *iScience* **9,** 347–358 (2018).

124. Ni, F., Yu, W.-M., Wang, X., Fay, M. E., Young, K. M., Qiu, Y., Lam, W. A., Sulchek, T. A., Cheng, T., Scadden, D. T. & Qu, C.-K. Ptpn21 Controls Hematopoietic Stem Cell Homeostasis and Biomechanics. *Cell Stem Cell* **24,** 608-620.e6 (2019).

125. Bongiorno, T., Gura, J., Talwar, P., Chambers, D., Young, K. M., Arafat, D., Wang, G., Jackson-Holmes, E. L., Qiu, P., McDevitt, T. C. & Sulchek, T. Biophysical subsets of embryonic stem cells display distinct phenotypic and morphological signatures. *PLOS ONE* **13,** e0192631 (2018).

126. Masaeli, M., Sollier, E., Amini, H., Mao, W., Camacho, K., Doshi, N., Mitragotri, S., Alexeev, A. & Di Carlo, D. Continuous Inertial Focusing and Separation of Particles by Shape. *Phys. Rev. X* **2,** 031017 (2012).

127. Wu, Z., Chen, Y., Wang, M. & Chung, A. J. Continuous inertial microparticle and blood cell separation in straight channels with local microstructures. *Lab. Chip* **16,** 532–542 (2016).

128. Nawaz, A. A., Urbanska, M., Herbig, M., Nötzel, M., Kräter, M., Rosendahl, P., Herold, C., Toepfner, N., Kubánková, M., Goswami, R., Abuhattum, S., Reichel, F., Müller, P., Taubenberger, A., Girardo, S., Jacobi, A. & Guck, J. Intelligent image-based deformation-assisted cell sorting with molecular specificity. *Nat. Methods* **17,** 595–599 (2020).

129. Fox, M. B., Esveld, D. C., Valero, A., Luttge, R., Mastwijk, H. C., Bartels, P. V., van den Berg, A. & Boom, R. M. Electroporation of cells in microfluidic devices: a review. *Anal. Bioanal. Chem.* **385,** 474–485 (2006).

130. Joo, B., Hur, J., Kim, G.-B., Yun, S. G. & Chung, A. J. Highly Efficient Transfection of Human Primary T Lymphocytes Using Droplet-Enabled Mechanoporation. *ACS Nano* **15,** 12888–12898 (2021).

131. Liu, A., Islam, M., Stone, N., Varadarajan, V., Jeong, J., Bowie, S., Qiu, P., Waller, E. K., Alexeev, A. & Sulchek, T. Microfluidic generation of transient cell volume exchange for convectively driven intracellular delivery of large macromolecules. *Mater. Today* **21,** 703–712 (2018).

132. Timm, A. C., Shankles, P. G., Foster, C. M., Doktycz, M. J. & Retterer, S. T. Toward Microfluidic Reactors for Cell-Free Protein Synthesis at the Point-of-Care. *Small Weinh. Bergstr. Ger.* **12,** 810–817 (2016).

133. Sharma, S., Zapatero-Rodríguez, J., Estrela, P. & O'Kennedy, R. Point-of-Care Diagnostics in Low Resource Settings: Present Status and Future Role of Microfluidics. *Biosensors* **5,** 577–601 (2015).

134. Warkiani, M. E., Wu, L., Tay, A. K. P. & Han, J. Large-Volume Microfluidic Cell Sorting for Biomedical Applications. *Annu. Rev. Biomed. Eng.* **17,** 1–34 (2015).

135. Shen, Y., Yalikun, Y. & Tanaka, Y. Recent advances in microfluidic cell sorting systems. *Sens. Actuators B Chem.* **282,** 268–281 (2019).

136. Hochstetter, A., Vernekar, R., Austin, R. H., Becker, H., Beech, J. P., Fedosov, D. A., Gompper, G., Kim, S.-C., Smith, J. T., Stolovitzky, G., Tegenfeldt, J. O., Wunsch, B. H., Zeming, K. K., Krüger, T. & Inglis, D. W. Deterministic Lateral Displacement: Challenges and Perspectives. *ACS Nano* **14,** 10784–10795 (2020).

137. Hur, S. C., Henderson-MacLennan, N. K., McCabe, E. R. B. & Di Carlo, D. Deformability-based cell classification and enrichment using inertial microfluidics. *Lab. Chip* **11,** 912 (2011).

138. San-Miguel, A. & Lu, H. *Microfluidics as a tool for C. elegans research*. *WormBook Online Rev. C Elegans Biol. Internet* (WormBook, 2018). at <https://www.ncbi.nlm.nih.gov/books/NBK174829/>

139. Lecault, V., White, A. K., Singhal, A. & Hansen, C. L. Microfluidic single cell analysis: from promise to practice. *Curr. Opin. Chem. Biol.* **16,** 381–390 (2012).

140. Park, J. W., Vahidi, B., Taylor, A. M., Rhee, S. W. & Jeon, N. L. Microfluidic culture platform for neuroscience research. *Nat. Protoc.* **1,** 2128–2136 (2006).

141. Taylor, A. M., Blurton-Jones, M., Rhee, S. W., Cribbs, D. H., Cotman, C. W. & Jeon, N. L. A microfluidic culture platform for CNS axonal injury, regeneration and transport. *Nat. Methods* **2,** 599–605 (2005).

142. Sulchek, T. A., Alexeev, A. & Wang, G. Microfluidic device for separation of particles. (2013). at <https://patents.google.com/patent/US8356714B2/en>

143. Wang, G., Mao, W., Byler, R., Patel, K., Henegar, C., Alexeev, A. & Sulchek, T. Stiffness Dependent Separation of Cells in a Microfluidic Device. *PLOS ONE* **8,** e75901 (2013).

144. Wang, G., Crawford, K., Turbyfield, C., Lam, W., Alexeev, A. & Sulchek, T. Microfluidic cellular enrichment and separation through differences in viscoelastic deformation. *Lab. Chip* **15,** 532–540 (2014).

145. SULCHEK, T., Alexeev, A. & Tasadduq, B. Methods for Continuous Sorting of Cells Based on Molecular Adhesion. (2019). at <https://patents.google.com/patent/US20190360909A1/en>

146. Joung, J., Konermann, S., Gootenberg, J. S., Abudayyeh, O. O., Platt, R. J., Brigham, M. D., Sanjana, N. E. & Zhang, F. Genome-scale CRISPR-Cas9 knockout and transcriptional activation screening. *Nat. Protoc.* **12,** 828–863 (2017).

147. Sanjana, N. E., Shalem, O. & Zhang, F. Improved vectors and genome-wide libraries for CRISPR screening. *Nat. Methods* **11,** 783–784 (2014).

148. McClain, M. A., Culbertson, C. T., Jacobson, S. C., Allbritton, N. L., Sims, C. E. & Ramsey, J. M. Microfluidic Devices for the High-Throughput Chemical Analysis of Cells. *Anal. Chem.* **75,** 5646–5655 (2003).

149. Reece, A., Xia, B., Jiang, Z., Noren, B., McBride, R. & Oakey, J. Microfluidic techniques for high throughput single cell analysis. *Curr. Opin. Biotechnol.* **40,** 90–96 (2016).

150. Choi, G., Tang, Z. & Guan, W. Microfluidic high-throughput single-cell mechanotyping: Devices and applications. *Nanotechnol. Precis. Eng.* **4,** 045002 (2021).

151. Zhang, J., Yan, S., Sluyter, R., Li, W., Alici, G. & Nguyen, N.-T. Inertial particle separation by differential equilibrium positions in a symmetrical serpentine micro-channel. *Sci. Rep.* **4,** 4527 (2014).

152. Iv, C. W. S., Reyes, C. D. & López, G. P. Microfluidic cell sorting: a review of the advances in the separation of cells from debulking to rare cell isolation. *Lab. Chip* **15,** 1230–1249 (2015).

153. Inglis, D. W., Davis, J. A., Austin, R. H. & Sturm, J. C. Critical particle size for fractionation by deterministic lateral displacement. *Lab. Chip* **6,** 655–658 (2006).

154. Yamada, M., Nakashima, M. & Seki, M. Pinched Flow Fractionation: Continuous Size Separation of Particles Utilizing a Laminar Flow Profile in a Pinched Microchannel. *Anal. Chem.* **76,** 5465–5471 (2004).

155. Kuntaegowdanahalli, S. S., Bhagat, A. A. S., Kumar, G. & Papautsky, I. Inertial microfluidics for continuous particle separation in spiral microchannels. *Lab. Chip* **9,** 2973–2980 (2009).

156. Miller, B., Jimenez, M. & Bridle, H. Cascading and Parallelising Curvilinear Inertial Focusing Systems for High Volume, Wide Size Distribution, Separation and Concentration of Particles. *Sci. Rep.* **6,** 36386 (2016).

157. Saias, L., Autebert, J., Malaquin, L. & Viovy, J.-L. Design, modeling and characterization of microfluidic architectures for high flow rate, small footprint microfluidic systems. *Lab. Chip* **11,** 822–832 (2011).

158. Mach, A. J. & Di Carlo, D. Continuous scalable blood filtration device using inertial microfluidics. *Biotechnol. Bioeng.* **107,** 302–311 (2010).

159. Warkiani, M. E., Guan, G., Luan, K. B., Lee, W. C., Bhagat, A. A. S., Chaudhuri, P. K., Tan, D. S.-W., Lim, W. T., Lee, S. C., Chen, P. C. Y., Lim, C. T. & Han, J. Slanted spiral microfluidics for the ultra-fast, label-free isolation of circulating tumor cells. *Lab. Chip* **14,** 128–137 (2013).

160. Liu, Z., Huang, F., Du, J., Shu, W., Feng, H., Xu, X. & Chen, Y. Rapid isolation of cancer cells using microfluidic deterministic lateral displacement structure. *Biomicrofluidics* **7,** 011801 (2013).

161. Rosendahl, P., Plak, K., Jacobi, A., Kraeter, M., Toepfner, N., Otto, O., Herold, C., Winzi, M., Herbig, M., Ge, Y., Girardo, S., Wagner, K., Baum, B. & Guck, J. Real-time fluorescence and deformability cytometry. *Nat. Methods* **15,** 355–358 (2018).

162. Grimmer, A., Chen, X., Hamidović, M., Haselmayr, W., Ren, C. L. & Wille, R. Simulation before fabrication: a case study on the utilization of simulators for the design of droplet microfluidic networks. *RSC Adv.* **8,** 34733–34742 (2018).

163. Islam, M., Brink, H., Blanche, S., DiPrete, C., Bongiorno, T., Stone, N., Liu, A., Philip, A., Wang, G., Lam, W., Alexeev, A., Waller, E. K. & Sulchek, T. Microfluidic Sorting of Cells by Viability Based on Differences in Cell Stiffness. *Sci. Rep.* **7,** 1997 (2017).

164. Sader, J. E., Chon, J. W. M. & Mulvaney, P. Calibration of rectangular atomic force microscope cantilevers. *Rev. Sci. Instrum.* **70,** 3967–3969 (1999).

165. Tinevez, J.-Y., Perry, N., Schindelin, J., Hoopes, G. M., Reynolds, G. D., Laplantine, E., Bednarek, S. Y., Shorte, S. L. & Eliceiri, K. W. TrackMate: An open and extensible platform for single-particle tracking. *Methods* **115,** 80–90 (2017).

166. Ershov, D., Phan, M.-S., Pylvänäinen, J. W., Rigaud, S. U., Blanc, L. L., Charles-Orszag, A., Conway, J. R. W., Laine, R. F., Roy, N. H., Bonazzi, D., Duménil, G., Jacquemet, G. & Tinevez, J.-Y. *Bringing TrackMate into the era*

of machine-learning and deep-learning. 2021.09.03.458852 (2021). doi:10.1101/2021.09.03.458852

167. Schneider, C. A., Rasband, W. S. & Eliceiri, K. W. NIH Image to ImageJ: 25 years of image analysis. *Nat. Methods* **9,** 671–675 (2012).

168. Schindelin, J., Arganda-Carreras, I., Frise, E., Kaynig, V., Longair, M., Pietzsch, T., Preibisch, S., Rueden, C., Saalfeld, S., Schmid, B., Tinevez, J.-Y., White, D. J., Hartenstein, V., Eliceiri, K., Tomancak, P. & Cardona, A. Fiji: an open-source platform for biological-image analysis. *Nat. Methods* **9,** 676–682 (2012).

169. Gervais, T., El-Ali, J., Günther, A. & Jensen, K. F. Flow-induced deformation of shallow microfluidic channels. *Lab. Chip* **6,** 500 (2006).

170. Gervais, T., El-Ali, J., Günther, A. & Jensen, K. F. Flow-induced deformation of shallow microfluidic channels. *Lab. Chip* **6,** 500–507 (2006).

171. Islam, M., Raj, A., McFarland, B., Brink, H. M., Ciciliano, J., Fay, M., Myers, D. R., Flowers, C., Waller, E. K., Lam, W., Alexeev, A. & Sulchek, T. Stiffness based enrichment of leukemia cells using microfluidics. *APL Bioeng.* **4,** 036101 (2020).

172. Stone, N. E., Voigt, A. P., Cooke, J. A., Giacalone, J. C., Hanasoge, S., Mullins, R. F., Tucker, B. A. & Sulchek, T. Label-free microfluidic enrichment of photoreceptor cells. *Exp. Eye Res.* **199,** 108166 (2020).

173. Stone, N. E., Raj, A., Young, K. M., DeLuca, A. P., Chrit, F. E., Tucker, B. A., Alexeev, A., McDonald, J., Benigno, B. B. & Sulchek, T. Label-free microfluidic enrichment of cancer cells from non-cancer cells in ascites. *Sci. Rep.* **11,** 18032 (2021).

174. Golpanian, S., Schulman, I. H., Ebert, R. F., Heldman, A. W., DiFede, D. L., Yang, P. C., Wu, J. C., Bolli, R., Perin, E. C., Moyé, L., Simari, R. D., Wolf, A. & Hare, J. M. Concise Review: Review and Perspective of Cell Dosage and Routes of Administration From Preclinical and Clinical Studies of Stem Cell Therapy for Heart Disease. *Stem Cells Transl. Med.* **5,** 186–191 (2016).

175. Antfolk, M., Magnusson, C., Augustsson, P., Lilja, H. & Laurell, T. Acoustofluidic, Label-Free Separation and Simultaneous Concentration of Rare Tumor Cells from White Blood Cells. *Anal. Chem.* **87,** 9322–9328 (2015).

176. Corrigan-Curay, J., Kiem, H.-P., Baltimore, D., O'Reilly, M., Brentjens, R. J., Cooper, L., Forman, S., Gottschalk, S., Greenberg, P., Junghans, R., Heslop, H., Jensen, M., Mackall, C., June, C., Press, O., Powell, D., Ribas, A., Rosenberg, S., Sadelain, M., Till, B., Patterson, A. P., Jambou, R. C., Rosenthal, E., Gargiulo, L., Montgomery, M. & Kohn, D. B. T-cell immunotherapy: looking forward. *Mol. Ther. J. Am. Soc. Gene Ther.* **22,** 1564–1574 (2014).

177. Volpatti, L. R. & Yetisen, A. K. Commercialization of microfluidic devices. *Trends Biotechnol.* **32,** 347–350 (2014).

178. Doench, J. G. Am I ready for CRISPR? A user's guide to genetic screens. *Nat. Rev. Genet.* **19,** 67–80 (2018).

179. Love, M. I., Huber, W. & Anders, S. Moderated estimation of fold change and dispersion for RNA-seq data with DESeq2. *Genome Biol.* **15,** 550 (2014).

180. Egeberg, D. L., Lethan, M., Manguso, R., Schneider, L., Awan, A., Jørgensen, T. S., Byskov, A. G., Pedersen, L. B. & Christensen, S. T. Primary cilia and aberrant cell signaling in epithelial ovarian cancer. *Cilia* **1,** 15 (2012).

181. Ishikawa, T. Axoneme Structure from Motile Cilia. *Cold Spring Harb. Perspect. Biol.* **9,** a028076 (2017).

182. Torre, L. A., Trabert, B., DeSantis, C. E., Miller, K. D., Samimi, G., Runowicz, C. D., Gaudet, M. M., Jemal, A. & Siegel, R. L. Ovarian cancer statistics, 2018. *CA. Cancer J. Clin.* **68,** 284–296 (2018).

183. Committee on the State of the Science in Ovarian Cancer Research, Board on Health Care Services, Institute of Medicine, & National Academies of Sciences, Engineering, and Medicine. *Ovarian Cancers: Evolving Paradigms in Research and Care*. (National Academies Press (US), 2016). at <http://www.ncbi.nlm.nih.gov/books/NBK367618/>

184. McKenzie, A. J., Hicks, S. R., Svec, K. V., Naughton, H., Edmunds, Z. L. & Howe, A. K. The mechanical microenvironment regulates ovarian cancer cell morphology, migration, and spheroid disaggregation. *Sci. Rep.* **8,** 7228 (2018).

185. Lu, T. & Anvari, B. Characterization of the Viscoelastic Properties of Ovarian Cancer Cells Membranes by Optical Tweezers and Quantitative Phase Imaging. *Front. Phys.* **8,** 514 (2020).

186. Efremov, Yu. M., Dokrunova, A. A., Efremenko, A. V., Kirpichnikov, M. P., Shaitan, K. V. & Sokolova, O. S. Distinct impact of targeted actin

cytoskeleton reorganization on mechanical properties of normal and malignant cells. *Biochim. Biophys. Acta BBA - Mol. Cell Res.* **1853,** 3117–3125 (2015).

187. Pachenari, M., Seyedpour, S. M., Janmaleki, M., Shayan, S. B., Taranejoo, S. & Hosseinkhani, H. Mechanical properties of cancer cytoskeleton depend on actin filaments to microtubules content: Investigating different grades of colon cancer cell lines. *J. Biomech.* **47,** 373–379 (2014).

188. Suresh, S. Biomechanics and biophysics of cancer cells. *Acta Mater.* **55,** 3989–4014 (2007).

189. Ketene, A. N., Roberts, P. C., Shea, A. A., Schmelz, E. M. & Agah, M. Actin filaments play a primary role for structural integrity and viscoelastic response in cells. *Integr. Biol.* **4,** 540–549 (2012).

190. Ketene, A. N., Schmelz, E. M., Roberts, P. C. & Agah, M. The effects of cancer progression on the viscoelasticity of ovarian cell cytoskeleton structures. *Nanomedicine Nanotechnol. Biol. Med.* **8,** 93–102 (2012).

191. Krämer, A., Green, J., Pollard, J. & Tugendreich, S. Causal analysis approaches in Ingenuity Pathway Analysis. *Bioinformatics* **30,** 523–530 (2014).

192. Jiang, J.-G., Ning, Y.-G., Chen, C., Ma, D., Liu, Z.-J., Yang, S., Zhou, J., Xiao, X., Zhang, X. A., Edin, M. L., Card, J. W., Wang, J., Zeldin, D. C. & Wang, D. W. Cytochrome P450 Epoxygenase Promotes Human Cancer Metastasis. *Cancer Res.* **67,** 6665–6674 (2007).

193. Dennis, G., Sherman, B. T., Hosack, D. A., Yang, J., Gao, W., Lane, H. C. & Lempicki, R. A. DAVID: Database for Annotation, Visualization, and Integrated Discovery. *Genome Biol.* **4,** R60 (2003).

194. Hosack, D. A., Dennis, G., Sherman, B. T., Lane, H. C. & Lempicki, R. A. Identifying biological themes within lists of genes with EASE. *Genome Biol.* **4,** R70 (2003).

195. Politz, O., Siegel, F., Bärfacker, L., Bömer, U., Hägebarth, A., Scott, W. J., Michels, M., Ince, S., Neuhaus, R., Meyer, K., Fernández-Montalván, A. E., Liu, N., von Nussbaum, F., Mumberg, D. & Ziegelbauer, K. BAY 1125976, a selective allosteric AKT1/2 inhibitor, exhibits high efficacy on AKT signaling-dependent tumor growth in mouse models. *Int. J. Cancer* **140,** 449–459 (2017).

196. Li, P., Sheng, C., Huang, L., Zhang, H., Huang, L., Cheng, Z. & Zhu, Q. MiR-183/-96/-182 cluster is up-regulated in most breast cancers and increases cell proliferation and migration. *Breast Cancer Res.* **16,** 473 (2014).

197. Sarver, A. L., Li, L. & Subramanian, S. MicroRNA miR-183 Functions as an Oncogene by Targeting the Transcription Factor EGR1 and Promoting Tumor Cell Migration. *Cancer Res.* **70,** 9570–9580 (2010).

198. Ren, L.-H., Chen, W.-X., Li, S., He, X.-Y., Zhang, Z.-M., Li, M., Cao, R.-S., Hao, B., Zhang, H.-J., Qiu, H.-Q. & Shi, R.-H. MicroRNA-183 promotes proliferation and invasion in oesophageal squamous cell carcinoma by targeting programmed cell death 4. *Br. J. Cancer* **111,** 2003–2013 (2014).

199. Zhou, J., Zhang, C., Zhou, B. & Jiang, D. miR-183 modulated cell proliferation and apoptosis in ovarian cancer through the TGF-β/Smad4 signaling pathway. *Int. J. Mol. Med.* **43,** 1734–1746 (2019).

200. Sun, X., Xu, Y., Zhang, S., Li, X., Wang, Y., Zhang, Y., Zhao, X., Li, Y. & Wang, Y. MicroRNA-183 suppresses the vitality, invasion and migration of human osteosarcoma cells by targeting metastasis-associated protein 1. *Exp. Ther. Med.* **15,** 5058–5064 (2018).

201. Yang, C.-L., Zheng, X.-L., Ye, K., Ge, H., Sun, Y.-N., Lu, Y.-F. & Fan, Q.-X. MicroRNA-183 Acts as a Tumor Suppressor in Human Non-Small Cell Lung Cancer by Down-Regulating MTA1. *Cell. Physiol. Biochem. Int. J. Exp. Cell. Physiol. Biochem. Pharmacol.* **46,** 93–106 (2018).

202. Shu, J., Xia, Z., Li, L., Liang, E. T., Slipek, N., Shen, D., Foo, J., Subramanian, S. & Steer, C. J. Dose-dependent differential mRNA target selection and regulation by let-7a-7f and miR-17-92 cluster microRNAs. *RNA Biol.* **9,** 1275–1287 (2012).

203. Zhu, J., Liang, C., Hua, Y., Miao, C., Zhang, J., Xu, A., Zhao, K., Liu, S., Tian, Y., Dong, H., Zhang, C., Li, P., Su, S., Qin, C. & Wang, Z. The metastasis suppressor CD82/KAI1 regulates cell migration and invasion via inhibiting TGF-β 1/Smad signaling in renal cell carcinoma. *Oncotarget* **8,** 51559–51568 (2017).

204. Liu, W. M., Zhang, F., Moshiach, S., Zhou, B., Huang, C., Srinivasan, K., Khurana, S., Zheng, Y., Lahti, J. M. & Zhang, X. A. Tetraspanin CD82 Inhibits Protrusion and Retraction in Cell Movement by Attenuating the Plasma Membrane-Dependent Actin Organization. *PLOS ONE* **7,** e51797 (2012).

205. Huang, D. W., Sherman, B. T. & Lempicki, R. A. Systematic and integrative analysis of large gene lists using DAVID bioinformatics resources. *Nat. Protoc.* **4,** 44–57 (2008).

206. Westhoff, M. A., Serrels, B., Fincham, V. J., Frame, M. C. & Carragher, N. O. Src-Mediated Phosphorylation of Focal Adhesion Kinase Couples Actin and Adhesion Dynamics to Survival Signaling. *Mol. Cell. Biol.* **24,** 8113–8133 (2004).

207. Duperret, E. K., Dahal, A. & Ridky, T. W. Focal-adhesion-independent integrin-αv regulation of FAK and c-Myc is necessary for 3D skin formation and tumor invasion. *J. Cell Sci.* **128,** 3997–4013 (2015).

208. Domoto, T., Pyko, I. V., Furuta, T., Miyashita, K., Uehara, M., Shimasaki, T., Nakada, M. & Minamoto, T. Glycogen synthase kinase-3β is a pivotal mediator of cancer invasion and resistance to therapy. *Cancer Sci.* **107,** 1363–1372 (2016).

209. Endersby, R., Zhu, X., Hay, N., Ellison, D. W. & Baker, S. J. Nonredundant Functions for Akt Isoforms in Astrocyte Growth and Gliomagenesis in an Orthotopic Transplantation Model. *Cancer Res.* **71,** 4106–4116 (2011).

210. Iliopoulos, D., Polytarchou, C., Hatziapostolou, M., Kottakis, F., Maroulakou, I. G., Struhl, K. & Tsichlis, P. N. MicroRNAs Differentially Regulated by Akt Isoforms Control EMT and Stem Cell Renewal in Cancer Cells. *Sci. Signal.* **2,** ra62–ra62 (2009).

211. Shi, X., Wang, J., Lei, Y., Cong, C., Tan, D. & Zhou, X. Research progress on the PI3K/AKT signaling pathway in gynecological cancer (Review). *Mol. Med. Rep.* **19,** 4529–4535 (2019).

212. Liu, A., Yu, T., Young, K., Stone, N., Hanasoge, S., Kirby, T. J., Varadarajan, V., Colonna, N., Liu, J., Raj, A., Lammerding, J., Alexeev, A. & Sulchek, T. Cell Mechanical and Physiological Behavior in the Regime of Rapid Mechanical Compressions that Lead to Cell Volume Change. *Small* **16,** 1903857 (2020).

213. Darling, E. M., Topel, M., Zauscher, S., Vail, T. P. & Guilak, F. Viscoelastic properties of human mesenchymally-derived stem cells and primary osteoblasts, chondrocytes, and adipocytes. *J. Biomech.* **41,** 454–464 (2008).

214. Bongiorno, T., Kazlow, J., Mezencev, R., Griffiths, S., Olivares-Navarrete, R., McDonald, J. F., Schwartz, Z., Boyan, B. D., McDevitt, T. C. & Sulchek, T.

Mechanical stiffness as an improved single-cell indicator of osteoblastic human mesenchymal stem cell differentiation. *J. Biomech.* **47,** 2197–2204 (2014).

215. Bongiorno, T., Chojnowski, J. L., Lauderdale, J. D. & Sulchek, T. Cellular Stiffness as a Novel Stemness Marker in the Corneal Limbus. *Biophys. J.* **111,** 1761–1772 (2016).

216. Christoforou, N., Miller, R. A., Hill, C. M., Jie, C. C., McCallion, A. S. & Gearhart, J. D. Mouse ES cell–derived cardiac precursor cells are multipotent and facilitate identification of novel cardiac genes. *J. Clin. Invest.* **118,** 894–903 (2008).

217. Wachsstock, D. H., Schwartz, W. H. & Pollard, T. D. Affinity of alpha-actinin for actin determines the structure and mechanical properties of actin filament gels. *Biophys. J.* **65,** 205–214 (1993).

218. Lammerding, J., Fong, L. G., Ji, J. Y., Reue, K., Stewart, C. L., Young, S. G. & Lee, R. T. Lamins A and C but Not Lamin B1 Regulate Nuclear Mechanics*. *J. Biol. Chem.* **281,** 25768–25780 (2006).

219. Eckersley-Maslin, M. A., Bergmann, J. H., Lazar, Z. & Spector, D. L. Lamin A/C is Expressed in Pluripotent Mouse Embryonic Stem Cells. *Nucleus* **4,** 53–60 (2013).

220. Pajerowski, J. D., Dahl, K. N., Zhong, F. L., Sammak, P. J. & Discher, D. E. Physical plasticity of the nucleus in stem cell differentiation. *Proc. Natl. Acad. Sci.* **104,** 15619–15624 (2007).

221. Zhang, J., Rao, R. V., Spilman, P., Mangada, J., Xie, L., Vitelli, C., Gorostiza, O. F., Madden, D. T., Zeng, X., Jin, K., Hart, M. J., Bredesen, D. E. & Galvan, V. Endogenously EGFP-Labeled Mouse Embryonic Stem Cells. *Aging Dis.* **2,** 18–29 (2011).

222. Okabe, S., Forsberg-Nilsson, K., Spiro, A. C., Segal, M. & McKay, R. D. Development of neuronal precursor cells and functional postmitotic neurons from embryonic stem cells in vitro. *Mech. Dev.* **59,** 89–102 (1996).

223. Esue, O., Tseng, Y. & Wirtz, D. Alpha-actinin and filamin cooperatively enhance the stiffness of actin filament networks. *PloS One* **4,** e4411 (2009).

224. Sen, S., Dong, M. & Kumar, S. Isoform-specific contributions of alpha-actinin to glioma cell mechanobiology. *PloS One* **4,** e8427 (2009).

225. Batalov, I. & Feinberg, A. W. Differentiation of Cardiomyocytes from Human Pluripotent Stem Cells Using Monolayer Culture. *Biomark. Insights* **10,** 71–76 (2015).

226. Grancharova, T., Gerbin, K. A., Rosenberg, A. B., Roco, C. M., Arakaki, J. E., DeLizo, C. M., Dinh, S. Q., Donovan-Maiye, R. M., Hirano, M., Nelson, A. M., Tang, J., Theriot, J. A., Yan, C., Menon, V., Palecek, S. P., Seelig, G. & Gunawardane, R. N. A comprehensive analysis of gene expression changes in a high replicate and open-source dataset of differentiating hiPSC-derived cardiomyocytes. *Sci. Rep.* **11,** 15845 (2021).

227. Giannakis, M., Hodis, E., Jasmine Mu, X., Yamauchi, M., Rosenbluh, J., Cibulskis, K., Saksena, G., Lawrence, M. S., Qian, Z. R., Nishihara, R., Van Allen, E. M., Hahn, W. C., Gabriel, S. B., Lander, E. S., Getz, G., Ogino, S., Fuchs, C. S. & Garraway, L. A. RNF43 is frequently mutated in colorectal and endometrial cancers. *Nat. Genet.* **46,** 1264–1266 (2014).

228. Korff, S., Woerner, S. M., Yuan, Y. P., Bork, P., von Knebel Doeberitz, M. & Gebert, J. Frameshift mutations in coding repeats of protein tyrosine phosphatase genes in colorectal tumors with microsatellite instability. *BMC Cancer* **8,** 1–8 (2008).

229. Seshagiri, S., Stawiski, E. W., Durinck, S., Modrusan, Z., Storm, E. E., Conboy, C. B., Chaudhuri, S., Guan, Y., Janakiraman, V., Jaiswal, B. S., Guillory, J., Ha, C., Dijkgraaf, G. J. P., Stinson, J., Gnad, F., Huntley, M. A., Degenhardt, J. D., Haverty, P. M., Bourgon, R., Wang, W., Koeppen, H., Gentleman, R., Starr, T. K., Zhang, Z., Largaespada, D. A., Wu, T. D. & de Sauvage, F. J. Recurrent R-spondin fusions in colon cancer. *Nature* **488,** 660–664 (2012).

230. Shin, J.-W., Buxboim, A., Spinler, K. R., Swift, J., Christian, D. A., Hunter, C. A., Léon, C., Gachet, C., Dingal, P. C. D. P., Ivanovska, I. L., Rehfeldt, F., Chasis, J. A. & Discher, D. E. Contractile Forces Sustain and Polarize Hematopoiesis from Stem and Progenitor Cells. *Cell Stem Cell* **14,** 81–93 (2014).

231. Hu, L., Ni, F., Wang, X., Fay, M. E., Young, K. M., Lam, W. A., Sulchek, T. A. & Qu, C.-K. Decreased cell stiffness enhances leukemia development and progression. *Leukemia* **34,** 2493–2497 (2020).

232. Wang, K., Li, G., Read, A. T., Navarro, I., Mitra, A. K., Stamer, W. D., Sulchek, T. & Ethier, C. R. The relationship between outflow resistance and trabecular meshwork stiffness in mice. *Sci. Rep.* **8,** 5848 (2018).

233. Wang, K., Read, A. T., Sulchek, T. & Ethier, C. R. Trabecular meshwork stiffness in glaucoma. *Exp. Eye Res.* **158,** 3–12 (2017).

234. Li, G., Lee, C., Read, A. T., Wang, K., Ha, J., Kuhn, M., Navarro, I., Cui, J., Young, K., Gorijavolu, R., Sulchek, T., Kopczynski, C., Farsiu, S., Samples, J., Challa, P., Ethier, C. R. & Stamer, W. D. Anti-fibrotic activity of a rho-kinase inhibitor restores outflow function and intraocular pressure homeostasis. *eLife* **10,** e60831 (2021).

235. Santner, S. J., Dawson, P. J., Tait, L., Soule, H. D., Eliason, J., Mohamed, A. N., Wolman, S. R., Heppner, G. H. & Miller, F. R. Malignant MCF10CA1 cell lines derived from premalignant human breast epithelial MCF10AT cells. *Breast Cancer Res. Treat.* **65,** 101–110 (2001).

236. Mathur, A. B., Collinsworth, A. M., Reichert, W. M., Kraus, W. E. & Truskey, G. A. Endothelial, cardiac muscle and skeletal muscle exhibit different viscous and elastic properties as determined by atomic force microscopy. *J. Biomech.* **34,** 1545–1553 (2001).

237. Dahl Kris Noel, Ribeiro Alexandre J.S., & Lammerding Jan. Nuclear Shape, Mechanics, and Mechanotransduction. *Circ. Res.* **102,** 1307–1318 (2008).

238. Pajerowski, J. D., Dahl, K. N., Zhong, F. L., Sammak, P. J. & Discher, D. E. Physical plasticity of the nucleus in stem cell differentiation. *Proc. Natl. Acad. Sci. U. S. A.* **104,** 15619–15624 (2007).

239. Lombardi, M. L. & Lammerding, J. Altered mechanical properties of the nucleus in disease. *Methods Cell Biol.* **98,** 121–141 (2010).

240. Wolf, K. & Friedl, P. Molecular mechanisms of cancer cell invasion and plasticity. *Br. J. Dermatol.* **154,** 11–15 (2006).

241. Wolf, K., Wu, Y. I., Liu, Y., Geiger, J., Tam, E., Overall, C., Stack, M. S. & Friedl, P. Multi-step pericellular proteolysis controls the transition from individual to collective cancer cell invasion. *Nat. Cell Biol.* **9,** 893–904 (2007).

242. Zink, D., Fischer, A. H. & Nickerson, J. A. Nuclear structure in cancer cells. *Nat. Rev. Cancer* **4,** 677–687 (2004).

243. Khatau, S. B., Hale, C. M., Stewart-Hutchinson, P. J., Patel, M. S., Stewart, C. L., Searson, P. C., Hodzic, D. & Wirtz, D. A perinuclear actin cap regulates nuclear shape. *Proc. Natl. Acad. Sci.* **106,** 19017–19022 (2009).

244. Das, A., Barai, A., Monteiro, M., Kumar, S. & Sen, S. Nuclear softening is essential for protease-independent migration. *Matrix Biol.* **82,** 4–19 (2019).

245. Janota, C. S., Calero-Cuenca, F. J. & Gomes, E. R. The role of the cell nucleus in mechanotransduction. *Curr. Opin. Cell Biol.* **63,** 204–211 (2020).

246. Khatau, S. B., Kim, D.-H., Hale, C. M., Bloom, R. J. & Wirtz, D. The perinuclear actin cap in health and disease. *Nucleus* **1,** 337–342 (2010).

247. Friedl, P., Wolf, K. & Lammerding, J. Nuclear mechanics during cell migration. *Curr. Opin. Cell Biol.* **23,** 55–64 (2011).

248. Fu, Y., Chin, L. K., Bourouina, T., Liu, A. Q. & VanDongen, A. M. J. Nuclear deformation during breast cancer cell transmigration. *Lab. Chip* **12,** 3774–3778 (2012).

249. Beadle, C., Assanah, M. C., Monzo, P., Vallee, R., Rosenfeld, S. S. & Canoll, P. The Role of Myosin II in Glioma Invasion of the Brain. *Mol. Biol. Cell* **19,** 3357–3368 (2008).

250. Schoumacher, M., Goldman, R. D., Louvard, D. & Vignjevic, D. M. Actin, microtubules, and vimentin intermediate filaments cooperate for elongation of invadopodia. *J. Cell Biol.* **189,** 541–556 (2010).

251. Yamauchi, K., Yang, M., Jiang, P., Yamamoto, N., Xu, M., Amoh, Y., Tsuji, K., Bouvet, M., Tsuchiya, H., Tomita, K., Moossa, A. R. & Hoffman, R. M. Real-time in vivo dual-color imaging of intracapillary cancer cell and nucleus deformation and migration. *Cancer Res.* **65,** 4246–4252 (2005).

252. Jemal, A., Siegel, R., Ward, E., Murray, T., Xu, J., Smigal, C. & Thun, M. J. Cancer Statistics, 2006. *CA. Cancer J. Clin.* **56,** 106–130 (2006).

253. Goff, B. A., Mandel, L. S., Drescher, C. W., Urban, N., Gough, S., Schurman, K. M., Patras, J., Mahony, B. S. & Andersen, M. R. Development of an ovarian cancer symptom index. *Cancer* **109,** 221–227 (2007).

254. Davidson, B., Espina, V., Steinberg, S. M., Flørenes, V. A., Liotta, L. A., Kristensen, G. B., Tropé, C. G., Berner, A. & Kohn, E. C. Proteomic Analysis of Malignant Ovarian Cancer Effusions as a Tool for Biologic and Prognostic Profiling. *Clin. Cancer Res.* **12,** 791–799 (2006).

255. Thomázy, V. & Fésüs, L. Differential expression of tissue transglutaminase in human cells. *Cell Tissue Res.* **255,** 215–224 (1989).

256. Satpathy, M., Nakshatri, H. & Matei, D. Transglutaminase 2 is overexpressed in ovarian cancer and facilitates the adhesion of cancer cells to fibronectin. *Cancer Res.* **66,** 800–800 (2006).

257. Zhang, Y., Cao, L., Nguyen, D. & Lu, H. TP53 mutations in epithelial ovarian cancer. *Transl. Cancer Res.* **5,** (2016).

258. Yu, H.-J., Serebryannyy, L. A., Fry, M., Greene, M., Chernaya, O., Hu, W.-Y., Chew, T.-L., Mahmud, N., Kadkol, S. S., Glover, S., Prins, G., Strakova, Z. & Lanerolle, P. de. Tumor Stiffness Is Unrelated to Myosin Light Chain Phosphorylation in Cancer Cells. *PLOS ONE* **8,** e79776 (2013).

259. Serebryannyy, L. A., Parilla, M., Annibale, P., Cruz, C. M., Laster, K., Gratton, E., Kudryashov, D., Kosak, S. T., Gottardi, C. J. & de Lanerolle, P. Persistent nuclear actin filaments inhibit transcription by RNA polymerase II. *J. Cell Sci.* **129,** 3412–3425 (2016).

260. Liu, H., Wen, J., Xiao, Y., Liu, J., Hopyan, S., Radisic, M., Simmons, C. A. & Sun, Y. In Situ Mechanical Characterization of the Cell Nucleus by Atomic Force Microscopy. *ACS Nano* **8,** 3821–3828 (2014).

261. Guilluy, C., Osborne, L. D., Van Landeghem, L., Sharek, L., Superfine, R., Garcia-Mata, R. & Burridge, K. Isolated nuclei adapt to force and reveal a mechanotransduction pathway in the nucleus. *Nat. Cell Biol.* **16,** 376–381 (2014).

262. Kroemer, G., Galluzzi, L., Vandenabeele, P., Abrams, J., Alnemri, E. S., Baehrecke, E. H., Blagosklonny, M. V., El-Deiry, W. S., Golstein, P., Green, D. R., Hengartner, M., Knight, R. A., Kumar, S., Lipton, S. A., Malorni, W., Nuñez, G., Peter, M. E., Tschopp, J., Yuan, J., Piacentini, M., Zhivotovsky, B., Melino, G., & Nomenclature Committee on Cell Death 2009. Classification of cell death: recommendations of the Nomenclature Committee on Cell Death 2009. *Cell Death Differ.* **16,** 3–11 (2009).

263. Li, S., Chien, S. & Brånemark, P. I. Heat shock-induced necrosis and apoptosis in osteoblasts. *J. Orthop. Res. Off. Publ. Orthop. Res. Soc.* **17,** 891–899 (1999).

264. Honda, O., Kuroda, M., Joja, I., Asaumi, J., Takeda, Y., Akaki, S., Togami, I., Kanazawa, S., Kawasaki, S. & Hiraki, Y. Assessment of secondary necrosis of Jurkat cells using a new microscopic system and double staining method with annexin V and propidium iodide. *Int. J. Oncol.* **16,** 283–288 (2000).

265. Lai, C.-C., Shih, T.-P., Ko, W.-C., Tang, H.-J. & Hsueh, P.-R. Severe acute respiratory syndrome coronavirus 2 (SARS-CoV-2) and coronavirus disease-2019 (COVID-19): The epidemic and the challenges. *Int. J. Antimicrob. Agents* **55,** 105924 (2020).

266. Nanchal, R. S. & Truwit, J. D. Recent advances in understanding and treating acute respiratory distress syndrome. *F1000Research* **7,** F1000 Faculty Rev-1322 (2018).

267. Li, D., Ren, W., Jiang, Z. & Zhu, L. Regulation of the NLRP3 inflammasome and macrophage pyroptosis by the p38 MAPK signaling pathway in a mouse model of acute lung injury. *Mol. Med. Rep.* **18,** 4399–4409 (2018).

268. Man, S. M., Ekpenyong, A., Tourlomousis, P., Achouri, S., Cammarota, E., Hughes, K., Rizzo, A., Ng, G., Wright, J. A., Cicuta, P., Guck, J. R. & Bryant, C. E. Actin polymerization as a key innate immune effector mechanism to control Salmonella infection. *Proc. Natl. Acad. Sci. U. S. A.* **111,** 17588–17593 (2014).

269. Nagy, A., Rossant, J., Nagy, R., Abramow-Newerly, W. & Roder, J. C. Derivation of completely cell culture-derived mice from early-passage embryonic stem cells. *Proc. Natl. Acad. Sci. U. S. A.* **90,** 8424–8428 (1993).

270. Joza, N., Susin, S. A., Daugas, E., Stanford, W. L., Cho, S. K., Li, C. Y., Sasaki, T., Elia, A. J., Cheng, H. Y., Ravagnan, L., Ferri, K. F., Zamzami, N., Wakeham, A., Hakem, R., Yoshida, H., Kong, Y. Y., Mak, T. W., Zúñiga-Pflücker, J. C., Kroemer, G. & Penninger, J. M. Essential role of the mitochondrial apoptosis-inducing factor in programmed cell death. *Nature* **410,** 549–554 (2001).

271. Cerf, A., Cau, J.-C., Vieu, C. & Dague, E. Nanomechanical Properties of Dead or Alive Single-Patterned Bacteria. *Langmuir* **25,** 5731–5736 (2009).

272. Lam, W. A., Rosenbluth, M. J. & Fletcher, D. A. Chemotherapy exposure increases leukemia cell stiffness. *Blood* **109,** 3505–3508 (2007).

273. MacQueen, L. A., Thibault, M., Buschmann, M. D. & Wertheimer, M. R. Electromechanical deformation of mammalian cells in suspension depends on their cortical actin thicknesses. *J. Biomech.* **45,** 2797–2803 (2012).

274. Nikolaev, N. I., Müller, T., Williams, D. J. & Liu, Y. Changes in the stiffness of human mesenchymal stem cells with the progress of cell death as measured by atomic force microscopy. *J. Biomech.* **47,** 625–630 (2014).

275. Jeong, J., Frohberg, N. J., Zhou, E., Sulchek, T. & Qiu, P. Accurately tracking single-cell movement trajectories in microfluidic cell sorting devices. *PLOS ONE* **13,** e0192463 (2018).

276. Kim, K. S., Cho, C. H., Park, E. K., Jung, M.-H., Yoon, K.-S. & Park, H.-K. AFM-detected apoptotic changes in morphology and biophysical property caused by paclitaxel in Ishikawa and HeLa cells. *PloS One* **7,** e30066 (2012).